



**REGULATION AND SIGNALING OF PHOSPHOLIPASES:
THE LIGHT AT THE END OF THE TUNNEL**

FERNANDO SALGADO POLO

Regulation and cell signaling of phospholipases: the light at the end of the tunnel

Fernando Salgado Polo

COLOFON

Activity and signaling of phospholipases: the light at the end of the tunnel

PhD thesis, Utrecht University, The Netherlands

ISBN: 978-94-6469-064-4

Author: Fernando Salgado Polo

Cover design: María Dolores Polo Corrales (@Douleurspol)

Lay-out: Stefanie van den Herik || HerikMedia || herikmedia.nl

Printing: ProefschriftMaken || proefschriftmaken.nl

Printed with financial support from the Netherlands Cancer Institute.

Regulation and cell signaling of phospholipases:
the light at the end of the tunnel

Regulatie en celsignalering van fosfolipasen:
het licht aan het einde van de tunnel
(met een samenvatting in het Nederlands)

Fosfolipasas, su regulación y señalización celular:
la luz al final del túnel
(con resumen en español)

Proefschrift

ter verkrijging van de graad van doctor aan de
Universiteit Utrecht
op gezag van de
rector magnificus, prof. dr. H.R.B.M Kummeling,
ingevolge het besluit van het college voor promoties
in het openbaar te verdedigen op

maandag 31 oktober 2022 des middags te 2.15 uur

door

Fernando Salgado Polo

geboren op 28 april 1993
te Cáceres, Extremadura, Spanje

Promotor:

Prof. dr. A. Perrakis

Beoordelingscommissie:

Prof. dr. A.S. Akhmanova

Prof. dr. ir. B.M.T. Burgering

Dr. C. Jamieson

Dr. ir. B.J.C. Janssen

Prof. dr. T.K. Sixma

Paranimfen:

S.R. Bruekner

N.A. Reilly

Dit proefschrift werd medemogelijk gemaakt met financiële steun van Oncode Institute en de stichting Koningin Wilhelmina Fonds (KWF) voor de Nederlandse Kankerbestrijding.

To my family and friends for their never-ending support.

A mi familia y amigos por su apoyo constante y sin fin.

“Once an idea has taken hold of the brain,
it’s almost impossible to eradicate.”

Leonardo DiCaprio, Inception (2010)

«Una vez que una idea se ha apoderado del cerebro,
es casi imposible erradicarla».

Leonardo DiCaprio, Origen (2010)

Table of contents

Part A – Autotaxin (ATX)	9
A1 Introduction to autotaxin	11
A2 Lysophosphatidic acid produced by autotaxin acts as an allosteric modulator of its catalytic efficiency	23
A3 Imaging autotaxin in vivo with ¹⁸ F-labeled positron emission tomography ligands	61
A4 Structure-based design of a novel class of autotaxin inhibitors based on endogenous allosteric modulators	85
A5 The structural binding mode of the six autotaxin inhibitor types that differentially affect catalytic and non-catalytic functions	111
A6 A novel type IV autotaxin inhibitor ameliorates acute liver injury and nonalcoholic steatohepatitis	135
A7 Autotaxin facilitates selective LPA receptor signaling	165
A8 Additional publications on autotaxin	203
A9 General discussion of Part A	211
Part B – Glycerophosphodiester phosphodiesterases (GDPD)	221
B1 Introduction to glycerophosphodiester phosphodiesterases (GDPDs)	223
B2 Sequence-dependent trafficking and activity of GDE2, a GPI-specific phospholipase promoting neuronal differentiation	229
B3 Contactins are specifically cleaved by GDE3: new implications in glioblastoma	259
B4 General discussion of Part B	273
Addendum	279
Interview: First person – Fernando Salgado-Polo	280
List of publications	284
Curriculum vitae (English)	286
<i>Curriculum vitae</i> (español)	287
Summary	288
Nederlandse samenvatting	292
Resumen en español	296
Acknowledgements / Agradecimientos	300



Part A

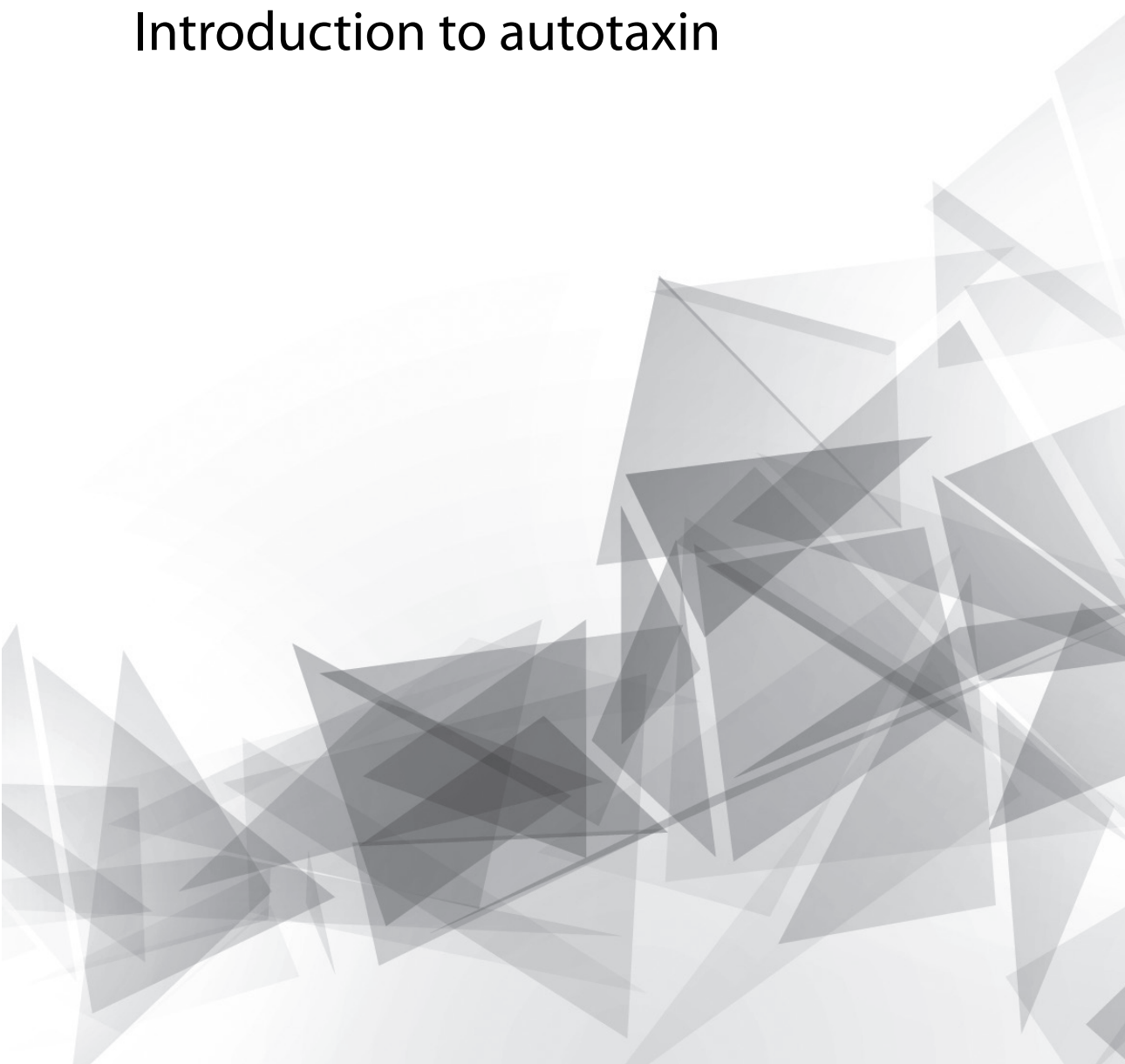
Autotaxin (ATX)





Chapter A1

Introduction to autotaxin



Autotaxin: the main extracellular LPA producer

Autotaxin (ATX or ENPP2) is an extracellular enzyme originally identified as a tumor cell autocrine motility factor. Structurally, ATX belongs to the ectonucleotide pyrophosphatase/phosphodiesterase (ENPP) family, which consists of seven members closely related to the bacterial NPP family^[1]. While ENPP1,3,4,5 specifically hydrolyze different nucleotide species, ENPP2,6,7 are specific for phospholipidic substrates. ATX is unique within the ENPP family, as it is the sole member showing lysophospholipase D (lysoPLD) activity (EC 3.1.4.39), making it the main responsible for the hydrolysis of lysophosphatidylcholine (2-acyl-*sn*-glycero-3-phosphocholines or LPC) to produce the bioactive lipid lysophosphatidic acid (monoacyl-*sn*-glycerol-3-phosphate or LPA) (Figure 1) ^{[2]-[4]}.

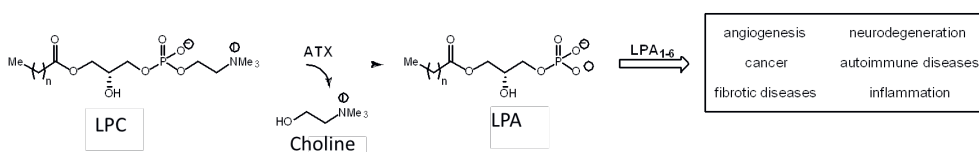


Figure 1. Schematic representation of the lysophospholipase D activity of ATX on LPC, which releases LPA and choline. The resulting LPA can act on its cognate LPA receptors and trigger cellular responses, such as fibrosis and inflammation.

The ATX/LPA signaling axis

LPC is the natural substrate hydrolyzed by ATX into choline, its polar headgroup, and LPA^[2]. Structurally, LPA contains a phosphate headgroup and one acyl chain covalently bound to the glycerol backbone, which can occur in positions *sn*-1 and *sn*-2. Physiologically, both LPC and LPA are present as distinct species that differ in chain length and saturation, and represent a minor phospholipid type in lipid bilayers ($\leq 3\%$) and in blood plasma (8-12%). Normal LPC plasma concentrations are approximately 200 μM in humans^[4], mostly produced by the liver from partial hydrolysis of phosphatidylcholine catalyzed by phospholipase A₂^[5]. Once in plasma, LPC is mainly transported by bovine serum albumin (BSA), and can be quickly taken up by cells and reacylated in the lyso position to form new PC that can be incorporated in lipid bilayers^[6].

Bioactive LPA is mainly produced in plasma by ATX catalytic activity. Inhibition of ATX leads to a rapid decrease in circulating LPA, and abolishes the effects of LPC on migration and survival^[7]. Thus, LPC signaling effects are ultimately determined by ATX activity converting it to LPA. LPA is an active albumin-bound component of serum, but it can also be found in saliva, follicular fluid and malignant effusions, among others. As opposed to membrane-forming lipids, LPA has not been detected to play a role in membrane disruption, as all its functions occur via cell signaling, where it mediates a wide variety of growth factor-like

functions in almost every mammalian cell type^[8].

The cell signaling functions of extracellular LPA are triggered once it is recognized by one of the six LPA receptors (LPA-R) identified to date: LPA₁₋₆^{[9]-[11]}. LPA-Rs are G protein-coupled receptors (GPCRs) that can trigger numerous downstream signaling pathways upon agonist binding, including those mediated by cyclic AMP (cAMP), the AKT or ERK kinases, and Ras and Rho family GTPases^[9]. These pathways enact diverse processes ranging from migration and proliferation to wound healing and cytokine production^[12]. However, final signaling output will greatly depend on plasma LPA concentration, which depends on its dephosphorylation by membrane-bound lipid phosphate phosphatases (LPPs)^[13]. LPA has a short half-life of approximately 3 minutes in mice; thus, it needs to be delivered optimally upon production to reach its recipient LPA-Rs^{[13], [14]}. Ultimately, the signaling effect of bioactive LPA will depend on the balance of LPC hydrolysis by lysoPLDs and dephosphorylation by LPPs. To ensure signaling efficiency, it has been hypothesized that ATX could play a role in delivering LPA to the cell surface, in a mechanism called juxtacrine signaling^[15].

Pathophysiology of the ATX/LPA signaling axis

The ATX/LPA signaling axis is vital for embryonic development and has been implicated in many (patho)physiological processes, including vascular development^[16], cancer metastasis, and other human diseases, such as fibrosis^[17] and cholestatic pruritus^[18]. Moreover, the ATX/LPA signaling takes place in the cancer cell microenvironment, as it has been reported in various cancers such as breast, ovarian and melanoma. Accordingly, increased expression of ATX or individual LPA-Rs has been associated with enhanced tumor progression, aggressiveness, angiogenesis, metastasis and chemo-resistance in mouse models^[19]. In this regard, the activation of the ATX/LPA signaling axis is necessary to promote neoplastic transformation of cells that trigger the transition to a metastatic state, whereas LPA-R deficiency has been shown to have a protective effect on colon carcinogenesis^[20].

Autotaxin's structure & the tripartite site

ATX is translated as a pre-proenzyme, containing an N-terminal signal peptide followed by an additional octapeptide^[21]. Firstly, the signal peptide, necessary to target ATX for secretion, is cleaved by a signal peptidase. Secondly, the resulting proprotein requires the removal of the octapeptide by proprotein convertases, such as furin, creating the active form of ATX. This proteolytically processed ATX is present in plasma, and shows its native folding and structural domains^[21] (Fig.2A). Starting from the N-terminus of ATX, there

are two somatomedin B (SMB)-like domains, which are followed by the central catalytic phosphodiesterase (PDE) domain, and an inactive nuclease-like domain next to the C-terminus (Fig.2A). Within the PDE domain, ATX presents a bimetallic active site with two Zn^{2+} atoms, and resembles that of other members of the alkaline phosphatase family^[15]. The PDE domain has a tripartite binding site composed of (i) a catalytic bimetallic site next to a hydrophilic shallow groove that accommodates the glycerol moiety of lipid substrates, (ii) a hydrophobic pocket that binds acyl chains, and (iii) a partially hydrophobic tunnel in a T-junction leading to the other side of the PDE domain^{[15], [22]}. Importantly, the tunnel binds steroid molecules^[23], and has been proposed to serve as an 'exit channel' for LPA^{[22], [24]}.

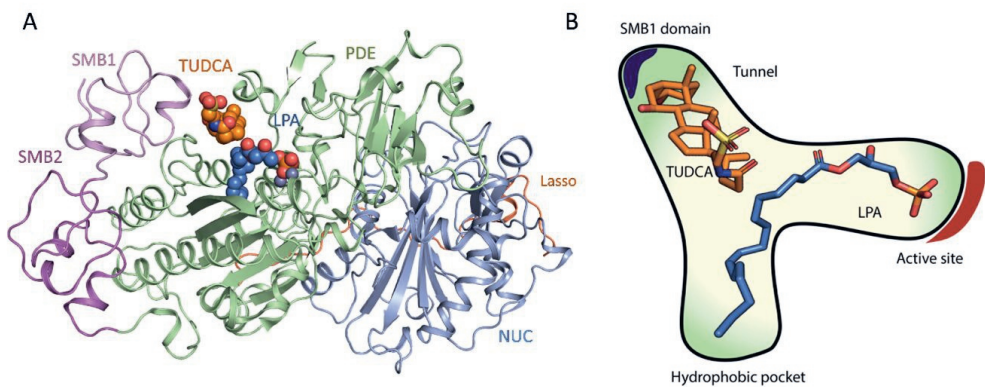


Figure 2. Structure of ATX and its tripartite site bound to LPA and the bile salt TUDCA. (A) Crystal structure of rat ATX bound to bile salts (PDB ID 5dlw). ATX presents four distinct domains: two somatomedin B-like domains (SMB-1 and SMB-2), the active catalytic phosphodiesterase (PDE) domain, and an inactive nuclease-like domain. (B) Cartoon representation of ATX tripartite site, consisting of a catalytic site, a hydrophobic pocket and a tunnel that acts as an allosteric regulator of ATX activity.

Autotaxin's activity

Several assays have been developed over the last 10 years to evaluate ATX activity. There are two classes of activity assays depending on whether they use the physiological substrate or unnatural ATX substrates^[25]. The first class of assays is based on the hydrolysis of LPC by ATX into the products LPA and choline. These products can be measured by employing liquid chromatography-tandem mass spectrometry (LCMS), radiometry, colorimetry or fluorimetry. The fluorimetric measure of ATX activity is a commonly used method consisting of two coupling enzymes: choline oxidase and horseradish peroxidase (HRP)^[26]. In this assay, choline oxidase converts choline into betaine and hydrogen peroxide, which

in turn can be used by HRP to oxidize homovanillic acid (HVA), resulting in its dimerization and fluorophoric state. (Figure 3)^[26].

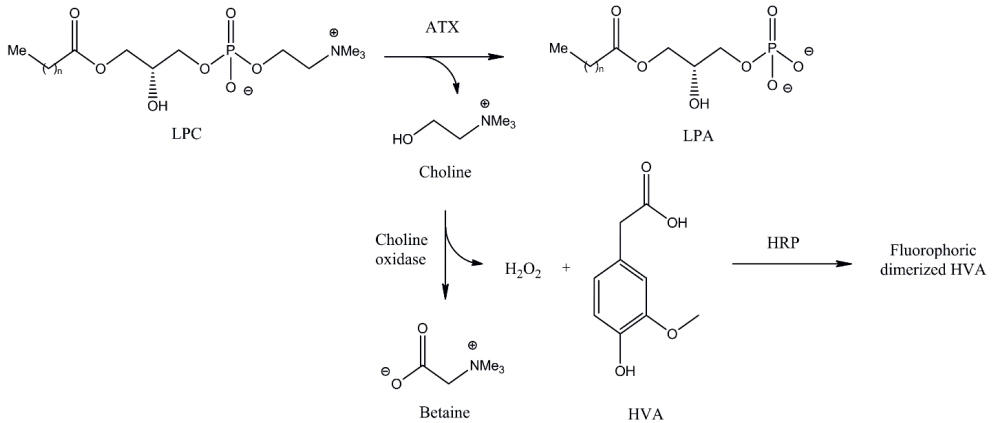


Figure 3. Choline release coupled reaction to measure ATX activity.

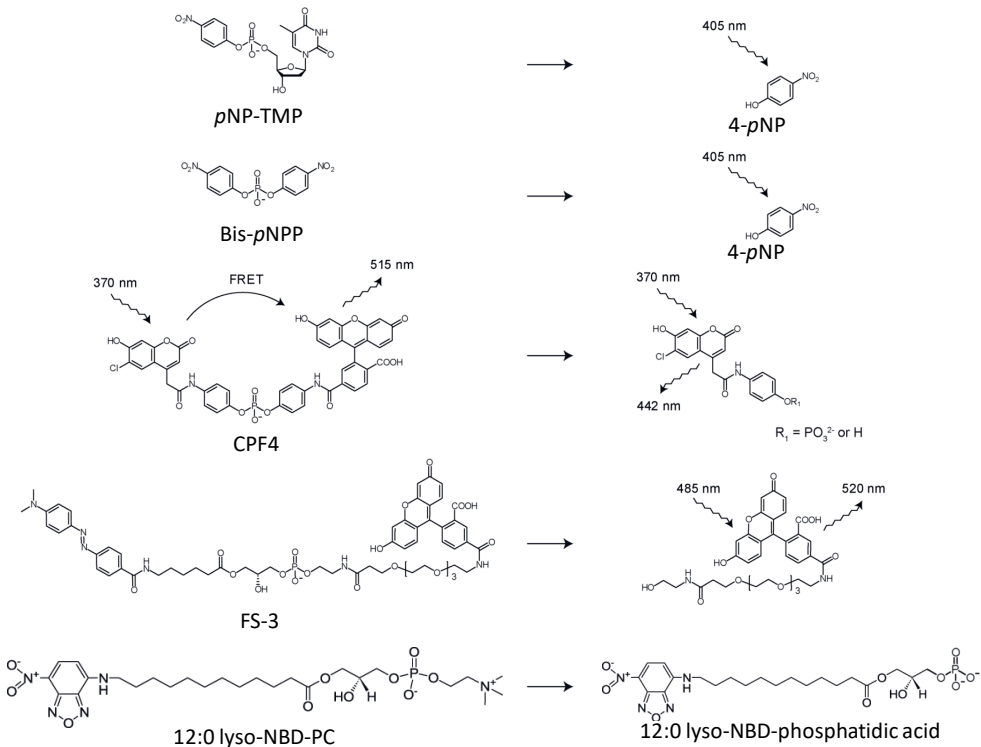


Figure 4. Main synthetic substrates available to study ATX catalytic activity and their subsequent products that can be measured after cleavage.

The second method measures ATX activity using synthetic substrates, which allows a direct measurement of the phosphodiesterase activity without additional enzymes. There is a wide variety of unnatural substrates, including the nucleotide thymidine 5′monophosphate *p*-nitrophenyl ester (*p*NP-TMP)^[2], bis(*p*-nitrophenyl) phosphate (bis-*p*NPP)^[27], the Förster resonance energy transfer (FRET) ligand CPF4^[28], the fluorogenic substrate 3 (FS-3)^[29], and the fluorescent probe lyso-NBD-PC (Figure 4)^[29]. These assays are widely used to screen through inhibitors for ATX as they have a low cost and provide a direct readout^[30].

Autotaxin’s inhibitor family

The structural characterization of the ATX tripartite site (Fig.2B) has created a remarkable potential for selective inhibitor design^{[31]–[33]} that includes lipid-based inhibitors^[34], DNA aptamers^[35] and small molecules. The latter can be classified in four distinct types depending on their binding modes to the tripartite site^[36] (Fig.5). Type I inhibitors mimic the LPC mode of binding and include HA155 ($IC_{50} = 5.7 \text{ nM}$)^[3] and PF-8380 ($IC_{50} = 1.7 \text{ nM}$)^[37], which have been also validated to lower LPA levels in vivo. Type II ATX inhibitors obstruct lipid binding to the hydrophobic pocket, such as PAT-078 and PAT-494^[32]. Type III inhibitors occupy the allosteric regulatory tunnel, modulating ATX activity by non-competitive inhibition, such as the steroids 7 α -hydroxycholesterol, tauroursodeoxycholic acid (TUDCA) ($IC_{50} = 11 \text{ }\mu\text{M}$) or ursodeoxycholic acid (UDCA) ($IC_{50} = 9 \text{ }\mu\text{M}$)^[23].

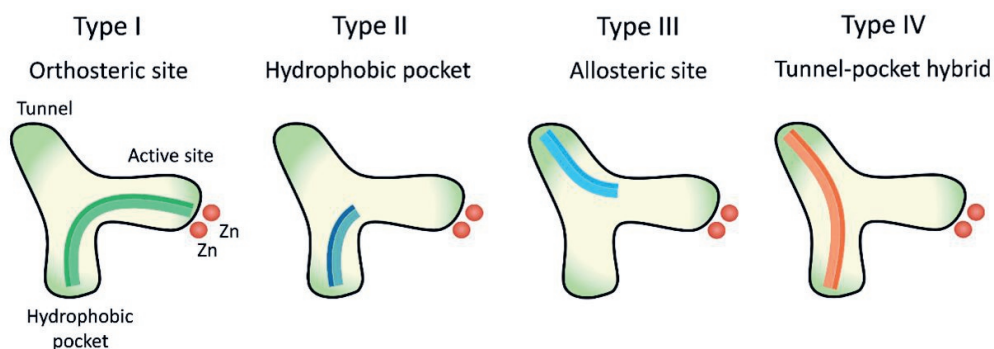


Figure 5. The four types of ATX small molecule inhibitors in relation to their binding mode.

Based on the binding mode of pocket-occupying type I and tunnel-binding type III inhibitors, efforts were made to synthesize the novel tunnel-pocket hybrids, or type IV inhibitors. These were initially designed by fusing functional fragments of type I and type III inhibitors, which resulted in Cpd17 ($IC_{50} = 14 \text{ nM}$)^[38], but were also obtained by serendipity followed by specific structure-based design, as is the case of GLPG1690^[39]. In

the past years, studies on type III and type IV inhibitors have shown that the ATX tunnel is a novel allosteric site modulating ATX activity. This modulation has been hypothesized to occur by disturbing the catalytic cleavage of substrates and/or by modulating LPA product uptake and its delivery to its cognate LPARs^[23]. In such a mechanism, ATX not only drives the formation of LPA, but also ensures specificity in LPA signaling. However, the mechanisms underlying tunnel modulation have not been characterized.

Scope of Part A of this thesis

In light of the crystal structure of ATX, I wondered how LPA was able to modulate the activity of ATX, as it was a controversial topic in the field. In **Chapter A2**, we performed a bottom-up kinetic, biophysical and molecular dynamics study to elucidate (i) if the LPA molecules produced by ATX could bind at the tunnel, and (ii) if its effect could be summarized in a single, elegant and comprehensive kinetic model.

In **Chapter A3**, we wanted to explore the potential of the (tunnel-pocket-binding) type IV compounds for non-invasive *in vivo* detection and quantitation of ATX. For that, we collaborated with the group of dr. Steven Liang in Harvard Medical School to synthesize and characterize fluorinated type IV compounds. These would next be used as positron emission tomography (PET) radiotracers for ATX detection in *in vivo* liver disease models.

Considering the fact than only tunnel-binding (*i.e.* type III and IV) ATX inhibitors have reached clinical trials, we decided to produce a novel inhibitor binding mode. In **Chapter A4**, we aimed to synthesize, crystallize and characterize, both *in vitro* and in cell-based assays, the tunnel-active site binders, or type V ATX inhibitors. For this work, we collaborated with the University of Strathclyde, Glasgow.

As this research was expanding on the already 20-year-old ATX inhibitor family, in **Chapter A5**, we decided to comprehensively analyze all their co-crystal structures. In this review, we classified all ATX-binding compounds into distinct inhibitor types based on their binding modes within the tripartite site.

Together with the group of dr. Ruchi Bansal in the University of Twente, we wanted to evaluate the therapeutic potential of type I and type IV ATX inhibitors in liver disease. Thus, in **Chapter A6**, I present an *in vitro* and cell-based study where we compared the potential benefit of type IV over type I compounds. Next, the efficacy of type IV Cpd17 was extensively studied in two *in vivo* mouse models.

In **Chapter A7**, I retrace my steps to the results from Chapter 2 to answer a crucial question

in the field: does the ATX tunnel play a role in LPA signaling? To address this, I wanted to first analyze the signaling output of LPA in cells expressing or lacking ATX expression. Next, I aimed to study the effect of ATX mutants and ATX inhibitors on LPA signaling in inducible cells only expressing a single LPA receptor at the time. Lastly, together with the Belgo-Dutch company Galapagos NV, we contrasted two low nanomolar-affinity inhibitors in an *in vivo* fibrosis model. The results of this chapter are critical regarding their implications for the ATX/LPA signaling axis, as well as the clinical benefit of blocking the ATX tunnel.

Next, in **Chapter A8**, I summarize my contributions in five independent projects related to the ENPP protein family, ATX inhibitor design, homology-based structural analysis, and immunotherapy. Lastly, the various results of Part A of this thesis are discussed in **Chapter A9**, commenting on their implications and future research outlook.

References

- [1] R. Borza, F. Salgado-Polo, W. H. Moolenaar, A. Perrakis, *J. Biol. Chem.*, **2022**, 298, 101526.
- [2] A. Tokumura, E. Majima, Y. Kariya, K. Tominaga, K. Kogure, K. Yasuda, K. Fukuzawa, *J. Biol. Chem.*, **2002**, 277, 39436.
- [3] H. M. H. G. Albers, A. Dong, L. A. van Meeteren, D. A. Egan, M. Sunkara, E. W. van Tilburg, K. Schuurman, O. van Tellingen, A. J. Morris, S. S. Smyth, W. H. Moolenaar, H. Ovaa, *Proc. Natl. Acad. Sci. U. S. A.*, **2010**, 107, 7257.
- [4] P. G. Munder, M. Modolell, R. Andressen, H. U. Weltzien, O. Westphal, *Springer Semin. Immunopathol.*, **1979**, 2, 187..
- [5] J. Aoki, A. Taira, Y. Takanezawa, Y. Kishi, K. Hama, T. Kishimoto, K. Mizuno, K. Saku, R. Taguchi, H. Arai, *J. Biol. Chem.*, **2002**, 277, 48737.
- [6] M. Croset, N. Brossard, a Polette, M. Lagarde, *Biochem. J.*, **2000**, 345 Pt 1, 61.
- [7] M. G. K. Benesch, Y. M. Ko, T. P. W. McMullen, D. N. Brindley, *FEBS Lett.*, **2014**, 588, 2712.
- [8] W. H. Moolenaar, L. A. Van Meeteren, B. N. G. Giepmans, *BioEssays*, **2004**, 26, 870.
- [9] Y. C. Yung, N. C. Stoddard, J. Chun, *J. Lipid Res.*, **2014**, 55, 1192.
- [10] R. Taniguchi, A. Inoue, M. Sayama, A. Uwamizu, K. Yamashita, K. Hirata, M. Yoshida, Y. Tanaka, H. E. Kato, Y. Nakada-Nakura, Y. Otani, T. Nishizawa, T. Doi, T. Ohwada, R. Ishitani, J. Aoki, O. Nureki, *Nature*, **2017**, 548, 356.
- [11] J. E. Chrencik, C. B. Roth, M. Terakado, H. Kurata, R. Omi, Y. Kihara, D. Warshaviak, S. Nakade, G. Asmar-Rovida, M. Mileni, H. Mizuno, M. T. Griffith, C. Rodgers, G. W. Han, J. Velasquez, J. Chun, R. C. Stevens, M. A. Hanson, *Cell*, **2015**, 161, 1633.
- [12] L. A. van Meeteren, W. H. Moolenaar, *Prog. Lipid Res.*, **2007**, 46, 145..
- [13] J. L. Tomsig, A. H. Snyder, E. V. Berdyshev, A. Skobeleva, C. Mataya, V. Natarajan, D. N. Brindley, K. R. Lynch, *Biochem. J.*, **2009**, 419, 611.
- [14] H. M. H. G. Albers, L. J. D. Hendrickx, R. J. P. van Tol, J. Hausmann, A. Perrakis, H. Ovaa, *J. Med. Chem.*, **2011**, 54, 4619.
- [15] J. Hausmann, S. Kamtekar, E. Christodoulou, J. E. Day, T. Wu, Z. Fulkerson, H. M. H. G. H. G. Albers, L. A. Van Meeteren, A. J. S. S. Houben, L. Van Zeijl, S. Jansen, M. Andries, T. Hall, L. E. Pegg, T. E. Benson, M. Kasiem, K. Harlos, C. W. V. Vander Kooi, S. S. Smyth, H. Ovaa, M. Bollen, A. J. Morris, W. H. Moolenaar, A. Perrakis, L. A. Van Meeteren, L. Van Zeijl, S. Jansen, M. Andries, T. Hall, L. E. Pegg, T. E. Benson, M. Kasiem, K. Harlos, C. W. V. Vander Kooi, S. Susan, H. Ovaa, M. Bollen, A. J. Morris, W. H. Moolenaar, A. Perrakis, *Nat. Struct. Mol. Biol.*, **2011**, 18, 198.
- [16] L. A. van Meeteren, P. Ruurs, C. Stortelers, P. Bouwman, M. A. van Rooijen, J. P. Pradere, T. R. Pettit, M. J. O. Wakelam, J. S. Saulnier-Blache, C. L. Mummery, W. H. Moolenaar, J. Jonkers, *Mol. Cell. Biol.*, **2006**, 26, 5015.
- [17] H. Kanda, R. Newton, R. Klein, Y. Morita, M. D. Gunn, S. D. Rosen, *Nat. Immunol.*, **2008**, 9, 415.
- [18] A. E. Kremer, J. J. W. W. Martens, W. Kulik, F. Ruëff, E. M. M. Kuiper, H. R. van Buuren, K. J. van Erpecum, J. Kondrackiene, J. Prieto, C. Rust, V. L. Geenes, C. Williamson, W. H. Moolenaar, U. Beuers, R. P. J. Oude Elferink, *Gastroenterology*, **2010**, 139, 1018.e1.

- [19] O. Peyruchaud, L. Saier, R. Leblanc, *Cancers (Basel)*, **2019**.
- [20] S. Khurana, A. Tomar, S. P. George, Y. Wang, M. R. Siddiqui, H. Guo, G. Tigyi, S. Mathew, *Exp. Cell Res.*, **2008**, 314, 530.
- [21] S. Jansen, *J. Cell Sci.*, **2005**, 118, 3081.
- [22] H. Nishimasu, S. Okudaira, K. Hama, E. Mihara, N. Dohmae, A. Inoue, R. Ishitani, J. Takagi, J. Aoki, O. Nureki, *Nat. Struct. Mol. Biol.*, **2011**, 18, 205.
- [23] W. Keune, J. Hausmann, R. Bolier, D. Tolenaars, A. Kremer, T. Heidebrecht, R. Joosten, M. Sunkara, A. Morris, E. Matas-Rico, W. Moolenaar, R. Oude Elferink, A. Perrakis, *Nat. Commun.*, **2016**, 7, 11248.
- [24] F. Salgado-Polo, A. Fish, M.-T. Matsoukas, T. Heidebrecht, W.-J. Keune, A. Perrakis, *J. Biol. Chem.*, **2018**, 293, jbc. RA118.004450.
- [25] H. M. H. G. Albers, H. Ovaa, *Chem. Rev.*, **2012**, 112, 2593.
- [26] S. Imamura, Y. Horiuti, *J. Biochem.*, **1978**, 83, 677..
- [27] F. CG, C. Bigman, R. Richardson, L. van Meeteren, W. Moolenaar, G. Prestwich, *Org. Lett.*, **2006**, 8, 2023.
- [28] H. Takakusa, K. Kikuchi, Y. Urano, S. Sakamoto, K. Yamaguchi, T. Nagano, *J. Am. Chem. Soc.*, **2002**, 124, 1653..
- [29] L. P. Saunders, W. Cao, W. C. Chang, R. a Albright, D. T. Braddock, E. M. De La Cruz, *J. Biol. Chem.*, **2011**, 286, 30130.
- [30] L. A. Van Meeteren, P. Ruurs, E. Christodoulou, J. W. Goding, H. Takakusa, K. Kikuchi, A. Perrakis, T. Nagano, W. H. Moolenaar, *J. Biol. Chem.*, **2005**, 280, 21155.
- [31] J. Hausmann, W.-J. Keune, A. L. Hipgrave Ederveen, L. van Zeijl, R. P. Joosten, A. Perrakis, *J. Struct. Biol.*, **2016**, 195, 199..
- [32] A. J. Stein, G. Bain, P. Prodanovich, A. M. Santini, J. Darlington, N. M. P. Stelzer, R. S. Sidhu, J. Schaub, L. Goulet, D. Lonergan, I. Calderon, J. F. Evans, J. H. Hutchinson, D. H. Johnson, B. M. Shrier, J. S. O. Neal, J. A. Knutzen, *Mol. Pharmacol.*, **2015**, 88, 982.
- [33] P. Shah, A. Cheasty, C. Foxton, T. Raynham, M. Farooq, I. Gutierrez, A. Lejeune, M. Pritchard, A. Turnbull, L. Pang, P. Owen, S. Boyd, A. I. J. Stowell, A. M. Jordan, N. M. Hamilton, J. R. Hitchin, M. Stockley, E. MacDonald, M. Quesada, E. Trivier, J. Skeete, H. Ovaa, W. Moolenaar, H. Ryder, *Bioorg. Med. Chem. Lett.*, **2016**, 26, 5403..
- [34] K. R. Lynch, T. L. Macdonald, 2013
- [35] K. Kato, H. Ikeda, S. Miyakawa, S. Futakawa, Y. Nonaka, M. Fujiwara, S. Okudaira, K. Kano, J. Aoki, J. Morita, R. Ishitani, H. Nishimasu, Y. Nakamura, O. Nureki, *Nat. Struct. Mol. Biol.*, **2016**, 23, 395.
- [36] A. Joncour, N. Desroy, C. Housseman, X. Bock, N. Bienvenu, L. Chereil, V. Labeguere, C. Peixoto, D. Annot, L. Lepissier, J. Heiermann, W. J. Hengeveld, G. Pilzak, A. Monjardet, E. Wakselman, V. Roncoroni, S. Le Tallec, R. Galien, C. David, N. Vandervoort, T. Christophe, K. Conrath, M. Jans, A. Wohlkonig, S. Soror, J. Steyaert, R. Touitou, D. Fleury, L. Vercheval, P. Mollat, N. Triballeau, E. Van Der Aar, R. Brys, B. Heckmann, *J. Med. Chem.*, **2017**, 60, 7371.

- [37] J. Gierse, A. Thorarensen, K. Beltey, E. Bradshaw-pierce, L. Cortes-burgos, T. Hall, A. Johnston, M. Murphy, O. Nemirovskiy, S. Ogawa, L. Pegg, M. Pelc, M. Prinsen, M. Schnute, J. Wendling, S. Wene, R. Weinberg, A. Wittwer, B. Zweifel, J. Masferrer, *J. Pharmacol. Exp. Ther.*, **2010**, *2*, 310.
- [38] W. J. Keune, F. Potjewyd, T. Heidebrecht, F. Salgado-Polo, S. J. F. Macdonald, L. Chelvarajan, A. Abdel Latif, S. Soman, A. J. Morris, A. J. B. Watson, C. Jamieson, A. Perrakis, *J. Med. Chem.*, **2017**, *60*, 2006.
- [39] N. Desroy, C. Housseman, X. Bock, A. Joncour, N. Bienvenu, L. Cherel, V. Labeguere, E. Rondet, C. Peixoto, J. Grassot, O. Picolet, D. Annoot, N. Triballeau, A. Monjardet, E. Wakselman, V. Roncoroni, S. Le Tallec, R. Blanque, C. Cottreaux, N. Vandervoort, T. Christophe, P. Mollat, M. Lamers, M. Auberval, B. Hrvacic, J. Ralic, L. Oste, E. van der Aar, R. Brys, B. Heckmann, *J. Med. Chem.*, **2017**, *60*, 3580..



Chapter A2

Lysophosphatidic acid produced by autotaxin acts as an allosteric modulator of its catalytic efficiency

Fernando Salgado-Polo,¹ Alex Fish,¹ Minos-Timotheos Matsoukas,^{1,2} Tatjana Heidebrecht,¹ Willem-Jan Keune,¹ and Anastassis Perrakis^{1,*}

Affiliations:

¹ Department of Biochemistry, The Netherlands Cancer Institute, Plesmanlaan 121, 1066CX Amsterdam, the Netherlands.

² Department of Pharmacy, University of Patras, 26504, Patras, Greece.

* Correspondence: a.perrakis@nki.nl.

Based on:

Journal of Biological Chemistry. 2018, 293(37): 14312-14327.

Abstract

Autotaxin is a secreted glycoprotein and the only member of the ectonucleotide pyrophosphatase/phosphodiesterase family that converts lysophosphatidylcholine (LPC) into lysophosphatidic acid (LPA). LPA controls key responses such as cell migration, proliferation, and survival, implicating ATX-LPA signaling in various (patho)physiological processes and establishing it as a drug target. ATX structural and functional studies have revealed an orthosteric and an allosteric site, called the “pocket” and the “tunnel,” respectively. However, the mechanisms in allosteric modulation of ATX’s activity as a lysophospholipase D are unclear. Here, using the physiological LPC substrate, a new fluorescent substrate, and diverse ATX inhibitors, we revisited the kinetics and allosteric regulation of the ATX catalytic cycle, dissecting the different steps and pathways leading to LPC hydrolysis. We found that ATX activity is stimulated by LPA and that LPA activates ATX lysophospholipase D activity by binding to the ATX tunnel. A consolidation of all experimental kinetics data yielded a comprehensive catalytic model supported by molecular modelling simulations, and suggested a positive feedback mechanism that is regulated by the abundance of the LPA products activating hydrolysis of different LPC species. Our results complement and extend the current understanding of ATX hydrolysis in light of the allosteric regulation by ATX-produced LPA species, and have implications for the design and application of both orthosteric and allosteric ATX inhibitors.

Introduction

Autotaxin (ATX or ENPP2) is a secreted glycoprotein and a unique member of the ectonucleotide pyrophosphatase/phosphodiesterase (ENPP) family^[1]. It is the only ENPP family member with lysophospholipase D (lysoPLD) activity (EC 3.1.4.39), and it is the main enzyme responsible for the hydrolysis of lysophosphatidylcholine (2-acyl-*sn*-glycero-3-phosphocholine or LPC) to produce the bioactive lipid lysophosphatidic acid (monoacyl-*sn*-glycerol-3-phosphate or LPA)^{[2]-[4]}. LPA acts as a ligand for several LPA receptors (LPARs) showing overlapping activities. The ATX-LPA signaling axis is vital for embryonic development and has been implicated in many (patho)physiological processes, which include vascular development^[5], cancer metastasis^[6], and other human diseases, such as fibrosis^[7] and cholestatic pruritus^[8]. ATX is translated as a pre-proenzyme that is secreted to plasma upon its proteolytic processing, resulting in its native structural domains^{[9], [10]}. Close to the N-terminus, ATX presents two somatomedin B (SMB)-like domains, which are followed by the central catalytic phosphodiesterase (PDE) domain, and an inactive nuclease-like domain. Catalysis occurs in a bimetallic active site presenting two Zn²⁺ atoms, and resembles that of other members of the alkaline phosphatase family^[11]. The catalytic site of ATX is organized in a tripartite binding site, where the active site is followed by a shallow hydrophilic groove that accommodates the glycerol moiety of lipid substrates, and nucleotide substrates. This groove leads to a T-junction and two separate paths: a hydrophobic pocket where the acyl chain of the lipid substrate can bind^{[11]-[13]}, and a tunnel, also called in literature “hydrophobic channel”, leading to the other side of the PDE domain^[13]. The open tunnel is defined by the PDE and the SMB-1 domains and presents both hydrophobic and hydrophilic residues on its inner walls^[11].

ATX activity measurements often utilize specific synthetic unnatural fluorescent substrates that allow direct measurement of the phosphodiesterase activity^[14]: bis(*p*-nitrophenyl) phosphate (bis-*p*NPP)^[15], CPF4^[16], thymidine 5′monophosphate *p*-nitrophenyl (*p*NP-TMP)^[2], thymidine 5′monophosphate *p*-nitrophenyl (*p*NP-TMP)^[17], and the fluorescent probe 12-(*N*-methyl- *N*-(7-nitrobenz-2-oxa-1,3-diazol-4-yl)) (NBD)-LPC^[18]. Although such synthetic substrates are invaluable for inhibitor development, kinetic studies that aim to describe the physiological activity of ATX, should focus on the natural substrates^{[15], [19]}. Hydrolysis of the physiological substrate is commonly detected by a fluorimetric method consisting of two coupling enzymes: choline oxidase and horseradish peroxidase (HRP) (Fig.1)^[20]. In this assay, choline oxidase converts choline into betaine and hydrogen peroxide, which HRP in turn uses to oxidize homovanillic acid (HVA), causing dimerization of HVA, allowing to reach its fluorophoric state^[20]. This indirect fluorescence-based method is the only assay to measure ATX catalytic activity towards its physiological substrate.

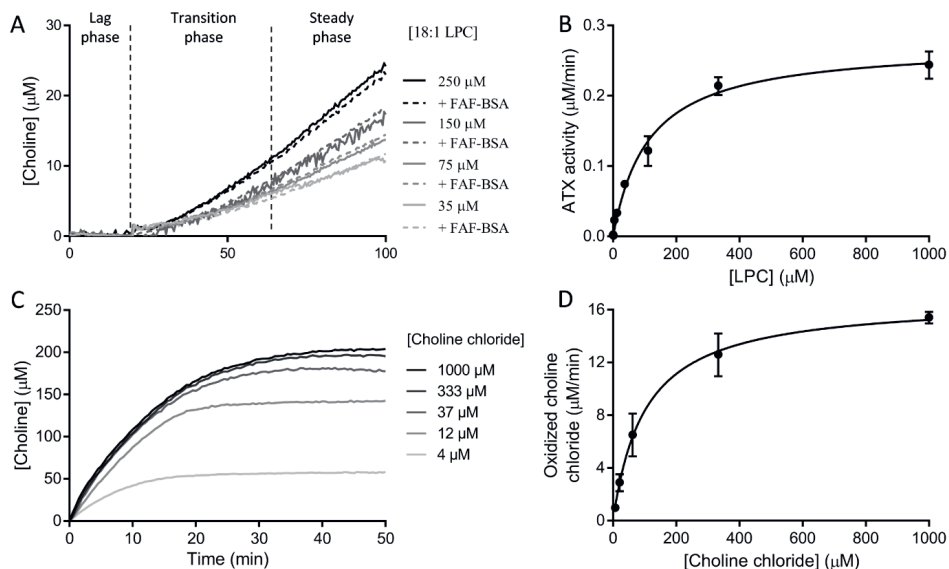


Figure 1. Enzyme kinetics described by ATX and choline oxidase for the hydrolysis of their physiological substrates. (A) The kinetics of ATX lysoPLD activity (20 nM) on LPC result in a double exponential-sigmoid choline secretion that can be measured by a coupled reaction with choline oxidase and HRP. This behaviour is independent of the presence of delipidated BSA acting as an LPC vehicle. (B) Michaelis-Menten kinetics derived from the linear part of lysoPLD activity measurements, as the ones shown in (A). (C) Choline chloride oxidation by choline oxidase follows a single exponential kinetics. (D) Michaelis-Menten kinetics for choline oxidase. In all cases, 1 U/ml choline oxidase and 1 U/ml HRP were used for the coupled assay. Data represent the averaged data of triplicate measurements.

An early study on ATX activity had put forward a model where LPA acts as an inhibitor of catalysis^[15]. Although that stands unquestioned for artificial ATX substrates (e.g. *p*NP-TMP and FS3), recent experiments from other groups^{[15], [18]}, could not corroborate a role of LPA in product inhibition of LPC hydrolysis. Importantly, a kinetic analysis by Saunders and colleagues reported on the substrate-specific kinetics of ATX towards NBD-LPC and FS-3 and provided valuable insight into the catalytic cycle of ATX^[18]. Their results showed that 12:0 NBD-LPC binding and hydrolysis were slow and rate-limiting, and provided clear evidence for a model where catalysis first leads to product release of choline and is followed by release of 12:0 NBD-LPA. This mechanism is also supported by subsequent structural studies that support an associative two-step in-line displacement mechanism^[21]. The slow release of LPA, taking place in the range of tens of seconds^[18], suggested a mechanism where ATX could also act as an LPA carrier, spreading LPA signal to distal locations from those where LPC was taken. Such a model is also supported by data that show that Autotaxin can be recruited to the cell surface binding both to integrins^{[13], [22]} and surface

heparin sulfate proteoglycans^[23].

In this study, we set out to examine key questions about ATX catalysis that help explain the allosteric modulation of its physiological activity as a lysophospholipase D. We first establish that ATX activity is stimulated by LPA using the physiological LPC substrate and a new fluorescent substrate. Following a bottom-up approach, we then model and validate the lysoPLD activity of ATX on LPC. Next, we used ATX inhibitors from different classes and molecular dynamics simulations to propose that the LPA activates ATX lysoPLD activity by binding to the ATX tunnel. Our results propose a novel concept in the way we understand ATX hydrolysis, helping explain ATX function *in vivo*, and aiding future inhibitor design and optimization.

Results

ATX hydrolysis presents a lag phase

ATX lysoPLD kinetics on LPC always present an initial lag phase, which is followed by a linear phase in which ATX reaches its maximal catalytic activity as LPC is consumed (Fig.1A). The recorded choline oxidation signal can be better described by a double exponential rather than a single exponential ($P < 0.0001$) that would be characteristic of Michaelis-Menten kinetics. Regardless of this feature, the linear part of the kinetics of LPC cleavage has been usually analysed to describe ATX's kinetic parameters (Fig.1B, Table 1). As it has not been clear whether the lag phase is an artefact of the coupled assay or some intrinsic LPA-mediated regulation of ATX catalytic cycle takes place^[20], we set out to revisit the model for ATX catalysis.

Table 1. Comparative table of the Michaelis-Menten-derived kinetic parameters of choline oxidation, and 18:1 LPC and 18:1 NBD-PEG4 LPE cleavage with respect to those reported for 12:0 lyso-NBD-PC^[18].

Kinetic Parameters	Choline Oxidase	18:1 LPC	NBD-PEG4 LPE	NBD-LPC
K_M (μM)	121 \pm 23	112 \pm 22	0.88 \pm 0.09	308 \pm 195
k_{cat} (s^{-1})	1.32 \pm 0.04	0.016 \pm 0.01	0.021 \pm 0.003	0.06 \pm 0.01
k_{cat}/K_M ($\mu\text{M}^{-1} \text{s}^{-1}$)	1.08*10 ⁻² \pm 1.0*10 ⁻⁴	2.1*10 ⁻⁴ \pm 1.0*10 ⁻⁵	2.38*10 ⁻² \pm 2*10 ⁻⁴	1.9*10 ⁻⁴ \pm 7*10 ⁻⁵

We have first excluded trivial parameters such as changes in temperature or slight variations in buffer composition between different substrate concentrations, by carefully controlling experimental conditions. Importantly, the lag phase is observed in the

absence or the presence of fatty acid-free (FAF) bovine serum albumin (BSA), implying that the initial lag phase is independent of the presence of a lipid vehicle. Then, we wanted to exclude the possibility that the observed behaviour of choline release, is due to the kinetics of oxidation of choline by choline oxidase (EC 1.1.3.17) yielding betaine and two H_2O_2 molecules. Choline oxidation and subsequent HVA dimerization over time are described by hyperbolic kinetics (Fig.1C) compatible with the Michaelis-Menten approximation. The parameters derived for this reaction ($K_M = [98 - 144 \mu\text{M}]$ and $k_{cat} = [1.28 - 1.36 \text{ s}^{-1}]$, Fig.1D, Table 1) fit well to the ones reported for the enzymatic activity of choline oxidase in literature ($K_M = [0.1 - 2 \text{ mM}]$ and $k_{cat} [1 - 3 \text{ s}^{-1}]$)^[24].

To confirm the observed lag phase, we also used a direct readout assay using fluorescently labelled LPC. Existing fluorescently labelled substrates, such as 12:0 NBD-LPC, carry the label in the acyl chain, and are reporters of LPA binding and release^[18] and thus not useful to measure the actual kinetics of catalysis and choline release in the first reaction step of the double displacement mechanism. To have a direct readout for choline release, Avanti Polar Lipids produced a new fluorescent substrate, namely 18:1 NBD-PEG4 LPE (Fig.2A). This chromophoric substrate presents a PEG4 linker between the ethanolamine moiety and the fluorophore, which provided the necessary flexibility to be cleaved off by ATX (Fig.2B), which is promiscuous to the nature of the head group. Interestingly, the direct measurement of head group release revealed that the lag phase in the beginning of ATX catalysis was still present (Fig.2C). The linear phase of the experimental data was fitted by the Michaelis-Menten derivation to obtain the kinetic parameters for the cleavage of this substrate, indicating that the NBD-PEG4-LPE K_M is 100-fold lower than that of LPC, whereas k_{cat} is in the same range. PF-8380^[25] and compound 17^[26] both inhibited NBD-PEG4-Ethanolamine release similarly to the choline release coupled reaction (Supplemental Table 1), suggesting that the binding mode of NBD-PEG4-LPE is similar to that of LPC. While this substrate confirmed that the lag phase is a genuine feature of ATX-mediated LPC hydrolysis, it presented some solubility issues and a quenching effect at concentrations higher than $15 \mu\text{M}$. Thus, we decided to use the native LPC substrate for further characterization.

LPA modulates ATX catalysis

Having established the lag phase and subsequent activation of ATX-mediated catalysis, we wanted to examine a possible role of LPA in this behaviour. We first revisited the role of LPA in modulating hydrolysis of various ATX substrates, by adding increasing amounts of LPA in different reporter reactions indicative of ATX phosphodiesterase activity. Consistently with previous results^{[13], [15]}, we observed that 18:1 LPA inhibited hydrolysis of bis-*p*NPP and *p*NP-TMP with an IC_{50} of $\sim 50 \text{ nM}$ (Fig.3A-B). This reduction in total ATX phosphodiesterase activity can be attributed to the competition exerted by LPA on active site-binding nucleotide substrates. However, analysing experimentally the cleavage of the

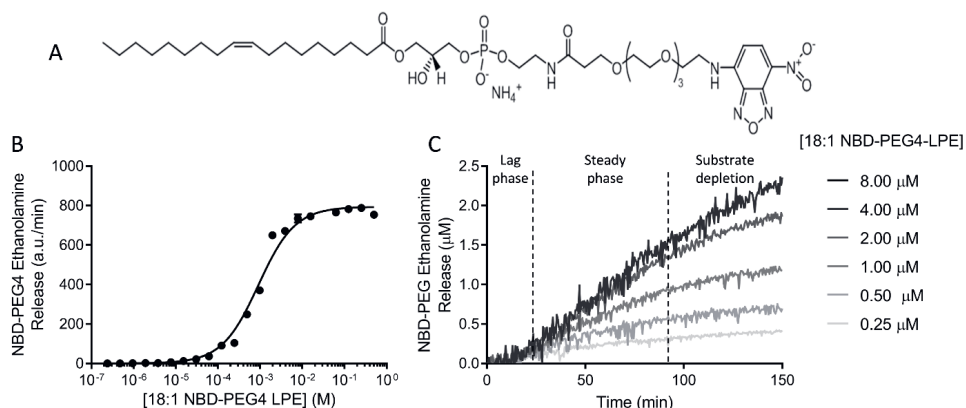


Figure 2. Cleavage of the novel probe 18:1 NBD-PEG4 LPE substrate by ATX lysoPLD activity presents initial lag phase. (A) molecular structure of NBD-PEG4 LPE, presenting an optimal $\lambda_{exc}/\lambda_{em} = 468/546$ nm. Product release was detected as a loss in fluorescence intensity at 546 nm with respect to that of the NBD-PEG4 LPE substrate. (B) Substrate concentration curve fit to the Michaelis-Menten equation employed to determine the kinetic parameters of NBD-PEG4-LPE by measure NBD-PEG4 ethanolamine release. (C) NBD-PEG4 ethanolamine release kinetics upon ATX lysoPLD activity, which follows a three-phase behaviour similar to that observed in Fig.1A. In all cases, 20 nM ATX was used and data represents means of triplicates \pm SEM.

physiological substrate 18:1 LPC while titrating increasing amounts of the homologous LPA species, we observed an activation of LPC hydrolysis up to $\sim 50\%$. The half maximum activation was observed in an LPA concentration that we define as AC_{50} , which was 1.4 ± 0.4 μM (Fig.3C). LPA modulation of ATX lysoPLD activity was also detected in the new direct readout assay. As observed in the choline release assay, activation by 18:1 LPA resulted in an AC_{50} value of 1.1 ± 0.3 μM (Fig.3D). Consistently, pre-incubating ATX with LPA for 30 minutes before supplying the LPC substrate reduced the length of the lag phase (Fig.3E-F).

Taken together, these assays point out to two separate LPA sites: an orthosteric high affinity (~ 50 nM) site, virtually identical to the primary LPC binding site that leads to catalysis or competition with minimal inhibitors and has been well characterized^{[15], [16], [27]}; and an allosteric low affinity (~ 1.5 μM) site that leads to an activation of LPC hydrolysis. These observations are of key importance to start understanding the lag phase we described above.

LPA binds to the ATX tunnel that acts as an allosteric regulatory site

The most likely candidate for an LPA allosteric binding site is the ATX tunnel, which has been shown to bind natural steroids^[28] and, importantly, has also been suggested to bind LPA in a series of crystal structures reported in^[11]; where the authors showed density for about six carbons of the acyl chain of LPA, bound to the tunnel. Aiming to confirm this

interaction, we designed a series of biochemical assays studying the modulation of ATX enzymatic activity by LPA in the presence of different well-characterized inhibitors that bind in the orthosteric and allosteric sites (Supplemental Figure 2).

The first of these inhibitors was the bile salt tauroursodeoxycholate (TUDCA), an inhibitor with IC_{50} of 11 μ M, which we previously reported to bind the allosteric site^[28]. The effect of LPA activation under conditions where ATX is partially inhibited by three TUDCA concentrations was measured. LPA can relieve inhibition by TUDCA, and LPA-mediated activation is more significant at higher concentrations of TUDCA, (Fig.4A-B) suggesting that TUDCA and LPA compete for the same site. In contrast, ATX partially inhibited by PF-8380, a well-established orthosteric site inhibitor^{[25], [26]} with an IC_{50} of 20 nM, reacts differently to LPA activation (Fig. 4D-E); the activation that LPA is able to exert was roughly the same as in the absence of PF-8380, indicating no interaction between the two, and that PF-8380 binding does not interfere with LPA-mediated activation. Consistently, when ATX is inhibited by compound 17^[26], a high-affinity (11 nM) “hybrid” orthosteric and allosteric site binding inhibitor, LPA activation can no longer be observed, especially at higher compound 17 inhibitor concentrations (Fig.4G-H).

In summary, we observe that LPA binding to the allosteric site, the tunnel, with an IC_{50} of 1.5 μ M, can directly compete with TUDCA binding (IC_{50} = 11 μ M) and relieve TUDCA mediated inhibition, but cannot activate PF-8380-mediated ATX inhibition further than the effect it exerts on un-inhibited ATX. Finally, LPA has hardly any effect on ATX inhibited by the strong inhibitor compound 17 (IC_{50} = 16 nM), as it cannot displace it from the orthosteric site binding pocket, nor can it activate by binding to allosteric site tunnel. Collectively, these experiments are all compatible with the hypothesis that LPA binds the tunnel to activate LPC hydrolysis.

Molecular dynamics simulations support LPA binding to the tunnel and point to its preferred entry route

To further test our hypothesis and assess if the tunnel can be occupied by LPA that acts as an allosteric activator, we performed a series of molecular dynamics (MD) simulations. We performed twelve replicas of the same simulation system, which contained the protein, one LPA 18:1 molecule already in the hydrophobic pocket and ten LPA molecules randomly placed in the solvent. In this system, all molecules had different random starting velocities, which were used to produce the MD trajectories. The LPA molecule placed in the hydrophobic pocket remained stable in this location in all simulations (Fig.5A). To visualise the binding of LPA in the tunnel, we plotted the molecular dynamics (MD) of all LPA molecules in the solvent from the equivalent atoms of the acyl lipid chain (C10 to C18) residing in the tunnel modelled in PDB entry 3nkp^[11]. In 50% of the simulations, one of the solvent-located LPA molecules moved towards the tunnel within the first 100 ns

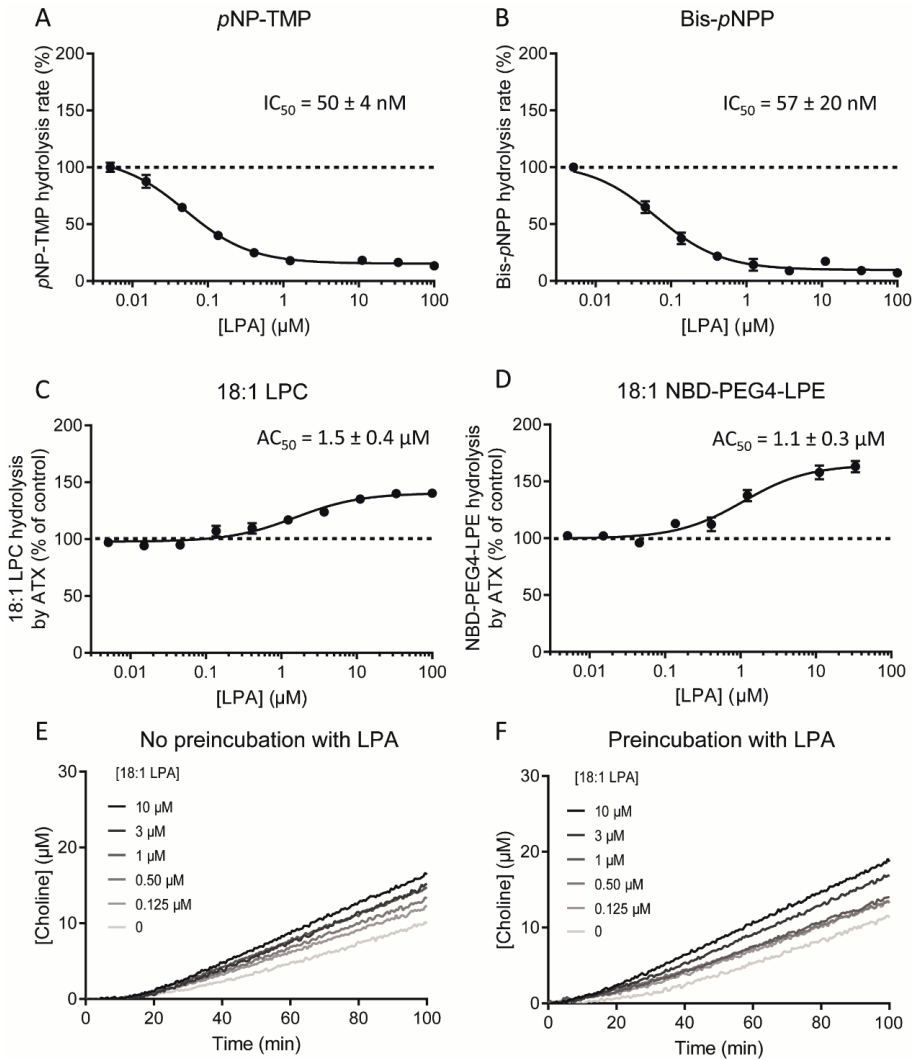


Figure 3. LPA modulates ATX catalysis, where it can act as an activator or inhibitor in a substrate-specific manner. (A, B) LPA inhibition of the hydrolysis of the unnatural ATX substrates pNP-TMP and bis-pNPP. IC_{50} values were obtained from these fits using Equation 5. (C) Effect of the addition of 18:1 LPA on human ATX β lysoPLD activity. LPA induced up to 45% increase in activity with respect to the control reaction. (D) Activation of the lysoPLD activity of ATX activity by 18:1 LPA using 18:1 NBD-PEG4 LPE as substrate yielded the same activation constant. This result confirmed that data obtained with the coupled assay is reproducible with the novel substrate. (E, F) The lag phase, which is approximately ten minutes long (E), can be reduced by incubating ATX with 18:1 LPA for 30 min before addition of LPC (F). In all experiments, 20 nM ATX was employed, and the error bars represent the SEM. from three different samples. The data was fitted using the same equation used for LPA inhibition Equation 10.

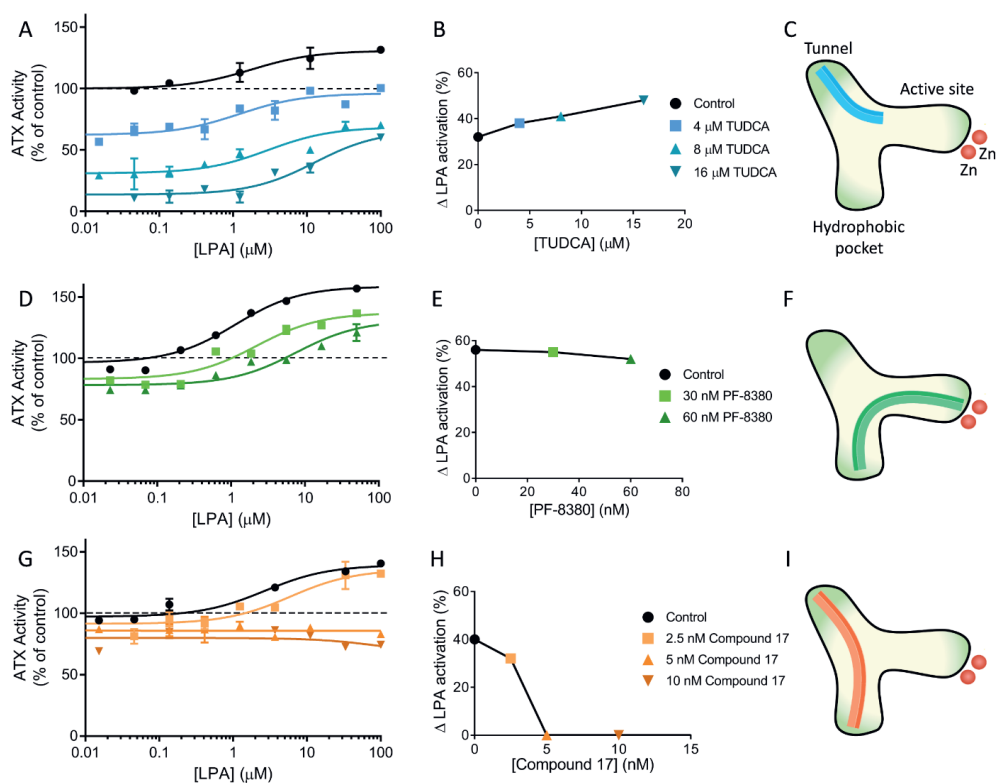


Figure 4. LPA activation in the presence of distinct inhibitors of ATX lysoPLD activity. (A) Relative change in activity of 20 nM ATX in the presence of the Type III (allosteric site-binding) inhibitor TUDCA (in a concentration that allows some residual activity) when LPA is added to the reaction; (B) Increase of ATX activity with respect to the TUDCA-bound control; the data displayed represent the mean value of triplicate measures \pm SEM. (C) Schematic representation of the binding sites of ATX bound to TUDCA; (D, E, F) Same as (A,B,C) for the Type I inhibitor (orthosteric site-binding) PF-8380; (G, H, I) Same as (A,B,C) for the Type IV inhibitor (allosteric-orthosteric site hybrid) Compound 17.

of the simulation (Fig.5B). In all binding occurrences, the pathway of entry to the tunnel took place by introducing the hydrophobic tail through the tunnel entry close to the hydrophobic groove of the protein (Supplemental Movie 1). Furthermore, once entering the tunnel, lipid molecules remained stable in position through the rest of the simulation, around residues L79, F211, F250, H252, W255, W261 and F275. Interactions of the LPA in the tunnel also involved electrostatic contacts between the phosphate group and R245, R257 and K249 (Fig.5C). Thus, the MD simulations suggest that the preferred entry route of LPA molecules involves a primary sensing of the area of the PDE domain around the tunnel, followed by the introduction of LPA hydrophobic tails into this cavity, to remain bound to ATX. Interestingly, in a 0.5 μ s control simulation where the bound LPA was left to

equilibrate without additional LPA in the solvent, it remained bound to ATX, and did not leave either by diffusing to the solvent, or moving through the tunnel as suggested in^[11]. The MD simulations support the hypothesis that the low affinity allosteric activation site for LPA is the tunnel.

A kinetic model explaining LPA modulation of ATX lysoPLD activity

Having validated our hypothesis that LPA binding to the ATX tunnel leads to activation of the catalytic activity of ATX towards LPC, we employed a bottom-up approach to construct a kinetic model explaining LPA activation. For this, we used the KinTek Global Kinetic ExplorerTM software^{[29], [30]}, allowing different types of experimental data to be fitted simultaneously and directly to user-defined reaction models, avoiding simplifying approximations (Fig.6). Our final model, accounting for LPA activation in the ATX catalytic pathway, is expressed in Figure 7.

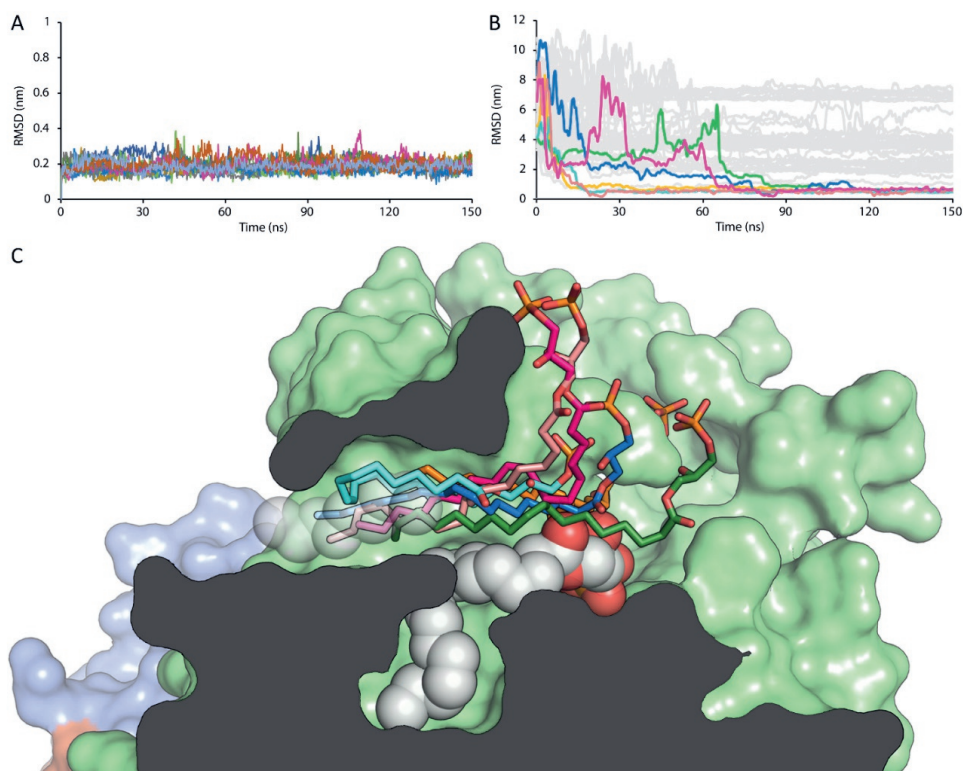
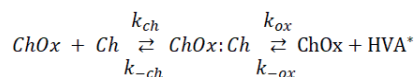


Figure 5. Molecular dynamics simulations of LPA binding to the tunnel of ATX. (A) RMSD values of the 18:1 LPA molecule (heavy atoms) bound to the hydrophobic pocket, derived from all simulations after protein backbone fitting. (B) RMSD values of the hydrophobic lipid tail (carbon atoms C10-C18) to the reference atoms from the refined 3npk crystal structure. Coloured lines represent the LPA molecules that entered the tunnel cavity of ATX, corresponding to the colours of Fig.5C, while grey lines represent the remaining LPA molecules (except the one in the hydrophobic

pocket) of the system. (C) Representation of the binding modes of 18:1 LPA molecules to the tunnel. The lipid molecules that entered and remained in the tunnel during the MD simulations are shown in stick representation and colours green, blue, magenta, salmon, cyan and orange. The carbon atoms used for the RMSD calculations are shown in white transparent spheres and the LPA molecule occupying the hydrophobic pocket is shown in white non-transparent spheres representation. The surface of the protein is colour coded as follows, PDE domain in light green, NUC domain in blue and the lasso loop in orange.

In addition to reactions directly related to hydrolysis of LPC to LPA and choline by ATX, as choline release is not directly observed, we needed to take into account the rates of the coupled reactions that result in the fluorescent readout of the HVA dimer (HVA^{*}). Through a series of titration experiments (for details, see methods), we showed that HVA oxidation by HRP is rapid, and we could describe choline conversion to HVA^{*} with a simplified reaction scheme (Fig.6A-B):



This scheme allowed us to take into account the exact rates of the conversion of choline to the fluorescent signal.

We then collected experimental data of titrations of [LPA], [LPC], and [ATX] versus each other; a complete list of all titrations is available in Methods and it is shown in Figure 6C-F. In the model, LPA_o refers to LPA binding to the orthosteric site (hydrophobic binding pocket) and LPA_a refers to LPA binding in the allosteric site (tunnel). Next, having the data and the complete model at hand, we needed to consider simplifications and test assumptions that would allow a robust fit of the most relevant kinetic parameters:

1. All diffusion-limited constants, k_{LPC} , $k_{LPA_o(1-2)}$ and $k_{LPA_a(1-3)}$ and k_{ch} were fixed to $100 \mu\text{M}^{-1} \text{s}^{-1}$
2. The hydrolysis reactions were considered practically non-reversible, and kinetic constants k_{-slow} and k_{-fast} were set to zero.
3. The inclusion of the ATX:LPA_o:LPA_a intermediate (VI), the presence of which is supported also by our MD data, is key to explain all data. From that complex, either LPA_o or LPA_a could leave ATX depending on their relative affinities for the orthosteric or allosteric sites.
4. To better define the binding of LPA to the orthosteric site, we included in the model the data from a titration of LPA inhibiting *p*NP-TMP hydrolysis by competing for binding to the orthosteric site, which allows defining better the affinity of LPA. Further, our model suggests that LPA can be released from the orthosteric site either when it's the only bound LPA species (III->I), or while another LPA molecule is bound to the allosteric site (VI->IV). To check if the dissociation constants for these two events are different, we first refined

Table 2. Kinetic parameters of the KinTek model. The confidence contours of each parameter depicted in Figure 7, were calculated employing FitSpace statistical analysis on KinTek at a $\chi^2 > 0.9901$ (Supplemental Figure 6).

Kinetic parameters	Parameter contour	Determined by	Derived parameters	Parameter contour
k_{LPC} ($\mu\text{M}^{-1} \text{s}^{-1}$)	100	Diffusion limited	K_{D-LPC1} (μM)	[1.56, 1.92]
k_{-LPC1} (s^{-1})	[155.5, 191.7]	Model		
$k_{2\text{slow}}$ (s^{-1})	[0.011, 0.014]	Model	$k_{\text{cat slow}}$ (s^{-1})	[0.011, 0.014]
$k_{-2\text{slow}}$ ($\mu\text{M}^{-1} \text{s}^{-1}$)	0	Non-reversible		
k_{LPC} ($\mu\text{M}^{-1} \text{s}^{-1}$)	100	Diffusion limited	K_{D-LPC2} (μM)	[0]
k_{-LPC2} (s^{-1})	~ 0	Model		
k_{LPA_o} ($\mu\text{M}^{-1} \text{s}^{-1}$)	100	Diffusion limited	K_{D-LPA_o} (μM)	[0.069, 0.077]
k_{-LPA_o} (s^{-1})	[6.87, 7.73]	$p\text{NP-TMP}$ competition		
k_{LPA_a} ($\mu\text{M}^{-1} \text{s}^{-1}$)	100	Diffusion limited	K_{D-LPA_a} (μM)	[1.52, 2.77]
k_{-LPA_a} (s^{-1})	[151.7, 276.7]	Model		
$k_{2\text{fast}}$ (s^{-1})	[0.039, 0.048]	Model	$k_{\text{cat fast}}$ (s^{-1})	[0.039, 0.048]
$k_{-2\text{fast}}$ ($\mu\text{M}^{-1} \text{s}^{-1}$)	0	Non-reversible		

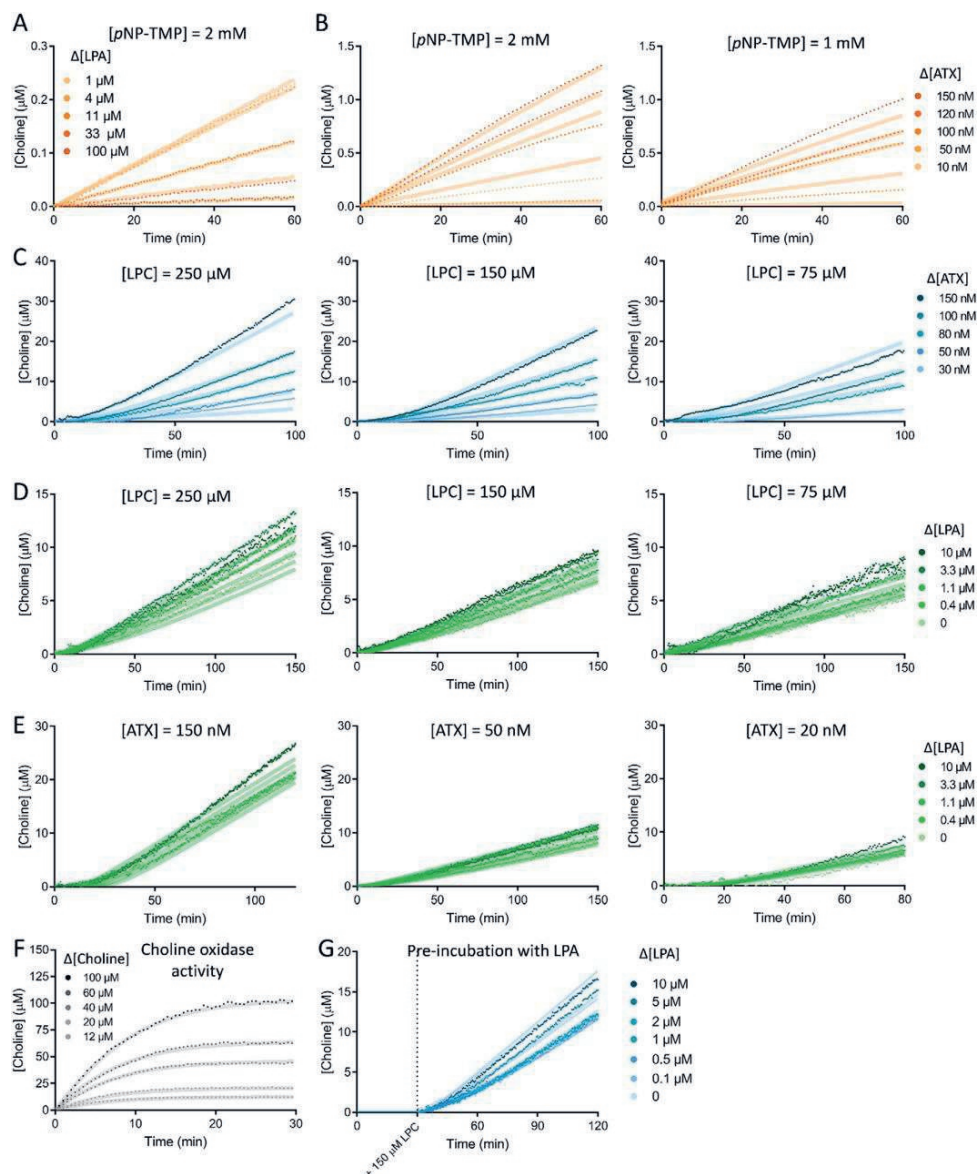


Figure 6. Key kinetic assays experimental data as fitted on KinTek Explorer™ (A) Implementation of the role of LPA as an inhibitor in pNP-TMP hydrolysis by ATX; this allowed determining K_{D-LPAO} . (B) Determination of the rate constants of ATX on pNP-TMP hydrolysis by titrations of ATX in two concentrations of pNP-TMP. (C) Estimation of K_{D-LPC} and k_{cat} (both fast and slow) by titration of ATX vs. different concentrations of 18:1 LPC. (D, E) Determination of the specific rate constants defining LPA-mediated ATX activation performed by titrating 18:1 LPA vs. different concentrations of LPC (D) and ATX (E). (F) Fit to choline oxidase activity upon addition of choline chloride (Fig.1C) (G) Fit to the experiment presented on Figure 3F; pre-incubation with different concentrations of 18:1

LPA showed a decrease in the lag phase of ATX catalysis upon addition of 150 μM LPC. In all cases, the transparent background line on each curve depicts the fit of the model to the experimental data which are represented as points. When not indicated, ATX concentration is 20 nM and LPC concentration is 150 μM .

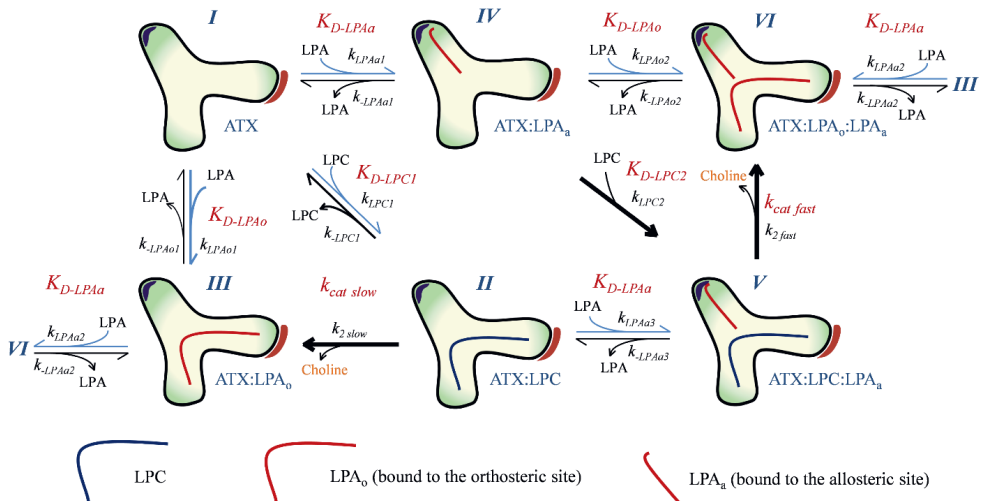


Figure 7. Kinetic model for the modulation of ATX activity by LPA shown as a cartoon representing the two ATX kinetic cycles (I-III and IV-VI). Starting from lipid-free ATX [I], LPC binding results to a transient complex [II] that undergoes slow hydrolysis (defined by $k_{\text{cat slow}}$): this corresponds to the initial slow phase of in vitro catalysis. Upon catalysis, LPC is converted to choline and LPA, which can remain bound to the orthosteric site [III] or dissociate from ATX, as defined by $K_{\text{D-LPAo}}$. This cycle represents the known catalytic pathway for LPC hydrolysis. LPA binding in the tunnel, however, can occur in lipid-free [I], LPC-bound ATX [II] or LPA_o-bound ATX [III] to yield the respective LPA-carrying species [IV, V & VI]. This binding is defined by $K_{\text{D-LPAa}}$, the dissociation constant for LPA in the allosteric site, which occurs independently of the presence of LPC in the orthosteric site. LPC in the presence of LPA bound in the tunnel [V] undergoes faster hydrolysis, defined by $k_{\text{cat fast}}$ and yields ATX with two bound LPA molecules [VI]: this is the steady state rate observed in ATX catalysis. Lastly, ATX bound to one LPA molecules in each site (VI) can lose either tunnel-bound LPA as defined by $K_{\text{D-LPA}}$ leading to ATX with LPA only bound to the orthosteric site (III) or it can lose the LPA bound in the orthosteric site as defined by $K_{\text{D-LPAo}}$ leading to ATX with LPA only bound to the allosteric site (IV). The final script used to define the model can be found in Supplemental Scheme 1, and the energy profiles for both catalytic pathways is shown in Supplemental Figure 7.

them independently; however, they converged to similar values within confidence limits (see Methods). Therefore, these dissociation constants, k_{-LPA01} and k_{-LPA02} , were constrained to be identical, and we refer to these as k_{-LPA0} . In other words, the ability of LPA to bind to the orthosteric site is independent of the presence of LPA in the allosteric site.

5. Then we wanted to check if the ability of LPA to bind to the allosteric site is independent of the presence of LPA in the orthosteric site. LPA can be released from the allosteric site in three instances: when it's the only bound LPA species (IV->I); when the orthosteric site contains LPA (VI->III); and when the orthosteric site contains LPC (V->II). To check if these three dissociation constants are different, we first refined them independently; however, they converged to similar values within confidence limits (see methods). Therefore, these dissociation constants, k_{-LPAa1} , k_{-LPAa2} and k_{-LPAa3} were constrained to be identical and we refer to these as k_{-LPAa} . In other words, the ability of LPA to bind to the allosteric site is independent of the presence of LPA or LPC in the orthosteric site.

6. Last, we wanted to check if the ability of LPC to bind to the orthosteric site is affected by the presence of LPA in the allosteric site. When the binding constants for LPC in the absence of LPA in the allosteric site (k_{-LPC1}) and in the presence thereof (k_{-LPC2}) were released, they did not converge to similar values. Namely, k_{-LPC2} reached zero when fitted, suggesting that LPC does not dissociate when LPA is bound to the allosteric site, and directly implying that the LPA-mediated activation of ATX is also mediated by stabilization of LPC binding.

7. In this model, we are not considering the binding of LPC to the allosteric site; this would not be much relevant as it would be unproductive for hydrolysis, and we have no data that would support such a hypothesis. Last but not least such an event is not necessary to explain our data.

Using the FitSpace algorithm included in KinTek Explorer, we analysed the fitted kinetic parameters to obtain their confidence contours (Supplemental Figure 6). These indicate the extent to which the defined reaction steps and their parameters are constrained by the experimental data^[30].

Our modelling suggests that LPC can dissociate quickly from the orthosteric site when there is no LPA in the allosteric site, but not when LPA is present in the allosteric site. Thus, binding of LPC to LPA-free ATX can often be unproductive, while binding of LPC to ATX that already carries LPA in the allosteric site, is more likely to be productive. Thus, the transient complex of ATX and LPC alone shows a slow apparent rate of hydrolysis (defined by $k_{cat\ slow}$) corresponding to the initial slow phase of in vitro catalysis, while the complex of ATX, LPC and LPA [V] undergoes faster hydrolysis, as observed in the linear steady state (Figures 1A, 2C, 3EF), and is a consequence of product accumulation as the reaction proceeds. In the absence of any evidence showing a rearrangement of the active site, we conclude that the stabilization of LPC in the orthosteric site by the presence of LPA in the allosteric site is the major reason for the apparent increase in the catalytic rate: the longer

residence time of LPC is more likely to be productive.

The kinetic model also allowed us to simulate the behaviour of intermediate species of the reaction over time (Fig.8A-B and Supplemental Figure 5). In the absence of LPA in the starting conditions, we observe a burst of the ATX:LPC intermediate, which is slowly replaced by the more “active” ATX:LPA_a:LPC species (Fig.8A). In contrast, when ATX was pre-incubated with 10 μM LPA, we see two ATX complexes with LPA building up: the ATX:LPA_o:LPA_a complex is the predominant species (~80%) while ATX:LPA_o is ~20%; free ATX is not present in these conditions. The slow build-up of the “active” ATX:LPA_a:LPC species is now formed rapidly after the addition of LPC, while the ATX:LPC species does not show the aforementioned “burst” observed in the absence of pre-incubation with LPA. Looking closer at the first tens of minutes and focusing on the observed fluorescent signal, the modelling data clearly recapitulate the experiments presented in Figure 3E-F.

Next, we examined the activation of the cleavage of all five LPC species available, against all the other LPA species available in a systematic manner. For practical reasons, here we only determined the percentage activation using as normalisation reference the activity of ATX for LPC alone in the start of the reaction. The activation is presented as a 2D heat map plot (Fig.9). The highest activation rates were measured when shorter LPA species were present in the hydrolysis of long LPC species and *vice versa*. This indicates that there is a “cumulative optimal length” of the chain length of the bound LPC and LPA species, likely needed to optimally reinforce the binding of the LPC and aid hydrolysis.

Different LPC and LPA species comply with the kinetic model for LPA-mediated activation

As *in vivo* several LPA species co-exist, we next studied whether the product-mediated activation was restricted to the 18:1 species. To that end, the cleavage of five LPC species (14:0, 16:0, 18:0, 18:1 and 22:0) was examined in the presence of their homologous LPA species (14:0, 16:0, 18:0, 18:1 and 22:4). In consequence, AC_{50} values, as well as the % activation were calculated using the Michaelis-Menten derivation (Supplemental Figure 3 and supplemental Table 4) and modelled using the same procedure and constraints as for LPA 18:1 (Table 3). The results indicated that there is a difference in activation depending on the selected lipid pair, from which the 16:0 and 18:0 species showed a higher activation. Just like 18:1 LPA-mediated activation, the increase in k_{cat} , as well as no LPC dissociation in the presence of LPA in the allosteric site (i.e. K_{D-LPC2} converged to zero when fitted), accounted for the activation event of the other species.

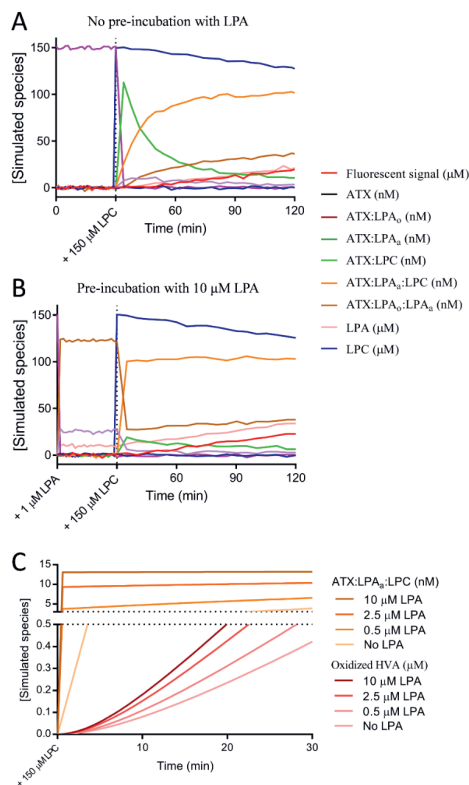
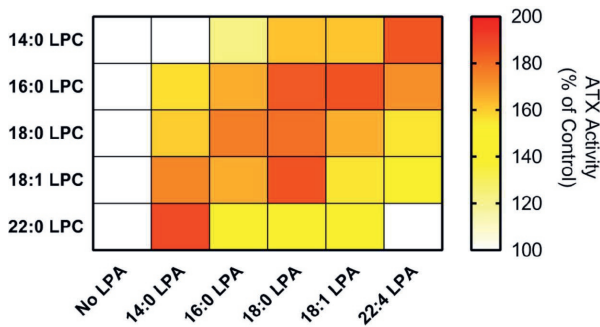


Figure 8. Time course simulation of ATX catalysis according to the kinetic model (A-B) Time course simulation performed in the presence of 150 nM ATX, 1.4 μM choline oxidase, in the absence (A) or presence of LPA (B). Such conditions were maintained for 30 min (as performed experimentally in Fig.3E-F), after which 150 μM LPC was added to initiate the reaction. In the simulations, the initial “burst” of the ATX:LPC (green) observed in the absence of LPA is lacking when pre-incubating with LPA, and is replaced by a burst of ATX:LPA_o:LPC (orange). The fluorescence intensity signal that would be observed experimentally is depicted in red. (C) Close-up at the lag phase and the variation of ATX:LPA_o:LPC and recorded fluorescence signal at four concentrations of LPA during the first 30 min of the simulations. The complete figures obtained from the simulations can be found in Supplemental Figure 5.

Table 3. Dissociation constants for LPC and its activating homologous LPA species fitted in the kinetic model (Fig.7).

LPC/LPA Species	K_{D-LPC1} (μM)	K_{D-LPA0} (nM)	K_{D-LPAa} (μM)	$k_{\text{cat slow}}$ (s^{-1})	$k_{\text{cat fast}}$ (s^{-1})	$k_{\text{cat fast}}/k_{\text{cat slow}}$
14:0	0.54 ± 0.08	62 ± 8	3.6 ± 0.2	0.067 ± 0.021	0.10 ± 0.05	1.5
16:0	0.7 ± 0.1	50 ± 3	2.5 ± 0.1	0.018 ± 0.011	0.21 ± 0.13	11.8
18:0	2.36 ± 0.03	56 ± 9	1.31 ± 0.6	0.020 ± 0.009	0.18 ± 0.05	8.8
18:1	1.71 ± 0.36	72 ± 9	2.05 ± 1.25	0.013 ± 0.003	0.043 ± 0.009	3.3
22:0 / 22:4	3.08 ± 0.05	38 ± 6	1.08 ± 0.15	0.004 ± 0.018	0.008 ± 0.003	2.1

**Figure 9.** Physiological interplay between shorter and longer-chain LPC and LPA species suggests preferred partnerships in LPA activation. The slopes measured for the linear phase of ATX lysoPLD activity (20 nM) changes in the presence of the indicated LPC and LPA molecular species. For each LPC species (150 μM), the different LPA species were titrated and ATX activity was normalized to the reaction in the absence of LPA, and the maximum increase in activity, as well as the AC_{50} values (Supplemental Tables 2 and 3) were calculated from equation 10.

Discussion

Understanding the mechanisms that underlie the role of LPA signaling in health and disease implies a complete understanding of LPA production of LPC by the ATX lysoPLD activity. While ATX catalysis has been extensively studied in recent years and reaction models have been proposed to explain LPC hydrolysis, many aspects are still poorly understood.

There has been some controversy in the literature, concerning the role of LPA in ATX catalysis. While it is widely accepted that LPA can inhibit hydrolysis of artificial substrates (which we confirm in this study), the role of LPA in LPC hydrolysis has been somewhat controversial. An initial study over a decade ago, showed some LPA product inhibition^[15], which has later been disputed^[31]. The data we present here show that the actual mechanism points to the opposing direction: different LPA species are able to activate ATX lysoPLD activity on different natural LPC substrates. On a related note, BrP-LPA has also been shown to inhibit approximately 75% of ATX lysoPLD activity on several LPC molecular species, also affecting plasma ATX activity and LPA levels *in vivo*^[32]. Although we note that we have been consistently unable to reproduce that data *in vitro*, we could speculate that the presence of the Br in the head group, might alter the interplay between LPC and LPA, and result in apparent inhibition, at least *in vivo*.

Saunders and colleagues described a model explaining NBD-LPC and FS-3 hydrolysis by ATX^[18]. Specifically, they showed that product release occurs in a sequential manner, where choline is released first and is then followed by LPA release. The discovery of the tunnel as an allosteric site which can modulate ATX activity^[28] offered an opportunity to extend this model. This also made it possible to explain previous observations that we were unable to rationalize before, namely the LPA mediated ATX activation and the lag phase that we have consistently observed in our choline release assays for LPA hydrolysis. The data we present here extend and complement the existing kinetic model, leading to a more complete understanding of LPC catalysis by ATX.

The key element in the new model is indeed the tunnel, an LPA-binding allosteric site. The first suggestion of LPA binding in the tunnel was reported in the mouse ATX crystal structure by Nishimasu and colleagues^[11]. Our data confirm that LPA binds to the tunnel; however, MD simulations do not support that the tunnel is an exit site for LPA newly formed in the binding pocket, as initially proposed. We do acknowledge, however, that the time scale of the MD simulations would not allow observing product release from the orthosteric site. Still, our model suggests that binding of LPA to the tunnel is more likely an independent event. In the absence of data showing that the tunnel can act as an exit site for LPA, the independent binding model should be preferred.

In our new kinetic model, we define two LPA hydrolysis rates, $k_{cat\ fast}$ and $k_{cat\ slow}$, which define the lag phase in ATX kinetics. The faster rate is observed when LPA accumulates (or is added exogenously) and is bound to the tunnel while an LPC binds in the catalytic orthosteric site (ATX:LPA_a:LPC). The observed activation by LPA in the allosteric site can be explained by stabilising that LPC in the orthosteric site, increasing its chances to undergo hydrolysis. This is reflected to our kinetic model, as the affinity of the orthosteric site for LPC is much higher than in the absence of LPA in the allosteric site, suggesting that every single binding event of LPC in the presence of LPA is catalytically productive. However, we cannot exclude conformational changes caused by LPA in the allosteric site that decrease the stability of the substrate when bound to the orthosteric site, reducing the activation energy for the catalytic event.

An important aspect of our model is that the activation occurs even between different LPC and LPA molecular species, a condition that reflects the *in vivo* situation. Certain LPC/LPA pairs in the orthosteric and allosteric sites result in a more active ATX. In a physiological situation, the presence of short LPA could accelerate hydrolysis of long LPC, and *vice versa*, creating exciting positive feedback loops between different substrates and products, and perplexing regulatory mechanisms.

Our data lead to two novel hypotheses that should be pursued in ATX research.

First, the allosteric and orthosteric site relationship suggests that different ATX inhibitors, specifically the ones that bind in the tunnel, can affect (positively or negatively) the production of specific LPA species. As it remains unclear how different LPAs signal to the different LPA receptors, such preferential inhibition, implies a likely different clinical outcome for different ATX inhibitors.

Second, it has been shown that ATX binds surface integrins through the SMB domains^{[13], [22], [33]}, whereas the longer isoform of ATX (ATX α) binds to heparan sulfate proteoglycans^[23]. While this binding will localize ATX at the cell surface, likely making LPA delivery to surface receptors more efficient, it cannot be excluded that it also affects the kinetics of LPC hydrolysis in our model. Indeed, as the SMB domains are involved in tunnel formation, integrin binding may enable LPA release from the orthosteric or the allosteric site. Taken together, these are exciting research hypotheses that warrant further investigation.

Experimental procedures

Cells and materials. Human and rat ATX were over-expressed and purified as described in^[34]. Briefly, HEK 293 Flp-In cells (Invitrogen) were grown in Dulbecco's modified Eagle's medium

(DMEM) containing 10% fetal bovine serum, glutamine and Penicillin-Streptomycin, which were obtained from Thermo Fischer (Massachusetts, USA). Additionally, cell culture was performed in the presence of Hygromycin (Invitrogen). After 4 d in culture, the medium was collected for purification. The culture medium was collected and centrifuged at 4,000 rpm for 15 min. Next, the obtained medium was filtered through a 0.65 μm bottle-top filter, which was subsequently applied at a flow rate of 8–10 ml min^{-1} onto a 10 ml POROS-20 MC column that had been pre-loaded with Ni^{2+} . The protein was eluted with 2-3 column volumes of a linear gradient of imidazole. Next, fractions were applied onto a Superose 6 10/30 size-exclusion column and concentrated afterwards.

For the kinetic studies, LPC (18:1), LPA (14:0, 16:0, 18:0, 18:1), 12:0 lyso-NBD-PC, 18:1 NBD-LPE and 18:1 NBD-PEG4 LPE were obtained from Avanti Polar Lipids Inc. (Alabaster, AL). Choline oxidase, Horseradish peroxidase, homovanillic acid, sodium TUDCA, choline chloride and fatty acid-free BSA were purchased from Sigma-Aldrich (St. Louis, Missouri). Hybrids and small-molecule ATX inhibitors were synthesized by the group of Craig Jamieson at the University of Strathclyde. Steady-state experiments were performed in Corning® 96- or 384-well OptiPlate from Sigma-Aldrich.

Kinetic measurements of ATX lysoPLD activity. The biochemical studies of ATX lysoPLD activity were performed with rat ATX (863 aa). Activity was measured by a coupled reaction with 1 U ml^{-1} choline oxidase and 2U ml^{-1} horseradish peroxidase (HRP) and 2 mM homovanillic acid (HVA). For the assays, 18:1 LPC was incubated with 20 nM ATX (obtained from HEK 293 Flip-In cells), reaching a final volume of 100 μl buffer, which contained 50 mM Tris, 0.01%, 50 mM CaCl_2 , Triton X-100, pH 7.4. Steady-state choline release was measured at 37 °C by HVA fluorescence at $\lambda_{\text{ex}} / \lambda_{\text{em}} = 320/460$ nm every 30 s for at least 60 min with a Pherastar plate reader (BMG Labtech)^[28]. Due to the presence of a lag phase during the first 10 min of ATX-dependent LPC hydrolysis (Fig.1A), the subsequent linear slope was used to perform all analyses.

For comparison between double exponential ($a_1 e^{-b_1 t} + a_2 e^{-b_2 t} + c$) and single exponential ($a_1 e^{-b_1 t} + c$) fluorescence kinetics over time, Akaike's Informative Criteria were used to establish the significance of the fits.

The resulting fluorescence intensity was converted to choline concentration by using a standard curve. This was prepared by titrating increasing concentrations of choline chloride in the reaction buffer in the absence of both LPC and ATX and measuring the end point of its conversion to the chromophoric form of HVA. The data were plotted with PRISM version 4 or 5 (GraphPad Software, San Diego, CA, USA) and presented as mean \pm standard error of the mean (SEM).

The slopes of ATX hydrolysis of 18:1 LPC, measured in choline concentration over time, were plotted against substrate concentration to obtain the kinetic parameters by means of nonlinear regression to Michaelis-Menten equation:

$$v = \frac{V_{max}c_{LPC}}{K_M + c_{LPC}} \quad (\text{Equation 1})$$

where, v represents velocity, measured in choline release over time, V_{max} is the maximum velocity obtained at a specific enzyme concentration, and K_M is the concentration of substrate (c_{LPC}) at which half of V_{max} is reached.

$$K_M = \frac{k_{-1} + k_2}{k_1} \quad (\text{Equation 2})$$

$$V_{max} = \frac{k_{cat}}{[E]_t} \quad (\text{Equation 3})$$

Measure of NBD-PEG4 LPE steady-state cleavage. Assays to assess ATX lysoPLD activity to hydrolyse the novel substrate NBD-PEG4 LPE were performed in the same conditions as described for LPC hydrolysis. Activity was monitored at $\lambda_{exc} / \lambda_{em} = 468/546$ nm. However, because of solubility problems, NBD-PEG4 LPE was dissolved in Ethanol:H₂O (1:1) 0.01% TX100. The slopes of the linear part of ATX activity were analysed using Graphpad Prism software to determine inhibition or activation in the distinct assays.

Inhibition of ATX lysoPLD activity. In order to determine the IC_{50} for the different inhibitors on lysoPLD ATX activity in the choline oxidase coupled assay, the velocity of the reaction was monitored for each compound as a function of time and the linear phase of the kinetics was taken from 60 min after the addition of ATX to the reaction buffer. The resulting fluorescence intensity signal over time was used to model all inhibitor concentrations simultaneously using the following formula^[26]:

$$F_t = F_0 + \left(\frac{v_{max} - v_{min}}{(1 + c_{inh}/IC_{50})} + v_{min} \right) t \quad (\text{Equation 4})$$

where F_t represents the observed fluorescence signal at time (t), F_0 is the background fluorescence signal at the start of each measurement, v_{max} and v_{min} were fitted for the minimum and maximum relative velocity, and c_{inh} corresponds to the inhibitor concentration for each assay. This equation allowed the calculation of the IC_{50} of each inhibitor. The previous equation can be derived by linear regression of each inhibitor concentration:

$$V = \frac{v_{max} - v_{min}}{(1 + c_{inh}/IC_{50})} + v_{min} \quad (\text{Equation 5})$$

Mechanistic Studies with ATX inhibitors. For initial comparison between competitive,

uncompetitive and non-competitive inhibition, assays measuring LPC hydrolysis by ATX lysoPLD activity were performed and analysed by nonlinear regression. For this purpose, three inhibitor concentrations, determined from the experimentally calculated IC_{50} and an additional control in the absence of inhibitor were used to obtain the slopes from the linear phase of ATX kinetics, as explained above. 20 nM rat ATX and 150 μ M LPC were added to the reaction buffer, and ATX was incubated for 30 min with each inhibitor. Slopes were taken from 60 min after the start of the reaction. The following equations were employed to describe each mode of inhibition^[28]:

$$V = \frac{V_{max}c_{LPC}}{K_M(1+c_i/K_i)+c_{LPC}} \text{ competitive inhibition} \quad (\text{Equation 6})$$

$$V = \frac{(\frac{V_{max}}{1+c_i/K_i})c_{LPC}}{K_M+c_{LPC}} \text{ non-competitive inhibition} \quad (\text{Equation 7})$$

$$V = \frac{V_{max}c_{LPC}}{K_M+c_{LPC}(1+c_i/\alpha K_i)} \text{ uncompetitive inhibition} \quad (\text{Equation 8})$$

where V is the observed velocity and c_{LPC} is the corresponding LPC concentration for each data point, and c_i is the inhibitor concentration for each curve; and K_i is the inhibition constant. Note that equation denotes K_i for competitive inhibition (i.e. binding in the absence of the substrate) and for uncompetitive inhibition (i.e. binding only in the presence of the substrate), where α will determine the type of inhibition: $\alpha < 1$ for uncompetitive inhibition, $\alpha > 1$ for competitive inhibition, and $\alpha = 1$ for non-competitive inhibition.

To calculate the percentage of certainty for each type of inhibition, the alpha value was calculated in the partial mixed inhibition model (Equation 9), and the significance of the analysis was assessed by Akaike's Informative Criteria.

$$V = \frac{V_{max}c_{LPA}(1+Part)}{K_M(1+c_i/K_i)+c_{LPA}(1+c_i/\alpha K_i)} \text{ partial mixed inhibition} \quad (\text{Equation 9})$$

where the new parameter $Part$ was defined as the partiality of the inhibition.

LPA Activation measurements. The activation assays using LPA were performed in a similar way as those done for the inhibitors. In this case, LPA was dissolved in Ethanol:H₂O (1:1), 0.01% TX-100 and was added to the reaction buffer. The presence of ethanol was taken into account and controls in the absence of ATX and/or LPC were employed to correct the kinetic data. Normally, the slopes were obtained from 60 min after ATX was added to the reaction buffer and were related to ATX activity in the same conditions but in the absence

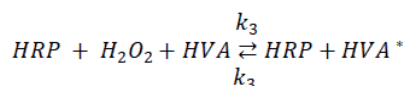
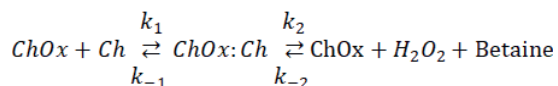
of LPA. In order to assess whether LPA activation could also take place with different LPA species, 14:0, 16:0, 18:0, and 18:1 LPA were diluted threefold, and data was analysed as described before.

Mechanistic study of LPA activation. To discriminate between the different structural components that take part in LPA activation of ATX lysoPLD activity, ATX was incubated for 30 min with different concentrations of inhibitors. ATX was subsequently added to the reaction buffer containing 150 μM 18:1 LPC, and 18:1 LPA was diluted threefold. The slopes were calculated from at least 60 min after the reaction was started. The calculation of the percentage of activation by LPA was related to ATX in the same conditions but in the absence of LPA and inhibitors, which represented 100% activity. AC_{50} was obtained from the following equation:

$$V = \frac{v_{max} - v_{min}}{(1 + c_{inh}/AC_{50})} + v_{min} \quad (\text{Equation 10})$$

Modelling on KinTek Explorer. KinTek Global Kinetic Explorer™ (version 6.3) was used to design reaction models, from which simulations could be performed. ATX catalysis models were written and tested in this software, following the workflow described in Supplemental Figure 1. The specific steps that were taken in each stage of the design is specified in the results section. Experimental data was fitted directly to the reaction model upon numerical integration of the rate equations using SpectraFit™. Additionally, the robustness of the described model was statistically analysed using the FitSpace Explorer™ software. This was used to define the confidence contour analysis, which allowed establishing the Chi^2 threshold at the boundaries between the different kinetic parameters. Consequently, complex relations between the kinetic constants can be detected and the extent to which the parameters are constrained by the experimental data can be addressed.

Two titration experiments, namely [Choline oxidase] vs. [Choline chloride] and [HRP] vs. [choline chloride], were performed to simplify the coupled reaction to detect choline release.



For the modelling of $K_{D-LPA\alpha}$ we performed titrations of [LPA] vs. [pNP-TMP]. Next, K_{D-LPC1} and K_{D-LPC2} were modelled by the titration of [LPC] vs. [ATX]. Lastly, LPA activation was explained by the titrations of [LPA] vs. [ATX], and [LPA] vs. [LPC], which allowed defining $k_{cat\ slow}$, $k_{cat\ fast}$ as well as $K_{D-LPA\alpha}$.

Molecular dynamics simulations. A structural model of human autotaxin (Uniprot code Q13822) in complex with 18:1 LPA was constructed with Modeller v9.7 using our previously reported crystal structures of rat autotaxin (PDB codes: 5dlw and 5dlt) as templates (94% sequence identity)^{[28], [35]}. All molecular dynamics (MD) simulations were performed using the GROMACS software v5.1^[36]. The ATX-LPA complex was then inserted in a pre-equilibrated box containing water. Apart from the 18:1 LPA molecule in the hydrophobic site, ten extra 18:1 LPA molecules were added to the simulation box in random positions, with a minimum distance of 40 Å to the tunnel. The AMBER99SB-ILDN force field was used for all the MD simulations along with the TIP3P water model^[37]. Force field parameters for the lipid molecules were generated using the general Amber force field (GAFF) and HF/6-31G*-derived RESP atomic charges^[38]. The reference system consisted of the protein, eleven 18:1 LPA molecules, ~58.500 water molecules and 17 Na⁺ ions (for total charge equilibrium) in a 12.5 x 12.5 x 12.5 nm simulation box, resulting in a total number of 189032 atoms. The system was energy minimized and subsequently subjected to a 10 ns MD equilibration, with an isothermal-isobaric ensemble, using isotropic pressure control and positional restraints on protein and lipid molecule coordinates. The resulting equilibrated system was replicated 12 times, random initial velocities were produced for each one of the replicas using a random seed and independent 150 ns MD trajectories were produced in a constant temperature of 310K, using separate v-rescale thermostats for the protein, the lipids and solvent molecules. A time step of 2 fs was used and all bonds were constrained using the LINCS algorithm. Lennard-Jones interactions were computed using a cut-off of 10 Å, and the electrostatic interactions were treated using PME with the same real-space cut-off. A control 500 ns simulation was also run without the ten surrounding LPA molecules, to examine the stability of LPA in the orthosteric pocket. All runs added up to a total simulation time of 2.4 μs.

Acknowledgements

We thank Wouter Moolenaar for his continued support and enthusiasm and Leonardo Pardo for providing infrastructure in the Laboratory of Computational Medicine, UAB, for the molecular dynamics simulations.

Supplemental information

Supplemental Table 1. Inhibition of the lysoPLD activity of ATX of NBD-PEG-LPE by distinct inhibitors. Inhibition of ATX activity by PF-8380, DC-80-1 and FP10.47, showing that 18:1 NBD-PEG4 LPE measures can be correlated to those obtained with the coupled reaction with choline oxidase. The data displayed represent the mean value of triplicate measures \pm SEM.

Inhibitor	% Inhibition	Experimental IC ₅₀
PF-8380	100	14 \pm 2 nM
DC-80-1	90	4 \pm 1 nM
Compound 17	100	17 \pm 3 nM

Supplemental Table 2. Percentage of activation of ATX lysoPLD activity in each combination of LPC and LPA.

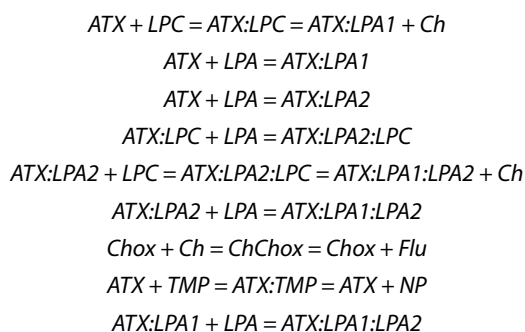
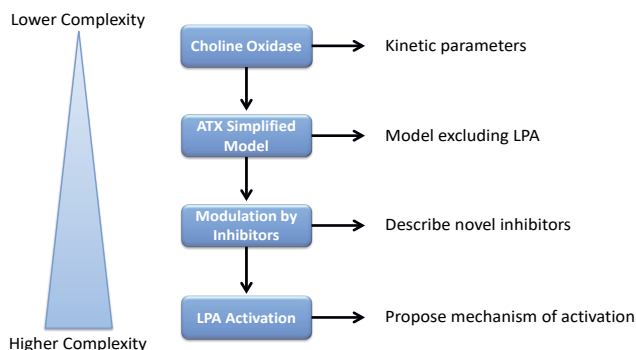
LPA % Activation	14:0 LPC	16:0 LPC	18:0 LPC	18:1 LPC	22:0 LPC
14:0 LPA	100 \pm 0	157 \pm 8	160 \pm 30	184 \pm 15	189 \pm 18
16:0 LPA	173 \pm 18	166 \pm 15	177 \pm 22	166 \pm 15	148 \pm 33
18:0 LPA	123 \pm 12	185 \pm 13	180 \pm 6	186 \pm 8	139 \pm 10
18:1 LPA	141 \pm 5	186 \pm 13	166 \pm 9	155 \pm 9	149 \pm 17
22:4 LPA	185 \pm 10	172 \pm 15	156 \pm 10	142 \pm 10	100 \pm 0

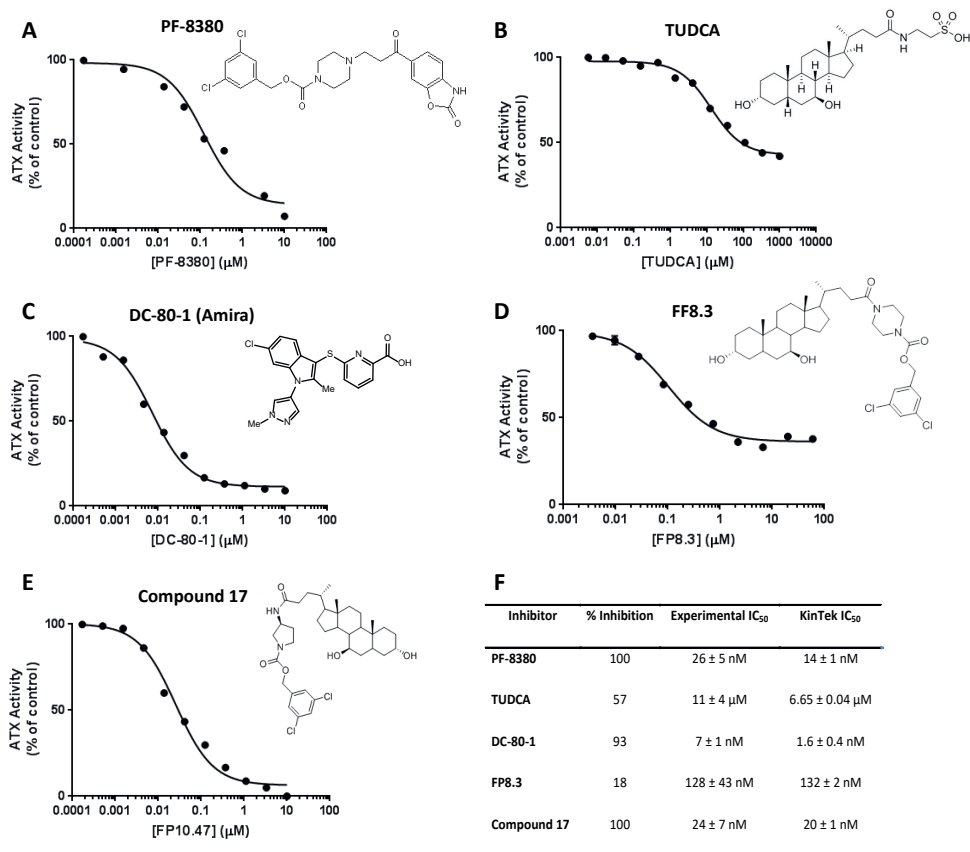
Supplemental Table 3. Activation constant (AC₅₀) calculated for each combination of LPC and LPA.

LPA AC ₅₀ (μ M)	14:0 LPC	16:0 LPC	18:0 LPC	18:1 LPC	22:0 LPC
14:0 LPA	-	1.6 \pm 0.8	3 \pm 3	1.9 \pm 0.9	3 \pm 2
16:0 LPA	3 \pm 2	2 \pm 1	1 \pm 1	2 \pm 1	3 \pm 4
18:0 LPA	2.8 \pm 2.7	2 \pm 1	0.2 \pm 0.1	0.5 \pm 0.2	2 \pm 1
18:1 LPA	1.0 \pm 0.4	4 \pm 1	0.8 \pm 0.4	1.5 \pm 0.9	2 \pm 2
22:4 LPA	1.2 \pm 0.5	3 \pm 2	1.1 \pm 0.9	2 \pm 1	-

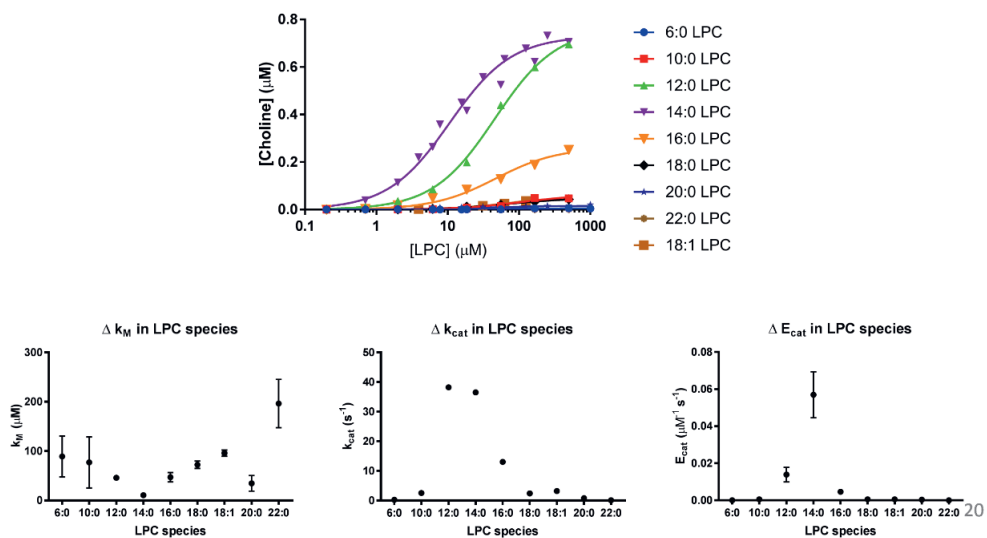
Supplemental Table 4. Kinetic parameters derived from the titration curves of different LPC molecular species.

LPC Species	k_{cat} (s^{-1})	K_M (μM)	E_{cat} ($\mu\text{M}^{-1} \text{s}^{-1}$)
6:0	0.005 ± 0.001	90 ± 42	0.00005 ± 0.00002
10:0	0.04 ± 0.01	77 ± 52	0.0006 ± 0.0002
12:0	0.64 ± 0.01	46 ± 3	0.014 ± 0.004
14:0	0.61 ± 0.01	11 ± 1	0.06 ± 0.01
16:0	0.22 ± 0.01	47 ± 9	0.005 ± 0.001
18:0	0.04 ± 0.01	72 ± 7	0.0006 ± 0.0002
18:1	0.054 ± 0.002	96 ± 6	0.0006 ± 0.0003
20:0	0.013 ± 0.001	35 ± 16	0.0004 ± 0.0001
22:0	0.0020 ± 0.0001	196 ± 50	0.000009 ± 0.000004

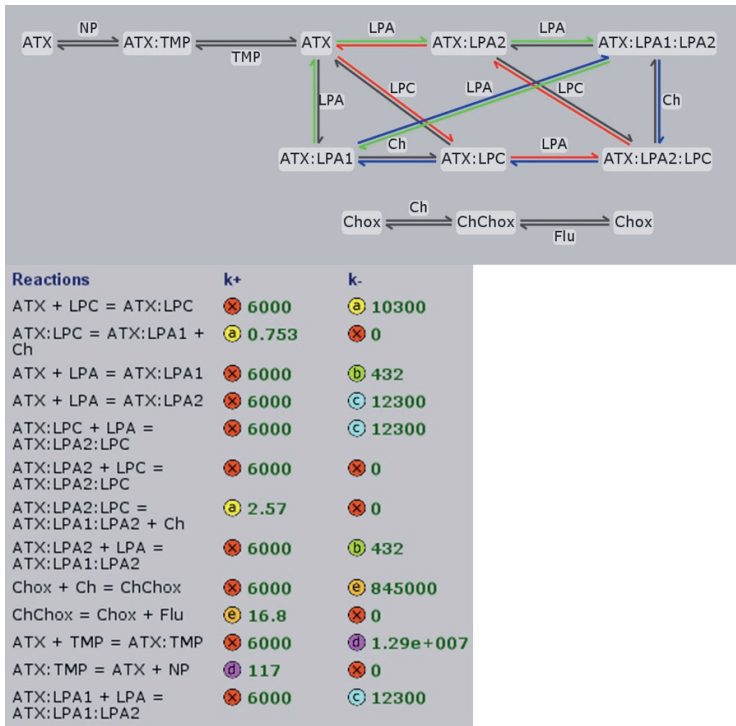
**Supplemental Scheme 1.** Script defining the kinetic model for LPA-mediated activation on KinTek Explorer.**Supplemental Figure 1.** Workflow of KinTek reaction model. Schematic representation of the bottom-up approach performed using the KinTek software.



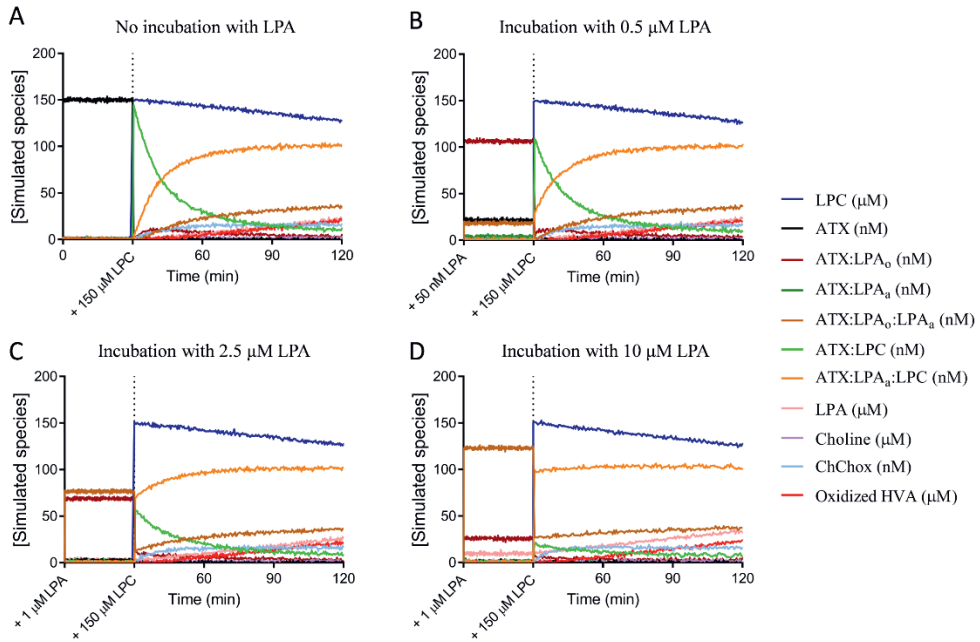
Supplemental Figure 2. Activity of ATX in the presence of selected compounds with different binding sites. A-E, inhibition of lysoPLD ATX activity measured as choline release using 18:1 LPC as substrate in the presence of different inhibitors. F, IC₅₀ and percentage of inhibition of lysoPLD activity caused by the inhibitors in the experiments shown at A-E, which could also be calculated using the KinTek reaction model for competitive or noncompetitive inhibition depending on the class of inhibitor. The same nonlinear regression fit used for LPA inhibition was employed to determine the IC₅₀ values (Equation 5).



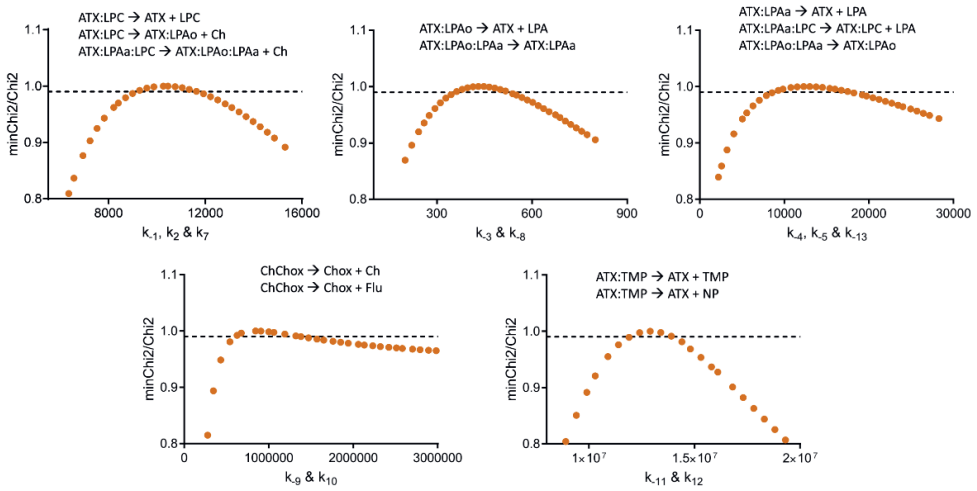
Supplemental Figure 3. Titration curves of different LPC molecular species used to calculate the kinetic parameters of Table 3.



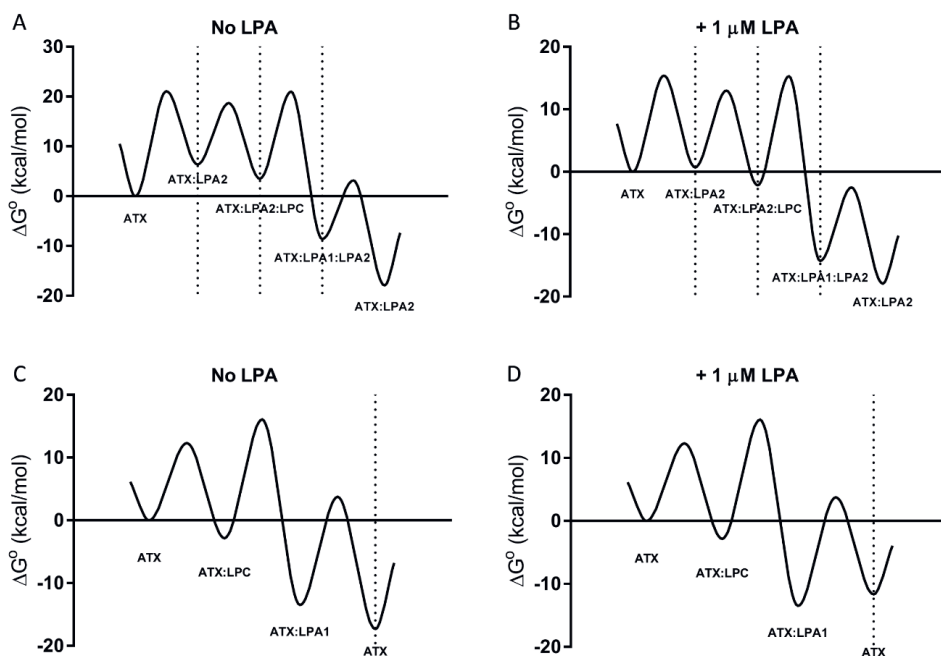
Supplemental Figure 4. Kinetic model for LPA-mediated activation as depicted on KinTek Explorer. Kinetic constants sharing the same letter depict coupled rate constants that will vary together in the same range when fitting the model to experimental data. When a rate constant has been fixed, showed with an "X", it will remain constant when fitting experimental data. "LPA1" refers to LPA bound to the orthosteric site, "LPA2" refers to LPA bound to the allosteric site, "Ch" is free choline, "Chox" is choline oxidase, "ChChox" is choline-bound choline oxidase, "Flu" is the fluorescent signal produced upon choline oxidase and HRP activities.



Supplemental Figure 5. Time course simulations of the behaviour of intermediate species of the kinetic model of ATX catalysis (extended data from Fig.8). The simulated experiment was defined as a time course of 120 s in the presence of 150 μM LPC (added after the first 30 s), 20 nM ATX and 1.4 μM choline oxidase. (A) In the generated data, we observed an initial burst of the ATX:LPC intermediate, which is followed by a progressive increase of ATX:LPA₀:LPC. This transition occurring in the first tens of minutes may explain the length of the lag phase, as well as the inhibitory role of LPA in the first catalytic cycles of LPC hydrolysis by ATX. (B-D) Upon pre-incubation with increasing concentrations of LPA, the initial burst of the “slow” ATX:LPC disappears and it is replaced by a high initial concentration of the “active” ATX:LPA₀:LPC.



Supplemental Figure 6. Confidence contour analysis for each kinetic parameter in the kinetic model for ATX catalysis. Each graph represents the rate constants defining the top reaction, as well as the additional coupled reactions fitted with the same confidence interval. In all cases, the Chi^2 threshold is 0.996 and it represents a fractional increase in Chi^2 that gives 95% confidence intervals.



Supplemental Figure 7. Display of a free energy profile for the LPC hydrolysis reaction model in the absence or presence of LPA. (A-B) Free energy profile of the thermodynamic cycle in which ATX is bound to LPA in the allosteric site (ATX:LPA2) when starting the reaction in the absence (A) or presence (B) of 1 μM LPA. The binding procedure of LPA to the allosteric site is more favorable when the total concentration of LPA in the reaction is closer to the AC_{50} ($\approx 1 \mu\text{M}$). The hydrolysis of LPC when LPA is bound in both the orthosteric and allosteric sites also presents a larger ΔG° for the hydrolysis to ATX:LPA1:LPA2 when 1 μM LPA is present. (C-D) Free energy profile of LPA inhibition via binding in the orthosteric site when no LPA is bound in the allosteric site. In the absence of LPA in the beginning of the reaction (C), the transition from ATX:LPA1 (LPA bound in the orthosteric site) to lipid-free ATX occurs with a negative ΔG° , whereas this event represents a positive ΔG° in the presence of 1 μM LPA (D), which stabilizes the ATX:LPA1 complex. These profiles were calculated using KinTek ExplorerTM with the reaction model depicted in Figure 7, and in the presence of 150 μM LPC and 20 nM ATX.

Supplementary Movie 1. Binding of an LPA molecule to the tunnel. The entry pathway of an LPA molecule to the tunnel, initiated at ~ 40 ns, as observed in one of the molecular dynamics simulations in a system comprising of the protein, water solvent (not shown), ions (not shown), the hydrophobic pocket LPA molecule (blue) and 10 randomly placed LPA molecules (only the one eventually binding to the tunnel is shown, in orange).

References

- [1] M. Bollen, R. Gijsbers, H. Ceulemans, W. Stalmans, C. Stefan, **2000**, 35, 393.
- [2] A. Tokumura, E. Majima, Y. Kariya, K. Tominaga, K. Kogure, K. Yasuda, K. Fukuzawa, *J. Biol. Chem.*, **2002**, 277, 39436.
- [3] H. M. H. G. Albers, A. Dong, L. A. van Meeteren, D. A. Egan, M. Sunkara, E. W. van Tilburg, K. Schuurman, O. van Tellingen, A. J. Morris, S. S. Smyth, W. H. Moolenaar, H. Ovaa, *Proc. Natl. Acad. Sci. U. S. A.*, **2010**, 107, 7257.
- [4] P. G. Munder, M. Modolell, R. Andressen, H. U. Weltzien, O. Westphal, *Springer Semin. Immunopathol.*, **1979**, 2, 187..
- [5] L. A. van Meeteren, P. Ruurs, C. Stortelers, P. Bouwman, M. A. van Rooijen, J. P. Pradere, T. R. Pettit, M. J. O. Wakelam, J. S. Saulnier-Blache, C. L. Mummery, W. H. Moolenaar, J. Jonkers, *Mol. Cell. Biol.*, **2006**, 26, 5015.
- [6] E. Barbayiannia, E. Kaffeb, V. Aidinisb, G. Kokotos, *Prog. Lipid Res.*, **2015**, 58, 76..
- [7] H. Kanda, R. Newton, R. Klein, Y. Morita, M. D. Gunn, S. D. Rosen, *Nat. Immunol.*, **2008**, 9, 415.
- [8] A. E. Kremer, J. J. W. W. Martens, W. Kulik, F. Ruëff, E. M. M. Kuiper, H. R. van Buuren, K. J. van Erpecum, J. Kondrackiene, J. Prieto, C. Rust, V. L. Geenes, C. Williamson, W. H. Moolenaar, U. Beuers, R. P. J. Oude Elferink, *Gastroenterology*, **2010**, 139, 1018.e1.
- [9] S. Jansen, *J. Cell Sci.*, **2005**, 118, 3081.
- [10] S. Koike, K. Keino-Masu, T. Ohto, M. Masu, *Genes Cells*, **2006**, 11, 133..
- [11] H. Nishimasu, S. Okudaira, K. Hama, E. Mihara, N. Dohmae, A. Inoue, R. Ishitani, J. Takagi, J. Aoki, O. Nureki, *Nat. Struct. Mol. Biol.*, **2011**, 18, 205.
- [12] A. Perrakis, W. H. Moolenaar, *J. Lipid Res.*, **2014**, 55, 1010.
- [13] J. Hausmann, S. Kamtekar, E. Christodoulou, J. E. Day, T. Wu, Z. Fulkerson, H. M. H. G. Albers, L. A. Van Meeteren, A. J. S. Houben, L. Van Zeijl, S. Jansen, M. Andries, T. Hall, L. E. Pegg, T. E. Benson, M. Kasiem, K. Harlos, C. W. V. Kooi, S. S. Smyth, H. Ovaa, M. Bollen, A. J. Morris, W. H. Moolenaar, A. Perrakis, *Nat. Struct. Mol. Biol.*, **2011**, 18, 198.
- [14] H. M. H. G. Albers, H. Ovaa, *Chem. Rev.*, **2012**, 112, 2593.
- [15] L. A. Van Meeteren, P. Ruurs, E. Christodoulou, J. W. Goding, H. Takakusa, K. Kikuchi, A. Perrakis, T. Nagano, W. H. Moolenaar, *J. Biol. Chem.*, **2005**, 280, 21155.
- [16] H. Takakusa, K. Kikuchi, Y. Urano, S. Sakamoto, K. Yamaguchi, T. Nagano, *J. Am. Chem. Soc.*, **2002**, 124, 1653..
- [17] F. CG, C. Bigman, R. Richardson, L. van Meeteren, W. Moolenaar, G. Prestwich, *Org. Lett.*, **2006**, 8, 2023.
- [18] L. P. Saunders, W. Cao, W. C. Chang, R. a Albright, D. T. Braddock, E. M. De La Cruz, *J. Biol. Chem.*, **2011**, 286, 30130.
- [19] W. H. Moolenaar, A. Perrakis, *Nat Rev Mol Cell Biol*, **2011**, 12, 674.
- [20] S. Imamura, Y. Horiuti, *J. Biochem.*, **1978**, 83, 677..
- [21] J. Hausmann, W.-J. Keune, A. L. Hipgrave Ederveen, L. van Zeijl, R. P. Joosten, A. Perrakis, *J. Struct. Biol.*, **2016**, 195, 199..

- [22] T. Wu, C. Vander Kooi, P. Shah, R. Charnigo, C. Huang, S. S. Smyth, A. J. Morris, *FASEB J.*, **2014**, 28, 861.
- [23] A. J. S. Houben, X. M. R. Van Wijk, L. A. Van Meeteren, L. Van Zeijl, E. M. A. Van De Westerlo, J. Hausmann, A. Fish, A. Perrakis, T. H. Van Kuppevelt, W. H. Moolenaar, *J. Biol. Chem.*, **2013**, 288, 510.
- [24] BRENDA, <http://www.brenda-enzymes.info/> (accessed May 25, 2018).
- [25] J. Gierse, A. Thorarensen, K. Beltey, E. Bradshaw-pierce, L. Cortes-burgos, T. Hall, A. Johnston, M. Murphy, O. Nemirovskiy, S. Ogawa, L. Pegg, M. Pelc, M. Prinsen, M. Schnute, J. Wendling, S. Wene, R. Weinberg, A. Wittwer, B. Zweifel, J. Masferrer, *J. Pharmacol. Exp. Ther.*, **2010**, 2, 310.
- [26] W. J. Keune, F. Potjewyd, T. Heidebrecht, F. Salgado-Polo, S. J. F. Macdonald, L. Chelvarajan, A. Abdel Latif, S. Soman, A. J. Morris, A. J. B. Watson, C. Jamieson, A. Perrakis, *J. Med. Chem.*, **2017**, 60, 2006.
- [27] S. Cavalli, A. J. S. A. Houben, H. M. H. G. Albers, E. E. W. Van Tilburg, A. de Ru, J. Aoki, P. van Veelen, W. W. H. Moolenaar, H. Ovaa, *Chemobiochem*, **2010**, 11, 2311.
- [28] W. Keune, J. Hausmann, R. Bolier, D. Tolenaars, A. Kremer, T. Heidebrecht, R. Joosten, M. Sunkara, A. Morris, E. Matas-Rico, W. Moolenaar, R. Oude Elferink, A. Perrakis, *Nat. Commun.*, **2016**, 7, 11248.
- [29] K. A. Johnson, Z. B. Simpson, T. Blom, *Anal. Biochem.*, **2009**, 387, 20..
- [30] K. A. Johnson, Z. B. Simpson, T. Blom, *Anal. Biochem.*, **2009**, 387, 30..
- [31] M. G. K. Benesch, Y. Y. Zhao, J. M. Curtis, T. P. W. McMullen, D. N. Brindley, *J. Lipid Res.*, **2015**, 56, 1134.
- [32] I. Nikitopoulou, E. Kaffe, I. Sevastou, I. Siriti, M. Samiotaki, D. Madan, G. D. Prestwich, V. Aidinis, *PLoS One*, **2013**, 8
- [33] Z. Fulkerson, T. Wu, M. Sunkara, C. Vander Kooi, A. J. Morris, S. S. Smyth, *J. Biol. Chem.*, **2011**, 286, 34654.
- [34] J. Hausmann, E. Christodoulou, M. Kasiem, V. De Marco, L. A. Van Meeteren, W. H. Moolenaar, D. Axford, R. L. Owen, G. Evans, A. Perrakis, *Acta Crystallogr. Sect. F Struct. Biol. Cryst. Commun.*, **2010**, 66, 1130.
- [35] B. Webb, A. Sali, *Protein Struct. Predict.*, **2014**, 1137, 1..
- [36] M. J. Abraham, T. Murtola, R. Schulz, S. Páll, J. C. Smith, B. Hess, E. Lindahl, *SoftwareX*, **2015**, 1, 19..
- [37] K. Lindorff-Larsen, S. Piana, K. Palmo, P. Maragakis, J. L. Klepeis, R. O. Dror, D. E. Shaw, *Proteins Struct. Funct. Bioinforma.*, **2010**, 78, 1950..
- [38] C. I. Bayly, P. Cieplak, W. Cornell, P. A. Kollman, *J. Phys. Chem.*, **1993**, 97, 10269..



Chapter A3

Imaging autotaxin *in vivo* with ^{18}F -labeled positron emission tomography ligands

Xiaoyun Deng,^{1,2,†} Fernando Salgado-Polo,^{3,†} Tuo Shao,^{1,†} Zhiwei Xiao,¹ Richard Van,⁴ Jiahui Chen,¹ Jian Rong,¹ Ahmed Haider,¹ Yihan Shao,⁴ Lee Josephson,¹ Anastassis Perrakis^{3,*} and Steven Liang^{1*}

Affiliations:

¹ Division of Nuclear Medicine and Molecular Imaging, Massachusetts General Hospital & Department of Radiology, Harvard Medical School, Boston, Massachusetts 02114, United States.

² Department of Nuclear Medicine, Tongji Hospital, Tongji Medical College, Huazhong University of Science and Technology, Wuhan 430030, China.

³ Oncode Institute and Division of Biochemistry, Netherlands Cancer Institute, Plesmanlaan 121, 1066 CX Amsterdam, The Netherlands.

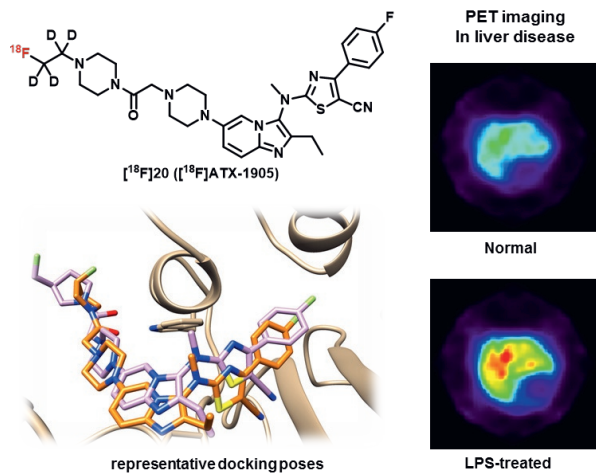
⁴ Department of Chemistry and Biochemistry, University of Oklahoma, Norman, Oklahoma 73019, United States.

† These authors contributed equally to this work.

* Correspondence: a.perrakis@nki.nl; liang.steven@mgh.harvard.edu.

Based on:

Journal of Medicinal Chemistry. 2021, 64(20): 15053-15068.



Abstract

Autotaxin (ATX) is a secreted phosphodiesterase that has been implicated in a remarkably wide array of pathologies, ranging from idiopathic pulmonary fibrosis and autoimmune disease to neurodegenerative disorders, metabolic syndrome and cancer. While ATX inhibitors have entered the clinical arena, a validated probe for positron emission tomography (PET) is currently lacking. With the aim to develop a suitable ATX-targeted PET radioligand, we have synthesized a focused library of 12 fluorinated imidazo[1,2-a]pyridine derivatives, determined their inhibition constants, and confirmed their binding mode by crystallographic analysis. Based on their promising *in vitro* properties, compounds **9c**, **9f**, **9h** and **9j** were radiofluorinated with average radiochemical yields ranging from 20–53% (decay-corrected), molar activities >37 GBq/μmol and excellent radiochemical purities >99%. Notably, PET imaging and *ex vivo* biodistribution studies revealed considerable radioactivity uptake in the bones following intravenous injection of [¹⁸F]**9c**, [¹⁸F]**9f** and [¹⁸F]**9h**, which was substantially reduced for [¹⁸F]**9j**. Given that non-specific radioactivity uptake in the bone indicates *in vivo* radiodefluorination, a deuterated analogue of [¹⁸F]**9j**, designated [¹⁸F]ATX-1905 ([¹⁸F]**20**), was designed and proved to be highly stable against *in vivo* radiodefluorination, as evidenced by PET imaging and biodistribution experiments. *In vitro* and *in vivo* specificity of [¹⁸F]ATX-1905 towards ATX was demonstrated in a mouse model of LPS-induced liver injury with ~2-fold increase of ATX (*ENPP2*) expression levels. Overall, our results suggest that [¹⁸F]ATX-1905 is a suitable PET probe for non-invasive quantification of ATX.

Introduction

Autotaxin (ATX), also known as ectonucleotide pyrophosphatase/pyrophosphodiesterase 2 (ENPP2), is a secretory glycoprotein that belongs to the ectonucleotide pyrophosphatase/phosphodiesterase (ENPP) family. Following ribosomal translation, ATX is secreted to the extracellular space, where it hydrolyzes extracellular lysophosphatidylcholine (LPC) into bioactive lysophosphatidic acid (LPA), while concurrently prompting the release of choline^[1]. Notably, LPA can trigger a variety of physiological events that play important roles in diverse cellular processes including cell proliferation, differentiation, survival, migration, motility cytoskeletal changes and calcium influx^[2-5]. The ATX-LPA signaling axis is associated with numerous physiological and pathophysiological processes, including cancer^[6, 7], chronic inflammation^[8, 9], fibrotic diseases^[10, 11], metabolic syndrome^[12], myocardial infarction^[13, 14] and autoimmune diseases^[15], and has been linked to alterations in the nutritional status^[12]. In oncology, ATX was found to be overexpressed in several malignancies^[6] including non-small cell lung (NSCL)^[16], hepatocellular^[17], breast^[18], thyroid^[19], renal^[20] and ovarian^[21] cancer. Further, ATX dysfunction has been implicated in lung^[21], liver^[22], renal^[23] and skin^[24] fibrosis conditions, along with chronic inflammatory diseases including multiple sclerosis^[25], arthritis^[26] and autoimmune encephalomyelitis^[27]. Given these broad implications, it is not surprising that strenuous efforts have been made to develop pharmacological modulators of the ATX-LPA axis, thus yielding a series of ATX inhibitors with distinct chemical scaffolds. Importantly, these chemical scaffolds are typically subdivided into four types according to their binding modes at the ATX tripartite active site (**Figure 1**)^[28, 29]. While type I inhibitors occupy the hydrophobic pocket of ATX and reach to the bimetallic active site, leaving the tunnel of ATX unoccupied, type II inhibitors occupy only the tunnel, and type III inhibitors bind to the tunnel but leave the pocket as well as the catalytic site unoccupied^[29-31]. Type IV inhibitors bind to the hydrophobic pocket and the tunnel of ATX and elicit an allosteric effect that precludes the binding of LPA and bile acid derivatives to the ATX tunnel, in addition to an orthosteric effect that prevents enzyme-substrate interactions at the ATX active site^[32]. Important examples of type I and type II inhibitors include PF-8380 and PAT-078, respectively^[29, 33-36], while PAT-347 constitutes a potent type III inhibitor^[29-31]. Type IV ATX inhibitors, include two different chemotypes, the rationally designed bile salt and PF-8380 hybrid Cpd17^[32] and GLPG1690^[37], or Ziritaxestat, the first candidate that entered clinical trials for the treatment of idiopathic pulmonary fibrosis (IPF). While the phase 3 trial of Ziritaxestat (NCT03733444) was recently interrupted due to adverse toxic effects, prior results clearly set a promising clinical landscape for ATX inhibition.

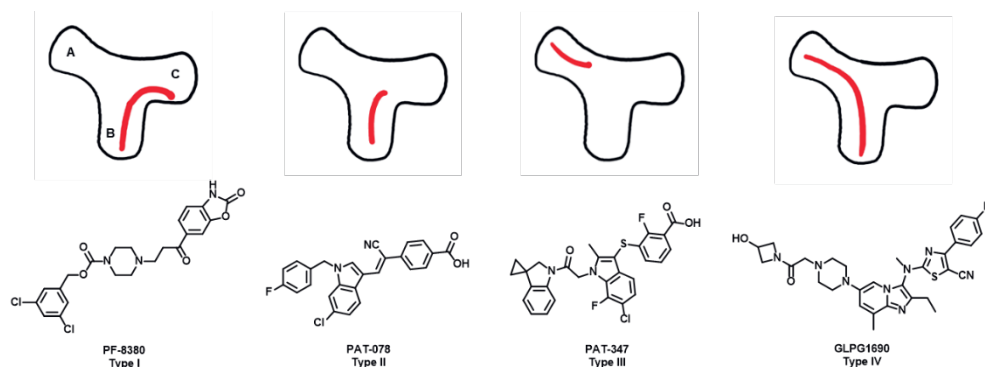


Figure 1. Representative ATX inhibitors of the four binding types. Type I, II, III, and IV inhibitors are represented in red. A, hydrophobic channel; B, hydrophobic pocket; C, catalytic site.

We sought to provide a quantitative imaging biomarker for the non-invasive assessment of biochemical and pharmacological processes involving ATX activity under healthy and diseased conditions. Thus, based on the favorable characteristics of the clinical candidate GLPG1690 in pharmacology and physiochemistry, we designed an array of fluorine-containing analogues, and performed pharmacologic evaluation as well as positron emission tomography (PET) studies of the most promising candidates using the respective ^{18}F -isotopologues. The availability of a suitable ATX-targeted PET radioligand would enable target engagement studies of novel ATX inhibitors, thereby facilitating their clinical development. There are currently no ATX specific PET ligands for human use, which represents an urgent clinical need. Herein, we present the synthesis of a small library of fluorine-bearing ATX inhibitors. The potential of these compounds was evaluated by their ability to inhibit ATX-mediated LPC hydrolysis, and the binding mode was confirmed by X-ray crystal structure analysis. Based on their *in vitro* characteristics, **9c**, **9f**, **9h** and **9j** were radiofluorinated and tested in biodistribution and/or PET studies. Due to a fast *in vivo* radiodefluorination, however, **9c**, **9f**, **9h** and **9j** were deemed unsuitable for PET imaging. To overcome this limitation, compound **20** was designed as a deuterated analogue of **9j** – with substantially improved stability. Compound **20** was found to be highly potent and was labeled with fluorine-18 for PET and biodistribution experiments. Biological evaluation of [Tager, 2008 #13][^{18}F]**20** in a lipopolysaccharide (LPS)-induced mouse model of liver injury confirmed the outstanding performance characteristics of [^{18}F]**20** for specific *in vivo* and *in vivo* visualization of ATX.

Results

Design of fluorinated ATX inhibitors amenable for labeling.

The reported ATX inhibitor **9a** and its fluoro-derivatives **9b-9k** were synthesized as depicted

in Scheme 1. Generally, fluorine-containing compounds varied on the nitrogen atom of the amide site, including azetidines, pyrrolidines, piperidines and piperazine derivatives. Initially, the cyclization of 3-(4-fluorophenyl)-3-oxopropanenitrile **1** and thiourea led to the formation of thiazole derivative **2** in 73% yield. Followed by the Sandmeyer reaction, compound **2** was converted to chloride **3** in 85% yield. Compound **5** was obtained in 73% yield via nucleophilic aromatic substitution of chloro-precursor **3** with the anion of amine **4**, which was generated *in situ*. After this coupling reaction, Boc-protected piperazine derivative **6** was synthesized in 73% yield. Subsequent deprotection with HCl, followed by alkylation with chloroacetamide derivatives **8** gave the desired products in yields ranging from 19-62%. The fluorine-containing building blocks for chloroacetamide **8** were derived from hydroxy derivatives except **8j**, which was synthesized from *tert*-butyl piperazine-1-carboxylate. In summary, candidate compounds **9a-9k** for ATX PET ligands were obtained from commercially available 3-(4-fluorophenyl)-3-oxopropanenitrile (**1**) in 6 steps with overall yields between 6-20%.

Pharmacological evaluation.

Upon synthesis, compounds **9a-9k** were screened for their *in vitro* activity towards ATX. For this purpose, we determined their ability to inhibit ATX lysoPLD activity by means of their K_i values, as determined by titrating the compounds into a mixture of ATX and the physiological substrate 18:1 LPC, fluorimetrically detecting choline release in real time, in a coupled reaction with choline oxidase and horseradish peroxidase. All candidates showed a two-digit nanomolar inhibitory activity on ATX, with K_i values ranging from 7 to 41 nM. As shown in **Table 1**, compound **9h** – bearing a 3-(fluoromethyl)pyrrolidine group – demonstrated the highest potency in our series, with a K_i value of 7 nM. Further, **9c-d**, **9f-g** and **9i-k** exhibited high potency with K_i values between 13-17 nM. Of note, the K_i values of fluoropyrrolidine derivatives **9c**, **9d** and **9e** were both higher than that of fluoromethylpyrrolidine **9h**. Given the superior binding affinity, compound **9h** was selected for radiofluorination and evaluation as a PET ligand.

Crystal structure-based analysis of the binding mode of the 9a-k series.

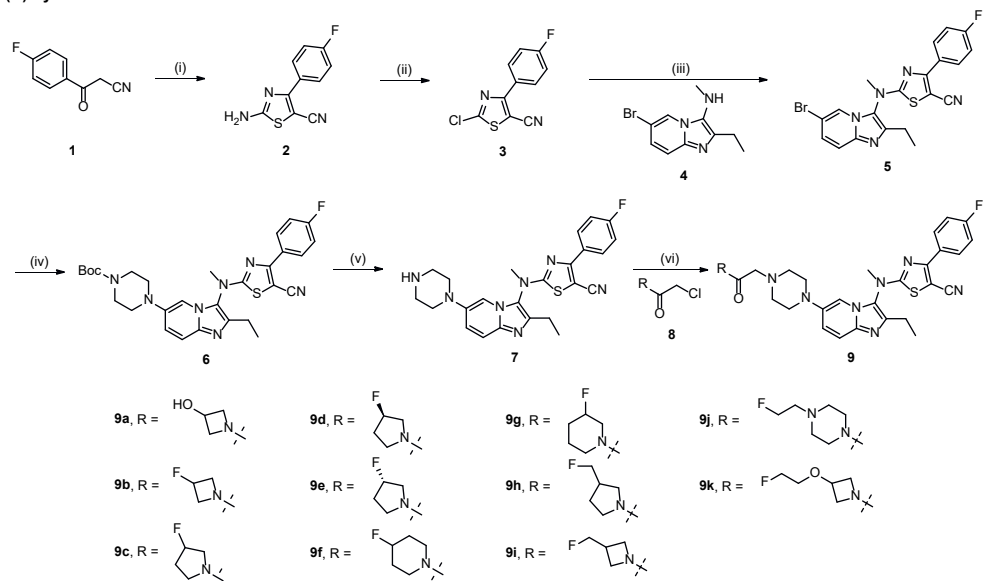
To assess the binding mode of compounds **9a-k** and support further structural optimization efforts, we aimed to determine the crystal structure of representative compounds from the 9a-k series bound to ATX. Compound **9d** was co-crystallized with rat ATX. The crystal structure was determined by molecular replacement and the resulting electron density clearly showed the bound ligand. The ligand was placed in the electron density occupying the tunnel and hydrophobic pocket and the structure was subsequently refined at 2.2 Å resolution to an $R_{\text{work}}/R_{\text{free}}$ of 19.3/26.8%, with excellent quality (99th percentile quality category according to Molprobity^[38]) (**Figure 2A**).

The binding mode adopted by compound **9d** places it in the type IV category, as intended

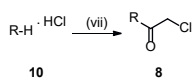
by design. High-affinity binding is mostly mediated by hydrophobic interactions with the aromatic residues at the ATX tunnel and the hydrophobic pocket (**Figure 2B-D**). Mostly van der Waals interactions to Trp254 (3.3 – 3.7 Å) and Phe274 (3.3 – 3.5 Å) appear important for binding. Notably, hydrogen bonding seems to be less crucial, with a single hydrogen bond between the carbonyl at the linker between the piperazine and the pyrrolidine rings, and the indole nitrogen of Trp260 (3.1 Å, with somewhat unfavorable geometry).

Scheme 1. Design and synthesis of fluorinated ATX inhibitors^a

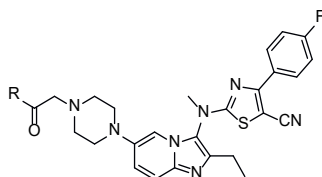
(A) Synthesis of ATX inhibitor 9a and fluorinated derivatives 9b-9k



(B) Synthesis of intermediate 8



^aReagents and conditions: (i) 1 equiv. pyridine, ethanol, 70 °C, 15 min, then 2 equiv. thiourea, 1 equiv. iodine, ethanol, room temperature, 1 h, 73%; (ii) 2 equiv. *tert*-butyl nitrite, 1.6 equiv. CuCl₂, acetonitrile, room temperature, 1.5 h, 85%; (iii) 1.2 equiv. **3**, 2 equiv. NaH (60%), tetrahydrofuran, 60 °C, 16 h, 73%; (iv) 1.5 equiv. *tert*-butyl piperazine-1-carboxylate, 10 mol% Pd₂dba₃, 20 mol% JohnPhos, 2 equiv. sodium *tert*-butoxide, toluene, room temperature, 10 min, 100 °C, 16 h, 73%; (v) 20 equiv. HCl (4 M in 1,4-dioxane), methanol, room temperature, 16 h, 98%; (vi) 2.5 equiv. **8**, 2.5 equiv. K₂CO₃, acetonitrile, 70 °C, 2 h, 19-62%; (vii) 1.2 equiv. chloroacetyl chloride, 2.2 equiv. K₂CO₃, dichloromethane, H₂O, room temperature, 2 h, 10-94%.

Table 1. Biological activity of compounds 9a-9k

Compound	R	Ki (nM)	Compound	R	Ki (nM)
9a		30 ± 6	9g		15 ± 3
9b		41 ± 8	9h		7 ± 1
9c		15 ± 3	9i		14 ± 2
9d		14 ± 3	9j		13 ± 2
9e		32 ± 6	9k		17 ± 3
9f		15 ± 2			

The co-crystal structure of compound **9d** was used in molecular docking to compare the predicted binding modes of **9a-k** series. As expected, the predicted binding poses for these compounds showed type IV binding. Further analysis for the docking pose of compound **9d** to ATX showed slightly closer hydrogen bonding of 3.0 Å of the carbonyl linker to the indole ring of Trp260, as compared to 3.1 Å found in the crystal structure (**Figure 2E**). Since compound **9h** exhibited the highest potency, its docking pose was compared with compound **9d**. Tighter binding was observed for compound **9h**, with a hydrogen bond distance of 2.8 Å to the indole ring of Trp260 (**Figure 2F**). Although the solvent exposed end of compound **9h** showed tighter binding, no significant differences were observed for the van der Waals interaction to Trp254 and Phe274 that was observed for compound **9d**.

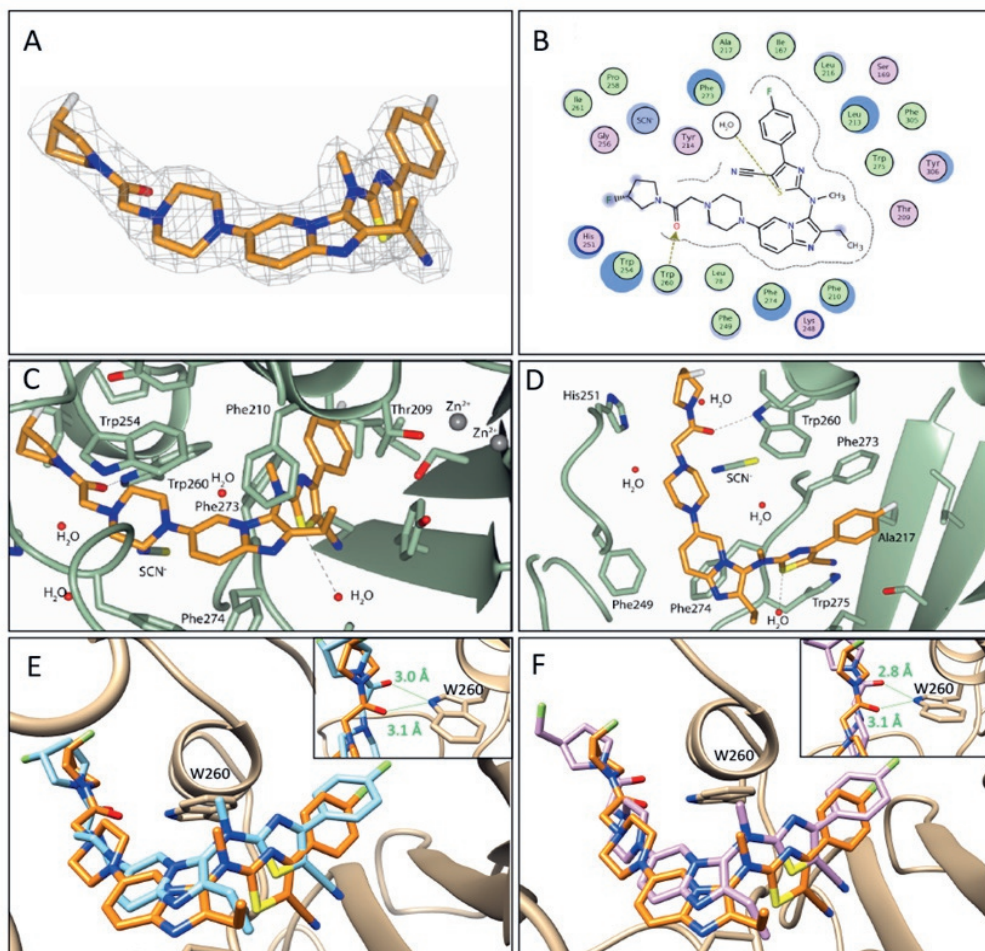
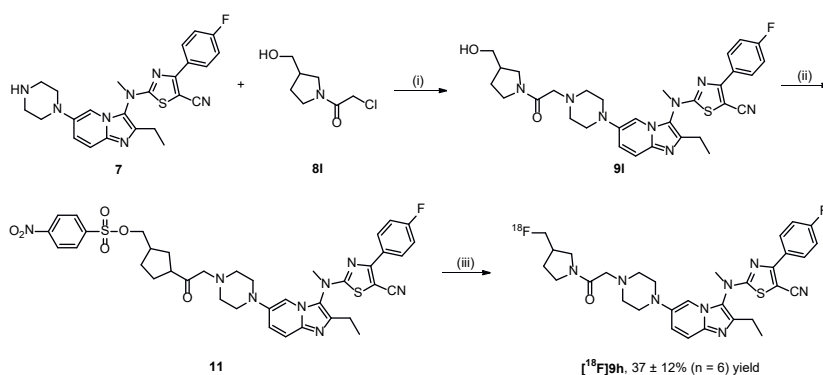


Figure 2. Binding mode of the lead compound **9c** within the ATX tunnel and hydrophobic pocket. (A) The fit of **9d** shown as a sticks model (carbon in orange; nitrogen in blue; oxygen in red; sulfur in yellow) to the $2mF_o-DF_c$ electron density map after refinement. (B) Two-dimensional depiction of **9d** binding mode. (C-D) Binding poses of **9d** and the ATX residues involved in binding (carbon in green; other atoms as before; a cartoon representation of the backbone is also visible). Hydrophobic and polar residues are indicated in green and pink, respectively; blue background indicates solvent exposure; and the dashed line represents a hydrogen bond to a water molecule. (E) The binding pose of compound **9d** from the co-crystal (orange) overlapped with the pose obtained from molecular docking (blue). Also shown is the hydrogen bonding distance with Trp260 (green line). (F) Docking poses for compound **9d** (orange) overlapped with compound **9h** (pink). Closer hydrogen bonding in was observed for the docked structure of compound **9h** indicated by the 2.8 Å distance of the carbonyl linker to the indole ring of Trp260 (green line).

Radiochemical synthesis of [^{18}F]9h

Attributed to the highest potency of compound **9h**, we designed and performed an efficient radiosynthesis of this lead molecule. The synthesis of precursor **11** and ^{18}F -labeling of **9h** is demonstrated in **Scheme 2**. The hydroxy intermediate **9i** was synthesized in 50% yield based on the method to the synthesis of **9a-9k**. After reaction of compound **9i** and 4-nitrobenzenesulfonyl chloride under base, precursor **11** was obtained in 88% yield with 4-nitrobenzenesulfonate as the leaving group. Then, compound **9h** was labeled with fluorine-18 via $\text{S}_{\text{N}}2$ displacement reactions (**Scheme 2**). Through screening of radiolabeling conditions, the combined use of $^t\text{BuOH}$ and MeCN as mixed solvents provided the highest conversion of [^{18}F]9h in decay-corrected radiochemical yield of 37% based on starting [^{18}F]fluoride at the end-of-synthesis (50 min synthesis time) with high radiochemical purity (>99%) and high molar activity (> 1 Ci/ μmol).

Scheme 2. Synthesis of Radiolabeling Precursor 18 and Radiosynthesis of [^{18}F]9h^a



^aReagents and conditions: (i) 2.5 equiv. **8**, 2.5 equiv. K_2CO_3 , acetonitrile, 70 °C, 2 h, 50%; (ii) 3 equiv. 4-nitrobenzenesulfonyl chloride, 5 equiv. triethylamine, dichloromethane, room temperature, 16 h, 88%; (iii) [^{18}F]F⁻, TBAOMs, $^t\text{BuOH}/\text{MeCN}$, 100 °C, 15 min.

PET image and ex vivo whole-body distribution study of [^{18}F]9h

Following the synthesis of our lead ATX ligand [^{18}F]9h, dynamic PET acquisition was carried out in CD-1 mice. Representative PET images (sagittal view, summed images at 0-5 min, 5-15 min, 15-30 min and 30-60 min intervals) are shown in **Figure 3**. PET images revealed a rapid systemic clearance, which was consistent with low expression level of ATX in periphery under normal conditions. Low brain uptake of [^{18}F]9h showed its limited applications in CNS-related diseases. The high bone uptake at 30 min post injection points towards substantial *in vivo* radiodefluorination of compound [^{18}F]9h. Further, *ex vivo* biodistribution studies with [^{18}F]9h confirmed the high accumulation of radioactivity in the bone from 15 min to 60 min (**Figure 4**). In addition, high activity in the liver, kidneys and small intestine indicated that [^{18}F]9h was possibly eliminated via urinary and

hepatobiliary pathways. The fast *in vivo* radiodefluorination led us to investigate other potent fluorinated ATX analogs from **Table 1**.

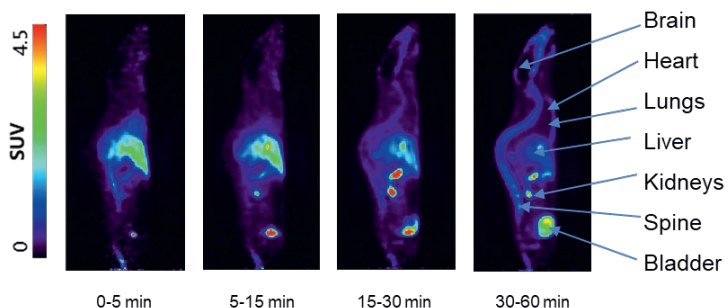


Figure 3. Representative PET images of [^{18}F]9h (sagittal view, summed images at 0-5 min, 5-15 min, 15-30 min, 30-60 min intervals) in CD-1 mice. Bone uptake (caused by radiodefluorination) in the spine was clearly visualized.

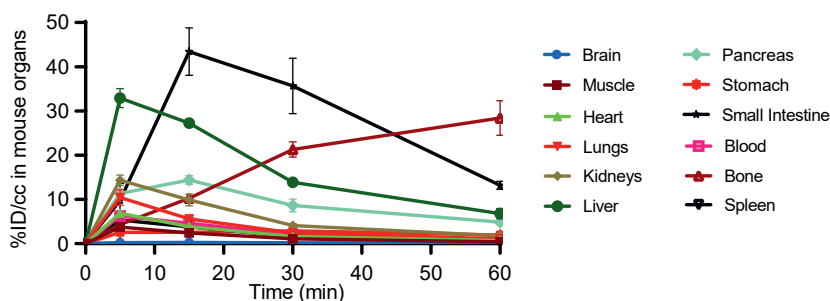


Figure 4. Whole-body biodistribution of [^{18}F]9h in major organs/tissues of CD-1 mice ($n = 4$) at 5, 15, 30 and 60 min post injection.

Radiosynthesis and bone uptake studies with [^{18}F]9c, [^{18}F]9f and [^{18}F]9j

In order to circumvent *in vivo* radiodefluorination, we selected **9c**, **9f** and **9j** as candidates for radiofluorination and potential *in vivo* evaluation. The syntheses of precursors **12**, **13** and **17** for the radiofluorination of **9c**, **9f** and **9j**, respectively, are shown in Scheme 3.

Precursors **12** and **13** were prepared in analogy to the synthesis of compound **11**, with yields of 47% and 83%, respectively. The synthesis of precursor **17** was accomplished from piperazine derivative **7** via four steps, including N-alkylation with chloroacetamide **8o**, removal of the Boc group under HCl conditions, nucleophilic substitution with 2-bromoethanol and treatment with 4-nitrobenzenesulfonyl chloride to form the chloride-substituted leaving group. Due to the fast *in situ* chlorination of 4-nitrobenzenesulfonate

by chloride anion, **17** was employed as a precursor for the radiofluorination of **9j**. Similarly, compounds [^{18}F]**9c** and [^{18}F]**9f** were obtained in decay-corrected radiochemical yields of 53% and 44%, respectively, high radiochemical purity (>99%) and high molar activity (> 1 Ci/ μmol). In addition, compound [^{18}F]**9j** was synthesized using a mixture of $t\text{BuOH}$ and DMSO at higher temperature, resulting in decay-corrected radiochemical yield of 20% at the end-of-synthesis (ca. 70 min synthesis time) with high radiochemical purity (>99%) and high molar activity (> 1 Ci/ μmol).

Ex vivo bone uptake studies were performed in CD-1 mice to evaluate the extent of radiodefluorination for compounds [^{18}F]**9c**, [^{18}F]**9f** and [^{18}F]**9j** at 30 and 60 min post injection. Results are summarized in **Figure 5** and compared to the previous results obtained with [^{18}F]**9h**. While a high accumulation of radioactivity in the bones (>10 %ID/g) was observed for compounds [^{18}F]**9c** and [^{18}F]**9f**, compound [^{18}F]**9j** showed a significantly reduced and moderate bone uptake (6.6 and 6.4 %ID/g at 30 and 60 min, respectively), which indicated that the [^{18}F]fluoroethyl piperazine moiety was relatively stable against defluorination *in vivo*.

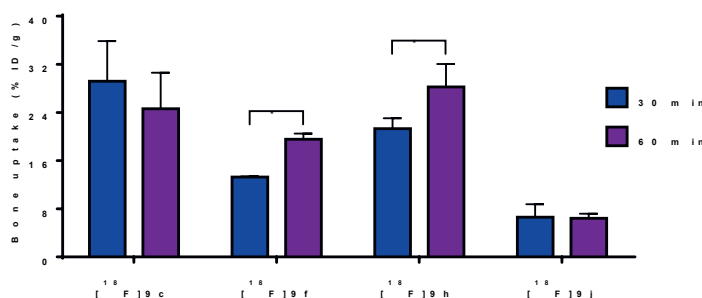
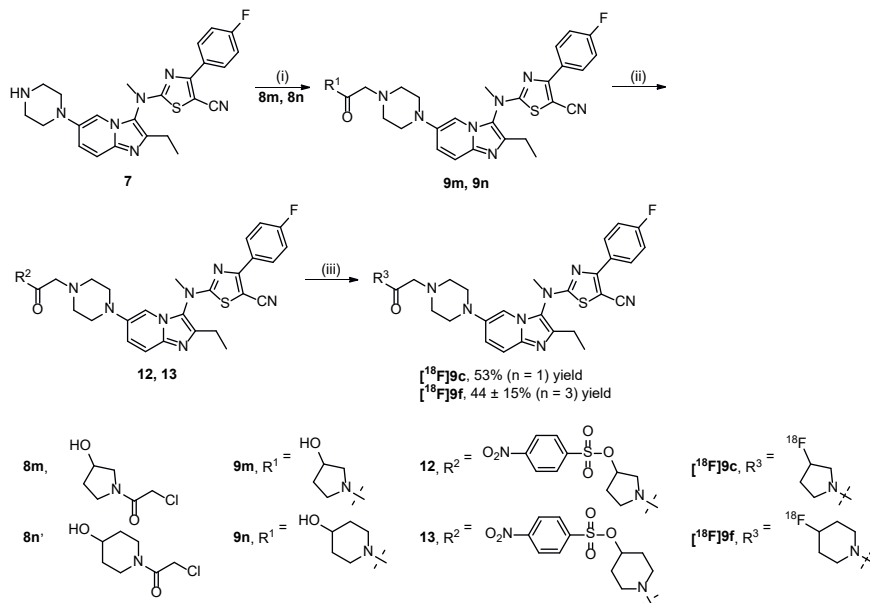
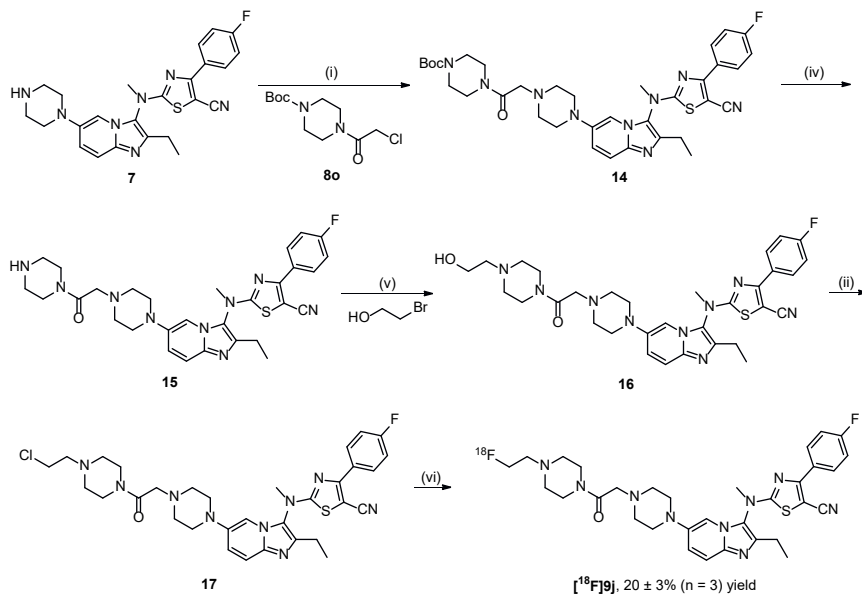


Figure 5. Ex vivo bone uptake of [^{18}F]**9c**, [^{18}F]**9f**, [^{18}F]**9h** and [^{18}F]**9j** ($n \geq 2$) in CD-1 mice at 30 min and 60 min post injection. Asterisks indicate statistical significance: $*p < 0.05$.

Radiosynthesis of deuterated compound [^{18}F]**20**

Deuterium substitution can be used as an effective medical chemistry tool to decrease the metabolic rate of candidate structures in drug and radioligand discovery^[39-41]. As such, this strategy has been employed to improve the metabolic stability of radiofluorinated compounds against *in vivo* radiodefluorination^[42-45]. Accordingly, we designed compound **20** as deuterated analog of **9j** that bears four deuterium atoms at the fluoroethyl side chain (**Scheme 4**). We hypothesized that compound **20** would exhibit negligible *in vivo* radiodefluorination, while maintaining binding potency towards ATX *in vitro* and *in vivo*.

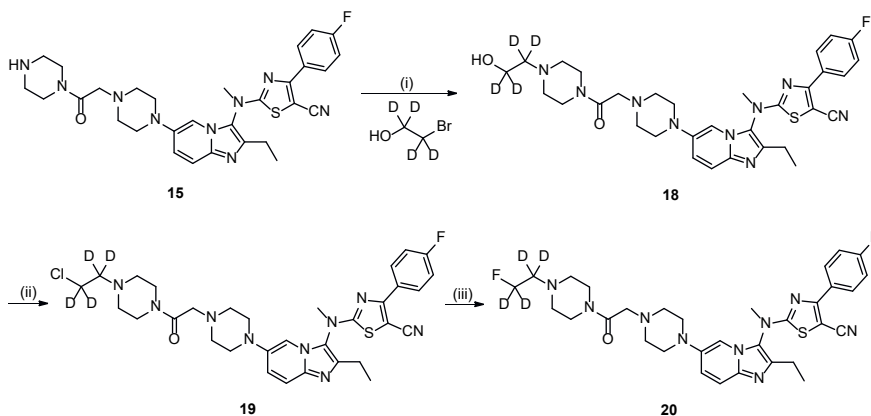
Scheme 3. Radiosynthesis of [¹⁸F]9c, [¹⁸F]9f and [¹⁸F]9j^a**(A) Synthesis of Radiolabeling Precursor 12 and 13; Radiosynthesis of [¹⁸F]9c and [¹⁸F]9f****(B) Synthesis of Radiolabeling Precursor 17; Radiosynthesis of [¹⁸F]9j**

^aReagents and conditions: (i) (vi) 2.5 equiv. **8**, 2.5 equiv. K₂CO₃, acetonitrile, 70 °C, 2 h, 19-52%; (ii) 3 equiv. 4-nitrobenzenesulfonyl chloride, 5 equiv. triethylamine, dichloromethane, room temperature, 16 h, 47-83%; (iii) [¹⁸F]F⁻, TBAOMs, ^tBuOH/MeCN, 100 °C, 15 min; (iv) 20 equiv. HCl (4 M in 1,4-dioxane), methanol, room temperature, 16 h, 98%; (v) 5.0 equiv. 2-bromoethanol, 6.0 equiv. triethylamine,

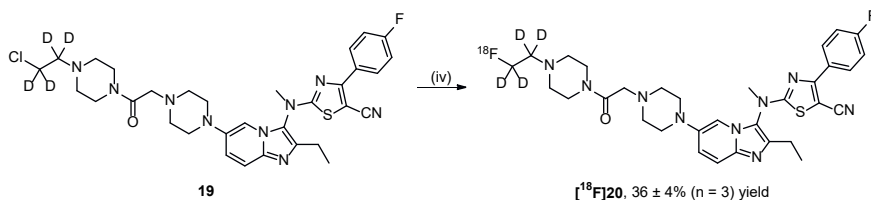
acetonitrile, 80 °C, 5 h, 53%; (vi) ^{18}F], TBAOMs, $^t\text{BuOH/DMSO}$, 120 °C, 15 min.

Scheme 4. Synthesis of radiolabeling precursor **19**, ligand **20** and radiosynthesis of ^{18}F]**20**^a

(A) Synthesis of Radiolabeling Precursor **19 and Ligand **20****



(B) Radiosynthesis of ^{18}F]20****



^aReagents and conditions: (i) 5.0 equiv. 2-bromoethanol ($1,1,2,2\text{-d}_4$), 6.0 equiv. triethylamine, acetonitrile, 80 °C, 5 h, 64%; (ii) 3 equiv. 4-nitrobenzenesulfonyl chloride, 5 equiv. triethylamine, dichloromethane, room temperature, 2 h, 66%; (iii) 5.0 equiv. CsF , MeCN , 100 °C, 3 h, 63%; (iv) ^{18}F], TBAOMs, $^t\text{BuOH/DMSO}$, 120 °C, 15 min.

Compound **20** was synthesized according to the preparation protocol of intermediate **17**. Briefly, deuterated 2-bromoethanol was used to synthesize **18** via nucleophilic substitution reaction with **15**. Following treatment with 4-nitrobenzenesulfonyl chloride and *in situ* chlorination, deuterated chloro-precursor **19** was formed and subsequently fluorination to afford target ligand **20**. A K_i value of 19 ± 3 nM was determined for ATX inhibitor **20**, which was slightly higher as compared to the non-deuterated analogue. Subsequently, ^{18}F]**20** was prepared from precursor **19** in an average decay-corrected radiochemical yield of $36 \pm 4\%$, > 99% radiochemical purity and > 1 Ci/ μmol molar activity.

PET image and ex vivo whole-body distribution study of [^{18}F]20 in normal mice

Dynamic PET acquisition with [^{18}F]20 was carried out in normal CD-1 mice. Representative PET images (sagittal view, summed images at 0-5 min, 5-15 min, 15-30 min and 30-60 min intervals) are shown in **Figure 6**. PET images revealed a rapid clearance of [^{18}F]20 in the whole body, which was consistent with the low expression levels of ATX in the periphery under physiological conditions. Attributed to relatively large molecular weight, [^{18}F]20 failed to cross the blood-brain barrier as indicated by PET images. In support of our hypothesis, no substantial bone uptake was observed using deuterated compound [^{18}F]20. Further, ex vivo biodistribution studies in CD-1 mice showed only marginal accumulation of radioactivity in the bone, which remained low up to 60 min post injection (**Figure 7**). While high initial uptake of [^{18}F]20 was observed in the small intestine, kidneys and liver, radioactivity in these organs declined rapidly at 30 min post injection. These results supported [^{18}F]20 as a potential ATX tracer to be validated in disease models.

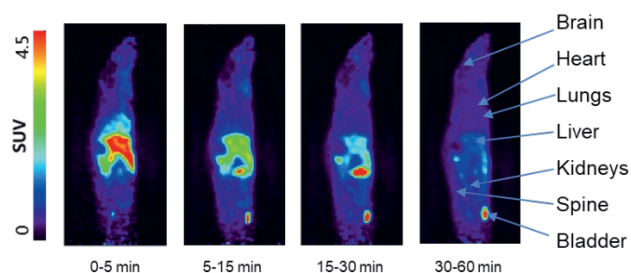


Figure 6. Representative PET images of [^{18}F]20 (sagittal view, summed images at 0-5 min, 5-15 min, 15-30 min, 30-60 min intervals) in CD-1 mouse. No substantial bone uptake was observed.

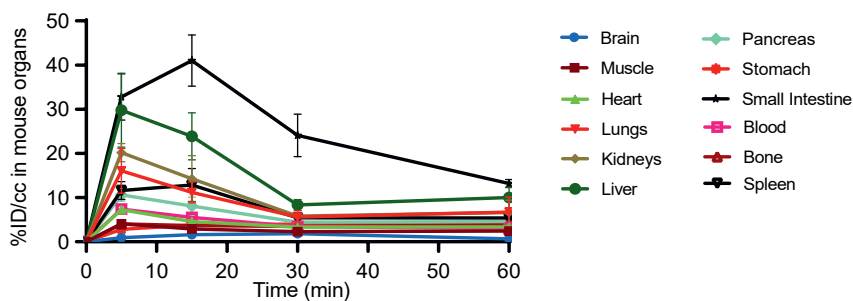


Figure 7. Whole body biodistribution ($n = 4$) of [^{18}F]20 in CD-1 mice. (B) Biodistribution of [^{18}F]20 in CD-1 mice ($n = 4$) in major organs/tissues at four time points (5, 15, 30 and 60 min) post injection.

PET study of [^{18}F]20 in an acute liver inflammation model.

Previous studies unveiled that LPS treatment increased ATX relative mRNA (*ENPP2*)

expression in primary liver cells^[46]. Therefore, as a proof of concept, we used a mouse model of LPS-induced liver injury and inflammation to evaluate the binding specificity and kinetics of ^{18}F]**20**. PET images of normal and LPS-treated mice showed an elevated accumulation of ^{18}F]**20** in the liver of LPS-treated mice, as compared to normal mice (**Figure 8A**). Further, liver time-activity curves (TACs, **Figure 8B**), as well as signal quantification by the area under the curve (AUC)_{30-60 min} (**Figure 8C**), suggesting an enhanced tracer uptake (84%) in the inflamed liver. A blocking study using ATX inhibitor **9a** (3mg/kg, iv) confirmed the specific binding to ATX. *In vitro* autoradiography study of ^{18}F]**20** was performed on healthy and LPS-treated mouse liver sections. The results shown in **Figure 8D** indicate a 92% increase of tracer uptake in the liver of LPS-treated mice, as compared healthy mouse liver sections. The upregulation of ATX in the liver at 24 hours following LPS treatment was further confirmed by RT-PCR analysis as shown in **Figure 8E**. Hepatic ATX (*ENPP2*) mRNA levels were increased by ~2-fold after LPS treatment. Thus, the increased retention of ^{18}F]**20** in the inflamed liver was in agreement with the increased ATX (*ENPP2*) expression levels observed by RT-PCR (**Figure 8E**), confirming the binding specificity of ^{18}F]**20** to ATX *in vivo*.

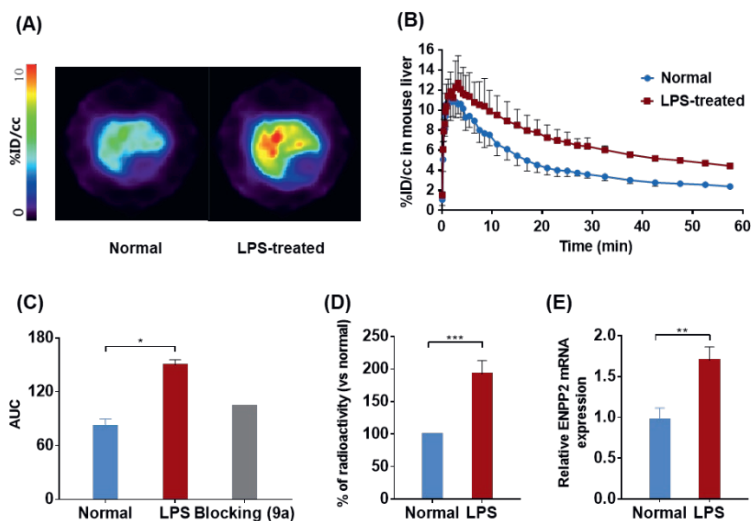


Figure 8. (A) Representative summed 60 min transverse PET images of ^{18}F]**20** in normal and LPS-treated mice. (B) Liver time-activity curves (TAC) of ^{18}F]**20** ID%/cc in normal and LPS-treated mice ($n = 3$). (C) Area under the curves (AUC) from 30 to 60 min for normal ($n = 3$), LPS-treated ($n = 3$) and blocking (**9a**, 3mg/kg, $n = 1$) mice. (D) Quantification of bound activity in liver sections from normal and LPS-treated mice after incubation with ^{18}F]**20** by autoradiography. (E) Relative ATX mRNA (*ENPP2*) expression in normal and LPS-treated mice. Data are presented as mean \pm SEM ($n = 3$) and analyzed by one-way ANOVA unless otherwise indicated. Asterisks indicate statistical significance: * $p < 0.05$, ** $p \leq 0.01$, *** $p \leq 0.001$.

Conclusions

We have successfully synthesized a focused library of fluorinated ATX inhibitors based on the clinical drug candidate, GLPG1690. We then evaluated the inhibition constants and confirmed the binding mode of the series by the crystal structure of one of our compound, selecting the most promising candidates for radiofluorination. ^{18}F -Isotopologues ^{18}F **9c**, ^{18}F **9f**, ^{18}F **9h**, ^{18}F **9j** and ^{18}F **20** were synthesized in good radiochemical yields, high molar activity and excellent radiochemical purity. *In vivo* PET studies and *ex vivo* biodistribution in normal mice demonstrated that ^{18}F **20** (^{18}F ATX-1905) was the best performing ligand, attributed to its minimal radiodefouorination *in vivo*. Subsequently, ^{18}F **20** was advanced to PET studies in a mouse model of LPS-treated liver injury and inflammation. Consistent with the results of *in vitro* autoradiography studies on liver sections from LPS-treated and sham mice, the binding specificity of ^{18}F **20** was excellent as confirmed by blocking studies. RT-PCR studies also demonstrated that ATX (*ENPP2*) expression was elevated in the liver of LPS-treated mice, correlating well with our PET results. Overall, our work has identified a novel ^{18}F -labeled ATX-targeted PET type IV ligand and demonstrated its preliminary application in a mouse model of liver injury, which could serve as an excellent entry point for further development of clinical applications.

Experimental procedures

The general procedure for the experimental section was described previously with minor modification in this work^[47]. All the chemicals employed in the syntheses were purchased from commercial vendors and used without further purification. Thin-layer chromatography (TLC) was conducted with 0.25 mm silica gel plates ($^{60}\text{F}_{254}$) and visualized by exposure to UV light (254 nm) or stained with potassium permanganate. Flash column chromatography was performed using silica gel (particle size 0.040-0.063 mm). Nuclear magnetic resonance (NMR) spectra were obtained on a Bruker spectrometer 300 MHz and/or a Varian spectrometer 500 MHz. Chemical shifts (δ) are reported in ppm and coupling constants are reported in Hertz. The multiplicities are abbreviated as follows: s = singlet, d = doublet, t = triplet, q = quartet, quint = quintet, sext = sextet, sept = septet, m = multiplet, br = broad signal, dd = doublet of doublets. For LC-MS/MS measurements, the ionization method is ESI using Agilent 6430 Triple Quad LC/MS. All tested ATX inhibitors showed purity more than 95% as determined by a reverse-phase HPLC (Gemini[®] 5 μm , NX-C18 110 Å column, 3 mm ID \times 150 mm). CD-1 mice (female; 7 weeks, 22-24 g) were kept on a 12 h light/12 h dark cycle and were allowed food and water *ad libitum*.

Protein production and crystallization. Rat ATX was over-expressed and purified as described previously^[49]. For crystallization- studies, ATX was incubated with **9c** (330 μM

in DMSO) at a 1:10 (protein:compound) ratio for at least 30 minutes. 1 ul of ATX:9c and 1 ul reservoir solution were mixed and equilibrated against 1 ml of reservoir using the hanging drop methods in a 24-well plate (Hampton Research). The reservoir solutions were a custom-made optimization screen (18–20% PEG 3350, 0.1–0.4 M NaSCN, and 0.1–0.4 M NH₄I). The best diffracting crystals were obtained at room temperature (293 K) after at least 7 days. All crystals were vitrified in cryo-protectant, which consisted of reservoir solution with the addition of 20% (v/v) glycerol.

Crystallographic data and methods. Co-crystal structure of compound **9d** and rat ATX was used for molecular docking via the software AutoDock Vina (AutoDock Vina, version 1.1.2) implemented in UCSF Chimera (UCSF Chimera, version 1.13.1). The initial protein structure was prepared through the Dock Prep function of UCSF Chimera which involved the addition of hydrogen atoms, deletion of solvent, and assigned AMBER ff14SB force field for standard residues.

The X-ray diffraction data for the ATX–inhibitor complexes were collected at SLS on beamline PXI (X06SA) at 100 K, and were recorded on an EIGER X 16M detector to a resolution of 1.6 Å. All datasets were processed on site using the SLS automated processing pipeline^[50]; the final dataset was integrated with XDS^[51] and scaled with AIMLESS^[52]; the useful data extended to 2.2 Å resolution. The structure was determined by molecular replacement using MOLREP^[53] with the structure of ATX (PDB 2XR9) as the search model. Model building and subsequent refinement were performed iteratively with COOT^[54], REFMAC5^[55], and PDB_REDO^[56]. Structure validation was carried out by MolProbity^[38]. The structure model and experimental diffraction data are deposited at the PDB under code 7P0K (Table 2).

Ex Vivo biodistribution and bone uptake study. The general procedure for ex vivo biodistribution studies was described previously^[47] with minor modification in this work. Briefly, a solution of [¹⁸F]**9h** or [¹⁸F]**20** (15 μCi/100 μL) was injected into CD-1 mice via tail vein. These mice (at each time point n = 4) were sacrificed at 5, 15, 30, and 60 min post tracer injection. Major organs, including whole brain, heart, liver, lung, spleen, kidneys, small intestine (including contents), muscle, and blood samples, were quickly harvested and weighted. The radioactivity present in these tissues was measured using 1480 Wizard γ counter (PerkinElmer), and all radioactivity measurements were automatically decay-corrected on the basis of the half-life of fluorine-18. The results are expressed as a percentage of the injected dose per gram of wet tissue (% ID/g). Bone uptake study of [¹⁸F]**9c**, [¹⁸F]**9f** and [¹⁸F]**9j** are performed similar with ex vivo biodistribution of [¹⁸F]**9h** and [¹⁸F]**20**.

In vitro autoradiography. The general procedure for in vitro autoradiography was

Table 2. Crystallographic details.

Compound	9d (7P0K)
Data collection	
wavelength (Å)	1.00000
resolution (Å)	2.20
space group	P2 ₁ 2 ₁ 2 ₁
unit cell a, b, c (Å), α, β, γ (deg)	61.60 86.68 145.77 $\alpha = \beta = \gamma = 90$
CC_{1/2}	0.992 (0.668)
R_{merge}	0.119 (0.960)
I/σI	7.8 (1.7)
completeness (%)	98.1 (99.2)
Redundancy	5.3 (5.2)
Refinement	
no. atoms	6742
Protein	6299
ligand/metal/glycan	134
water/iodine	309
TLS groups	1
R_{work}/R_{free} (%)	19.2/26.8
Validation	
rsmr/rmsZ bond lengths (Å)	0.0099/0.386
rsmr/rmsZ bond angles (deg)	1.775/0.674
Ramachandran preferred/outliers (%)	94.35/0.13
Ramachandran Z score	-1,859
Rotamers preferred (%)	97
MolProbity/Clash score (%ile)	99/99

^aHigh resolution shell in parentheses.

described previously with minor modification in this work^[57]. Mouse liver was cut into 20 μ m sections and stored at -80 °C until they were used for experiment. The mouse liver sections were preincubated with Tris-HCl buffer (pH = 7.4, 50 mM) solution for 20 min at ambient temperature, followed by incubation with [¹⁸F]**20** for 30 min at ambient temperature. After incubation, liver sections were washed with Tris buffer two times for 2 min and dipped in cold distilled water for 10 s. The liver sections were dried with cold air, then placed on imaging plates (BASMS2025, GE Healthcare, NJ, USA) for 60 min. Autoradiograms were obtained and ROIs were carefully drawn with the reference of naked-eye observation. Radioactivity was expressed as percentages of gray values versus normal mouse liver.

PET imaging studies. The general procedure for PET imaging was described previously with minor modification in this work^[57]. PET scans were carried out by a Genisys⁴ PET scanner. CD-1 mice were kept under anesthesia with 1.5% (v/v) isoflurane during the scan. The tracer was injected via a preinstalled catheter via the tail vein. A dynamic scan was

acquired for 60 min in three-dimensional list mode. For pretreatment studies, unlabeled inhibitor (3 mg/kg) dissolved in saline containing 10% ethanol and 5% Tween® 80 was injected at 2 min via the pre-embedded tail vein catheter before the injection of the tracer. The PET dynamic images were reconstructed using Amide software. Volume of interest in liver was placed using Amide. The radioactivity was decay-corrected and expressed as the standardized uptake value (SUV) or the percentage of the injected dose per cc (% ID/cc).

Biological evaluation. All animal experiments were conducted under the Institutional Animal Care and Use Committee of the Massachusetts General Hospital. Adult male CD1 mice (Charles River, Inc.) were used for the mouse model of LPS-induced liver injury and inflammation to demonstrate specificity of the ATX radiotracer. LPS-treated mice received an intraperitoneal injection of LPS from *E. coli* 055:B5 (Sigma-Aldrich, USA) in saline (3 mg/mL) at 15 mg/kg (5 mL/kg) dose 24 h prior to use, and sham mice received a saline injection.

Quantitative PCR (qPCR). Total RNA from liver tissue was isolated by QIA Shredder and RNeasy kit (Qiagen). Total RNA was reverse transcribed (RT) using a high-capacity cDNA reverse transcription kit with random primers (Applied Biosystems Inc.). To quantify gene expression, quantitative real-time PCR was performed using an ABI QuantStudio 3 system (Applied Biosystems Inc.) and Power Up SYBR green master mix (Thermo Fisher Scientific). Data were expressed as relative mRNA levels using the $\Delta\Delta$ CT method.

Acknowledgment

We thank the Division of Nuclear Medicine and Molecular Imaging, Radiology, MGH and Harvard Medical School, USA for general support.

References

- [1] H. M. Albers, H. Ovaa, *Chemical reviews* **2012**, 112, 2593.
- [2] M. Stracke, H. C. Krutzsch, E. J. Unsworth, A. Arestad, V. Cioce, E. Schiffmann, L. Liotta, *Journal of Biological Chemistry* **1992**, 267, 2524.
- [3] M.-E. Lin, D. R. Herr, J. Chun, *Prostaglandins & other lipid mediators* **2010**, 91, 130.
- [4] Y. Qian, M. Hamilton, A. Sidduri, S. Gabriel, Y. Ren, R. Peng, R. Kondru, A. Narayanan, T. Truitt, R. Hamid, *Journal of medicinal chemistry* **2012**, 55, 7920.
- [5] J. Chun, *In lysophospholipid receptors: signaling and biochemistry*. John Wiley & Sons, Inc **2013**, 813.
- [6] G. B. Mills, W. H. Moolenaar, *Nature Reviews Cancer* **2003**, 3, 582.
- [7] S. Willier, E. Butt, T. G. Grunewald, *Biology of the Cell* **2013**, 105, 317.
- [8] H. Kanda, R. Newton, R. Klein, Y. Morita, M. D. Gunn, S. D. Rosen, *Nature immunology* **2008**, 9, 415.
- [9] E. Barbayianni, E. Kaffe, V. Aidinis, G. Kokotos, *Progress in lipid research* **2015**, 58, 76.
- [10] J.-P. Pradère, J. Klein, S. Grès, C. Guigné, E. Neau, P. Valet, D. Calise, J. Chun, J.-L. Bascands, J.-S. Saulnier-Blache, *Journal of the American Society of Nephrology* **2007**, 18, 3110.
- [11] A. M. Tager, P. LaCamera, B. S. Shea, G. S. Campanella, M. Selman, Z. Zhao, V. Polosukhin, J. Wain, B. A. Karimi-Shah, N. D. Kim, *Nature medicine* **2008**, 14, 45.
- [12] K. D'Souza, G. Paramel, P. Kienesberger, *Nutrients* **2018**, 10, 399.
- [13] M. Navab, A. Chattopadhyay, G. Hough, D. Meriwether, S. I. Fogelman, A. C. Wagner, V. Grijalva, F. Su, G. Anantharamaiah, L. H. Hwang, *Journal of lipid research* **2015**, 56, 871.
- [14] S. S. Smyth, P. Mueller, F. Yang, J. A. Brandon, A. J. Morris, *Arteriosclerosis, thrombosis, and vascular biology* **2014**, 34, 479.
- [15] S. G. Bourgoin, C. Zhao, *Current opinion in investigational drugs (London, England: 2000)* **2010**, 11, 515.
- [16] Y. Yang, L.-j. Mou, N. Liu, M.-S. Tsao, *American journal of respiratory cell and molecular biology* **1999**, 21, 216.
- [17] G. Zhang, Z. Zhao, S. Xu, L. Ni, X. Wang, *Chinese medical journal* **1999**, 112, 330.
- [18] N. Panupinthu, H. Lee, G. B. Mills, *British journal of cancer* **2010**, 102, 941.
- [19] A. Kehlen, N. Englert, A. Seifert, T. Klonisch, H. Dralle, J. Langner, C. Hoang Vu, *International journal of cancer* **2004**, 109, 833.
- [20] M. Stassar, G. Devitt, M. Brosius, L. Rinnab, J. Prang, T. Schradin, J. Simon, S. Petersen, A. Kopp-Schneider, M. Zöller, *British journal of cancer* **2001**, 85, 1372.
- [21] U. Ray, S. Roy Chowdhury, M. Vasudevan, K. Bankar, S. Roychoudhury, S. S. Roy, *Molecular oncology* **2017**, 11, 491.
- [22] H. Ikeda, Y. Yatomi, *Clinica chimica acta* **2012**, 413, 1817.
- [23] J.-P. Pradère, J. Gonzalez, J. Klein, P. Valet, S. Grès, D. Salant, J.-L. Bascands, J.-S. Saulnier-Blache, J. P. Schanstra, *Biochimica et Biophysica Acta (BBA)-Molecular and Cell Biology of Lipids* **2008**, 1781, 582.

- [24] F. V. Castelino, G. Bain, V. A. Pace, K. E. Black, L. George, C. K. Probst, L. Goulet, R. Lafyatis, A. M. Tager, *Arthritis & Rheumatology* **2016**, *68*, 2964.
- [25] B. Hammack, K. Y. Fung, S. Hunsucker, M. Duncan, M. Burgoon, G. Owens, D. Gilden, *Multiple Sclerosis Journal* **2004**, *10*, 245.
- [26] A. F. Abdel-Magid, *ACS Med. Chem. Lett.* **2014**, *5*, 1072.
- [27] H. B. Streeter, R. Rigden, K. F. Martin, N. J. Scolding, D. C. Wraith, *Neurology-Neuroimmunology Neuroinflammation* **2015**, *2*, e93.
- [28] E. Barbayianni, V. Magrioti, P. Moutevelis-Minakakis, G. Kokotos, *Expert Opin. Ther. Pat.* **2013**, *23*, 1123.
- [29] A. J. Stein, G. Bain, P. Prodanovich, A. M. Santini, J. Darlington, N. M. Stelzer, R. S. Sidhu, J. Schaub, L. Goulet, D. Lonergan, *Molecular pharmacology* **2015**, *88*, 982.
- [30] W.-J. Keune, J. Hausmann, R. Bolier, D. Tolenaars, A. Kremer, T. Heidebrecht, R. P. Joosten, M. Sunkara, A. J. Morris, E. Matas-Rico, *Nature communications* **2016**, *7*, 11248.
- [31] G. Bain, K. E. Shannon, F. Huang, J. Darlington, L. Goulet, P. Prodanovich, G. L. Ma, A. M. Santini, A. J. Stein, D. Lonergan, *Journal of Pharmacology and Experimental Therapeutics* **2017**, *360*, 1.
- [32] W.-J. Keune, F. Potjewyd, T. Heidebrecht, F. Salgado-Polo, S. J. Macdonald, L. Chelvarajan, A. Abdel Latif, S. Soman, A. J. Morris, A. J. Watson, *Journal of medicinal chemistry* **2017**, *60*, 2006.
- [33] J. Gierse, A. Thorarensen, K. Beltey, E. Bradshaw-Pierce, L. Cortes-Burgos, T. Hall, A. Johnston, M. Murphy, O. Nemirovskiy, S. Ogawa, *Journal of Pharmacology and Experimental Therapeutics* **2010**, *334*, 310.
- [34] J. Hausmann, S. Kamtekar, E. Christodoulou, J. E. Day, T. Wu, Z. Fulkerson, H. M. Albers, L. A. Van Meeteren, A. J. Houben, L. Van Zeijl, *Nature structural & molecular biology* **2011**, *18*, 198.
- [35] H. Nishimasu, S. Okudaira, K. Hama, E. Mihara, N. Dohmae, A. Inoue, R. Ishitani, J. Takagi, J. Aoki, O. Nureki, *Nature structural & molecular biology* **2011**, *18*, 205.
- [36] P. Shah, A. Cheasty, C. Foxton, T. Raynham, M. Farooq, I. F. Gutierrez, A. Lejeune, M. Pritchard, A. Turnbull, L. Pang, *Bioorganic & medicinal chemistry letters* **2016**, *26*, 5403.
- [37] N. Desroy, C. Housseman, X. Bock, A. Joncour, N. Bienvenu, L. Cheral, V. Labeguere, E. Rondet, C. Peixoto, J.-M. Grassot, *J. Med. Chem.* **2017**, *60*, 3580.
- [38] V. B. Chen, W. B. Arendall, 3rd, J. J. Headd, D. A. Keedy, R. M. Immormino, G. J. Kapral, L. W. Murray, J. S. Richardson, D. C. Richardson, *Acta Crystallogr D Biol Crystallogr* **2010**, *66*, 12.
- [39] T. G. Gant, *Journal of Medicinal Chemistry* **2014**, *57*, 3595.
- [40] E. M. Russak, E. M. Bednarczyk, *The Annals of pharmacotherapy* **2018**, *53*, 211.
- [41] T. Pirali, M. Serafini, S. Cargnin, A. A. Genazzani, *Journal of medicinal chemistry* **2019**, *62*, 5276.
- [42] M. Kuchar, C. Mamat, *Molecules (Basel, Switzerland)* **2015**, *20*, 16186.
- [43] M. Schou, C. Halldin, J. Svg, V. W. Pike, H. Hall, B. Gulys, P. D. Mozley, D. Dobson, E. Shchukin, R. B. Innis, L. Farde, *Synapse (New York, N.Y.)* **2004**, *53*, 57.
- [44] M. Jahan, O. Eriksson, P. Johnstrm, O. Korsgren, A. Sundin, L. Johansson, C. Halldin, *EJNMMI research* **2011**, *1*, 33.
- [45] A. Haider, L. C. Gobbi, J. Kretz, C. Ullmer, A. Brink, M. Honer, T. J. Woltering, D. Muri, H. Iding, M. Brkler, M. Binder, C. Bartelmus, I. Knuesel, P. Pacher, A. Mller Herde, F. Spinelli, H. Ahmed,

- K. Atz, C. Keller, M. Weber, R. Schibli, L. Mu, U. Grether, S. M. Ametamey, *Journal of medicinal chemistry* **2020**.
- [46] E. Kaffe, A. Katsifa, N. Xylourgidis, I. Ninou, M. Zannikou, V. Harokopos, P. Foka, A. Dimitriadis, K. Evangelou, A. N. Moulas, U. Georgopoulou, V. G. Gorgoulis, G. N. Dalekos, V. Aidinis, *Hepatology (Baltimore, Md.)* **2017**, *65*, 1369.
- [47] O. Trott, A. J. Olson, *Journal of computational chemistry* **2010**, *31*, 455.
- [48] W.-J. Keune, J. Hausmann, R. Bolier, D. Tolenaars, A. Kremer, T. Heidebrecht, R. P. Joosten, M. Sunkara, A. J. Morris, E. Matas-Rico, W. H. Moolenaar, R. P. Oude Elferink, A. Perrakis, *Nature communications* **2016**, *7*, 11248.
- [49] J. E. Day, T. Hall, L. E. Pegg, T. E. Benson, J. Hausmann, S. Kamtekar, *Acta Crystallogr Sect F Struct Biol Cryst Commun* **2010**, *66*, 1127.
- [50] J. A. Wojdyla, J. W. Kaminski, E. Panepucci, S. Ebner, X. Wang, J. Gabadinho, M. Wang, *J Synchrotron Radiat* **2018**, *25*, 293.
- [51] W. Kabsch, *Acta Crystallogr D Biol Crystallogr* **2010**, *66*, 133.
- [52] P. R. Evans, *Acta Crystallogr D Biol Crystallogr* **2011**, *67*, 282.
- [53] A. Vagin, A. Teplyakov, *Acta Crystallogr D Biol Crystallogr* **2010**, *66*, 22.
- [54] P. Emsley, B. Lohkamp, W. G. Scott, K. Cowtan, *Acta Crystallogr D Biol Crystallogr* **2010**, *66*, 486.
- [55] G. N. Murshudov, P. Skubák, A. A. Lebedev, N. S. Pannu, R. A. Steiner, R. A. Nicholls, M. D. Winn, F. Long, A. A. Vagin, *Acta Crystallogr D Biol Crystallogr* **2011**, *67*, 355.
- [56] R. P. Joosten, F. Long, G. N. Murshudov, A. Perrakis, *IUCrJ* **2014**, *1*, 213.
- [57] X. Deng, A. Hatori, Z. Chen, K. Kumata, T. Shao, X. Zhang, T. Yamasaki, K. Hu, Q. Yu, L. Ma, *ChemMedChem* **2019**, *14*, 303.



Chapter A4

Structure-based design of a novel class of autotaxin inhibitors based on endogenous allosteric modulators

Jennifer M. Clark,^{1,†} Fernando Salgado-Polo,^{2,†} Simon J. F. Macdonald,³ Tim N. Barrett,³ Anastassis Perrakis² and Craig Jamieson^{1,*}

Affiliations:

¹ Department of Pure and Applied Chemistry, University of Strathclyde, 295 Cathedral Street, Glasgow, G1 1XL, United Kingdom.

² OncoCode Institute and Division of Biochemistry, Netherlands Cancer Institute, Plesmanlaan 121, 1066CX, Amsterdam, The Netherlands.

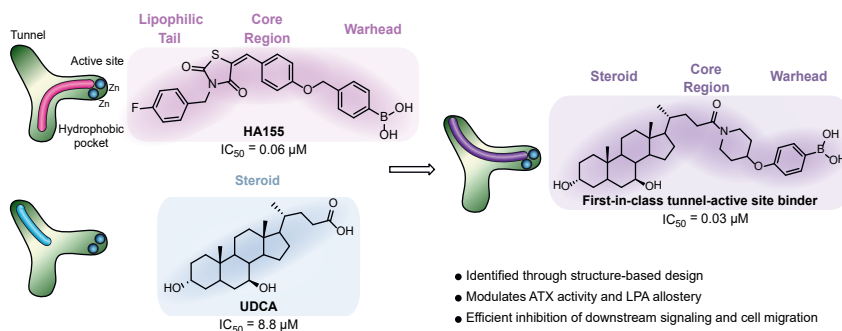
³ Medicines Design, GlaxoSmithKline R&D, Stevenage, Hertfordshire, SG1 2NY, United Kingdom

† These authors contributed equally to this work.

* Correspondence: craig.jamieson@strath.ac.uk; a.perrakis@nki.nl.

Based on:

Journal of Medicinal Chemistry. 2022, 65(8): 6338-6351.



Abstract

Autotaxin (ATX) facilitates the hydrolysis of lysophosphatidylcholine (LPC) to lysophosphatidic acid (LPA), a bioactive phospholipid, which acts on its cognate receptors to facilitate a diverse range of cellular effects in multiple tissue types. Abnormal LPA expression can lead to the progression of diseases such as cancer and fibrosis. Modulation of ATX has been predominantly based around the generation of orthosteric inhibitors (Type I) that structurally resemble the natural product, LPA, and exhibited excellent potency *in vitro*; however, their therapeutic efficacy has been limited. Previously, we identified a potent ATX steroid-derived hybrid (partially orthosteric and allosteric) inhibitor which did not form interactions with the catalytic site. Herein, we describe the design, synthesis and biological evaluation of a focused library of novel steroid-derived analogues armed with a key warhead pharmacophore targeting the bimetallic catalytic site. Subsequent studies undertaken on exemplar compounds revealed an entirely unique class of ATX inhibitors of Type V designation, which demonstrate significant pathway-relevant biochemical and phenotypic data. In this aspect, our lead compounds modulated LPA-mediated ATX allostery, and achieved indirect blockage of LPA₁ internalisation, in line with the observed reduction in downstream signaling cascades and chemotaxis induction. Accordingly, these novel Type V ATX inhibitors represent a promising exploitable tool to effectively inactivate the ATX-LPA signaling axis.

Introduction

The diversity associated with the ectonucleotide pyrophosphatase/phosphodiesterase (ENPP) family of enzymes has inspired extensive research into their independent pathophysiological functions. Of the seven structurally-related enzymes, all of which elicit varying cell signaling responses, autotaxin (ATX, ENPP2) is unique in that it is the only non-membrane bound family member^[1], therefore representing an attractive and clinically relevant biomarker.

First identified in 1992^[2], autotaxin was originally defined as an autocrine motility factor. It was later established to be the fundamental mediator responsible for release of the bioactive signaling lipid lysophosphatidic acid (LPA), a family of lysolipids with differing length and saturation of their single aliphatic chain, through the cleavage of the corresponding lysophosphatidyl-choline (LPC) moiety^[3]. Binding of LPA to its cognate G-protein coupled receptors, LPA₁₋₆, initiates its biological activity through receptor activation provoking a cascade of cellular responses, including survival, migration and proliferation (**Figure 1A**). The ATX-LPA axis has been implicated in many clinical indispositions, for example, cancer^[4,5], inflammation^[6], fibrosis^[7], and autoimmune^[8] and cardiovascular diseases^[9]. Given its well defined role in a plethora of pathological and physiological modalities, in addition to its extracellular nature, ATX has been actively pursued over the years as an attractive target for drug discovery in industry and academia alike.

ATX can be sub-divided into three main domains: two N-terminal somatomedin β -like (SMB) domains, a phosphodiesterase/catalytic (PDE) domain and a C-terminal (inactive) nuclease domain (NUC) connected by a lasso loop (**Figure 1B**)^[3,10,11]. The natural LPA substrates bind in the phosphodiesterase (PDE) catalytic domain, forming a tripartite binding site: a deep hydrophobic pocket, the bimetallic active site where substrate hydrolysis takes place, and a solvent accessible hydrophobic tunnel (**Figure 1C**)^[3,10,11]. The ATX tunnel serves in turn as a secondary LPA binding site, which results in the increase of the catalytic rate of LPC hydrolysis.

A raft of ATX inhibitors have been reported in the past decade, which has ultimately led to the classification of four inhibitor types with distinct binding modes in ATX (**Figure 1D**)^[12-17]. A significant fraction of these fall into the category of orthosteric site modulators (type I), as they function to competitively block substrate binding by binding in the active site and hydrophobic pocket. Perhaps two of the most pertinent tool compounds of this nature are **1** (HA155) and **2** (PF-8380), both of which are equipped with defined chemotypes which are structurally comparable to those in LPA: a lipophilic tail, core and linker region, and a distinct warhead. Additionally, hydrophobic pocket binders (type II) compete with substrate binding, without the need of a warhead targeted for the active

site, such as CRT0273750^[18] and PAT-494^[17].

Conversely, ATX tunnel binders (type III) owe their modest inhibitory effect to their non-competitive binding mode in the tunnel. In this regard, our extensive structural investigation into the function of the hydrophobic tunnel led to the discovery that sterols, for example, tauroursodeoxycholic acid (TUDCA) and ursodeoxycholic acid (UDCA), are partial non-competitive modulators with micromolar affinity for the ATX tunnel^[19].

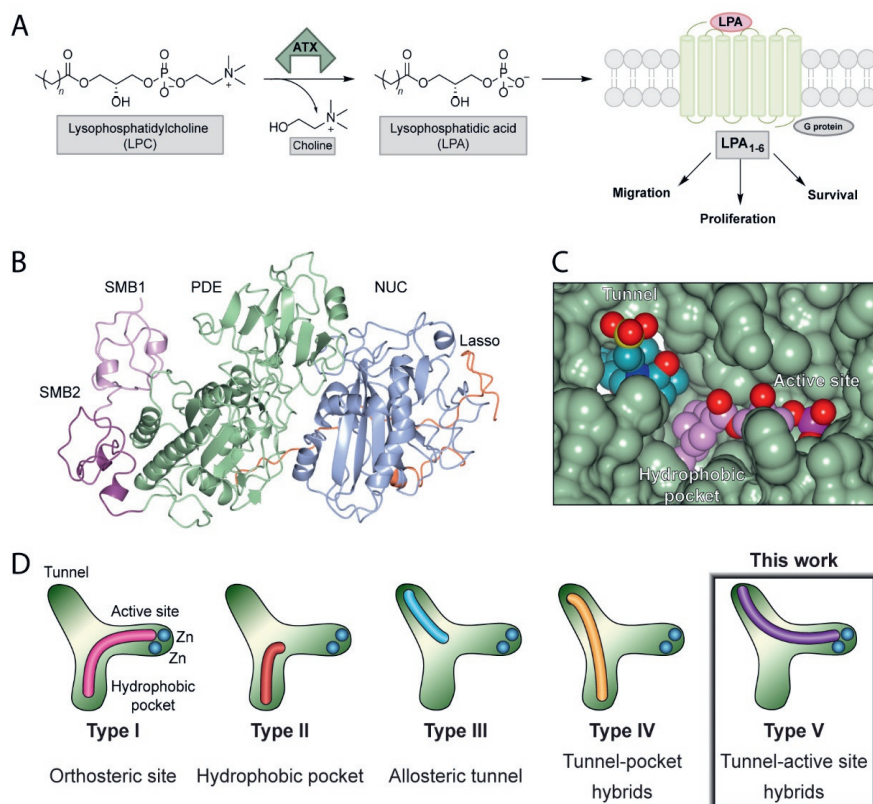


Figure 1. The ATX-LPA signaling axis and ATX inhibitor family. **A**, formation of LPA by ATX-mediated hydrolysis of LPC and subsequent receptor recognition and activation. **B**, domain structure of ATX. **C**, Surface representation of the ATX tripartite site within the PDE domain, where 18:1 LPA (pink) and TUDCA (blue) are bound in the orthosteric site and the tunnel, respectively (PDB 5DLW). **D**, classification of the distinct binding modes within the ATX inhibitor family.

Recent progress in inhibitor diversification has led to the evolution of potent hybrid inhibitors (type IV) binding in both the hydrophobic pocket and the hydrophobic tunnel

of ATX, such as **3** (GLPG 1690)^[20] which reached phase III clinical trials, and the steroid derivative **4**^[14].

We have previously reported the structure-driven evolution of potent type IV competitive inhibitors based upon bile salts that act as weak allosteric inhibitors, which facilitated the development of lead compound **4**. Based on the success of **4** in the reduction of LPA levels *in vivo*, we considered further exploitation of this natural product-derived tunnel-binding skeleton, in combination with an appropriate warhead targeting the active site, which could give rise to a previously unexplored binding mode in terms of ATX inhibition.

A4

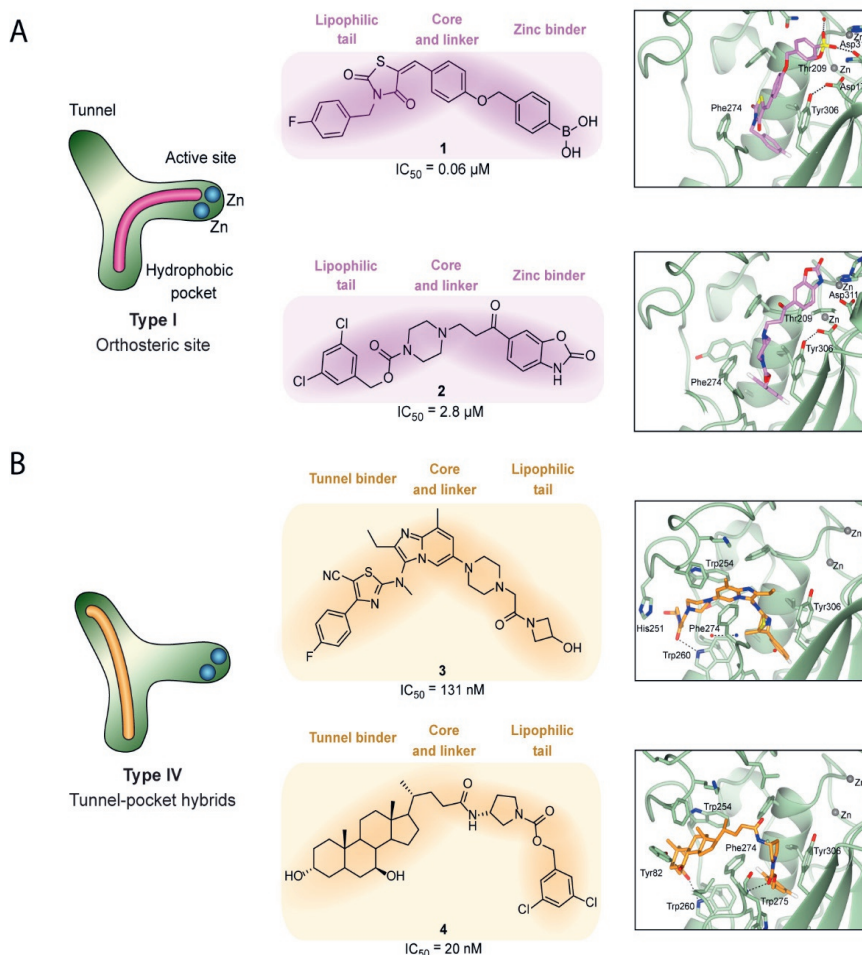


Figure 2. Relevant type I and type IV inhibitors employed for SAR studies. A: Examples of Type I ATX inhibitors which bind orthosterically in the hydrophobic pocket and active site. Structures of **1** (PDB 2XRG) and **2** (PDB 5L0K) are shown with their main interactions. **B:** Examples of Type IV ATX inhibitors which bind allosterically in the tunnel and hydrophobic pocket. Structures of **3** (PDB

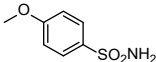
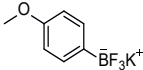
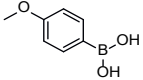
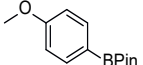
5MHP) and **4** (PDB 5M0M) are shown with their main interactions.

In this manuscript, we demonstrate the amalgamation of key structural features from two design hypotheses based on both endogenous allosteric modulators and competitive orthosteric ATX inhibitors, facilitating the development of novel "Type V" steroid-derived inhibitors of ATX. A fragment-type biochemical screen identified boron-containing functionalities as suitable warheads, which in conjunction with the steroidal anchor, were critical for achieving potency. We then characterized the effect of the novel compound type on ATX kinetics, which provided further confirmation of its binding in the ATX tunnel, hampering both ATX activity and LPA allostery. Cell-based experimental approaches indicated that our compounds optimally acted upon ATX activity, yielding in turn a reduction in LPA₁ internalisation and downstream signaling activation, which translated into a less migratory phenotype.

Results and discussion

A small fragment-type screen identified four warheads for attachment to the steroid manifold which were predicted to interact with the active site based on their analogy with **1**^[21] and SAR-derived analogues of **2**. Activity of these fragments against ATX was determined by measuring LPC hydrolysis in a choline-release biochemical assay which indicated that boron-containing warheads (**6-8**) were more favorable candidates than the sulfonamide (**5**).

Table 1. Fragment-type biochemical screen for selected compounds **1-4**

Compound Number	Legend Reference	Fragment Structure
5	SO ₂ NH ₂	
6	BF ₃ K	
7	B(OH) ₂	
8	BPin	

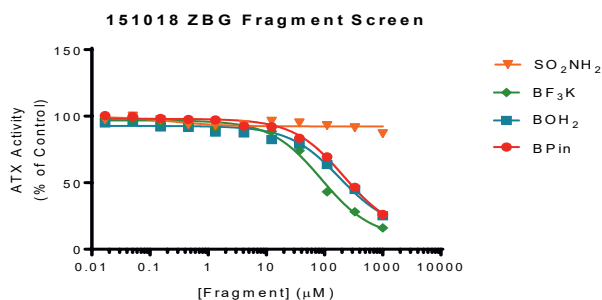


Figure 3. Preliminary screen of fragment-type compounds indicate potential warhead candidates. The choline oxidase-coupled activity assay was used to assess inhibition of LPC hydrolysis by selected fragment compounds **5-8**.

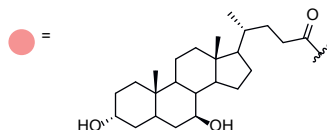
Due to the novelty associated with the postulated binding mode, our preliminary SAR investigation was focused on probing the length of spacer required between the warhead and steroid core for optimal biological activity. Despite the lower inhibition of the sulfonamide fragment in the screen, sulfonamides have precedent as active site binders for ATX, and are more synthetically tractable in comparison to the boron-containing warheads. Therefore, the SAR was initially focused on optimizing compound length with the sulfonamide warhead.

Our initial studies showed that propyl-linked compound **10** with *para*-sulfonamide substitution on the aryl ring displayed encouraging levels of potency (**10**, $IC_{50} = 0.4 \mu\text{M}$) compared to the progenitor steroid (**9**, $IC_{50} = 9 \mu\text{M}$) when measured using an LPC hydrolysis assay, shown in **Table 2**. Activity was lost completely on truncation (**11**, $IC_{50} > 10 \mu\text{M}$) and homologation (**12**, $IC_{50} > 10 \mu\text{M}$) demonstrating that there was a narrow window in optimal linker length in order to achieve potency. These results indicated that a three-carbon linker was most beneficial to potency.

Boron-containing warheads were anticipated to be more active than their sulfonamide counterparts and a series of matched pairs were generated to explore this proposal (Table 3). A ten-fold increase in potency was observed moving from the ethyl-linked *meta*-substituted pinacol boronate (**13**, $IC_{50} = 14 \mu\text{M}$) to the *para*-substituted pinacol boronate (**14**, $IC_{50} = 1.5 \mu\text{M}$) which corroborated our hypothesis that *para*-substitution was preferred. This was further substantiated by homologating the linear linker to the propyl derivative which resulted in a further ten-fold increase in ATX inhibition for *meta*- (**15**, $IC_{50} = 0.15 \mu\text{M}$) and *para*-substituted pinacol boronate (**16**, $IC_{50} = 0.07 \mu\text{M}$). This indicated that the intrinsic functionality associated with boron-containing motifs plays an important role in inhibitory activity, and was better tolerated in combination with an appropriate length of linker. Pleasingly, analogues bearing a pendant trifluoroborate (**17**, $IC_{50} = 0.07 \mu\text{M}$) or

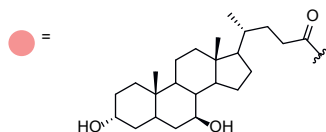
boronic acid (**18**, $IC_{50} = 0.05 \mu\text{M}$) retained inhibition of ATX when compared to pinacol boronate **16**.

Table 2. Evaluation of Sulfonamide Analogues



Compound Number	Structure	IC_{50} (μM)	Residual Activity (%)
9		9	60.8
10		0.4	75.1
11		> 10	30.5
12		> 10	66.3

These results reflected the observations generated from the fragment-type biochemical screen, revealing the inherent versatility of all three boron-containing warheads in practice. We believe that partial hydrolysis of the boronate ester occurs under enzymatic assay conditions which explains the comparable activity between the protected boronic acids (boronates) and the free boronic acid. A parameter that was also of importance throughout our SAR campaign, in addition to IC_{50} , was the percentage of residual activity for each compound in our biochemical assay. We used this as a tool to aid us in determining the efficacy of each warhead component. As we have demonstrated, moving away from the sulfonamide to boron-containing warheads was instrumental in achieving full inhibition of ATX. This further reinforces our initial findings in the fragment screen which highlighted the boronate ester, trifluoroborate and boronic acid as superior warheads.

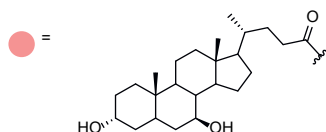
Table 3. Evaluation of Linear Boron Analogues

Compound Number	Structure	IC ₅₀ (μM)	Residual Activity (%)
13		14	14.7
14		1.5	1.4
15		0.15	1.7
16		0.07	0.3
17		0.07	1.1
18		0.05	0.6

The flexibility associated with linear compounds is largely unfavorable based on thermodynamic considerations however; we reasoned that this could be easily rectified by introducing conformational restraint. With suitable warheads in hand, we next examined compound trajectory by restricting rotational freedom in the linker region whilst preserving length. Incorporation of *N*-containing saturated heterocyclic cores (**19-21**, Table 4) combined with the pinacol borane warhead maintained potency with negligible difference noted. Of the three cores, piperidine **19** was selected for further optimization. Pleasingly, our most prominent result was obtained by accessing trifluoroborate (**22**, IC₅₀ = 0.05 μM) and boronic acid (**23**, IC₅₀ = 0.03 μM) derivatives harnessing a piperidine core. Both analogues also demonstrate minimal residual activity which reflects their efficacy

as active site binders. Boronic acid **23** represented a 400-fold increase in activity in comparison to the progenitor steroid (**9**, $IC_{50} = 11 \mu\text{M}$).

Table 4. Evaluation of Cyclic Boron Analogues



Compound Number	Structure	IC_{50} (μM)	Residual Activity (%)
19		0.08	0.2
20		0.21	7.7
21		0.20	9.8
22		0.05	0.0
23		0.03	0.0

To gain a comprehensive insight into the binding mode of **22** and **23**, these analogues were co-crystallised with ATX and determined their crystal structure by X-ray crystallography to 2.5 and 2.1 Å resolution, respectively. In all structures, the electron density following molecular replacement^[22] and automated refinement^[23–25], clearly confirmed the intended binding mode of all compounds in the tunnel and the active site (Figure 4A,C). Modelling the compounds and subsequent refinement, allowed assigning a clear, unique conformation for all compounds (Figure 4B,D), and resulted in structures of excellent quality^[26].

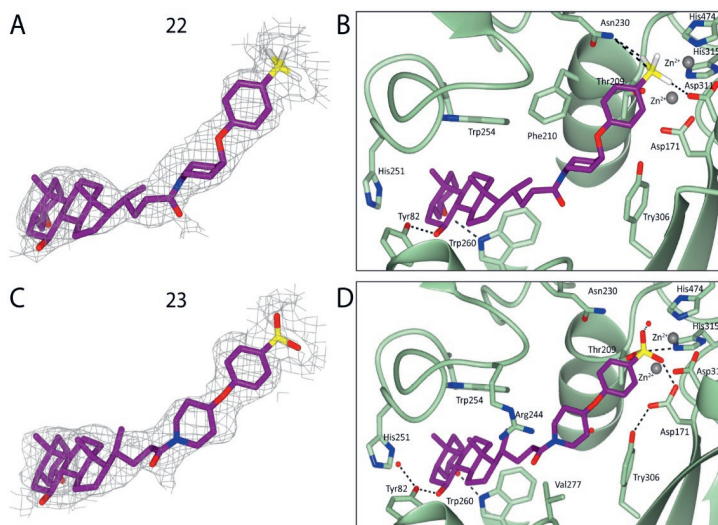


Figure 4. Crystal structures of ATX bound to **22 and **23** confirm their novel binding mode.** Fit of **22** (A) and **23** (B) to electron density. Binding modes of **22** (C) and **23** (D) at the ATX tripartite site. Dashed lines indicate hydrogen bonds.

The trifluoroborate warhead of **22** at the active site bore resemblance to the binding mode of the phosphate group of LPA bound at the ATX active site (PDB 5DLW). Specifically, this yielded hydrogen bond interactions with Asn230 and Thr209 via one of the fluorine atoms; a second fluorine was shown to coordinate to one of the proximal zinc ion of the catalytic site (Figure 5A).

Conversely, boronic acid warheads have been well-described in the literature based upon the crystallization of HA155 (Figure 2A)^[27]. As was expected, the binding pose of **23** at the active site boronic acid warhead entirely resembled that of HA155, which indicates that appropriate orientation was achieved by the length and flexibility of the core region (Figure 4D,5B). Specifically, the proximity of the boron atom resulted in a reversible covalent bond with the γ -OH group of Th209. Such reversibility has been previously indicated as a key element in the success of potential ATX inhibitors targeting the active site using boronic acids^[28]. Equally relevant for its binding were the hydrogen bonds formed with Asp171 and Asp311 from one of the hydroxyl groups of the boronic acid, which also coordinated with the proximal zinc ion. The remaining hydroxyl hydrogen-bonded with the main chain of Thr209, as well as a water molecule. In summary, this intricate bond network facilitated the blockage of the ATX active site and explains the high potency of **23**.

Closer inspection of the steroid moiety revealed similar interactions for both **22** and **23** (Figure 4 and Figure 5). Within the tunnel, they both receive two hydrogen bonds from Trp260 to OH-3 and Tyr82 to OH-5. As expected, the binding mode of the steroid moiety in

both compounds fully resembles both the related steroid derivative Compound **4** (Figure 2B) and TUDCA (Figure 1C). Lastly, a number of hydrophobic interactions are formed by the compounds in the ATX tunnel, specifically with Leu78, Phe210, Leu243, Phe249, Trp254, Trp260, Phe274 and Trp275.

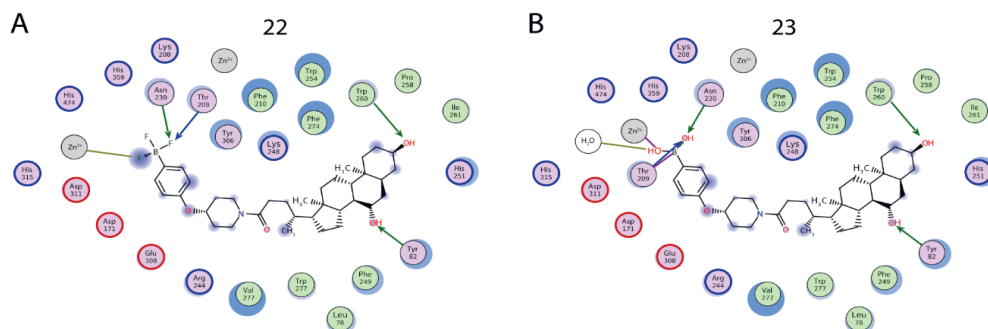


Figure 5. Two-dimensional depiction of the binding modes of the most potent Type V compounds. Orientation of **22** (A) and **23** (B) bound at the ATX tunnel and active site. Side and main chain Hydrogen bonds are indicated in green and blue arrows, respectively, Hydrogen bonds with water molecules are represented in gold, coordination to a metal atom is indicated in grey and the covalent bond of **23** with Thr209 is indicated in purple.

Upon defining the structural mode of binding of **22** and **23**, we next wanted to corroborate their potency and mechanism of inhibition (Figure 6A-B). As we anticipated, analysis of the inhibition by **22** and **23** confirmed the competitive nature of inhibition over a non-competitive mode ($\alpha > 1$, $\alpha = 1$), and showed K_i values of 24 ± 4 nM and 9 ± 1 nM, respectively. Accordingly, the results agreed with the mode of inhibition of the progenitor boronic acid HA155, but contrasts with the progenitor steroid UDCA, which acts as a weak non-competitive inhibitor of LPC hydrolysis. Expectedly, the mechanism of action in this emerging lead series switched by targeting the active site.

To better understand the relevance of substrate preference to the potency of **22** and **23**, we next analysed their inhibitory activity on the hydrolysis of LPC species with different acyl chain length. As noted in Figure 6C and Table 6, both compounds were equally active in the inhibition of 14:0, 16:0 and 18:1 LPC hydrolysis. Strikingly, inhibition of 20:0 LPC hydrolysis only resulted in ~50% of the catalytic rate of the inhibitor-free control, signifying that both compounds behave as partial inhibitors of longer acyl chains.

We have previously described that ATX activity for the hydrolysis of its natural LPC substrates follows a double catalytic cycle^[29]. At low LPA concentrations, ATX hydrolyses LPC at a lower rate, but, as the concentration of the LPA product increases and binds to its secondary binding site, the ATX tunnel, the catalytic turnover augments by approximately

40%. This increase in activity can be represented as a function of LPA concentration, which provides an activation constant (AC_{50}) of approximately $1 \mu\text{M}$. When we examined **22** and **23** in this experimental setup, we observed that addition of inhibitor at concentrations close or lower to the IC_{50} value (to allow residual activity) resulted in a dose-dependent decrease of the observed LPA-mediated activation of ATX activity (Figure 7), suggestive of type IV compounds, and in sharp contrast to type I compounds that do not ameliorate LPA-mediated activation. This experiment confirms the binding mode and also complements our data on the relevance of competing LPA binding in the tunnel to reduce its subsequent increase in catalytic rate.

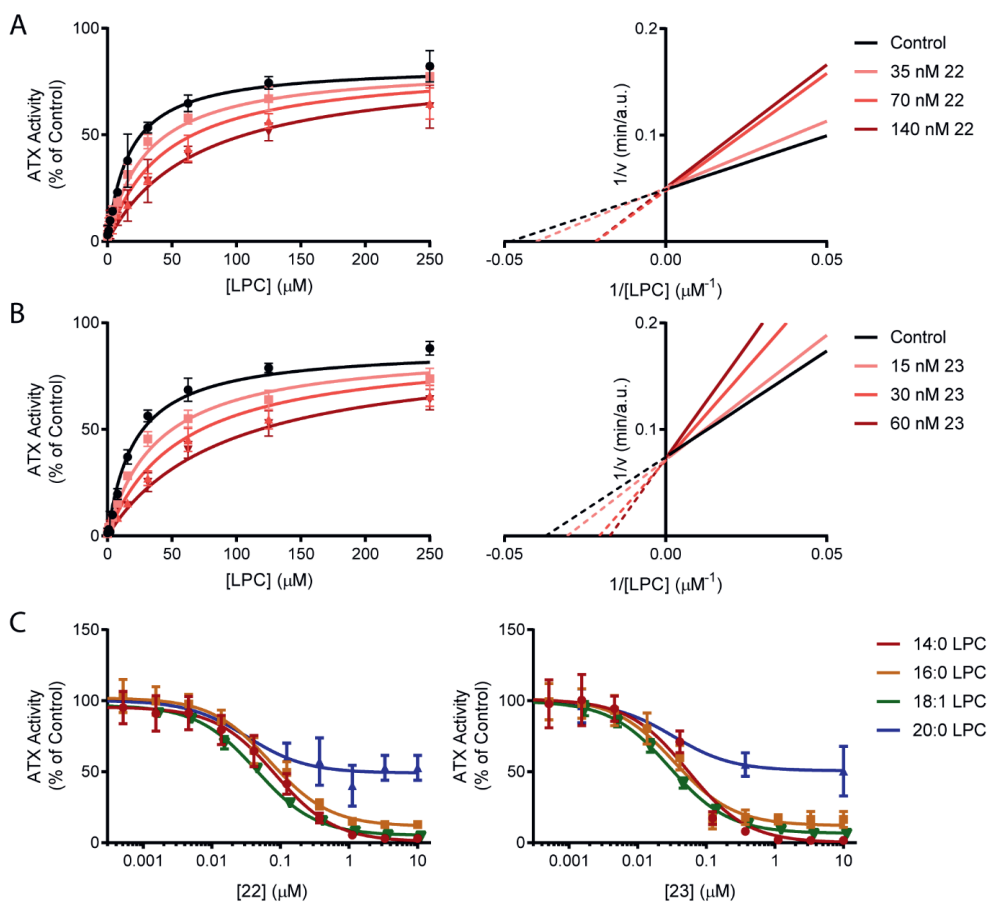


Figure 6. Determination of the mode of inhibition and substrate preference of **22 and **23**.** The choline oxidase-coupled activity assay was used to detect inhibition of LPC hydrolysis. (A-B) LPC titration at increasing concentrations of **22** and **23**. In the left panels, non-linear regression to the Michaelis-Menten equation was employed, from which the inhibition constants were derived $K_i = 24 \pm 4 \text{ nM}$ (A) and $9 \pm 1 \text{ nM}$ (B). In the right panels, Lineweaver-Burk linear regressions of the same data. Crossing of the ordinate axis at the same $1/v$ value denotes competitive inhibition. Percentage

of competitive vs. non-competitive inhibition was 98.84% and $\alpha = 9.783$ for **22** (A), and 98.58% and $\alpha = 8.573$ for **23**. (B) for competitive inhibition. (C) Titration of **22** (left) and **23** (right) for IC_{50} determination of the indicated LPC species. All assays were performed with 150 μ M LPC and 20 nM ATX. The mean of three independent experiments \pm s.d. is plotted. Statistical analysis of the mode of inhibition was assessed by Akaike's informative criteria.

Table 6. Potency of **22** and **23** in the inhibition of the hydrolysis of different LPC species.

LPC	22 IC_{50} (μ M)	22 Residual Activity (%)	23 IC_{50} (μ M)	23 Residual Activity (%)
14:0	0.084	0.7	0.054	0.0
16:0	0.072	11.6	0.034	12.0
18:1	0.045	5.1	0.029	6.7
20:0	0.032	49.1	0.033	50.7

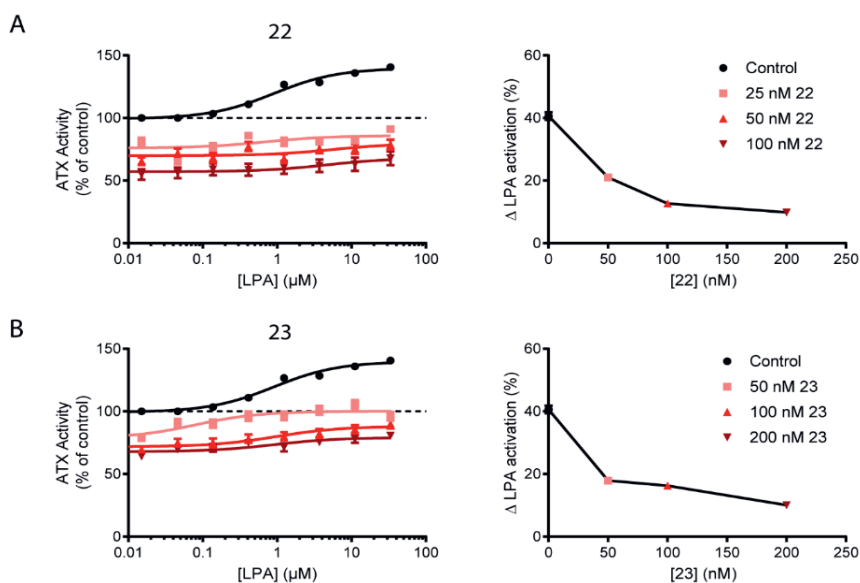


Figure 7. Type V compounds outcompete LPA in the ATX tunnel, abolishing allostery. (A-B) LPA activation in the absence or presence of **22** or **23**. (Left panels) Dose-dependent LPA-related increase in activity of 20 nM ATX pre-incubated with the compounds in a concentration that still allowed residual activity (>50% at the highest inhibitor concentration). (Right panels) Increase of ATX activity with respect to the compound-free control; the data displayed represent the mean value of triplicate measures \pm SEM.

The biochemical characterisation of **22** and **23** helped to validate the novel Type V compounds as potent inhibitors at the ATX level. However, an essential factor in their physiological success requires that they effectively decrease LPAR activation and downstream signaling cascades, which in the case of GPCRs can be followed by receptor

internalisation. For that purpose, we challenged inducible LPA₁-HA stable HeLa-Flp-In cells with free ATX in the presence of 18:1 LPC and quantified LPA₁ internalisation by confocal imaging. As can be seen on Figure 8A, stimulation of HeLa cells with ATX inhibited by **22** or **23** resulted in a significant decrease of LPA₁ internalization of approximately 75%. This can be understood as the indirect effect upon blocking LPA production, which hampered receptor activation and endocytosis.

To further corroborate the effect of **22** and **23**, we studied the context of downstream LPAR-dependent cellular responses. Among other signals, LPA₁ activation results in Gα_i- and Gα_{12/13}-driven cascades via PI3K and RhoA activation, respectively. Downstream targets of this signaling pathway are the phosphorylation of the AKT and ERK proteins. We thus utilised human transformed skin fibroblasts (BJeH) which were stimulated with uninhibited or compound-bound ATX, showing that **22** and **23** reduce approximately 60% of the maximal effective cell response compared to positive controls (uninhibited ATX incubated with LPC), as measured by the levels of phosphorylated AKT and ERK (P-AKT and P-ERK), indicated in Figure 8B. The half-maximal effective concentration (EC₅₀) that can be assigned to the emerging Type V compounds was measured in the same assay, and showed EC₅₀ values of ~100 nM and ~60 nM for **22** and **23**, respectively; interestingly a two-fold higher *in situ* EC₅₀ with respect to measured *in vitro* IC₅₀ values for LPC hydrolysis.

It is noteworthy that fibroblasts, BJeH cells among those, usually co-express LPA₁ and LPA₆ at high levels, which can harden the efforts to decipher receptor-specific cellular responses^[30]. However, given the slight degree of disagreement in the literature as to which Gα subunits couple to LPA₆, we made use of the nanomolar-affinity LPA_{1/2/3} antagonist Ki16425 to negate the contribution of LPA₆^[31]. The results revealed that directly antagonising LPA₁ amounted to the effects of inhibiting ATX activity by **22** and **23**, which consequently prevents LPA₁ activation and its Gα_i- and PI3K-dependent signaling responses.

To further characterise the effect of **23** in efficiently attenuating LPAR activation, the chemotaxis induced by Gα_{12/13}-driven was put to a test. To this end, we employed the Boyden chamber methodological approach and quantitated the amount of MDA-MB-231 cells that traversed through a fibronectin-coated filter towards a chemoattractant. As quantitated on Figure 8C, challenging cells with compound-bound or free ATX resulted in a reduction of ~50% of cell migration, with an EC₅₀ value in the range of 200 nM. Since this well-studied cell line mainly expresses LPA₁, in addition to lower levels of LPA_{2/3}, it can be inferred from the data that **23** efficiently diminished LPA production and signaling through these receptors.

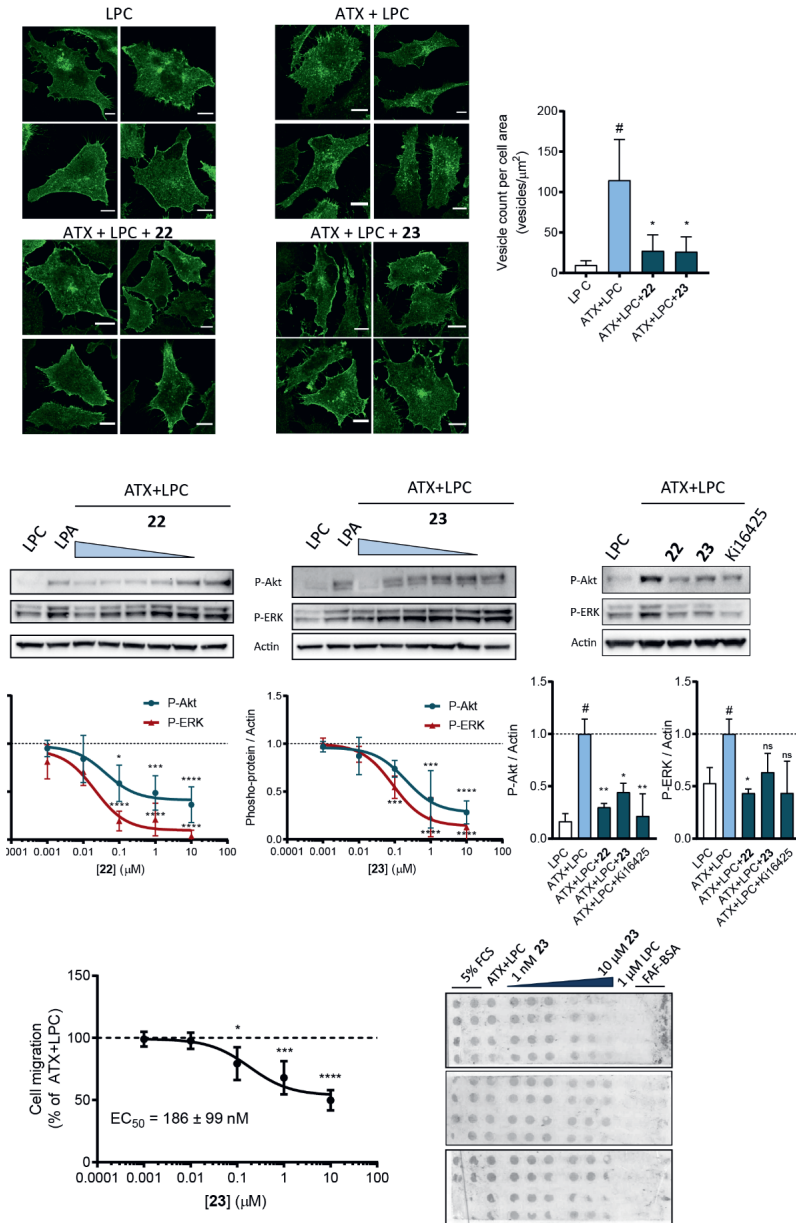


Figure 8. Type V compounds effectively counteract the activation of several hallmarks of the ATX-LPA signaling axis. (A) Left panel, representative confocal images of stained LPA₁-HA (48-h expression) in HeLa-Flp-In cells, where it localizes mainly to the cell surface or intracellular vesicles. Right panel, quantification of LPA₁ intracellular vesicles. At least 20 cells from three independent preparations were segmented and analysed by ImageJ to calculate the number of intracellular vesicles (median±interquartile range); *P<0.05 (one-way ANOVA). (B) BJcH fibroblasts were challenged with the indicated reagents for 15 min. Representative Western blots of three independent experiments

are shown, and the mean of three independent experiments \pm s.d. is plotted (C) Breast cancer MDA-MB-231 cells were allowed to migrate towards the chemoattractants-containing solutions for four hours. Median \pm s.e.m. of the quantitated filters on the right was used for the analysis. For (B) and (C), inhibitor concentrations were 10, 1, 0.1, 0.01, 0.001 μ M; for the remaining reagents, the next concentrations were used: 1 μ M 18:1 LPC, 1 μ M 18:1 LPA, 20 nM ATX, 10 μ M Ki16425.

Conclusion

In summary, we successfully report a first-in-class Autotaxin inhibitor of Type V designation based on the endogenous steroid modulator, UDCA, which targets the hydrophobic tunnel and active site of the phosphodiesterase domain. Our design approach was constructed through careful consideration and consolidation of previous SAR analysis from both allosteric and orthosteric libraries of ATX compounds which led to the identification of **23**. A 400-fold enhancement in potency compared to the progenitor steroid is demonstrated in addition to a switch in mechanism of inhibition from non-competitive to competitive by tethering an active warhead to the weak endogenous steroid. Our hypothesis is substantiated by crystallographic data of compounds from the lead series bound to ATX. Biochemical and cell-based data for compound **22** and **23** reveal a competitive mode of inhibition and excellent properties in inhibiting LPA-dependent pathways in cells, as assessed with a panel of relevant assays in different cell lines. These disease-relevant phenotypic studies provide a solid baseline to investigate further the impact of this type ATX inhibitor in fibroproliferative diseases.

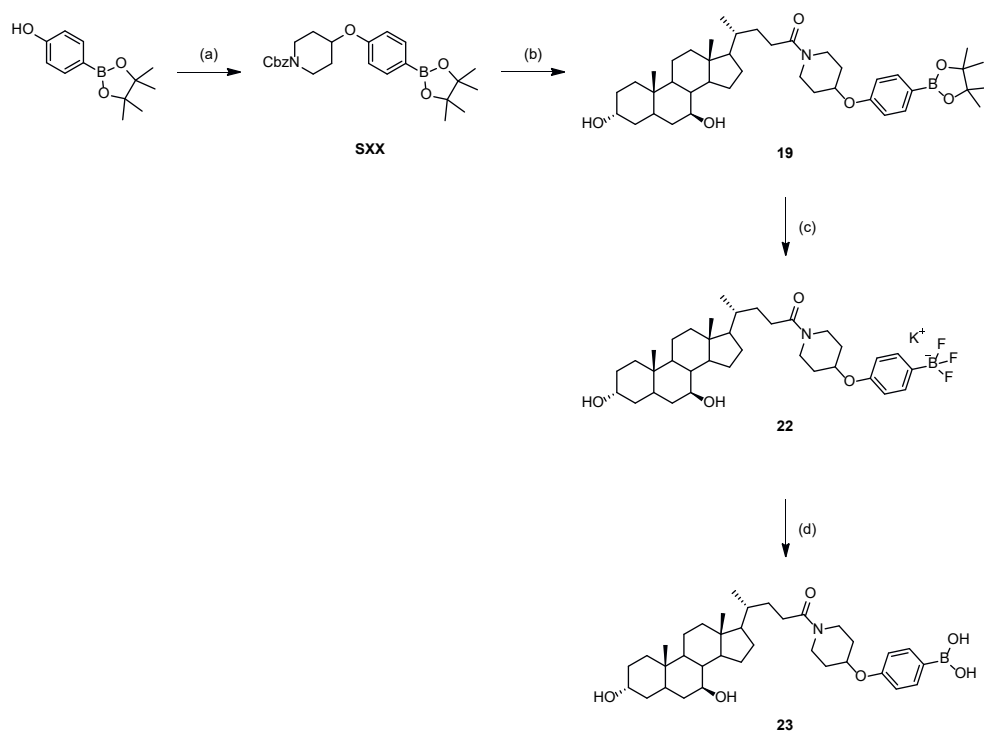
Experimental procedures

Chemistry. Pinacol boronate intermediate S25 could be synthesized from the respective phenol via a CMBP-mediated Mitsunobu reaction with the corresponding secondary Cbz-protected amino alcohol in excellent yield. Subsequent protecting group removal followed by HATU-mediated amine coupling with UDCA led to the generation of pinacol boronate 19 in good yield. Compound 19 could be easily converted to the corresponding trifluoroborate 22 in moderate yield using modified conditions reported by Lennox and Lloyd-Jones. Sequential SiO₂ hydrolysis of trifluoroborate 22 provided boronic acid 23 in moderate yield. All other compounds were synthesized in an analogous fashion with full experimental details in the Supplementary Information.

Protein production and crystallization. Rat ATX was over-expressed and purified as described previously^[32]. For the crystallisation studies, ATX was incubated with each screened compound at a 1:10 (protein:compound) ratio for at least 30 minutes. Crystals

were grown for at least 7 days in a 24-well optimization screen (18–20% PEG 3350, 0.1–0.4 M NaSCN, and 0.1–0.4 M NH_4I). In all cases, the best diffracting crystals were obtained at room temperature (293 K) by mixing 1 μL of protein:compound solution and 1 μL of reservoir solution. All crystals were vitrified in cryoprotectant, which consisted of reservoir solution with the addition of 20% (v/v) glycerol. Other solvent:protein ratios tested per condition were 1:2, 2:1.

Scheme 1 ^a



^a Conditions for cyclic boronates: (a) CMBP, toluene, 120 °C; (b) Pearlman's catalyst, H_2 , methanol, rt then UDCA, DIPEA, HATU, DMF, rt; (c) KF (aq), L-(+)-tartaric acid, acetonitrile/ H_2O (1:1), rt; (d) SiO_2 , H_2O , rt.

Crystallographic data and methods. The X-ray diffraction data for the ATX–inhibitor complexes with **22** were collected at ESRF on beamline MASSIF1^[33] and complexes with **23** were collected at SLS on beamline PXIII^[34] at 100 K, and were recorded on a PILATUS 2M-F detector to a resolution of 2.00 and 2.40 Å, respectively. All data were processed and integrated with XDS^[34]. All compounds were processed on site using the SLS automated processing pipeline and scaled with AIMLESS^[35]. The structures were determined by molecular replacement using MOLREP^[22] with the structure of ATX (PDB 2XR9) as the

search model. Model building and subsequent refinement were performed iteratively with COOT^[23], REFMAC5^[24], and PDB_REDO^[25]. Structure validation was carried out by MolProbity^[26]. The structure models and experimental diffraction data were deposited at the PDB under codes 7Z0M and 7Z0N for compounds **22** and **23**, respectively. Crystallographic data and refinement details are available in Table 7.

Table 7. Crystallographic details.

Data Collection	22 (7Z0M)	23 (7Z0N)
Wavelength (Å)	1.0000	1.0000
Resolution (Å)	2.00	2.40
Space group	P12 ₁	P12 ₁
Unit cell a b c (Å), β (deg)	62.3 89.0 76.5, 102.7	62.8 89.6 77.6, 102.8
Data quality statistics		
CC _{1/2}	0.998 (0.834)	0.982 (0.760)
R _{merge}	0.043 (0.484)	0.099 (0.621)
<I/σI>	8.3 (1.2)	7.8 (1.7)
Completeness (%)	99 (98)	99.9 (100)
Redundancy	2.9 (2.9)	3.4 (3.5)
Refinement		
No. atoms	6599	6877
protein	6241	6412
ligand/metal/glycan	148	186
water/iodine	210	279
TLS groups	1	1
R _{work} /R _{free} (%)	22.6/27.9	19.8/26.3
Validation		
rsmsd/rmsZ bond lengths (Å)	0.0111/0.718	0.0080/0.517
rsmsd/rmsZ bond angles (deg)	1.536/0.898	1.484/0.865
Ramachandran preferred/outliers (%)	94.09/0.00	93.89/0.13
Ramachandran Z score	-2.30	-2.35
Rotamers preferred (%)	91.00	90.26
MolProbity/Clash score (%ile)	90/90	90/99

^aHigh resolution shell in parentheses.

Biochemical assays and modelling of kinetic data. The biochemical studies of ATX lysoPLD activity were performed with ATX. Activity was measured by a coupled reaction with 1 U ml⁻¹ choline oxidase and 2U ml⁻¹ horseradish peroxidase (HRP) and 2 mM homovanillic acid (HVA) (all from Sigma-Aldrich). For the assays, 14:0, 16:0, 18:1 20:0 LPC (Avanti polar Lipids Inc.) was incubated with 20 nM ATX, reaching a final volume of 100 μl buffer, which contained 50 mM Tris, 0.01%, 50 mM CaCl₂, Triton X-100, pH 7.4. Steady-state choline release was measured at 37 °C by HVA fluorescence at λ_{ex} / λ_{em} = 320/460 nm in Corning® 96- or 384-well OptiPlate (Sigma-Aldrich) and with a Pherastar plate reader (BMG Labtech). To determine the IC₅₀ for the different inhibitors on ATX activity,

the velocity of the reaction was monitored for each compound as a function of time and the linear phase of the kinetics was taken from 60 min after the addition of ATX to the reaction buffer. The resulting fluorescence intensity signal over time was used to model all inhibitor concentrations simultaneously using the following formula, where v_{max} and v_{min} were fitted for the minimum and maximum relative velocity, and c_i corresponds to the inhibitor concentration for each assay^[19]:

$$V = \frac{v_{max} - v_{min}}{(1 + c_i / IC_{50})} + v_{min} \quad (\text{Equation 1})$$

Competition with LPA allostery. The activation assays using LPA were performed in a similar way as those done for the inhibitors. In this case, LPA was dissolved in Ethanol: H₂O (1:1), 0.01% TX-100 and was added to the reaction buffer. The presence of ethanol was taken into account and controls in the absence of ATX and/or LPC were employed to correct the kinetic data. ATX was incubated for 30 min with different concentrations of inhibitors and subsequently added to the reaction buffer containing 150 μM 18:1 LPC and different starting concentrations of 18:1 LPA. The slopes were calculated from at least 60 min after the addition of ATX. The percentage of LPA-driven activation was normalised to ATX in the absence of LPA and inhibitors, which represented 100% activity. Lastly, the activation constant or AC₅₀ was obtained from the following equation:

$$V = \frac{v_{max} - v_{min}}{(1 + c_i / AC_{50})} + v_{min} \quad (\text{Equation 2})$$

Mechanistic Studies with ATX inhibitors. For initial comparison between competitive and non-competitive inhibition, we performed assays measuring LPC hydrolysis in the presence of three inhibitor concentrations (0.5 IC₅₀, IC₅₀ and 2 IC₅₀) or with uninhibited ATX, from which slopes taken from 60 min after the start of the reaction were fit in two non-linear equations^[19]:

$$V = \frac{V_{max} c_{LPC}}{K_M (1 + c_i / K_i) + c_{LPC}} \quad \text{competitive inhibition} \quad (\text{Equation 3})$$

$$V = \frac{\left(\frac{V_{max}}{1 + c_i / K_i}\right) c_{LPC}}{K_M + c_{LPC}} \quad \text{non-competitive inhibition} \quad (\text{Equation 4})$$

where V is the observed velocity and c_{LPC} is the corresponding LPC concentration for each data point, and c_i is the inhibitor concentration for each curve; and K_i is the inhibition constant. To statistically determine the chance of each type of inhibition, we calculated the α value in the partial mixed inhibition model (Equation 5), where $Part$ defines the partiality of the inhibition, and $\alpha > 1$ or $\alpha = 1$ correspond to competitive and non-competitive inhibition modes, respectively. Lastly, we utilised the Akaike's Informative

Criteria to assess the significance of the analysis.

$$V = \frac{V_{max}c_{LPA}(1+P_{art})}{K_M(1+c_i/K_i)+c_{LPA}(1+c_i/\alpha K_i)} \text{ partial mixed inhibition} \quad (\text{Equation 5})$$

AKT and ERK phosphorylation by Western-blotting. 100,000 BJeH cells were seeded in 12-well tissue culture plates and allowed to grow for 24 h in DMEM (GIBCO, Life Technologies) containing 10% FCS (Thermo Scientific) and 100 U mL⁻¹ streptomycin/penicillin (GIBCO, Life Technologies). Next, they were washed twice with PBS and serum starved O/N. ATX 20 nM was incubated with inhibitors for 30 min in serum free medium containing 0.05% (w/v) fatty acid-free BSA (total volume 1 mL). Medium from the 12-well plates was removed and replaced with 1 mL of ATX-inhibitor mixture. Cells were stimulated for 15 min, medium was removed, and plates were immediately frozen on dry ice and stored at -80 °C. For Western blotting, cells were washed with cold PBS, lysed in RIPA buffer, supplemented with protease inhibitors (Pierce), 20 mM NaF and 1 mM Orthovanadate, and spun down. Protein concentration was measured using a BCA protein assay kit (Pierce), and LDS sample buffer (NuPAGE, Invitrogen) 1 mM dithiothreitol (DTT) were added to the lysate. 20 µg total protein were loaded on SDS-PAGE pre-cast gradient gels (4–12% Nu-Page Bis-Tris, Invitrogen), followed by transfer to nitrocellulose membrane. Non-specific protein binding was blocked by 5% BSA in PBS-Tween (0.1%); primary antibodies were: phospho-Akt (Ser473), catalogue number: D93, dilution: 1:1,000; phospho-ERK1/2 (Thr202/Tyr204), catalogue number: D13.14.4E, dilution: 1:2,000; from Cell Signaling Technology. They were incubated O/N at 4°C in PBS-tween with 5% BSA, containing 0.1% NaN₃. Blots were then incubated for 1 hour at RT with monoclonal anti-β-actin antibody, clone AC-15, dilution: 1:10,000, from Sigma, which was dissolved in PBS-tween with 5% skimmed milk containing 0.1% NaN₃. Horseradish peroxidase-conjugated secondary antibodies (goat anti-mouse (Bio-Rad), catalogue number: 1721011; goat anti-rabbit (Pierce), catalogue number: 1858415) were incubated for 1h at room temperature in PBS-tween with 2.5% BSA, and developed using ECL Western blot reagent.

Production of LPA₁-HA-expressing HeLa-Flp-In cells. Human LPA₁ cDNA amplified by PCR to remove its stop codon and add the restriction sites for *Bam*HI and *Xho*I, after which it was subcloned in an in-house produced pDNA5.1-HA vector. 0.2 µg of the resulting vector and 1.8 µg pOG44 Flp-Recombinase Expression Vector (Invitrogen) were incubated with 6 µl Fugene6 (Invitrogen) in 200 µl OptiMEM (Gibco) for 30 minutes, after which the mix was added to previously produced HeLa-Flp-In cells^[37]. Their medium was refreshed 24 hours later, and selection with 1 µg/mL puromycin was started and maintained with resistant cells.

Confocal microscopy for LPA₁ internalisation. Serum-starved LPA₁-HA-expressing HeLa-Flp-In cells cultured on 24 mm (#1,5) were treated with 1 µM LPC and 20 nM ATX in the

presence or the absence of **22** or **23** for 15 min in DMEM containing 0.05% fatty acid-free BSA. Subsequently, coverslips were washed and fixed with 4% PFA, permeabilised with 0.1% Triton X-100 and blocked with 2% BSA for 1 hour. Incubation with anti-HA antibody (3F10 from Roche Diagnostics; 1:200) was done for 1 hour, followed by incubation with donkey anti-rat Alexa Fluor 488-conjugated antibody (**A-21208** from Invitrogen; 1:200) for 1 hour at room temperature. For confocal microscopy, cells were washed with PBS, mounted with Immuno-Mount™ (Thermo Scientific), visualized on a LEICA TCS-SP5 confocal microscopy (63x objective) and analysed using ImageJ software.

Cell migration assay. Migration of MDA-MB-231 cells was performed using 48-well chemotaxis chambers (Neuro Probe, Inc.) equipped with 8 mm-pore polycarbonate membranes, which were coated with either fibronectin (10 µg/mL) (F1141, Sigma-Aldrich). Cells (2×10^6 cells/mL) were added to the upper chamber. 0.05% fatty acid-free BSA was used as a lysophospholipid carrier. Cells were allowed to migrate for 4 h at 37 °C in humidified air containing 5% CO₂. Migrated cells were fixed in Diff-Quik Fix and stained using Diff-Quik II. Migration was quantified by colour intensity measurements using Photoshop software.

Additional Procedures. Additional details on methods are presented in the online version.

Acknowledgements

We thank University of Strathclyde and Netherlands Cancer Institute for supporting work on Autotaxin for J.M.C. and F.S.-P.. For financial support we thank: Medical Research Scotland and GlaxoSmithKline for a PhD studentship for J.M.C.

High resolution mass spectral data was obtained at the EPSRC Mass Spectrometry facility at the University of Swansea, U.K. X-ray diffraction data were collected at the European Synchrotron Radiation Facility (ESRF) and the Swiss Light Source (SLS). This work benefited from access to the NKI Protein Facility at Instruct-NL, an Instruct-ERIC centre.

Supplemental information

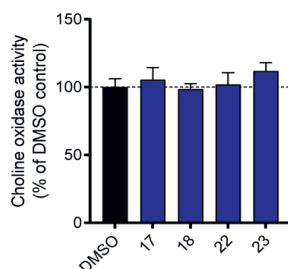


Figure S1. Internal control to assess the potential reactivity of different warheads with the choline oxidase-coupled activity assay. 50 μM choline chloride was incubated with all reaction components in the absence of ATX and LPC.

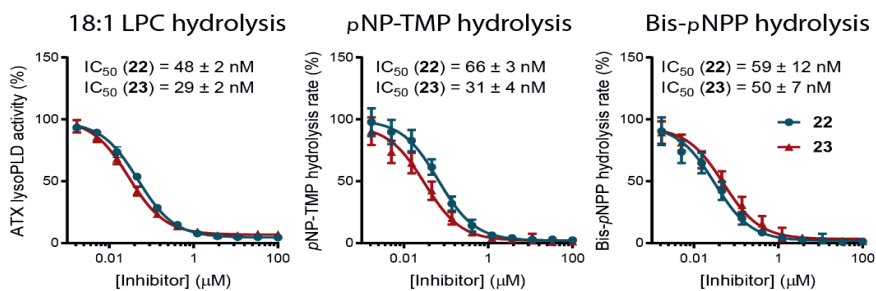


Figure S2. Determination of the potency of **22** and **23** in the hydrolysis of the physiological ATX substrate 18:1 LPC (150 μM), and the synthetic nucleotide substrates pNP-TMP (1 mM) and Bis-pNPP (1 mM). IC₅₀ values are indicated for inhibition in the presence of 20 nM ATX in all cases. The mean of three independent experiments \pm s.d. is plotted.

References

- [1] C. Stefan, S. Jansen, M. Bollen, *Trends Biochem Sci.* **2005**, *30*, 542.
- [2] M. L. Stracke, H. C. Krutzsch, E. J. Unsworth, A. Arestad, V. Ciocce, E. Schiffmann, L. A. Liotta, *J. Biol. Chem.* **1992**, *267*, 2524.
- [3] A. Perrakis, W. H. Moolenaar, *J. Lipid Res.* **2014**, *55*, 1010.
- [4] M. G. K. Benesch, Y. M. Ko, T. P. W. McMullen, D. N. Brindley, *FEBS Lett.* **2014**, *588*, 2712.
- [5] S. Willier, E. Butt, T. G. P. Grunewald, *Biol. Cell* **2013**, *105*, 317.
- [6] Y. Zhao, V. Natarajan, *Biochim. Biophys. Acta - Mol. Cell Biol. Lipids* **2013**, *1831*, 86.
- [7] G. Bain, K. E. Shannon, F. Huang, J. Darlington, L. Goulet, P. Prodanovich, G. L. Ma, A. M. Santini, A. J. Stein, D. Lonergan, et al., *J. Pharmacol. Exp. Ther.* **2016**, *360*.
- [8] S. G. Bourgoin, C. Zhao, *Curr. Opin. Investig. Drugs* **2010**, *11*, 515.
- [9] C. M. Rivera-Lopez, A. L. Tucker, K. R. Lynch, *Angiogenesis* **2008**, *11*, 301.
- [10] H. Nishimasu, S. Okudaira, K. Hama, E. Mihara, N. Dohmae, A. Inoue, R. Ishitani, J. Takagi, J. Aoki, O. Nureki, *Nat. Struct. Mol. Biol.* **2011**, *18*, 205.
- [11] H. Nishimasu, R. Ishitani, J. Aoki, O. Nureki, *Trends Pharmacol. Sci.* **2012**, *33*, 138.
- [12] J. Gierse, A. Thorarensen, K. Beltey, E. Bradshaw-Pierce, L. Cortes-Burgos, T. Hall, A. Johnston, M. Murphy, O. Nemirovskiy, S. Ogawa, et al., *J. Pharmacol. Exp. Ther.* **2010**, *334*, 310.
- [13] H. M. H. G. Albers, L. J. D. Hendrickx, R. J. P. van Tol, J. Hausmann, A. Perrakis, H. Ovaa, *J. Med. Chem.* **2011**, *54*, 4619.
- [14] W.-J. Keune, F. Potjewyd, T. Heidebrecht, F. Salgado-Polo, S. J. F. Macdonald, L. Chelvarajan, A. Abdel Latif, S. Soman, A. J. Morris, A. J. B. Watson, et al., *J. Med. Chem.* **2017**, *60*, 2006.
- [15] C. A. Kuttruff, M. Ferrara, T. Bretschneider, S. Hoerer, S. Handschuh, B. Nosse, H. Romig, P. Nicklin, G. J. Roth, *ACS Med. Chem. Lett.* **2017**, *8*, 1252.
- [16] L. M. Miller, W. J. Keune, D. Castagna, L. C. Young, E. L. Duffy, F. Potjewyd, F. Salgado-Polo, P. E. García, D. Semaan, J. M. Pritchard, et al., *J. Med. Chem.* **2017**, *60*, 722.
- [17] A. J. Stein, G. Bain, P. Prodanovich, A. M. Santini, J. Darlington, N. M. P. Stelzer, R. S. Sidhu, J. Schaub, L. Goulet, D. Lonergan, et al., *Mol. Pharmacol.* **2015**, *88*, 982.
- [18] P. Shah, A. Cheasty, C. Foxton, T. Raynham, M. Farooq, I. F. Gutierrez, A. Lejeune, M. Pritchard, A. Turnbull, L. Pang, et al., *Bioorganic Med. Chem. Lett.* **2016**, *26*, 5403.
- [19] W.-J. Keune, J. Hausmann, R. Bolier, D. Tolenaars, A. Kremer, T. Heidebrecht, R. P. Joosten, M. Sunkara, A. J. Morris, E. Matas-Rico, et al., *Nat. Commun.* **2016**, *7*, 11248.
- [20] N. Desroy, C. Housseman, X. Bock, A. Joncour, N. Bienvenu, L. Cheral, V. Labeguere, E. Rondet, C. Peixoto, J.-M. Grassot, et al., *J. Med. Chem.* **2017**, *60*, 3580.
- [21] H. M. H. G. Albers, L. A. van Meeteren, D. A. Egan, E. W. van Tilburg, W. H. Moolenaar, H. Ovaa, *J. Med. Chem.* **2010**, *53*, 4958.
- [22] A. Vagin, A. Teplyakov, *Acta Crystallogr Sect D Struct Biol.* **2010**, *66*, 22.
- [23] P. Emsley, B. Lohkamp, W. G. Scott, K. Cowtan, *Acta Crystallogr Sect D Struct Biol.* **2010**, *66*, 486.
- [24] G. N. Murshudov, P. Skubák, A. A. Lebedev, N. S. Pannu, R. A. Steiner, R. A. Nicholls, M. D. Winn, F. Long, A. A. Vagin, *Acta Crystallogr Sect D Struct Biol.* **2011**, *67*, 355.

- [25] R. P. Joosten, F. Long, G. N. Murshudov, A. Perrakis, *IUCrJ* **2014**, *1*, 213.
- [26] V. B. Chen, W. B. Arendall, J. J. Headd, D. A. Keedy, R. M. Immormino, G. J. Kapral, L. W. Murray, J. S. Richardson, D. C. Richardson, *Acta Crystallogr Sect D Struct Biol.* **2010**, *66*, 12.
- [27] J. Hausmann, S. Kamtekar, E. Christodoulou, J. E. Day, T. Wu, Z. Fulkerson, H. M. H. G. Albers, L. A. van Meeteren, A. J. S. Houben, L. van Zeijl, et al., *Nat. Struct. Mol. Biol.* **2011**, *18*, 198.
- [28] S. Katsamakos, A. G. Papadopoulos, D. Hadjipavlou-Litina, *Molecules* **2016**, *21*.
- [29] F. Salgado-Polo, A. Fish, M. T. Matsoukas, T. Heidebrecht, W. J. Keune, A. Perrakis, *J. Biol. Chem.* **2018**, *293*, 14312.
- [30] "The Human Protein Atlas," can be found under <https://www.proteinatlas.org/humanproteome/cell/cell+line>.
- [31] H. Ohta, K. Sato, N. Murata, A. Damin, E. Malchinkhuu, J. Kon, T. Kimura, M. Tobo, Y. Yamazaki, T. Watanabe, et al., *Mol. Pharmacol.* **2003**, *64*, 994.
- [32] J. E. Day, T. Hall, L. E. Pegg, T. E. Benson, J. Hausmann, S. Kamtekar, *Acta Crystallogr. Sect. F Struct. Biol. Cryst. Commun.* **2010**, *66*, 1127.
- [33] M. W. Bowler, D. Nurizzo, R. Barrett, A. Beteva, M. Bodin, H. Caserotto, S. Delagenière, F. Dobias, D. Flot, T. Giraud, et al., *J. Synchrotron Radiat.* **2015**, *22*, 1540.
- [34] W. Kabsch, *Acta Crystallogr Sect D Struct Biol.* **2010**, *66*, 133.
- [35] P. R. Evans, *Acta Crystallogr Sect D Struct Biol.* **2011**, *67*, 282.
- [36] W. Keune, J. Hausmann, R. Bolier, D. Tolenaars, A. Kremer, T. Heidebrecht, R. Joosten, M. Sunkara, A. Morris, E. Matas-Rico, et al., *Nat. Commun.* **2016**, *7*, 11248.
- [37] T. E. F. Kujit, M. Omerzu, A. T. Saurin, G. J. P. L. Kops, *Chromosoma* **2014**, *123*, 471.



Chapter A5

The structural binding mode of the six autotaxin inhibitor types that differentially affect catalytic and non-catalytic functions

Fernando Salgado-Polo and Anastassis Perrakis*

Affiliation:

Oncode Institute and Division of Biochemistry, Netherlands Cancer Institute, Plesmanlaan 121. 1066 CX, Amsterdam, the Netherlands.

*Correspondence: a.perrakis@nki.nl.

Based on:

Cancers (Basel). 2019, 11(10), 1577

Abstract

Autotaxin (ATX) is a secreted lysophospholipase D, catalysing the conversion of lysophosphatidylcholine (LPC) to bioactive lysophosphatidic acid (LPA). LPA acts through two families of G protein-coupled receptors (GPCRs) controlling key cellular responses, and it is implicated in many physiological processes and pathologies. ATX, therefore, has been established as an important drug target in the pharmaceutical industry. Structural and biochemical studies of ATX have shown that it has a bimetallic nucleophilic catalytic site, a substrate-binding (orthosteric) hydrophobic pocket that accommodates the lipid alkyl chain, and an allosteric tunnel that can accommodate various steroids and LPA. In this review, first, we review what is known about ATX-mediated catalysis, crucially in light of allosteric regulation. Then, we present the known ATX catalysis-independent functions, including binding to cell surface integrins and proteoglycans. Next, we analyse all crystal structures of ATX bound to inhibitors and present them based on the six inhibitor types that are established based on the binding to the orthosteric and/or the allosteric site. Finally, in light of these data we discuss how mechanistic differences might differentially modulate the activity of the ATX-LPA signaling axis, and clinical applications including cancer.

Introduction

Lysophosphatidic acid (1- or 2-acyl-*sn*-glycero-3-phosphate or LPA) is a bioactive lipid found in many body fluids and involved in many physiological and pathological processes. Historically, LPA had been identified as a growth factor in serum that could induce motility in fibroblasts and cancer cells through G protein-coupled receptors (GPCRs)^{[1], [2]}. Subsequent research identified specific LPA GPCRs (LPA₁₋₆), which have distinct expression patterns^[3]. Deregulation of the LPA signaling axis has been linked to different diseases, such as liver disease^[4], fibrosis^[5], pruritus^[6], multiple sclerosis^[7], inflammation, and cancer^{[8], [9]}.

The LPA receptors are classified into distinct families, the EDG (LPA₁₋₃) and non-EDG (LPA₄₋₆) families. The crystallographic structures of LPA₁ and LPA₆ have provided the field with key mechanistic indications with respect to their ligand binding mode^{[10], [11]}. Namely, a structural comparison between the LPA₁ and LPA₆ substrate-binding sites has indicated contrasting LPA binding modes from the extracellular milieu or the plasma membrane, respectively. The former is consistent with a model by which LPA is carried by a lipid chaperone, such as albumin, to bind to the flexible N-terminal domain of LPA₁ and deliver LPA specifically^[10], whereas the latter would not require lipid-carrying molecules^{[12], [13]}.

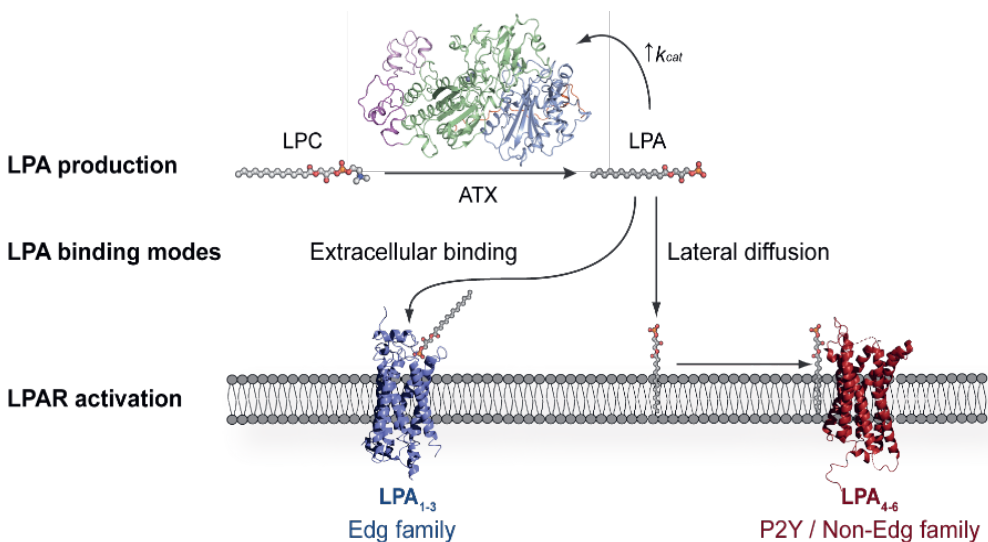


Figure 1. Distinct modes for lysophosphatidic acid (LPA) binding to its cognate G protein-coupled receptors (GPCRs) proposed based on their crystallographic structures. Autotaxin (ATX) is the main producer of LPA, which can then bind to the extracellularly open lipid-binding pocket of LPA₁₋₃, potentially assisted by lipid chaperones, or diffuse laterally towards the membrane-open ligand-binding site of LPA₄₋₆.

Since LPA can promote a plethora of downstream signaling events, both its production

and degradation are tightly regulated, resulting in an estimated half-life of approximately three minutes in circulation^{[14]–[16]}. Such a short-lived existence is due to its fast degradation by three membrane-bound lipid phosphate phosphatases (LPPs), which cleave the LPA phosphate group and release signaling-inactive monoacylglycerol^{[17], [18]}. Contrary to this, LPA production originates from the following two sources: phosphatidic acid hydrolysis by PLA_{1/2} and from the enzymatic conversion of lysophosphatidylcholine (1- or 2-acyl-*sn*-glycero-3-phosphocholine or LPC) to LPA by a lysophospholipase D (lysoPLD) that has been established to be autotaxin (ATX) (Figure 1)^{[19], [20]}. ATX-catalysed production constitutes the main physiological source of extracellular LPA, and therefore ATX has been widely studied as a target for drug development^{[14], [21], [22]}.

ATX is the only member of the ectonucleotide pyrophosphatase/phosphodiesterase family (ENPP) that presents lysoPLD activity (EC 3.1.4.39) over lysophospholipids^[22]. ATX is first translated as a pre-proenzyme that undergoes two proteolytic processing steps, resulting in a mature, glycosylated and secreted form^[23]. The determination of the structure of ATX by X-ray crystallography enabled the determination of its domain organization, i.e., the two N-terminal somatomedin B (SMB) like domains are followed by a central catalytic phosphodiesterase (PDE) domain, which is adjacent to an inactive nuclease-like domain. Substrate hydrolysis requires a bimetallic active site containing two Zn²⁺ ions and a threonine nucleophile, which act in an associative two-step in-line displacement catalytic mechanism^[24].

Structural studies have also established that ATX has a unique tripartite binding site. The catalytic bimetallic site is next to a hydrophilic shallow groove that accommodates the hydrophilic glycerol moiety of lipid substrates. This groove is connected by a T-junction to a hydrophobic pocket where acyl chains can bind, and a tunnel (often called the “hydrophobic channel”) that leads to the other side of the PDE domain^[25]. It is noteworthy that the tunnel (or channel) is only partially hydrophobic in nature and has hydrophilic patches, unlike the pocket (Figure 2). The tunnel binds steroid molecules^[26], as well as the LPA product^{[27], [28]}, which results in a modulation of catalytic efficiency. Thus, we refer to the tunnel as the allosteric site, while we refer to the substrate-binding, hydrophilic groove and the hydrophobic pocket, as the orthosteric site (Figure 3).

The Autotaxin Inhibitor Family

Initially, classical ATX inhibitors relied on lipid analogues targeting ATX based on similarities with sphingosine-1-phosphate (S1P) or LPA. Activity-based lead discovery campaigns, using artificial substrates as activity reporters, subsequently made important contributions, many of which are reviewed by Castagna *et al.* and Nikolaou *et al.*^{[29], [30]}.

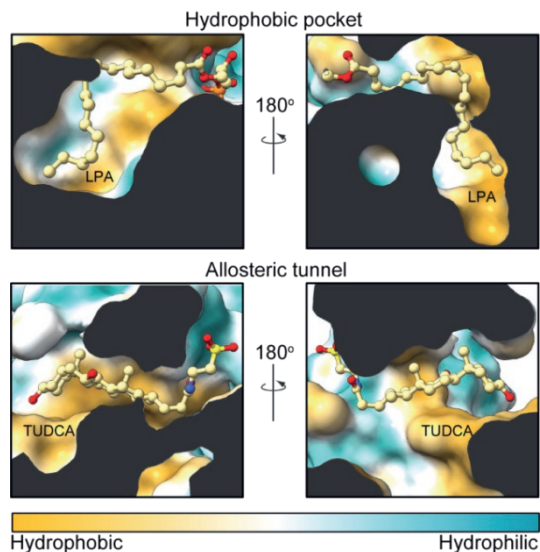


Figure 2. Hydrophobicity comparison between the pocket and the tunnel. Side sections of ATX (PDB: 5dlw) showing the modes of binding of LPA and tauroursodeoxycholic acid (TUDCA) in the orthosteric and allosteric sites, respectively. The (partly hydrophobic) tunnel presents hydrophilic patches that accommodate the polar moieties of TUDCA. Protein surface was colored from orange to turquoise using ChimeraX (version 0.91).

The structural characterization of rat and mouse ATX structures in 2011^{[25], [27]}, enabled a remarkable potential for selective inhibitor design by focusing on the three-dimensional architecture of the ATX active site. While attention initially focused on the lipid-binding pocket and the catalytic site, current emphasis is on the so-called tripartite site that we introduced earlier (Figure 3).

The tripartite ATX binding site represents a remarkable potential for selective design of inhibitors. Over time, ATX inhibitors of a distinct chemical nature were designed, including lipid-based inhibitors^[31], DNA aptamers^[32], as well as small molecules. The last group, the focus of this review, can be in turn classified in six distinct types (I, II, III, IV, V and VI) depending on their binding mode to the ATX tripartite site (Figure 4)^[33].

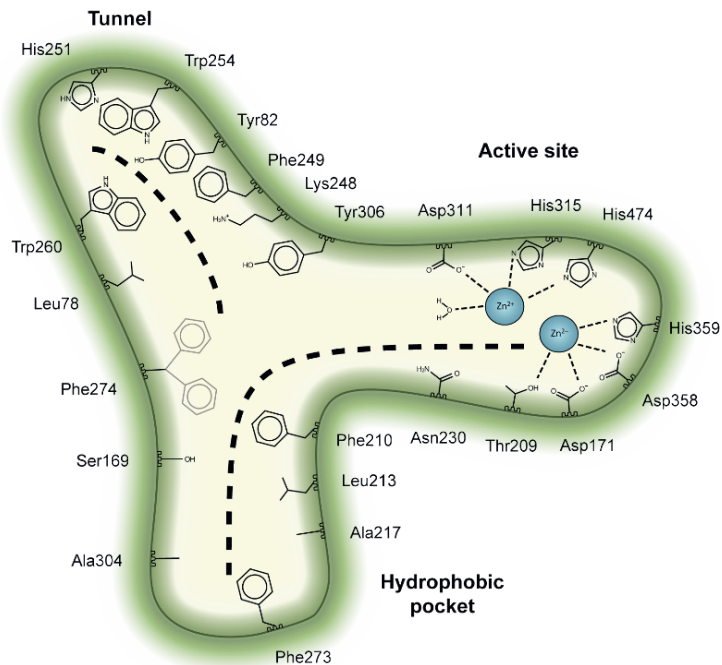


Figure 3. Key residues involved in binding the six classes of ATX inhibitors. Cartoon depiction of the ATX tripartite site and the crucial interacting residues for inhibitor binding. The dashed lines depict the binding site for type lysophosphatidylcholine (LPC) or LPA at the orthosteric site, as well as the binding site for steroids at the tunnel.

In this review, we will present the six families of ATX inhibitors from a structural biology perspective, as they are classified depending on their occupancy of the orthosteric and/or the allosteric site. Next, we will discuss how the different types of inhibitors might interfere with catalytic and non-catalytic functions to differentially affect the ATX-LPA signaling axis *in vivo*.

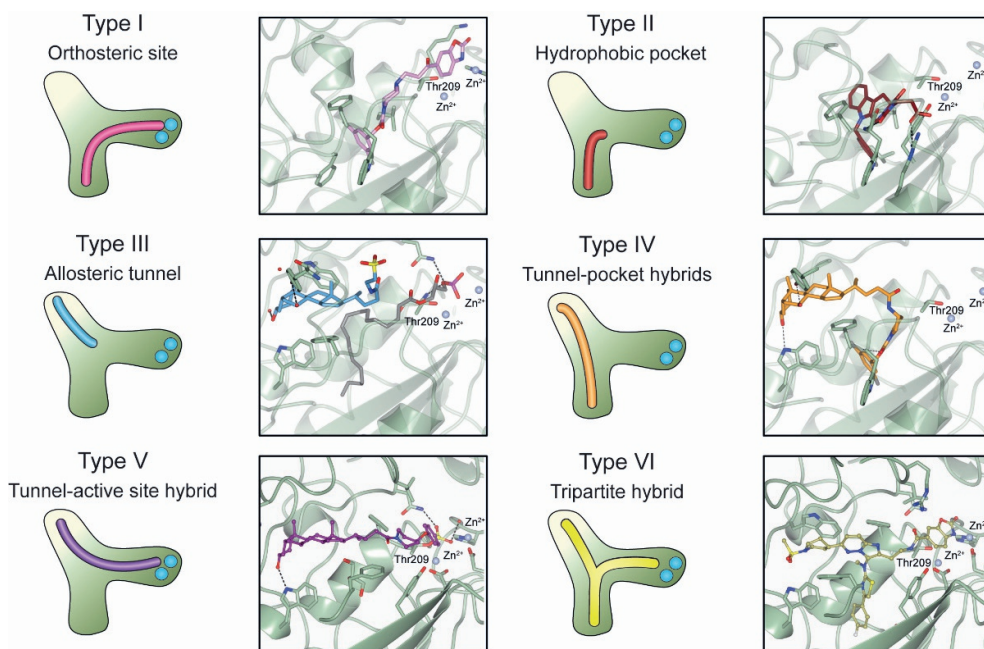


Figure 4. Classification of the six reported ATX inhibitor types based on their binding modes. **Left:** schematic view of the binding modes; **right:** crystallographic structures of ATX bound to compounds from each type; **from top to bottom:** PF-8380 (5l0k), PAT-352 (4zg9), TUDCA (5dlw), FP-Cpd 17 (5m0m), JMC-23 (7z0n) and G410125 (unpublished data).

Table 1. Common interactions needed in distinct types of ATX inhibitors.

Type	Residues Establishing Ligand Contacts (Rat ATX)		
	Active Site-Hydrophilic Groove	Hydrophobic Pocket	Allosteric Tunnel
I	Common	Thr209, Asp311, His474	-
	Frequent	His315, His359	Leu213, Phe273, Phe274*, Trp275
II	Common	-	Leu213, Phe274*, Trp276
	Frequent	-	Phe273, Tyr306
III	Common	-	Lys248, Phe249, Trp254, Trp260
	Frequent	-	Phe274*
IV	Common	-	Leu213, Phe273, Trp275, Tyr306
	Frequent	-	Phe274*, Phe210
V	Common	Asp171, Thr209, Asn230, Asp311	Tyr82, Phe249, Trp260
	Frequent	-	-
VI	Common	-	Phe249, Trp260
	Frequent	Not available	Not available

* Phe274 sidechain has two predominant conformers at the pocket-tunnel boundary depending on the interacting ligand.

In this review we focus on compounds for which there is a crystal structure available. We present, by inhibitor type, the common interactions with ATX (Table 1), known application in in vivo models (Table 2), and discuss their properties in light of their experimentally determined binding pose. It should be noted that due to the unclear naming of some inhibitors as “compound #” in the literature, we will refer to those as “FL-Cpd-#”, where FL stands for the first and last names of the publication’s first author.

Table 2. ATX inhibitors employed in in vivo models. Further details discussed in^{[21], [34], [35]}.

Type	Inhibitor	Disease	LPA inhibition	Clinical trials	References
I	SBJ-Cpd 1	Inflammation Multiple sclerosis	>50%	-	[7]
I	PF-8380	Glioblastoma Liver fibrosis	>90% >90%	-	[36] [4]
I	GK442	Pulmonary fibrosis	Not available	-	[37]
I	BMP22	Melanoma metastasis	50%	-	[38]
II	GWJ-A-23	Pulmonary fibrosis inflammation	50%	-	[39] [40]
III	PharmAkea -Cpd A-E	Metabolic disorder	25–35%	-	[41]
III	PAT-505, PAT-048	Liver fibrosis Skin fibrosis	40–80%	-	[42]
III	Cudetaxestat, BLD-0409, PAT-409	Idiopathic pulmonary fibrosis	Not available	Phase I	[43]
IV	Ziritaxestat, GLPG1690	Idiopathic pulmonary fibrosis	84–95%	Discontinued at Phase III	[43], [44]
IV	BBT-877	Idiopathic pulmonary fibrosis	Not available	Phase I	[43]
?	IOA-289	Selected solid tumors	Not available	Phase I	[43]
?	ONO-8430506	Breast cancer Thyroid cancer	>60% >70%	-	[45] [46]

Sbj-Cpd 1: ###; PF-8380:###; GK442:####; BMP22:### GWJ-A-23:### PAT:### ONO:##

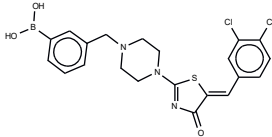
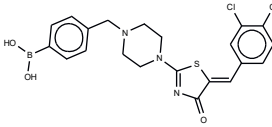
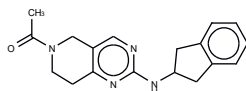
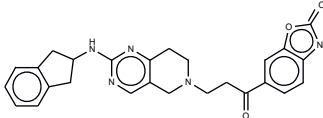
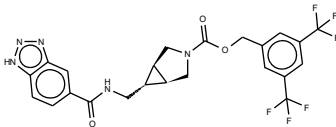
Type I Inhibitors

Type I compounds occupy the orthosteric site, mimicking the LPC substrate mode of binding. As such, they include competitive inhibitors with a long and flexible structure that occupies the catalytic site, the shallow groove, and the hydrophobic pocket. Several analogues based on LPA have naturally been put forward as ATX inhibitors such as: cyclic phosphatidic acid or cPA ($IC_{50} = 0.14 \mu\text{M}$, bis-*p*NPP)^[47], thiophosphate ($IC_{50} = 0.6 \mu\text{M}$, bis-*p*NPP)^[48], α -bromomethylene phosphonates like BrP-LPA ($IC_{50} = 0.7\text{--}1.6 \mu\text{M}$, LPC)^[49], the synthetic analogue for S1P FTY720-P ($K_i = 0.2 \mu\text{M}$, Bis-*p*NPP)^[50], and the most potent lipid-based inhibitor S32826 ($IC_{50} = 5.6 \text{ nM}$, LPC)^[51]. The latter showed poor in vivo stability, which prevented it from further use in animal models.

The first small molecule type I inhibitors were thiazolidinediones discovered in a screen using the artificial substrate CPF4^{[14], [25]}. Optimization led to the identification of HA-130 ($IC_{50} = 28$ nM, LPC), a boronic acid-based inhibitor that could attack the nucleophilic oxygen at the catalytic threonine, and it was able to hamper LPA production both in vivo and in vitro^[14]. Moreover, a positional isomer of HA-130, HA-155 ($IC_{50} = 5.7$ nM, LPC) (Table 3) was co-crystallized with ATX, which revealed interactions with Thr209, Asp311, His359 and His474 at the active site, as well as Leu213 and Phe274 in the hydrophobic pocket (Figure 3, Table 1). This series was subjected to structure-activity improvement studies based on the HA-155 crystal structure. These consisted, in trial, of the different linkers added to the thiazolidine-2,4-dione core^[52].

Table 3. Type I ATX inhibitors based on their kinetic and crystallographic analysis.

	Type I Inhibitor	PDB ID	Activity (IC_{50})	References
	HA-155	2xrg	5.7 nM	[25], [52]
	PF8380	510k	1.7 nM	[53], [54]
	FP-Cpd 3	5m0e	-	[54]
	MK-Cpd 10	3wav	180 nM *	[55]
	2BoA	3wav	580 nM *	[55]

	3wax	13 nM *	[55]
3BoA			
	3way	22 nM *	[55]
4BoA			
	5I0b	520 nM	[53]
SBJ-Cpd 1			
	5I0e	2.5 nM	[53]
SBJ-Cpd 2			
	5ohi	2.2 nM	[56]
BI-2545			

* denotes that TG-mTMP was used as the substrate for reporting the IC_{50} .

Subsequently, numerous type I ATX small molecule inhibitors have appeared in both academic and patent literature. An example of these are the thiazolone derivatives similar to the HA series produced by Kawaguchi and collaborators^[55]. A library of 81,600 compounds was screened for inhibiting the hydrolysis of the fluorescence probe TG-mTMP. This led to the identification of KM-Cpd 10 (180 nM, TG-mTMP), 2BoA (580 nM, TG-mTMP), 3Boa (13 nM, TG-mTMP), and 4BoA (22 nM, TG-mTMP), which were co-crystallized with ATX (Table 3). These structures revealed interactions with Arg284, as well as hydrophobic contacts with Trp260 and Phe274 (Figure 3, Table 1). Moreover, these compounds were able to decrease LPA levels both *in vitro* and *in vivo*^[55].

The most potent type I inhibitor to date is PF-8380 (IC_{50} = 1.7 nM, LPC) (Table 3), reported by Pfizer^{[53], [54]}. In general, it has been widely used because of its high potency and its favourable pharmacokinetic properties, which has allowed *in vivo* evaluation of ATX inhibition. PF-8380 is a benzoxazolone that exhibits the general chemotype of lipophilic tail, core spacer, and acidic head group. This general motif contains a benzoxazolone as the


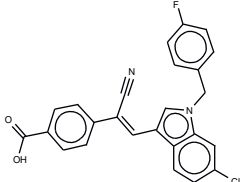
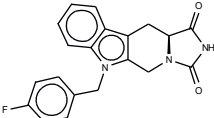
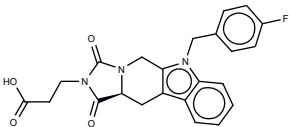
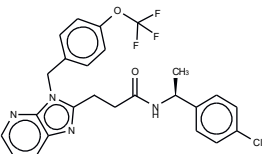
acidic head group, a functionalized piperazine as the spacer, and the dichlorocarbamate moiety as the lipophilic portion^{[53], [54]}. In the active site, the acidic head group makes essential interactions with one of the Zn²⁺ ions, and the lipophilic tail is accommodated within the hydrophobic pocket. Moreover, it is in close proximity to Thr209 and has hydrophobic interactions with Leu213, Phe273, and Phe274, as well as a hydrogen bond with the Trp275 amino group (Figure 3). The addition of a hydroxyethyl group to PF-8380 resulted in FP-Cpd-3, which had an increased solubility and was co-crystallisation with ATX (Table 3)^[57]. ATX inhibition with PF-8380 was shown to attenuate bleomycin-induced pulmonary fibrosis, owing to decreased LPA levels in plasma and bronchioalveolar lavage fluid, together with a decrease in inflammation and collagen deposition (Table 2), however, effectiveness of treatment with this compound varies in the literature^{[34], [58]}. Recently, treatment of mice on a high-fat diet with PF-8380 reduced plasma LPA levels, resulting in lower diet-induced cardiac dysfunction and inflammatory response^[59].

The compound SBJ-Cpd-1 (IC₅₀ = 520 nM, LPC)^[7] (Table 3) was obtained from an aminopyrimidine series that was further improved by the addition of benzoxazolone moiety present in PF-8380. This was crucial for synthesizing the far more active SBJ-Cpd-2 (IC₅₀ = 2.5 nM, LPC), which reaches the active site Zn²⁺ ions in a similar manner to that of PF-8380. Additionally, it also contacts Asp171, Asp311, His315, and His474 at the active site, and Leu213, Phe273, Phe274, and Trp275 at the pocket (Figure 3, Table 1). This compound was further tested in rats by a single oral dose (10 mg kg⁻¹), where plasma LPA levels decreased 80% upon 12 h treatment (Table 2). Lastly, another relevant compound shown to behave type I inhibitors is the a benzotriazole BI-2545 (2.2 nM, LPC)^[56] (Table 3), which was able to reduce LPA levels both in vitro and in vivo.

Type II Inhibitors

Type II ATX inhibitors owe their effect solely to binding to the hydrophobic pocket, where they obstruct LPC accommodation. As a result, this competitive mode of binding avoids interaction with the catalytic zinc ions, which may offer selectivity advantages over other inhibitors. The artificial ATX substrate, FS-3, was used by PharmAkea to screen small molecule compounds, from which they identified four indole-based analogues with high inhibitory potency. Among these, three lead type II compounds were reported, namely PAT-078 (IC₅₀ = 472 nM; LPC), PAT-494 (IC₅₀ = 20 nM; LPC), and PAT-352 (IC₅₀ = 26 nM; LPC)^[42] (Table 4). The structures of these compounds revealed common hydrophobic interactions between their vinyl-nitrile or hydantoin moieties, and Leu213, Leu216, Phe274, Trp275, and Tyr306 (Figure 3, Table 1).

Table 4. Type II ATX inhibitors based on their kinetic and crystallographic analysis.

	Type II Inhibitor	PDB ID	Activity (IC ₅₀)	References
	PAT-078	4zg6	472 nM	[42]
	PAT-494	4zga	20 nM	[42]
	PAT-352	4zg9	26 nM	[42]
	CRT0273750	5lia	1 nM	[60]


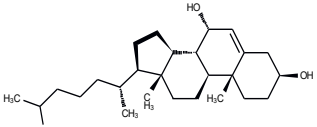
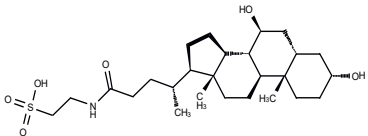
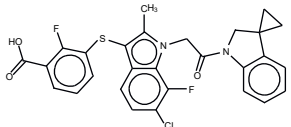
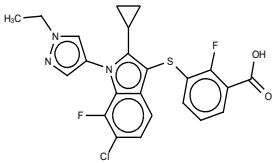
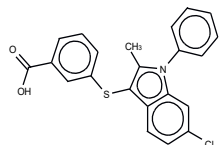
The artificial ATX substrate FS-3 was also used as readout for a high-throughput screen from a collection of 87,865 compounds. Upon a preliminary selection of 1.2% best hits, the physiological LPC choline release assay was used, from which the imidazo [4,5-b] biyridine-derivative CRT0273750 (IC₅₀ = 1 nM, LPC; 14 nM human plasma LPC)^[61] was identified (Table 4). The crystal structure of ATX in complex with CRT0273750 indicated that the compound binds at the hydrophobic pocket, as well as with the boundaries of the ATX tunnel, but 5 Å away from the active site. As a consequence, it establishes a hydrogen bond with Lys247, and hydrophobic interactions with Leu213, Phe248, Trp254, Phe273, Phe274, and Trp275 (Table 1). In vitro data showed that this compound could inhibit migration of 4T1 cells. Moreover, the compound was effective in reducing 18:1 LPA levels in vitro in human plasma, as well as in in vivo samples from MDA-MB-231-luc tumor bearing Balb-c nu/nu mice (Table 2)^[61]. Lastly, the short phosphonate lipid analogue GWJ-A-23^[60] was used in models for lung fibrosis and inflammation, where it resulted in a 50% decrease of LPA concentrations in bronchioalveolar lavage fluid (Table 2)

Type III Inhibitors

Type III inhibitors specifically occupy the allosteric regulatory tunnel, modulating ATX activity by noncompetitive inhibition. We have reported that 7- α -hydroxycholesterol (Table 5) is commonly present in purified mammalian ATX structures, but this does not have an observable inhibitory activity. However, other steroids, namely, bile salts such as tauroursodeoxycholic acid (TUDCA) ($IC_{50} = 10.4 \mu\text{M}$; LPC) or ursodeoxycholic acid (UDCA) ($IC_{50} = 8.8 \mu\text{M}$; LPC) exert modest and partial (always leaving residual activity) noncompetitive inhibition of lysoPLD activity (Table 5)^[26]. The ATX co-crystal, with 18:1 LPA bound at the orthosteric site and TUDCA bound at the tunnel, confirmed the noncompetitive mode of inhibition. TUDCA interacts with ATX, forming a hydrogen bond with Trp260 and hydrophobic stacking with Trp254 and Phe274 (Figure 3). The mechanism underlying its inhibition may occur by counteracting the modulatory action of LPA in the tunnel^[28].

A5

Table 5. Type III ATX inhibitors based on their kinetic and crystallographic analysis.

	Type IV Inhibitor	PDB ID	Activity (IC_{50})	References
	7- α -hydroxycholesterol	5dlt	undetermined	[26]
	TUDCA	5dlw	10.4 μM	[26]
	PAT-347	4zg7	0.3 nM	[42]
	PAT-505	5kxa	2 nM	[62]
	LM-Cpd 51	5lqq	81 nM	[63]

The identification of type II indole-based ATX inhibitors, as discussed above, also yielded a type III compound, namely PAT-347 ($IC_{50} = 0.3$ nM; LPC) (Table 5)^[42]. The crystal structure of ATX bound to both PAT-347 and 14:0 LPA confirmed its noncompetitive binding mode. PAT-347 accommodates at the tunnel by π - π interactions between its indole moiety and Phe274 and His251. Moreover, its benzoic acid makes another π - π interaction with Phe249. It also contacts with Lys248, Trp254, and Trp260. More recently, the pharmacokinetic properties of two novel compounds, PAT-505 ($IC_{50} = 2$ nM; LPC) and PAT-048 ($IC_{50} = 1.1$ nM; LPC), were assessed (Table 5)^{[62], [64]-[66]}. The crystal structure of PAT-505 bound to ATX showed a very similar binding mode to that of PAT-347, namely, by interacting with Lys248, Phe249, His251, Trp254, Trp260, and Phe274, but also Ser81 and Val277 (Table 1). Clinical assays with PAT-048, showed better pharmacodynamics results, and this was used for in vivo assays with a bleomycin-induced mouse model for dermal fibrosis. Pharmacological inhibition of ATX activity markedly attenuated skin fibrosis upon treatment with 10 mg kg^{-1} PAT-048, which related to a 75% inhibition of ATX activity after 24 h and >90% at double dose (Table 2). It is worthy to mention that five new patented PharmAkea compounds, namely, PharmAkea-Cpd A-E ($IC_{50} = <0.5$ μ M; LPC) have been recently used in metabolic disorder treatment, where they showed a decrease of fasting blood glucose levels in mice fed with a high-fat diet (Table 2)^[41].

Amira Pharmaceuticals reported a structure-activity evolution study, which resulted in a new series of indole-derived type III compounds^[66], and the identification of LM-Cpd 51^[63] (Table 5). The co-crystal structure with rat ATX showed that the compound binds in the tunnel, establishing stacking interactions with Trp254, as well as hydrophobic interactions with Phe249, Trp260, and Phe274 (Table 1).

Type IV Inhibitors

Type IV compounds occupy the binding pocket and the tunnel, but do not contact the catalytic site. Such compounds have been discovered either by design, fusing parts of a type I and a type III inhibitor, such as in FP-Cpd-17 ($IC_{50} = 14$ nM)^[57], or by serendipity, during a high-throughput screen followed by specific structure-based design, such as in GLPG1690^[67] (Table 6).

We reported the structure-guided design and chemical evolution of bile salts, from weak physiological noncompetitive inhibitors into potent competitive type IV compounds^[57]. This was achieved by using the PF-8380 dichlorocarbamate moiety as a pocket-binding lipophilic portion. By design, these compounds did not interact with the active site residues, but still hampered LPC or LPA binding. The best lead compounds differed chiefly regarding spacers connecting the steroid and the dichlorocarbamate moieties, i.e., linear amide linker, piperazine, and piperidine for FP-Cpd-5 ($IC_{50} = 202$ nM; LPC), -11 ($IC_{50} = 814$ nM; LPC), and -17 ($IC_{50} = 20$ nM; LPC), respectively (Table 6)^[57]. Moreover, a very short

spacer yielded no measurable inhibitory activity, which explains why FP-Cpd-11 exhibited a five-fold lower activity than FP-Cpd-17. These compounds were co-crystallized with rat ATX, showing how these types of inhibitors accommodate at both the tunnel and the pocket. Specifically, they all made hydrogen bonds with Tyr81 and Trp260 at the tunnel and established π - π interactions with Phe273 and Trp274 in the hydrophobic pocket (Table 6, Table 1)^[57]. Lastly, these type IV compounds were used in in vitro cell assays, where they showed a decrease of LPA-driven downstream phosphorylation of Akt in BJEh fibroblasts^[57].

Table 6. Type IV ATX inhibitors based on their kinetic and crystallographic analysis.


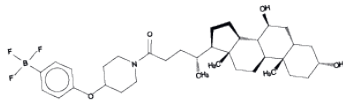
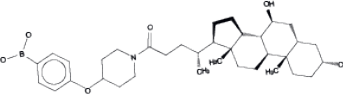
	Type IV Inhibitor	PDB ID	Activity (IC ₅₀)	References
	FP-Cpd 5	5m0s	202 nM	[57]
	FP-Cpd 11	5m0d	814 nM	[57]
	FP-Cpd 17	5m0m	20 nM	[57]
	AJ-Cpd 9	5m7m	357 nM	[33]
	GLPG1690	5mhp	27 nM	[67]

The Belgo-Dutch company Galapagos NV serendipitously discovered the only other confirmed type IV compound series. They used a high-throughput screen, where they identified an imidazo [1,2-a] pyridine series, from which the very potent compounds GLPG1690 ($IC_{50} = 27$ nM; LPC)^[67] and AJ-Cpd-9 ($IC_{50} = 357$ nM; LPC)^[33] were obtained by structure-activity evolution (Table 6). Moreover, the crystal structures of these compounds confirmed their binding mode to ATX. GLPG1690 makes a hydrogen bond with Trp254, π - π interactions with Phe274, and further hydrophobic interactions with Phe250 and Phe275. AJ-Cpd-9 makes a hydrogen bond with Trp260 and hydrophobic interactions with Trp254, Phe250, Phe260, and Phe275 (Table 1,6). After pharmacokinetics and pharmacodynamics analyses^{[44],[68]}, *in vivo* experiments showed that administration of GLPG1690 to bleomycin-treated mice resulted in a reduction of lung fibrosis, which was linked to a dose-dependent reduction of plasma LPA 18:2 levels (90%) (Table 2)^{[33],[67]}. This compound has shown very promising results in advanced clinical trials against idiopathic lung fibrosis and has recently progressed to phase III clinical trials for IPF^[69].

Type V Inhibitors

In analogy to the tunnel-pocket hybrid ATX inhibitors, we used the structural knowledge of type I and III compounds to synthesize the novel series of tunnel-active site binders or type V inhibitors^[70] (Table 7). Compound design focused on the combination of tunnel-binding UDCA^[57] with different warheads targeting the catalytic site. This resulted in the nanomolar-affinity compounds JMC-Cpd 22 and JMC-Cpd 23 (Table 7), which showed an excellent reduction of *in vitro* LPA synthesis, and cell-based ATX-derived LPA signaling in HeLa and fibroblast cell lines^[70]. The development and characterization of these compounds is explained in depth in **Chapter A4**.

Table 7. Type V ATX inhibitors based on their kinetic and crystallographic analysis.


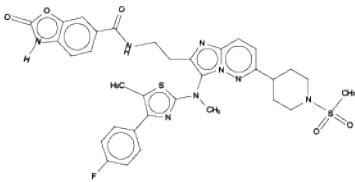
	Type V Inhibitor	PDB ID	Activity (IC_{50})	References
	JMC-Cpd 22	7z0m	50 nM	[70]
	JMC-Cpd 23	7z0n	30 nM	[70]

Type VI Inhibitors

Our group joined Galapagos NV to perform the structure-activity optimization of a novel and yet unpublished type of ATX inhibitors, namely the tripartite binders or type VI inhibitors (Table 8). In contrast to previous inhibitor types, this new binding mode is a comprehensive blockade of all three sites in ATX. Synthesis started from an imidazo [1,2-a] pyridine core series, analogous to the design of GLPG1690, which was the basis for the addition of three functional branches. Firstly, binding to the hydrophobic pocket was enabled by a fluorophenyl moiety, similar to type I HA-155 and type II PAT-494 (Tables 3-5). Secondly, binding to the tunnel was ensured by a piperidine ring substituted with a methylated sulphonyl moiety; this represents a novel binding mode to block the ATX tunnel, different from those present in types III-V (Tables 4-7). Lastly, optimization focused on the length and linker type to reach the active site, resulting in a benzoxazolone warhead inspired in the design of PF8380 (Table 3).

A5

Table 8. Type VI ATX inhibitors based on their kinetic analysis.

	Type VI Inhibitor	PDB ID	Activity (IC ₅₀)	References
	G410125	(unpublished data)	26 nM	(unpublished data)

Conclusions

The different types of ATX inhibitors could have different outcomes that go beyond the simple orthosteric inhibition of catalytic activity. While we know that LPA binding to the allosteric site is likely increasing the catalytic rate of ATX, possible roles of the tunnel in delivering LPA to its receptors, perhaps in an interplay between surface integrins and proteoglycans, have not been exploited. The fact that Edg and non-Edg receptors have different binding pocket characteristics could imply that LPA delivery through the tunnel could be receptor dependent.

Type I inhibitors would effectively stop LPA production from LPC but would not affect any independent function of the allosteric site. Type IV inhibitors, however, would also abolish any functionality of the allosteric site, expelling bound LPA. We suggest that the clinical success of the type IV compound, GLPG1690, is not independent from its mode of binding and inhibition, interfering with the allosteric tunnel. Albeit some ATX inhibitors

have shown promising results in animal cancer models^{[47], [71], [72]}, none have progressed to clinical trials, at least to our knowledge. One should consider the different types of inhibitors in the context of cancer therapy. We suggest that a type IV inhibitor occupying the low-affinity allosteric tunnel could prove much more effective, in the context of a tumour with high local LPA concentration that could displace the inhibitor from the high-affinity orthosteric site. It is our expectation that autotaxin inhibitors will have a dynamic comeback in the context of cancer therapy.

Acknowledgments

The authors would like to thank Wouter Moolenaar for critically reading the manuscript.

References

- [1] E. van Corven, A. Groenink, K. Jalink, T. Eichholtz, W. Moolenaar, *Cell*, **1989**, 59, 45.
- [2] K. Jalink, E. J. Van Corven, W. H. Moolenaar, *J. Biol. Chem.*, **1990**, 265, 12232..
- [3] J. Wang, Y. Sun, J. Qu, Y. Yan, Y. Yang, H. Cai, *Expert Rev. Mol. Diagn.*, **2016**, 16, 1103.
- [4] E. Kaffe, A. Katsifa, N. Xylourgidis, I. Ninou, M. Zannikou, V. Harokopos, P. Foka, A. Dimitriadis, K. Evangelou, A. N. Moulas, U. Georgopoulou, V. G. Gorgoulis, G. N. Dalekos, V. Aidinis, *Hepatology*, **2017**, 65, 1369.
- [5] A. M. Tager, P. LaCamera, B. S. Shea, G. S. Campanella, M. Selman, Z. Zhao, V. Polosukhin, J. Wain, B. A. Karimi-Shah, N. D. Kim, W. K. Hart, A. Pardo, T. S. Blackwell, Y. Xu, J. Chun, A. D. Luster, *Nat. Med.*, **2008**, 14, 45.
- [6] A. E. Kremer, J. J. W. W. Martens, W. Kulik, F. Ruëff, E. M. M. Kuiper, H. R. van Buuren, K. J. van Erpecum, J. Kondrackiene, J. Prieto, C. Rust, V. L. Geenes, C. Williamson, W. H. Moolenaar, U. Beuers, R. P. J. Oude Elferink, *Gastroenterology*, **2010**, 139, 1018.e1.
- [7] K. Thirunavukkarasu, B. Tan, C. A. Swearingen, G. Rocha, H. H. Bui, D. J. McCann, S. B. Jones, B. H. Norman, L. A. Pfeifer, J. K. Saha, *J. Pharmacol. Exp. Ther.*, **2016**, 359, 207.
- [8] E. Barbayiannia, E. Kaffe, V. Aidinis, G. Kokotos, *Prog. Lipid Res.*, **2015**, 58, 76..
- [9] M. G. K. Benesch, X. Tang, G. Venkatraman, R. T. Bekele, D. N. Brindley, *J. Biomed. Res.*, **2016**, 30, 272.
- [10] J. E. Chrencik, C. B. Roth, M. Terakado, H. Kurata, R. Omi, Y. Kihara, D. Warshaviak, S. Nakade, G. Asmar-Rovida, M. Mileni, H. Mizuno, M. T. Griffith, C. Rodgers, G. W. Han, J. Velasquez, J. Chun, R. C. Stevens, M. A. Hanson, *Cell*, **2015**, 161, 1633.
- [11] R. Taniguchi, A. Inoue, M. Sayama, A. Uwamizu, K. Yamashita, K. Hirata, M. Yoshida, Y. Tanaka, H. E. Kato, Y. Nakada-Nakura, Y. Otani, T. Nishizawa, T. Doi, T. Ohwada, R. Ishitani, J. Aoki, O. Nureki, *Nature*, **2017**, 548, 356.
- [12] H. Zhang, K. Pluhackova, Z. Jiang, R. A. Böckmann, *Sci. Rep.*, **2016**, 6, 30655.
- [13] N. Stanley, L. Pardo, G. De Fabritiis, *Sci. Rep.*, **2016**, 6, 1.
- [14] H. M. H. G. Albers, A. Dong, L. A. van Meeteren, D. A. Egan, M. Sunkara, E. W. van Tilburg, K. Schuurman, O. van Tellingen, A. J. Morris, S. S. Smyth, W. H. Moolenaar, H. Ovaa, *Proc. Natl. Acad. Sci. U. S. A.*, **2010**, 107, 7257.
- [15] J. L. Tomsig, A. H. Snyder, E. V. Berdyshev, A. Skobeleva, C. Mataya, V. Natarajan, D. N. Brindley, K. R. Lynch, *Biochem. J.*, **2009**, 419, 611.
- [16] X. Tang, M. G. K. Benesch, J. Dewald, Y. Y. Zhao, N. Patwardhan, W. L. Santos, J. M. Curtis, T. P. W. McMullen, D. N. Brindley, *J. Lipid Res.*, **2014**, 55, 2389.
- [17] R. Jasinska, Q. Zhang, C. Pilquil, I. Singh, J. Xu, J. Dewald, D. A. Dillon, L. G. Berthiaume, G. M. Carman, D. W. Waggoner, D. N. Brindley, **1999**, 340, 677..
- [18] L. A. van Meeteren, W. H. Moolenaar, *Prog. Lipid Res.*, **2007**, 46, 145..
- [19] J. Aoki, A. Taira, Y. Takanezawa, Y. Kishi, K. Hama, T. Kishimoto, K. Mizuno, K. Saku, R. Taguchi, H. Arai, *J. Biol. Chem.*, **2002**, 277, 48737.

- [20] M. Umezu-Goto, Y. Kishi, A. Taira, K. Hama, N. Dohmae, K. Takio, T. Yamori, G. B. Mills, K. Inoue, J. Aoki, H. Arai, *J. Cell Biol.*, **2002**, 158, 227.
- [21] A. N. Matralis, A. Afantitis, V. Aidinis, *Med. Res. Rev.*, **2019**, 39, 976.
- [22] A. Tokumura, E. Majima, Y. Kariya, K. Tominaga, K. Kogure, K. Yasuda, K. Fukuzawa, *J. Biol. Chem.*, **2002**, 277, 39436.
- [23] S. Jansen, *J. Cell Sci.*, **2005**, 118, 3081.
- [24] J. Hausmann, W.-J. Keune, A. L. Hipgrave Ederveen, L. van Zeijl, R. P. Joosten, A. Perrakis, *J. Struct. Biol.*, **2016**, 195, 199..
- [25] J. Hausmann, S. Kamtekar, E. Christodoulou, J. E. Day, T. Wu, Z. Fulkerson, H. M. H. G. Albers, L. A. Van Meeteren, A. J. S. Houben, L. Van Zeijl, S. Jansen, M. Andries, T. Hall, L. E. Pegg, T. E. Benson, M. Kasiem, K. Harlos, C. W. V. Kooi, S. S. Smyth, H. Ovaa, M. Bollen, A. J. Morris, W. H. Moolenaar, A. Perrakis, *Nat. Struct. Mol. Biol.*, **2011**, 18, 198.
- [26] W. Keune, J. Hausmann, R. Bolier, D. Tolenaars, A. Kremer, T. Heidebrecht, R. Joosten, M. Sunkara, A. Morris, E. Matas-Rico, W. Moolenaar, R. Oude Elferink, A. Perrakis, *Nat. Commun.*, **2016**, 7, 11248.
- [27] H. Nishimasu, S. Okudaira, K. Hama, E. Mihara, N. Dohmae, A. Inoue, R. Ishitani, J. Takagi, J. Aoki, O. Nureki, *Nat. Struct. Mol. Biol.*, **2011**, 18, 205.
- [28] F. Salgado-Polo, A. Fish, M.-T. Matsoukas, T. Heidebrecht, W.-J. Keune, A. Perrakis, *J. Biol. Chem.*, **2018**, 293, jbc. RA118.004450.
- [29] D. Castagna, D. C. Budd, S. J. F. F. Macdonald, C. Jamieson, A. J. B. B. Watson, *J. Med. Chem.*, **2016**, 59, 5604.
- [30] A. Nikolaou, M. G. Kokotou, D. Limnios, A. Psarra, G. Kokotos, *Expert Opin. Ther. Pat.*, **2017**, 27, 815.
- [31] K. R. Lynch, T. L. Macdonald, 2013
- [32] K. Kato, H. Ikeda, S. Miyakawa, S. Futakawa, Y. Nonaka, M. Fujiwara, S. Okudaira, K. Kano, J. Aoki, J. Morita, R. Ishitani, H. Nishimasu, Y. Nakamura, O. Nureki, *Nat. Struct. Mol. Biol.*, **2016**, 23, 395.
- [33] A. Joncour, N. Desroy, C. Housseman, X. Bock, N. Bienvenu, L. Chereil, V. Labeguere, C. Peixoto, D. Annoot, L. Lepissier, J. Heiermann, W. J. Hengeveld, G. Pilzak, A. Monjardet, E. Wakselman, V. Roncoroni, S. Le Tallec, R. Galien, C. David, N. Vandervoort, T. Christophe, K. Conrath, M. Jans, A. Wohlkonig, S. Soror, J. Steyaert, R. Touitou, D. Fleury, L. Vercheval, P. Mollat, N. Triballeau, E. Van Der Aar, R. Brys, B. Heckmann, *J. Med. Chem.*, **2017**, 60, 7371.
- [34] I. Ninou, E. Kaffe, S. Müller, D. C. Budd, C. S. Stevenson, C. Ullmer, V. Aidinis, *Pulm. Pharmacol. Ther.*, **2018**, 52, 32.
- [35] I. Ninou, C. Magkrioti, V. Aidinis, *Front. Med.*, **2018**, 5, 1.
- [36] S. R. Bhave, D. Y. A. Dadey, R. M. Karvas, D. J. Ferraro, R. P. Kotipatruni, J. J. Jaboin, A. N. Hallahan, T. A. DeWees, A. G. Linkous, D. E. Hallahan, D. Thotala, *Front. Oncol.*, **2013**, 3, 1.
- [37] A. Nikolaou, I. Ninou, M. G. Kokotou, E. Kaffe, A. Afantitis, V. Aidinis, G. Kokotos, *J. Med. Chem.*, **2018**, 61, 3697.

- [38] S. Lee, Y. Fujiwara, J. Liu, J. Yue, Y. Shimizu, D. Norman, Y. Wang, R. Tsukahara, E. Szabo, R. Patil, S. Banerjee, D. D. Miller, L. Balazs, Ghosh, M. C., C. M. Waters, T. Oravec, G. Tigyi, *Mol Cancer Res*, **2015**, 13, 174.
- [39] N. Oikonomou, M. A. Mouratis, A. Tzouveleki, E. Kaffe, C. Valavanis, G. Vilaras, A. Karameris, G. D. Prestwich, D. Bouros, V. Aidinis, *Am. J. Respir. Cell Mol. Biol.*, **2012**, 47, 566.
- [40] G. Y. Park, Y. G. Lee, E. Berdyshev, S. Nyenhuis, J. Du, P. Fu, I. A. Gorshkova, Y. Li, S. Chung, M. Karpurapu, J. Deng, R. Ranjan, L. Xiao, H. A. Jaffe, S. J. Corbridge, E. A. B. Kelly, N. N. Jarjour, J. Chun, G. D. Prestwich, E. Kaffe, I. Ninou, V. Aidinis, A. J. Morris, S. S. Smyth, S. J. Ackerman, V. Natarajan, J. W. Christman, *Am. J. Respir. Crit. Care Med.*, **2013**, 188, 928.
- [41] J. F. Evans, WO 2016/028686A1, 2016
- [42] A. J. Stein, G. Bain, P. Prodanovich, A. M. Santini, J. Darlington, N. M. P. Stelzer, R. S. Sidhu, J. Schaub, L. Goulet, D. Lonergan, I. Calderon, J. F. Evans, J. H. Hutchinson, D. H. Johnson, B. M. Shrier, J. S. O. Neal, J. A. Knutzen, *Mol. Pharmacol.*, **2015**, 88, 982.
- [43] S. Bano, M. Al-Rashida, R. D. Alharthy, I. A. Khan, J. Iqbal, *Expert Opin. Ther. Pat.*, **2022**, 1.
- [44] T. M. Maher, E. M. van der Aar, O. Van de Steen, L. Allamassey, J. Desrivot, S. Dupont, L. Fagard, P. Ford, A. Fieuw, W. Wuyts, *Lancet Respir. Med.*, **2018**, 6, 627.
- [45] M. G. K. Benesch, X. Tang, T. Maeda, A. Ohhata, Y. Y. Zhao, B. P. C. Kok, J. Dewald, M. Hitt, J. M. Curtis, T. P. W. McMullen, D. N. Brindley, *FASEB J.*, **2014**, 28, 2655.
- [46] M. G. K. Benesch, Y. Y. Zhao, J. M. Curtis, T. P. W. McMullen, D. N. Brindley, *J. Lipid Res.*, **2015**, 56, 1134.
- [47] L. D. Baker, Y. Fujiwara, K. Pigg, R. Tsukahara, S. Kobatashi, H. Murofushi, A. Uchiyama, K. Murakami-Murofushi, E. Murph, G. B. Mills, G. Tigyi, *J Biol Chem*, **2006**, 281, 22786.
- [48] G. G. Durgam, T. Virag, M. D. Walker, R. Tsukahara, S. Yasuda, K. Liliom, L. A. van Meeteren, W. H. Moolenaar, N. Wilke, W. Siess, G. Tigyi, D. D. Miller, *J. Med. Chem.*, **2005**, 48, 4919.
- [49] I. Nikitopoulou, E. Kaffe, I. Sevastou, I. Siritoti, M. Samiotaki, D. Madan, G. D. Prestwich, V. Aidinis, *PLoS One*, **2013**, 8
- [50] L. A. van Meeteren, V. Brinkmann, J. S. Saulnier-Blache, K. R. Lynch, W. H. Moolenaar, *Cancer Lett.*, **2008**, 266, 203.
- [51] G. Ferry, N. Moulharat, J.-P. Pradere, P. Desos, A. Try, A. Genton, A. Giganti, M. Beucher-Gaudin, M. Lonchampt, M. Bertrand, J.-S. Saulnier-Blache, G. C. Tucker, A. Cordi, J. A. Boutin, *J. Pharmacol. Exp. Ther.*, **2008**, 327, 809.
- [52] H. M. H. G. Albers, L. J. D. Hendrickx, R. J. P. van Tol, J. Hausmann, A. Perrakis, H. Ova, *J. Med. Chem.*, **2011**, 54, 4619.
- [53] S. B. Jones, L. A. Pfeifer, T. J. Bleisch, T. J. Beauchamp, J. D. Durbin, V. J. Klimkowski, N. E. Hughes, C. J. Rito, Y. Dao, J. M. Gruber, H. Bui, M. G. Chambers, S. Chandrasekhar, C. Lin, D. J. McCann, D. R. Mudra, J. L. Oskins, C. A. Swearingen, K. Thirunavukkarasu, B. H. Norman, *ACS Med. Chem. Lett.*, **2016**, 7, 857.
- [54] J. Gierse, A. Thorarensen, K. Beltey, E. Bradshaw-pierce, L. Cortes-burgos, T. Hall, A. Johnston, M. Murphy, O. Nemirovskiy, S. Ogawa, L. Pegg, M. Pelc, M. Prinsen, M. Schnute, J. Wendling, S. Wene, R. Weinberg, A. Wittwer, B. Zweifel, J. Masferrer, *J. Pharmacol. Exp. Ther.*, **2010**, 2, 310.

- [55] M. Kawaguchi, T. Okabe, S. Okudaira, H. Nishimasu, R. Ishitani, H. Kojima, O. Nureki, J. Aoki, T. Nagano, *ACS Chem. Biol.*, **2013**, 8, 1713.
- [56] C. A. Kuttruff, M. Ferrara, T. Bretschneider, S. Hoerer, S. Handschuh, B. Nosse, H. Romig, P. Nicklin, G. J. Roth, *ACS Med. Chem. Lett.*, **2017**, 8, 1252.
- [57] W. J. Keune, F. Potjewyd, T. Heidebrecht, F. Salgado-Polo, S. J. F. Macdonald, L. Chelvarajan, A. Abdel Latif, S. Soman, A. J. Morris, A. J. B. Watson, C. Jamieson, A. Perrakis, *J. Med. Chem.*, **2017**, 60, 2006.
- [58] A. Katsifa, E. Kaffe, N. Nikolaidou-Katsaridou, A. N. Economides, S. Newbigging, C. McKerlie, V. Aidinis, *PLoS One*, **2015**, 10, 1.
- [59] J. Weng, S. Jiang, L. Ding, Y. Xu, X. Zhu, P. Jin, *J. Cell. Mol. Med.*, **2019**, 23, 1050.
- [60] G. Jiang, D. Madan, Prestwich, G. D., **2011**, 21, 5098.
- [61] P. Shah, A. Cheasty, C. Foxton, T. Raynham, M. Farooq, I. F. Gutierrez, A. Lejeune, M. Pritchard, A. Turnbull, L. Pang, P. Owen, S. Boyd, A. Stowell, A. Jordan, N. M. Hamilton, J. R. Hitchin, M. Stockley, E. MacDonald, M. J. Quesada, E. Trivier, J. Skeete, H. Ovaa, W. H. Moolenaar, H. Ryder, *Bioorganic Med. Chem. Lett.*, **2016**, 26, 5403.
- [62] G. Bain, K. E. Shannon, F. Huang, J. Darlington, L. Goulet, P. Prodanovich, G. L. Ma, A. M. Santini, A. J. Stein, D. Lonergan, C. D. King, I. Calderon, A. Lai, J. H. Hutchinson, J. F. Evans, S. Diego, G. B. California, **2017**, 2.
- [63] L. M. Miller, W. J. Keune, D. Castagna, L. C. Young, E. L. Duffy, F. Potjewyd, F. Salgado-Polo, P. E. García, D. Semaan, J. M. Pritchard, A. Perrakis, S. J. F. MacDonald, C. Jamieson, A. J. B. Watson, *J. Med. Chem.*, **2017**, 60, 722.
- [64] K. E. Black, E. Berdyshev, G. Bain, F. V. Castelino, B. S. Shea, C. K. Probst, B. A. Fontaine, I. Bronova, L. Goulet, D. Lagares, N. Ahluwalia, R. S. Knipe, V. Natarajan, A. M. Tager, *FASEB J.*, **2016**
- [65] F. V. Castelino, G. Bain, V. A. Pace, K. E. Black, L. George, C. K. Probst, L. Goulet, R. Lafyatis, A. M. Tager, *Arthritis Rheumatol.*, **2016**, 68, 2964.
- [66] J. H. Hutchinson, T. A. Parr, J. R. Roppe, N. S. Stock, D. Volkots, WO/2012/024620-A2, 2012
- [67] N. Desroy, C. Housseman, X. Bock, A. Joncour, N. Bienvenu, L. Cherel, V. Labeguere, E. Rondet, C. Peixoto, J. Grassot, O. Picolet, D. Annot, N. Triballeau, A. Monjardet, E. Wakselman, V. Roncoroni, S. Le Tallec, R. Blanque, C. Cottreaux, N. Vandervoort, T. Christophe, P. Mollat, M. Lamers, M. Auberval, B. Hrvacic, J. Ralic, L. Oste, E. van der Aar, R. Brys, B. Heckmann, *J. Med. Chem.*, **2017**, 60, 3580..
- [68] B. Blanque, R. D. N.; Dupont, S.; Cottreaux, C.; Marsais, F.; Lepescheux, L.; Monjardet, A.; Wakselman, E.; Laenen, W.; Russell, V.; van der Aar, E.; Brys, R.; Heckmann, http://files.glp.com/docs/website_1/Poster_ERS_2015_final.pdf
- [69] <http://hugin.info/133350/R/2183965/843660.pdf>
- [70] J. M. Clark, F. Salgado-Polo, S. J. F. Macdonald, T. N. Barrett, A. Perrakis, C. Jamieson, *J. Med. Chem.*, **2022**, 65, 6338.
- [71] H. Zhang, X. Xu, J. Gajewiak, R. Tsukahara, Y. Fujiwara, J. Liu, J. I. Fells, D. Perygin, A. L. Parrill, G. Tigyi, G. D. Prestwich, *Cancer Res.*, **2009**, 69, 5441.

- [72] R. Gupte, R. Patil, J. Liu, Y. Wang, S. C. Lee, Y. Fujiwara, J. Fells, A. L. Bolen, K. Emmons-Thompson, C. R. Yates, A. Siddam, N. Panupinthu, T. C. T. Pham, D. L. Baker, A. L. Parrill, G. B. Mills, G. Tigyi, D. D. Miller, *ChemMedChem*, **2011**, 6, 922.



Chapter A6

A novel type IV autotaxin inhibitor ameliorates acute liver injury and nonalcoholic steatohepatitis

Richell Booijink,^{1,2} Fernando Salgado-Polo,² Craig Jamieson,³ Anastassis Perrakis,^{2,*†} and Ruchi Bansal^{1,*†}

Affiliations:

¹ Translational Liver Research, Department of Medical Cell BioPhysics, Faculty of Science and Technology, University of Twente, Enschede, The Netherlands.

² Division of Biochemistry, Netherlands Cancer Institute, Amsterdam, and Oncode Institute, The Netherlands.

³ Department of Pure and Applied Chemistry, University of Strathclyde, Glasgow, United Kingdom.

† These authors contributed equally to this work.

* Correspondence: a.perrakis@nki.nl; r.bansal@utwente.nl.

Based on:

EMBO Medicinal Chemistry. 2022, 14(9): e16333.

Abstract

The lysophosphatidic acid (LPA) signaling axis is an important but rather underexplored pathway in liver disease. LPA is predominantly produced by Autotaxin (ATX) that has gained significant attention with an impressive number of ATX inhibitors (type I-IV) reported. Here, we evaluated the therapeutic potential of a (yet unexplored) type IV inhibitor, Cpd17, in liver injury. We first confirmed the involvement of the ATX-LPA signaling axis in human and murine diseased livers. Then, we evaluated the effects of Cpd17, in comparison with the classic type I inhibitor PF8380, *in vitro*, where Cpd17 showed higher efficacy. Thereafter, we characterized the mechanism-of-action of both inhibitors and found that Cpd17 was more potent in inhibiting RhoA-mediated cytoskeletal remodeling, and phosphorylation of MAPK/ERK and AKT/PKB. Finally, the therapeutic potential of Cpd17 was investigated in CCl₄-induced acute liver injury and diet-induced nonalcoholic steatohepatitis, demonstrating an excellent potential of Cpd17 in reducing liver injury in both disease models *in vivo*. We conclude that ATX inhibition, by type IV inhibitor in particular, has an excellent potential for clinical application in liver diseases.

Introduction

Liver diseases are an immense burden on today's modern society. Globally, millions of people suffer from liver diseases, causing approximately 2 million deaths per year^[1]. Among several etiological liver diseases, non-alcoholic fatty liver disease (NAFLD) and its severe and advanced form, non-alcoholic steatohepatitis (NASH) have been recognized as a major public health problem in Western countries^[2, 3].

Liver injury caused by different factors such as excessive fat and/or alcohol intake, hepatitis B/C viral infections and drug overdose, triggers hepatocyte injury and necrosis. This injury is accompanied by endoplasmic reticulum stress, inflammation through reactive oxygen species, and release of several pro-inflammatory cytokines and chemokines^[4]. Ongoing inflammation induces the release of pro-fibrogenic mediators, mainly by resident and infiltrating macrophages^[5], causing quiescent hepatic stellate cells (HSCs) to transdifferentiate into highly proliferative and activated HSCs (or myofibroblasts). These activated HSCs initiate a wound-healing response that is characterized by the accumulation of an excessive extracellular matrix (ECM) at the injured site. Upon persistent or chronic liver injury, chronic inflammation and ECM accumulation lead to liver fibrosis (scarring), cirrhosis (end-stage liver dysfunction)^[4, 6], and/or hepatocellular carcinoma (primary liver cancer)^[7].

Among several pathways that have been associated with liver diseases is the lysophosphatidic acid (LPA) signaling axis^[8]. Besides liver diseases, the LPA signaling pathway is also involved in numerous pathological conditions including chronic inflammatory disorders, fibrotic diseases and tumor progression^[9, 10]. It also plays a role in a plethora of biological processes including neurogenesis, vascular homeostasis, skeletal development and remodeling, and lymphocyte homing^[11-14].

LPAs are physiologically occurring, structurally simple water-soluble glycerol lysophospholipids that differ in length, and the number of saturated and unsaturated bonds of their alkyl chain. Their activity is exerted via the activation of downstream signaling pathways through six G-protein coupled receptors (GPCRs) specific for LPA. To date, six LPA receptors have been identified (LPA₁-LPA₆)^[15], that couple with different Gα subunits upon activation. More specifically, LPA receptor activation can occur through Gα(i/o) and Gα(12/13) driven cascades via phosphatidylinositol 3-kinase (PI3K) and RhoA respectively, resulting in cell survival and cytoskeletal remodeling respectively.

The majority of LPA in the blood is synthesized from lysophosphatidylcholine (LPC) through hydrolysis of its choline moiety by Autotaxin (ATX) or Ectonucleotide pyrophosphatase phosphodiesterase type II (ENPP2), a multi-functional and multi-domain protein that

possesses enzymatic lysophospholipase D (lysoPLD) activity^[16, 17]. Structurally, ATX has a catalytic phosphodiesterase (PDE) domain, which accommodates a tripartite binding site: a hydrophilic shallow groove adjacent to the catalytic site that harbors the glycerol moiety of the lysolipid substrate; a hydrophobic pocket that binds the acyl chain; and a tunnel leading to the other side of the PDE domain^[17]. Given the emerging association with diseases, ATX has gained enormous pharmacological and pharmacochemical attention, and an impressive number of ATX inhibitors has been reported^[18]. The only inhibitor to reach phase 3 clinical trial (for idiopathic pulmonary fibrosis) has been the GLPG1690 molecule^[19], a so-called type IV inhibitor. Type IV inhibitors occupy the tunnel and the pocket of ATX, in contrast with type I inhibitors e.g. PF8380, which targets the catalytic site and the pocket.

Elevated ATX levels were observed in patients with different etiological liver diseases that correlated with disease severity including non-alcoholic fatty liver disease (NAFLD)^[20-25]. Moreover, hepatocyte-specific genetic deletion of ATX resulted in abrogated liver damage, inflammation and diminished fibrosis, and deregulated fatty acid metabolism thereby attenuating HCC development suggesting ATX as an attractive drug candidate in liver fibrosis and cancer^[26]. ATX pharmacological inhibition in liver disease has been evaluated in only a few pre-clinical studies, with varying outcomes. The type I inhibitor PF8380, was found to reduce fibrosis, but not inflammation and necrosis, in a CCl₄-induced liver fibrosis mouse model^[26]. An ATX type III inhibitor, PAT-505, showed significant reduction of fibrosis score in two NASH mouse models, but no significant effect on inflammation, ballooning or steatosis^[27]. The ATX inhibitor EX_31, a tetrahydrocarboline derivative with unclear binding mode did not show any effect on liver-related markers in a liver cirrhosis and NASH rat model^[28].

We have previously hypothesized that the mechanistic differences between type I and type IV inhibitors, rather than inhibitor potency in preventing the enzymatic hydrolysis of LPC to LPA alone, can lead to different physiological activity^[18]. Here, we set out to examine the effect of type I and type IV inhibitors in liver disease models, as, despite the clear involvement of the ATX/LPA signaling pathway in liver diseases, inhibition of ATX has been underexplored in relevant liver disease models. We started by comparing the effects of our previously designed type IV Cpd17 inhibitor^[29], with the classic type I inhibitor PF8380 *in vitro*, which both have similar potency to inhibit LPC 18:0 to LPA conversion *in vitro* (IC₅₀ 20 nM and 2.8 nM, respectively). Our results examining the ability of the two inhibitors to inhibit downstream LPA signaling pathways *in situ* confirmed our hypothesis that Cpd17 has a better activity in cells. We were thus encouraged to examine Cpd17 in CCl₄-induced acute liver injury, and methionine- and choline-deficient (MCD) diet-induced NASH mouse models.

Results

Upregulation of Autotaxin in non-alcoholic steatohepatitis and liver fibrosis

Upregulation of ATX in chronic liver diseases, including NASH and liver cirrhosis, has been previously observed in animal models, as well as in human patients^[22, 26]. To confirm these findings, ATX (ENPP2) gene expression has been analyzed in human and mice livers. Analysis of mRNA expression levels revealed significantly elevated ENPP2/ATX expression in human NASH patients, compared to control healthy livers (**Figure 1A**). Similar upregulation of ATX gene expression was also observed in patients with liver cirrhosis (**Figure 1A**). Consistent with human data, ATX gene expression in mouse livers was upregulated in the MCD diet-induced NASH mouse model as well as in our CCl₄-induced liver fibrosis mouse model (**Figure 1B**).

We further examined the protein expression of ATX in human and mouse livers by immunostaining. Hereby, we also found an increase in ATX protein expression in human NASH and cirrhotic livers compared to normal livers (**Figure 1C**). As expected, this was confirmed in both MCD-induced NASH and CCl₄-induced cirrhosis mouse models compared to respective healthy controls (**Figure 1D**).

ATX inhibition in hepatocytes and LPS/IFN γ -activated pro-inflammatory macrophages

To inhibit the function of ATX, and thus the production of LPA and the related downstream signaling, we focused on the well-characterised type I inhibitor PF8380 (**Figure 2A**) and our type IV inhibitor Cpd17 (**Figure 2B**). These two inhibitors have similar potency in inhibiting the catalysis of LPC to LPA (IC₅₀ 2.8 nM and 20 nM respectively) but distinct binding modes on the ATX tripartite binding site. Their effect on LPC species that we have tested (**Supplemental Figure S1**) is similar, but shows interesting differences with Cpd17 being less potent in ameliorating hydrolysis of longer alkyl chain LPC species (**Figure 2 and supplemental Figure S1**). We have thus decided to check both inhibitors in specific assays *in vitro* to evaluate their therapeutic potential.

Previous studies have shown that different hepatotoxic stimuli stimulate hepatocyte ATX expression, leading to activation of fibrogenic pathways. Furthermore, hepatocyte-specific ablation and/or transgenic overexpression of ATX suggested a role of ATX/LPA in liver cirrhosis and HCC. Moreover, since ATX has shown to be involved in fatty acid metabolism^[26], in this study, we investigated the implication of pharmacological ATX inhibition using two different ATX inhibitors in fatty acid-treated hepatocytes. We induced lipid accumulation in human hepatocytes, HepG2 cells, by exposing them to pathophysiologically relevant concentrations of palmitic acid to mimic excessive influx

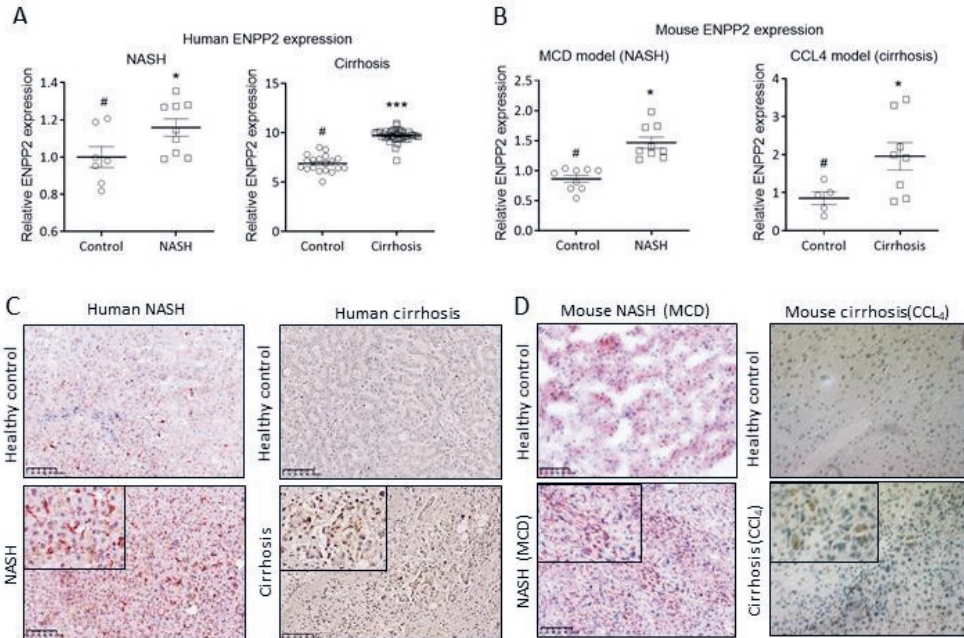


Figure 1: ATX (ENPP2) expression is upregulated in human and mouse livers. (A) ATX gene expression from publicly available datasets in NASH patients ($n=11$) compared to healthy controls ($n=9$); cirrhosis patients ($n=40$) compared to healthy controls ($n=19$). **(B)** Relative ATX gene expression in the MCD-diet-fed ($n=9$) compared to control mice ($n=9$); CCl_4 ($n=8$) compared to control mice ($n=5$). **(C)** Representative images (scale = 100 μm) of ATX stained liver sections from human NASH compared to healthy controls; human cirrhosis compared to healthy controls. **(D)** Representative images (scale = 100 μm) of ATX stained liver sections from MCD-died-fed NASH ($n=6$) and CCl_4 -induced liver fibrosis ($n=6$) mouse models compared to respective controls ($n=6$). Mean \pm SEM; two-tailed student's t -test; * $p<0.05$, *** $p<0.001$ denotes significance versus respective healthy controls.

of fatty acids into hepatocytes, and found that ATX inhibition by both Cpd17 and PF8380 reduced lipid accumulation in hepatocytes (**Figure 3A**).

Following hepatocellular damage, the inflammatory response plays a key role in the initiation and progression of liver fibrosis. Upon liver injury, infiltrating monocytes undergo differentiation into traditionally defined classically-activated (M1) macrophages, which mediate the initial inflammatory response, while alternatively-activated (M2) macrophages predominantly mediate the resolution phase^[32]. We thus investigated the effect of the PF8380 and Cpd17 in classically-activated mouse RAW macrophages. To investigate the effect of ATX inhibition on the migration of pro-inflammatory M1 (activated by IFN- γ and LPS) macrophages, we performed a scratch assay. 24h after making a scratch, LPS/IFN γ -activated pro-inflammatory macrophages showed a visibly

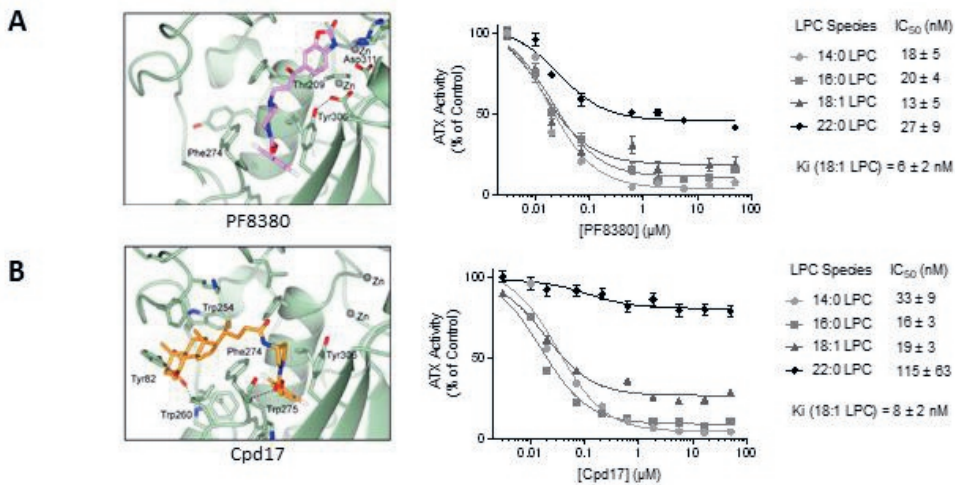


Figure 2: ATX inhibitors PF8380 and Cpd17 decrease LPA production. (A) Structural binding of PF8380 to ATX; Potency (IC₅₀) of PF8380 for inhibiting the catalysis of LPC to LPA. **(B)** Structural binding of type IV inhibitor Cpd17 to ATX; Potency (IC₅₀) of Cpd17 for inhibiting the catalysis of LPC to LPA.

significant increase in migration, compared to unpolarized (M0) macrophages (**Figure 3B-C**). Inhibition of ATX by PF8380 showed some decrease in macrophage migration; however, Cpd17 significantly reduced the percentage of cell migration compared to that of LPS/IFN γ -activated macrophages (**Figure 3B-C**). We further examined the efficacy of the inhibitors on the gene expression of inflammatory markers in both mouse and human macrophages. In mouse RAW macrophages, we observed that both PF8380 and Cpd17 significantly alleviated the LPS/IFN γ -induced expression of C-C chemokine 2 (CCL2), also known as monocyte chemoattractant protein 1 (MCP1), one of the key chemokines that regulate migration and infiltration of monocytes/macrophages. Moreover, Cpd17, but not PF8380, also alleviated the expression of other inflammatory markers i.e. inducible nitric oxide synthase (iNOS), tumor necrosis factor alpha (TNF- α) and Interleukin (IL)-1 β (**Figure 3D**). Similarly, in human THP1 macrophages, M1 activation through LPS and IFN γ led to an increase in gene expression of inflammatory markers CCL2, iNOS and IL-6. After 24h of treatment with both inhibitors, gene expression levels were significantly decreased (**Figure 3E**).

These results show that inhibition of ATX decreases lipid accumulation in hepatocytes, and attenuates LPS/IFN γ -induced pro-inflammatory macrophage activation and migration, both in murine as well as human cells. These results confirm the importance of the LPA/ATX pathway in liver inflammation. Furthermore, the results suggest that Cpd17 is somewhat more efficient than PF8380 in ameliorating induced steatotic and inflammatory phenotype.

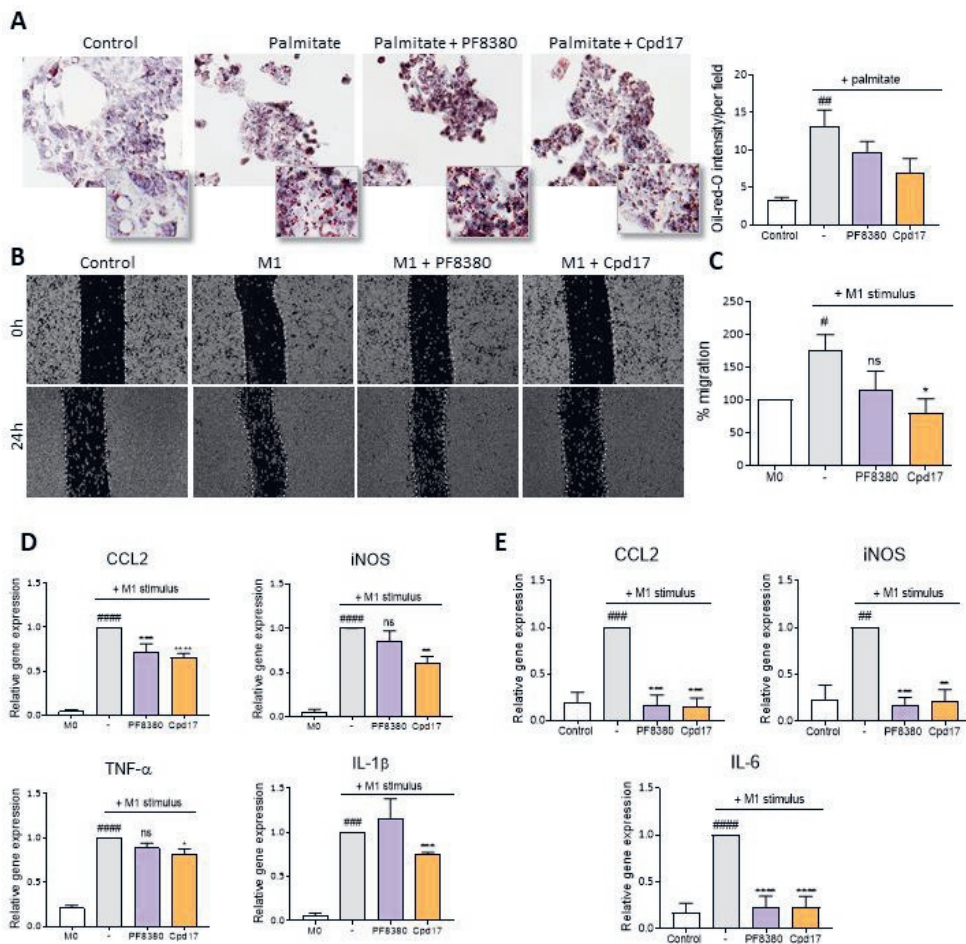


Figure 3: ATX inhibitors decrease steatosis in hepatocytes and pro-inflammatory expression and migration in LPS stimulated macrophages. (A) Representative images and quantification of HepG2 cells stained with oil-red-O after 48 hours treatment with or without 200 μ M palmitate with or without PF8380 or Cpd17. (B) Representative images (at 0h and 24h) and (C) quantitative analysis (after 24h) of migration by control (M0) and LPS-induced M1 RAW 264.7 macrophages treated with medium alone, PF8380 (1 μ M) or Cpd17 (1 μ M). (D) Relative gene expression (normalized with GAPDH) for CCL2, iNOS, TNF- α and IL-1 β in control (M0) and LPS- and IFN γ - induced M1 RAW 264.7 macrophages treated with medium alone, PF8380 (1 μ M) or Cpd17 (1 μ M). (E) Relative gene expression (normalized with 18S RNA) for CCL2, iNOS and IL-6 control (M0) and LPS-induced PMA-treated human THP1 macrophages treated with medium alone, PF8380 (1 μ M) or Cpd17 (1 μ M). Mean \pm SEM; one-way ANOVA with Bonferroni post-hoc test; [#] $p < 0.05$ denotes significance versus control (non-stimulated cells); ^{*} $p < 0.05$, ^{**} $p < 0.01$, ^{***} $p < 0.001$ denotes significance versus (palmitate or M1) stimulated cells; ns=not significant.

Inhibition of ATX in TGF β -activated HSCs

The elevated ATX gene expression in patients could be recapitulated upon the activation of fibrogenesis *in vitro* in HSCs. This observation strengthened the previously reported association between ATX expression and the development of liver fibrosis, and offered an attractive system for *in vitro* studies. We therefore next investigated the effect of PF8380 and Cpd17 in TGF β -activated LX2 cells (immortalized human HSCs). Upon TGF β activation, immunostainings revealed an increase in fibrosis-related proteins, collagen I (the major ECM protein) and α -SMA (a HSCs activation marker) (**Figure 4A**); addition of PF8380 or Cpd17 visibly decreased the protein levels (**Figure 4A**). Correspondingly, gene expression levels of collagen I, α -SMA and platelet-derived growth factor beta receptor (PDGFR β , involved in HSC proliferation and survival), increased significantly upon TGF β activation, showed some (non-significant) decrease after PF8380 treatment, but significant reduction after Cpd17 treatment (**Figure 4B**). During fibrogenesis, increase in liver stiffness and excessive ECM accumulation is mediated by HSCs differentiation into myofibroblasts as well as HSCs migration to the injured site^[33]. The migratory potential of activated HSCs was evaluated by a scratch assay. As observed previously, Cpd17 significantly reduced the wound healing response (**Figure 4C-D**), indicating a reduction in the migratory properties of the LX2 cells. Finally, we studied the effect of the two ATX inhibitors on the contractile properties of the LX2 cells using a 3D-collagen I contraction assay. Results showed that both PF8380 and Cpd17 significantly reduced TGF β -induced collagen I contraction of LX2 cells after 24h of treatment (**Figure 4E-F**); consistent with other results the effect was more pronounced with Cpd17 treatment.

Overall, these results further solidify the significant role of the LPA/ATX pathway in TGF β -induced activation, migration and contractility of human HSCs, and confirm that the ATX type IV inhibitor Cpd17 is more efficient in reducing the fibrotic effects caused by HSC activation.

PF8380 and Cpd17 differentially inhibit downstream signaling in LX2 cells and RAW macrophages

To investigate the mechanism by which PF8380 and Cpd17 affect inflammatory and fibrotic responses, we sought to dissect their downstream signaling effects in macrophages and HSCs respectively. A short overview of LPA-induced signaling pathways is depicted in **Figure 5A**. As all downstream signaling depends on the levels of ATX and the LPA₁₋₆ receptors, we first evaluated their gene expression levels in TGF β activated LX2 cells and in LPS/IFN γ -activated pro-inflammatory M1 macrophages (**Supplemental Figure S2**). We observed that all the LPA receptors (except LPA₄), as well as ENPP2, were upregulated in TGF β -activated LX2 cells; and all LPA receptors (except LPA₂ and LPA₅), and ENPP2 were significantly increased in LPS/IFN γ -induced pro-inflammatory M1 macrophages, consistent with existing literature^[26, 34-36] (**Supplemental Figure S2**).

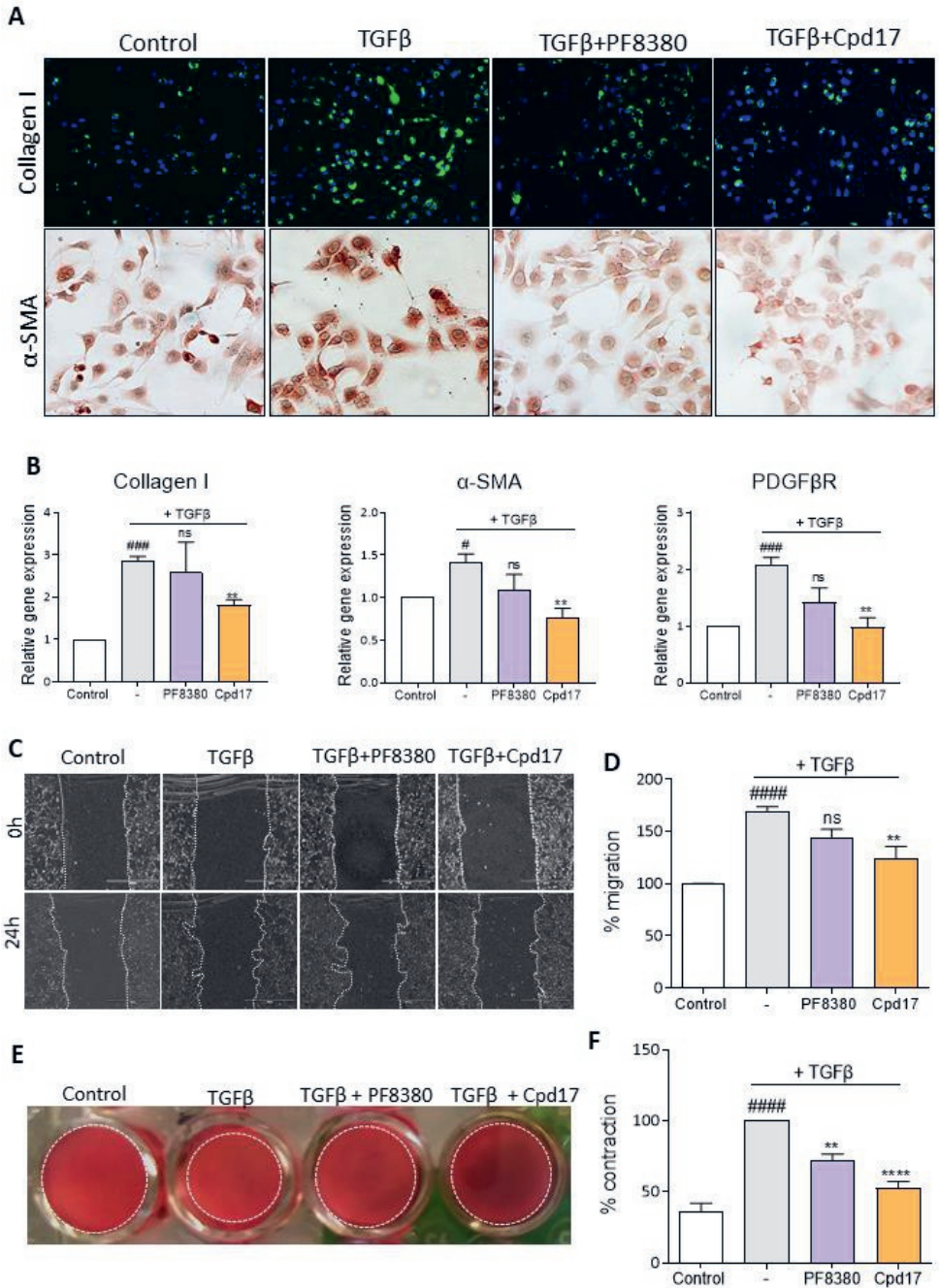


Figure 4: ATX inhibition decreases TGFβ-induced HSCs activation, migration and contraction. (A) Collagen I and α-SMA stained control and TGFβ-activated LX2 cells with or without PF8380 (1μM) or Cpd17 (1μM) (n=3). (B) Relative Collagen I, α-SMA and PDGFRβ gene expression (normalized with GAPDH) in control and TGFβ-activated LX2 cells with or without PF8380 (1μM) or Cpd17 (1μM) (n=3). (C)

Representative images (at 0h and 24h) and **(D)** quantitative analysis (after 24h) of migration by control and TGF β -activated LX2 cells with or without PF8380 (1 μ M) or Cpd17 (1 μ M) (n=3). **(E)** Representative images and **(F)** quantitative analysis showing 3D collagen gel contractility of control and TGF β -activated LX2 cells with or without PF8380 (1 μ M) or Cpd17 (1 μ M) (n=3). Mean \pm SEM; one-way ANOVA with Bonferroni post-hoc test; * p <0.05 denotes significance versus control (non-stimulated cells); * p <0.05, ** p <0.01, *** p <0.001 denotes significance versus (TGF β) stimulated cells.

We first monitored the G α (12/13)-mediated RhoA activation pathway that leads to cytoskeletal reorganization, as it relates to migration and contractility, which are hallmarks for mediating the fibrotic effect in HSCs. Consistently with the phenotypic observations, we observed that Cpd17, but not PF8380, strongly inhibited the ATX+LPC(LPA)-induced RhoA activation in LX2 cells (**Figure 5B**). We then checked the G α (i/o)-mediated phosphorylation of AKT and extracellular signal-regulated kinase (ERK). The maximal response in the amount of pAKT and pERK in LX2 cells is upon stimulation with ATX and the LPC substrate; this effect was ameliorated by both inhibitors in the case of pAKT accumulation, but only Cpd17 significantly suppressed pERK (**Figure 5C**). We then checked the alternative signaling pathway involving receptor internalization, by biotin labeling of surface proteins, immunoprecipitation, and visualization of the amount of LPAR1 in the cell surface (**Supplemental Figure S3A**). While treatment with ATX and LPC significantly decreased the amount of LPA₁ receptor in the cell surface, both inhibitors partially restored LPA₁ surface levels (**Figure 5D**). Finally, to confirm that the effects that we see are LPA-receptor dependent, we used the Ki16425 antagonist, mostly acting on LPA₁, and demonstrated that its application had effects similar to those of the ATX inhibitors, and particularly Cpd17, both in LX2 cells as well as in LPS/IFN γ -differentiated M1 macrophages (**Supplemental Figure S3B**).

These results demonstrate that ATX inhibition leads to signaling events on the downstream axis in cells that are relevant to the observed phenotypes. Crucially, the stronger effect of the Cpd17 inhibitor, specifically on RhoA activation, at least partially explains the consistent effect of the type IV inhibitor Cpd17 to ameliorate the effects in all our phenotypic assays. Our *in vitro* studies thus collectively suggested further analysis of the Cpd17 ATX inhibitor for therapeutic efficacy *in vivo*.

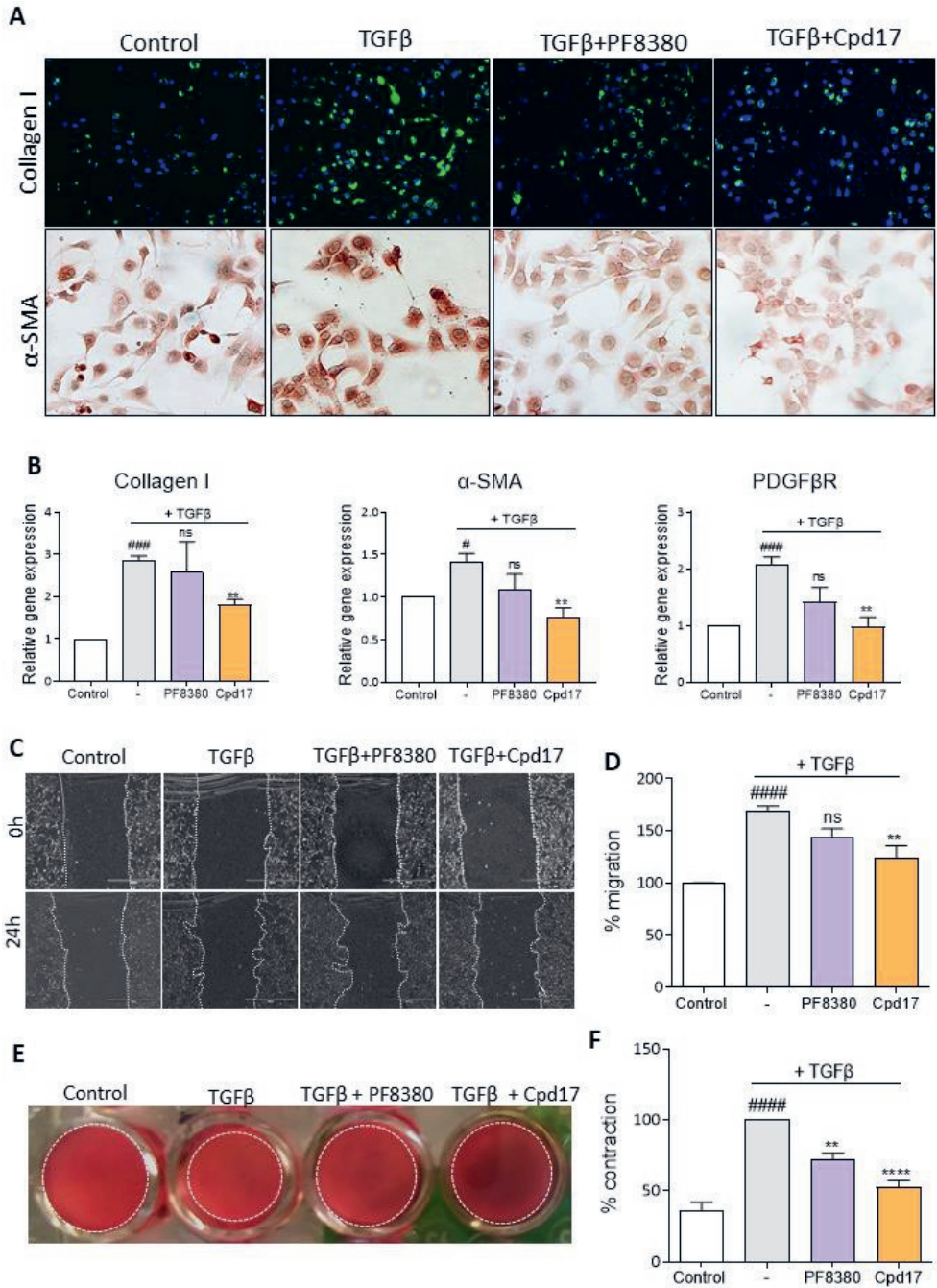


Figure 5: Inhibition of ATX results in blockade of LPAR-driven activation of stellate cells and macrophages. (A) Schematic overview of LPA-induced signaling pathways. (B) Top panel shows time-course stimulation to LPA and uninhibited or inhibited LPC-treated ATX followed by RhoA activation, measured as a YFP/CFP fluorescent ratio. Bottom panel depicts quantitation of the burst response

to the stimulants. **(C)** Representative images and quantification showing Western-blot analysis for p-Akt and p-ERK normalized with β -actin in control, LPC, LPA, ATX, ATX+LPC, ATX+LPC+PF8380, and ATX+LPC+Cpd17 stimulated LX2 cells. **(D)** Representative images and quantification showing Western-blot analysis for LPAR1 on the cell surface and in lysate, normalized with β -actin in lysate, in LPC, ATX+LPC, ATX+LPC+PF8380, and ATX+LPC+Cpd17 stimulated LX2 cells. Mean \pm SEM; one-way ANOVA with Bonferroni post-hoc test; * $p < 0.05$ denotes significance versus control (non-stimulated cells); * $p < 0.05$, *** $p < 0.001$ denotes significance versus ATX+LPC treated cells.

Cpd17 decreases acute liver damage in CCl₄-induced liver injury *in vivo*

The carbon tetrachloride (CCl₄)-induced liver injury mouse model was our first choice for analyzing the *in vivo* efficacy of Cpd17 (**Figure 6A**). While histological staining of the liver tissues showed an increase in inflammation, collagen I, and F4/80 protein expression in the CCl₄-induced mouse model, as expected, Cpd17 notably decreased all these markers upon treatment (**Figure 6B**). Interestingly, we found that liver weights (normalized to body weight) were significantly increased in diseased mice compared to healthy control mice. Liver weights of the Cpd17-treated mice were significantly lower compared to the diseased mice (**Figure 6C**). Additionally, serum transaminase ALT levels of mice treated with Cpd17 were also significantly reduced, compared to CCl₄-treated mice (**Figure 6D**). Altogether, these results suggest that inhibition of ATX by Cpd17 treatment leads to reduced liver inflammation and fibrogenesis in a CCl₄-induced liver injury mouse model.

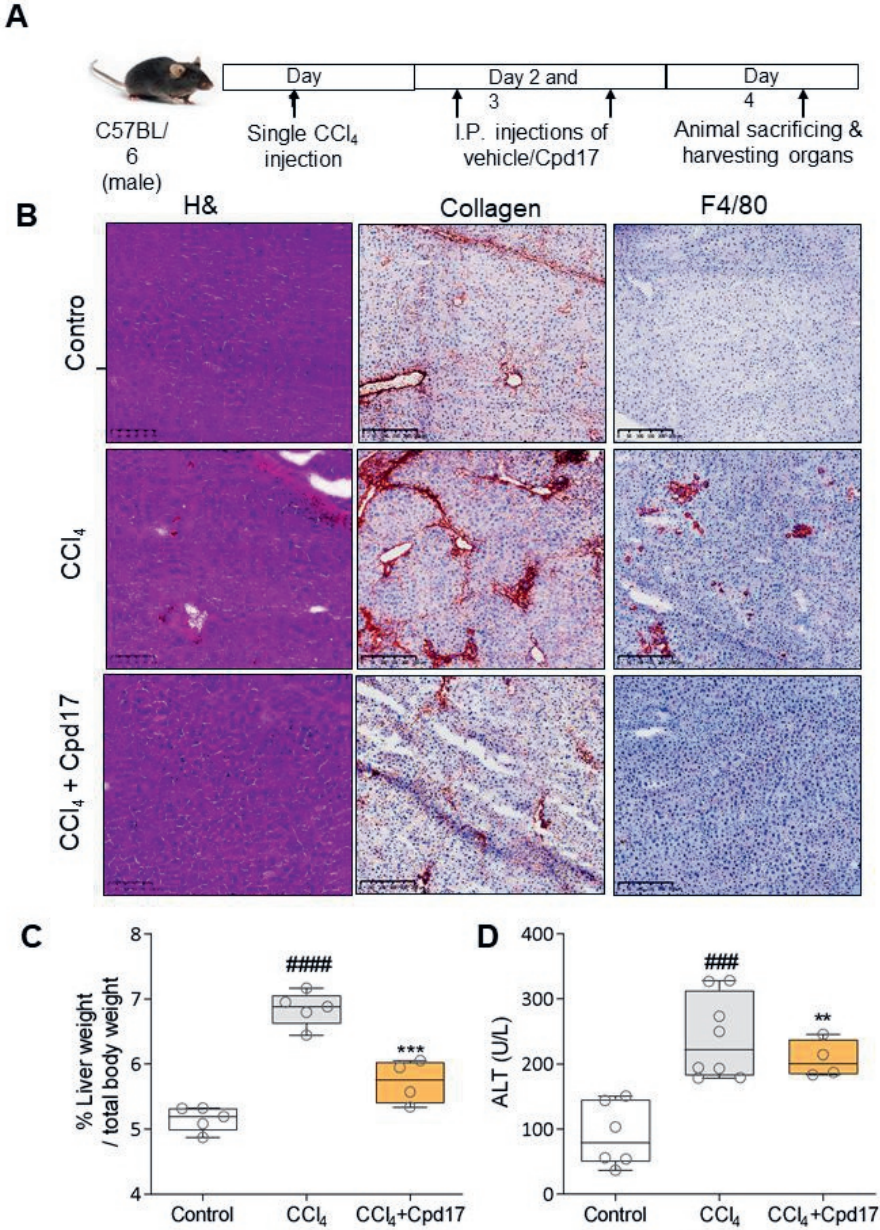


Figure 6: Cpd17 ameliorated CCl₄ induced acute liver injury. (A) Schematic showing CCl₄-mediated liver disease induction and Cpd17 treatment regimen. **(B)** Representative images (scale=100µm) of control (n=4), CCl₄ (n=4) and CCl₄+Cpd17 (n=4) liver sections stained with H&E, collagen-I and F4/80. **(C)** Liver weight to total body weight ratio. **(D)** Serum ALT levels. Mean ± SEM; one-way ANOVA with Bonferroni post-hoc test; *p<0.05 denotes significance versus controls; **p<0.01, ***p<0.001, ****p<0.0001 denotes significance versus CCl₄ mice.

Cpd17 ameliorates liver fibrogenesis and inflammation in methionine choline-deficient (MCD)-diet-induced NASH mouse model

Finally, we investigated the therapeutic efficacy of Cpd17 *in vivo* in a methionine- and choline-deficient (MCD)-diet induced NASH mouse model (**Figure 7A**). Morphological examination of the liver tissues directly after sacrificing, showed a distinctly visible pale and gross appearance suggesting hepatocellular damage in MCD-diet induced NASH mice as compared to the healthy control group; treatment with Cpd17 improved this appearance considerably (**Figure 7B**). Furthermore, we found that treatment with ATX inhibitor Cpd17 ameliorated hepatic inflammation and steatosis, as examined by H&E and Oil-red-O staining respectively (**Figure 7C-D**). Additionally, the MCD-diet resulted in increased intrahepatic protein expression of F4/80 (macrophage marker) and collagen I, compared to controls, as examined by immunostaining (**Figure 7E-F**). Strikingly, *in vivo* treatment with our ATX inhibitor led to a significantly decreased protein expression of both collagen I and F4/80, as shown in the microscopic images and quantitative staining analysis.

Serum plasma transaminases AST and ALT, indicators of liver damage, were significantly reduced in mice treated with Cpd17 compared to MCD-diet induced NASH mice, to near physiological values, further suggesting Cpd17 significantly improved liver function (**Figure 8A-B**). Moreover, collagen content in the livers, evaluated through hydroxyproline assay, further confirmed an increased total collagen I concentration in MCD- livers, which was decreased in Cpd17 treated mice (**Figure 8C**).

Total plasma cholesterol and triglyceride levels, indicators for liver steatosis (or NAFLD), increased significantly upon MCD diet-induced NASH. Interestingly, treatment with Cpd17 led to a significant decrease in both cholesterol and triglyceride serum levels (**Figure 8D-E**). Additionally, quantitative PCR revealed a decrease upon Cpd17 treatment in inflammatory markers F4/80, CCL2 and intracellular cell adhesion molecule (iCAM1), HSC specific marker α -SMA and liver steatosis marker CCAAT-enhancer-binding proteins (C/EBP)[37] (**Supplemental Figure S4**).

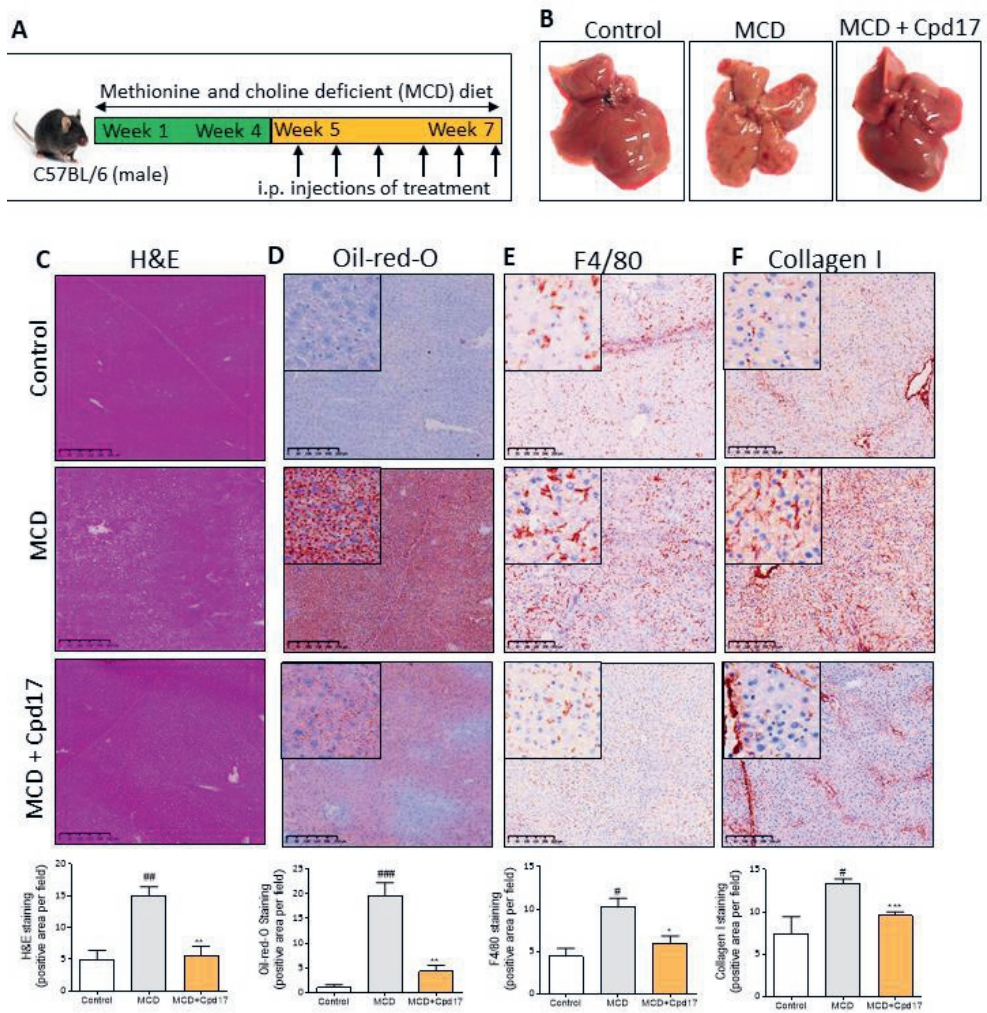


Figure 7: Cpd17 attenuated steatosis, inflammation and fibrosis in MCD-diet induced NASH mice. (A) Schematic showing NASH induction and Cpd17 treatment regimen. (B) Representative macroscopic images of livers from control (n=6), MCD (n=6) and MCD+Cpd17 (n=5). (C-F) Representative images (scale=100µm) and quantitative analysis of liver sections stained with (C) H&E, (D) oil-red-O, (E) F4/80 and (F) Collagen I. Mean + SEM; one-way ANOVA with Bonferroni post-hoc test; #p<0.05 denotes significance versus controls; *p<0.05, **p<0.01, ***p<0.001 denotes significance versus MCD mice.

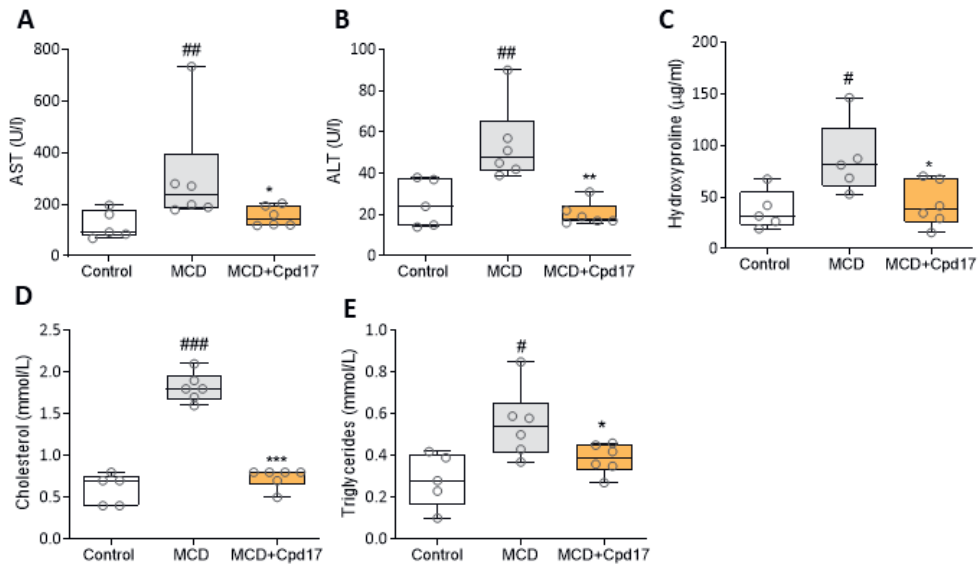


Figure 8: ATX inhibition improved general liver disease levels in MCD-diet induced NASH mice. (A-B) Serum AST and ALT, (C) liver hydroxyproline, (D) serum cholesterol and (E) serum triglyceride levels in control (n=6), MCD (n=6) and MCD+Cpd17 (n=5) mice. Mean ± SEM; one-way ANOVA with Bonferroni post-hoc test; #p<0.05 denotes significance versus controls; *p<0.05, **p<0.01, ***p<0.001 denotes significance versus MCD mice.

Discussion

The ATX/LPA signaling axis has previously been involved with the initiation and progression of liver diseases^[20-25]. Here, we show significant upregulation of ATX gene and protein expression in human liver NASH and cirrhosis patients, which we recapitulated in CCl₄-induced liver injury and MCD diet-induced NASH mouse models.

Having confirmed and strengthened the connection between ATX and liver disease, we showed that two different ATX inhibitors, PF8380 and Cpd17 have an effect in a variety of *in vitro* assays in hepatocytes, pro-inflammatory macrophages and activated HSCs. The inhibitors ameliorated the effect of different external stimuli that lead to the induction of fibrotic and inflammatory markers. We found that ATX inhibition attenuated TGFβ-induced expression of fibrotic markers in human HSCs, and LPS/IFNγ-stimulated expression of inflammatory markers in both mouse and human macrophages. We also showed a decrease in collagen I contraction of HSCs upon ATX inhibition, a measure of functional cellular activation^[38], and decreased migration of activated HSCs and macrophages. Further, examining the effect of these inhibitors on ATX/LPA-related downstream signaling in the same cells showed that they notably affected the RhoA pathway, which relates to

cytoskeletal organization and thus to fibrotic phenotypes. We also showed broader effects through the MAPK/ERK and AKT/PKB pathways, and that these signals go through LPA receptors. We thus establish that the mechanisms underlying the ATX inhibition have an effect on downstream signaling processes that influence inflammation and fibrogenesis.

The cell-based assays clearly showed that Cpd17 has a notably better potential in ameliorating fibrotic phenotypes and downstream signaling responses, compared to PF8380, which had already shown effectiveness in attenuating CCl₄-induced liver cirrhosis^[26]. PF8380 is a so-called type I inhibitor of ATX, which affects LPC hydrolysis to the signaling LPA molecule. However, the type I inhibitor PF8380 does not occupy the allosteric tunnel of ATX that leads to activity modulation^[39] and has been suggested to be implicated in presenting LPA to its cognate GPCRs^[40]. In contrast, Cpd17^[29] is a type IV inhibitor that prevents substrate binding and also occupies the ATX tunnel. Cpd17 is structurally (but not chemically) related to GLPG1690^[18], which has shown promise in treating IPF^[41].

Based on our *in vitro* results, we further evaluated ATX inhibition by Cpd17 *in vivo* in acute liver injury and NASH mouse models. We used the CCl₄-induced liver fibrosis model and the MCD-induced NASH mouse model, which showed characteristic lipid accumulation in hepatocytes, accompanied by intra-hepatic inflammation and fibrosis, as reported previously^[42]. Cpd17 has an effect both on MCD diet-induced hepatic steatosis, and in the CCl₄-induced liver injury model. These results are in accordance with the previous study in which adipose-specific ATX deficiency exhibited reduced lipid accumulation and hepatic steatosis associated with high-fat diet, while ATX overexpression was found to aggravate steatosis^[43]. Interestingly, previous studies with the potent Ex_31 inhibitor had no effect on CCl₄-induced liver fibrosis and choline-deficient amino acid-defined diet-induced liver injury^[28]. PAT-505, another ATX inhibitor, showed reduced fibrosis development in a high-fat diet-induced NASH mouse model with no significant effect on steatosis, inflammation or hepatocyte ballooning^[27]. Moreover, inhibition by PF8380 in CCl₄-induced liver disease models has shown to reduce plasma ATX activity and liver LPA levels by approximately 50%, and attenuate fibrosis based on histopathological scoring and collagen deposition in the liver^[26]. Based on our results, ATX inhibition by Cpd17 showed protection against CCl₄-induced acute liver injury, and decreased steatosis, inflammation and fibrosis in the NASH mouse model.

The excellent *in vitro* and *in vivo* efficacy of Cpd17 in liver disease models, together with GLPG1690 efficacy in treating IPF, argue that Type IV compounds are very promising agents in treating fibrotic diseases and possibly other pathologies related to the LPA/ATX axis. It must be noted, though, that the phase III Isabella trial for GLPG1690 was terminated due to adverse effects. Detailed results from the Isabella trial have not been

published to this moment and it is thus hard to speculate why it failed. If that was due to the off-target effects of the specific compound, this suggests a need to test alternative chemical scaffolds like Cpd17. In any case, our study not only validates ATX as an important therapeutic target in liver disease, but also suggests that specifically type IV compounds, such as Cpd17, GPLG1690, or structurally related inhibitors, are a valid strategy for clinical application. Should ATX inhibition prove to have toxic off-target effects, we believe that it is still important to suggest alternative strategies for inhibiting the LPA/ATX axis by e.g. targeting LPA receptors in hepatic stellate cells or macrophages. Finally, our results also suggest it worth exploring the role of the ATX/LPA axis and the effect of its inhibition in models of liver cancer, with potential therapeutic opportunities for HCC.

Conclusions

Based on the results in this study, we have clearly demonstrated the role of the ATX-LPA axis in NASH and liver cirrhosis. We have also shown that inhibition of ATX, using Cpd17, ameliorates fibrosis, inflammation and steatosis *in vitro* in HSCs and macrophages *in vitro*, as well as in NASH and liver cirrhosis mouse models. To the best of our knowledge, this is the first comprehensive study exploring the role and mechanism of a type IV ATX inhibitor in NASH and liver cirrhosis. ATX thus goes on to be stronger established as a potential therapeutic target in non-alcoholic steatohepatitis and liver cirrhosis.

Experimental procedures

Analysis of the ATX signaling mechanism in (liver) cells. AKT and ERK phosphorylation was performed by Western-blotting using the primary antibodies phospho-Akt (Ser473); phospho-ERK1/2 (Thr202/Tyr204), from Cell Signaling Technology. Rho GTPase measurements were conducted using a FRET pair consisting of RhoA-Cerulean3 and protein kinase N (PKN) fused to circularly permuted Venus^[30]. FRET is expressed as the ratio between acceptor and donor signals, set to 1 at the onset of the experiment. To assess the internalization of the LPA₁-HA receptor, we used surface biotin labeling. Detailed protocols are available as Supplemental Information (SI).

Effect of ATX inhibitors *in vitro*. Human hepatocytes (HepG2) were incubated with palmitate (0.2 mM) in complete culture medium and treated with no inhibitor (medium alone), PF8380 (Sigma) or Cpd17 ([29]) at 1 μ M for 24h. Cells were then fixed and stained using an Oil-red-O staining kit (Sigma). Mouse RAW macrophages and PMA-treated human THP1 macrophages were incubated with cell medium alone or M1 stimulus (100ng/mL LPS and 10ng/mL IFN γ), with or without 1 μ M of PF8380 or Cpd17 for 24h, and used for

qPCR and/or wound healing analysis. Human hepatic stellate cells (LX2 cells) were starved overnight with serum-free medium, and then treated with medium alone or 5ng/ml recombinant human TGF β with or without 1 μ M PF8380 or Cpd17 for 24h, and used for wound healing and qPCR analysis, or fixed with acetone:methanol (1:1), dried and stained for collagen-I and α -SMA. The 3D-collagen I contraction assay was performed as described earlier^[31]. Detailed protocols and cell lines are described as SI.

Animal Experiments. All the animal experiments performed in this study were in accordance with the guidelines and regulations for the Care and Use of Laboratory Animals, Utrecht University, The Netherlands. The protocols were approved by the Institutional Animal Ethics Committee of the University of Twente, The Netherlands. 6- to 8-week old male C57BL/6NRj mice purchased from Janvier Inc. Labs (Le Genest, France), were housed in standard SPF conditions in a Tecniplast IVC system (cage type 2L, blue line). For the carbon tetrachloride (CCl₄)-induced acute liver injury model, male C57BL/6NRj mice were treated with a single intraperitoneal injection of olive oil or CCl₄ (0.5ml/kg in olive oil) at day 1. At day 2 and day 3, CCl₄-treated mice received intraperitoneal administration of 5mg/kg Cpd17 or vehicle treatment (n=5 per group). On day 4, all mice were sacrificed, blood and livers were collected for subsequent analysis. For the methionine and choline deficient (MCD) diet-induced NASH model, C57BL/6NRj mice were fed with a standard chow or MCD diet for 7 weeks. Starting at week 5, the mice received intraperitoneal administrations of 5mg/kg Cpd17 or vehicle treatment 2 times per week, for a duration of 3 weeks, n=6 per group. All mice were sacrificed 24h after the last treatment, blood and livers were collected for further analysis. Alanine aminotransferase (ALT), aspartate aminotransferase (AST), total plasma cholesterol levels and plasma triglycerides levels were measured by standard automated laboratory methods.

Histological procedures included immunohistochemistry, immunofluorescence, Oil-Red-O staining, hematoxylin and eosin staining. For quantitative histological analysis, high resolution scans were made using NanoZoomer Digital Pathology (NDP2.0) viewer software (Hamamatsu Photonics) and analyzed using ImageJ. Detailed protocols are available as SI. Total liver hydroxyproline concentrations were determined using a hydroxyproline assay (Sigma) as per manufacturer's instructions.

Gene expression. For gene expression analysis in cells or liver tissues, standard protocols were used as detailed in SI. For ATX (ENPP2) analysis in human tissues, the transcriptomic datasets of liver tissue from patients with liver cirrhosis (GSE14323), and non-alcoholic steatohepatitis (GSE63067), from the National Center of Biotechnology Information Gene Expression Omnibus database (NCBI-GEO, <https://www.ncbi.nlm.nih.gov/geo/>) were analyzed using GEO2R.

Statistical analyses. All data is presented as the mean \pm standard error of the mean (SEM). The graphs and statistical analyses were performed using Graphpad Prism version 9.1.2 (Graphpad Prism Software, Inc., La Jolla, CA, USA). Comparisons with control groups were analyzed using unpaired students' t-test and/or multiple comparisons between different groups were performed by one-way analysis of variance (ANOVA) with Bonferroni post-hoc test. The differences were considered significant at $p < 0.05$.

Additional Procedures. Additional details on methods are presented in the online version.

Supplemental Information

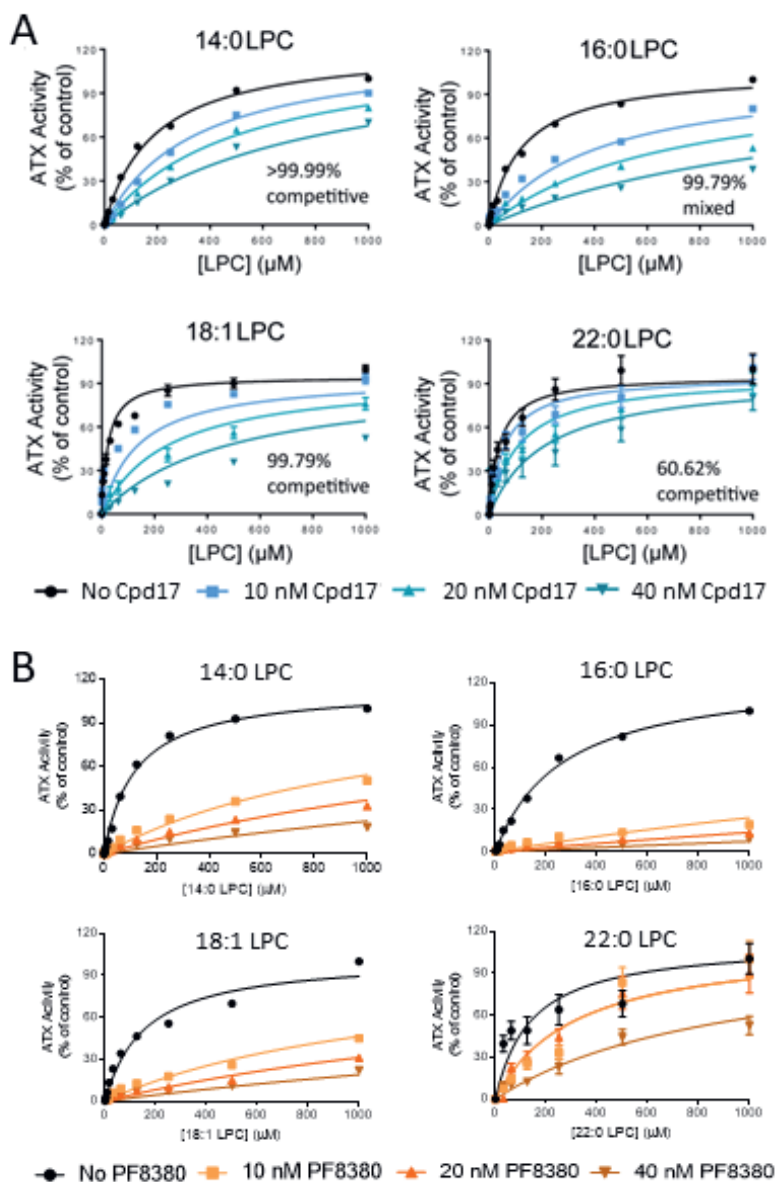


Figure S1: Cpd17 and PF8380 inhibit ATX activity over different LPC species. (A) Cpd17 and (B) PF8380 was incubated with 20 nM ATX for at least 30 min, upon which mixes were added to plates containing LPC, and reaction kinetics were followed over time. Activity slopes were quantitated by linear regression and plotted versus LPC concentration. Data represent the mean \pm SD of three different experiments. Quantitation of the type of inhibition was performed by comparison of non-linear regressions to competitive and non-competitive modes of inhibition.

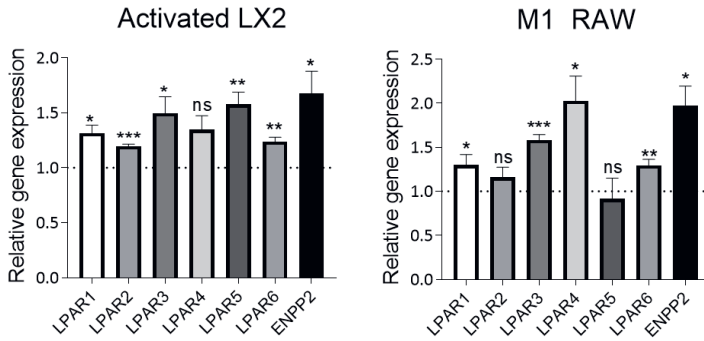


Figure S2: The ATX/LPA pathway is upregulated in activated LX2 cells and pro-inflammatory macrophages. Relative LPAR1-6 and ENPP2 gene expression (normalized with GAPDH) in TGF β -activated LX2 cells versus control (top, n=3) and in LPS/INF γ -stimulated M1 RAW macrophages versus control (bottom, n=3). Mean \pm SEM, one-way ANOVA with Bonferroni post-hoc test, *p<0.05, **p<0.01, ***p<0.001, ns=not significant.

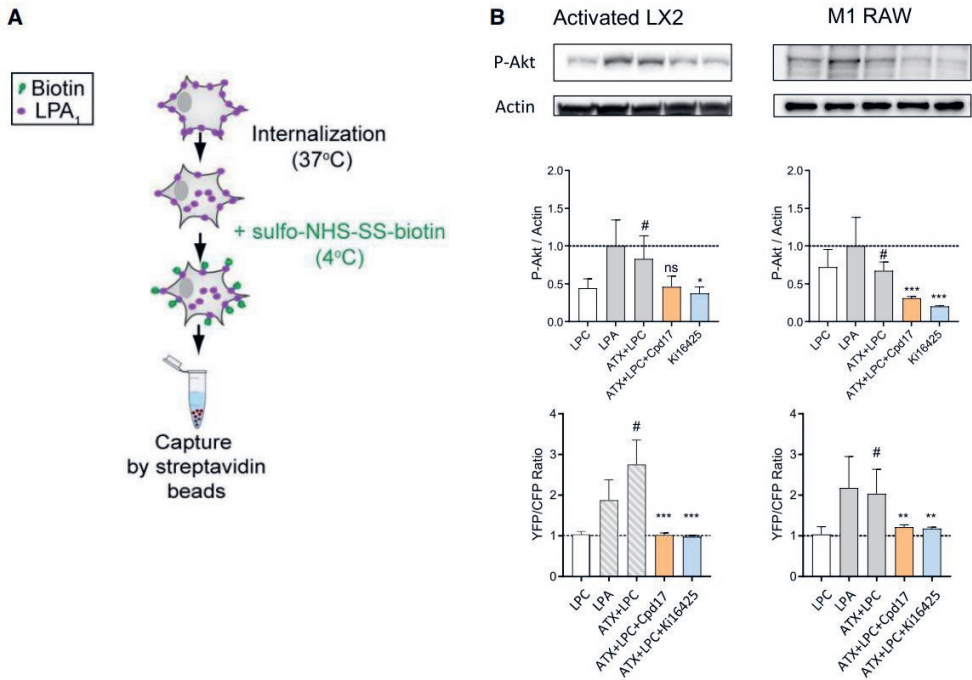


Figure S3: ATX inhibition by Cpd17 resembles antagonism of LPA₁ activation by Ki16425. (A) Schematic procedure of LPA₁ internalization assay for quantitation of surface localization. Data shown in **Figure 5D**. (B) Top panels show representative Western-blot images and quantitation of p-Akt normalized to β -actin. Serum-starved activated LX2 cells were treated for 10 min with the stimulants indicated in the graphs. Bottom plots show the quantitation of RhoA activation from time-course stimulation of activated and serum-starved LX2 cells. RhoA activation is measured as a YFP/CFP fluorescent ratio. Mean \pm SEM; one-way ANOVA with Bonferroni post-hoc test; # $p < 0.05$ denotes significance versus control (non-stimulated cells); * $p < 0.05$, ** $p < 0.01$, *** $p < 0.001$ denotes significance versus ATX+LPC treated cells.

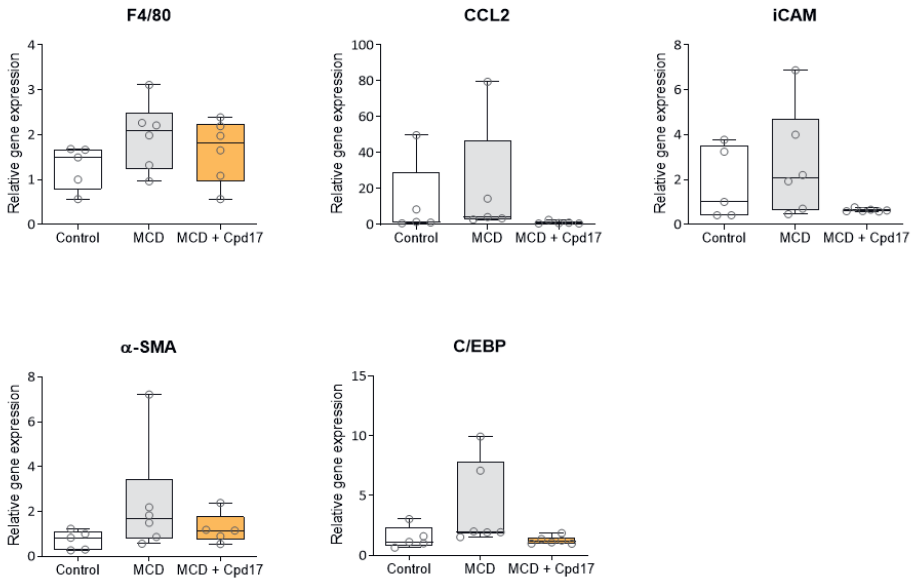


Figure S4: Effect of Cpd17 on NASH related genes in MCD-mouse model. Relative *F4/80*, *CCL2*, *iCAM*, α -*SMA* and *C/EBP* gene expression levels (normalized with *GAPDH*) from control ($n=6$), MCD ($n=6$) and MCD+Cpd17 ($n=5$) treated mice.

References

- [1] Asrani, S.K., et al., *Burden of liver diseases in the world*. J Hepatol, **2019**. 70, 151.
- [2] Marcellin, P. and B.K. Kutala, *Liver diseases: A major, neglected global public health problem requiring urgent actions and large-scale screening*. Liver International, **2018**. 38, 2.
- [3] Younossi, Z., et al., *Global burden of NAFLD and NASH: trends, predictions, risk factors and prevention*. Nat Rev Gastroenterol Hepatol, **2018**. 15, 20.
- [4] Byrne, C.D. and G. Targher, *NAFLD: A multisystem disease*. Journal of Hepatology, **2015**. 62, S47.
- [5] Kazankov, K., et al., *The role of macrophages in nonalcoholic fatty liver disease and nonalcoholic steatohepatitis*. Nature Reviews Gastroenterology & Hepatology, **2019**. 16, 145.
- [6] Francque, S.M., D. van der Graaff, and W.J. Kwanten, *Non-alcoholic fatty liver disease and cardiovascular risk: Pathophysiological mechanisms and implications*. J Hepatol, **2016**. 65, 425.
- [7] Anstee, Q.M., et al., *From NASH to HCC: current concepts and future challenges*. Nat Rev Gastroenterol Hepatol, **2019**. 16, 411.
- [8] Konerman, M.A., J.C. Jones, and S.A. Harrison, *Pharmacotherapy for NASH: Current and emerging*. J Hepatol, **2018**. 68, 362.
- [9] Choi, J.W., et al., *LPA receptors: subtypes and biological actions*. Annu Rev Pharmacol Toxicol, **2010**. 50, 157.
- [10] Balupuri, A., et al., *Discovery and optimization of ATX inhibitors via modeling, synthesis and biological evaluation*. European Journal of Medicinal Chemistry, **2018**. 148, 397.
- [11] van Meeteren, L.A. and W.H. Moolenaar, *Regulation and biological activities of the autotaxin-LPA axis*. Prog Lipid Res, **2007**. 46, 145.
- [12] Kano, K., et al., *Lysophosphatidic acid as a lipid mediator with multiple biological actions*. The Journal of Biochemistry, **2014**. 157, 81.
- [13] Tigyi, G. and A.L. Parrill, *Molecular mechanisms of lysophosphatidic acid action*. Prog Lipid Res, **2003**. 42, 498.
- [14] Sheng, X., et al., *Lysophosphatidic acid signaling in development*. Development, **2015**. 142, 1390.
- [15] Mutoh, T., R. Rivera, and J. Chun, *Insights into the pharmacological relevance of lysophospholipid receptors*. Br J Pharmacol, **2012**. 165, 829.
- [16] Moolenaar, W.H. and A. Perrakis, *Insights into autotaxin: how to produce and present a lipid mediator*. Nature Reviews Molecular Cell Biology, **2011**. 12, 674.
- [17] Hausmann, J., et al., *Structural basis of substrate discrimination and integrin binding by autotaxin*. Nat Struct Mol Biol, **2011**. 18, 198.
- [18] Salgado-Polo, F. and A. Perrakis, *The Structural Binding Mode of the Four Autotaxin Inhibitor Types that Differentially Affect Catalytic and Non-Catalytic Functions*. Cancers, **2019**. 11, 1577.
- [19] Zulfikar, S., et al., *Inhibitors of the Autotaxin-Lysophosphatidic Acid Axis and Their Potential in the Treatment of Interstitial Lung Disease: Current Perspectives*. Clinical pharmacology : advances and applications, **2020**. 12, 97.

- [20] Kondo, M., et al., *Increased serum autotaxin levels in hepatocellular carcinoma patients were caused by background liver fibrosis but not by carcinoma*. Clin Chim Acta, **2014**. 433, 128.
- [21] Nakagawa, H., et al., *Autotaxin as a novel serum marker of liver fibrosis*. Clin Chim Acta, **2011**. 412, 1201.
- [22] Fujimori, N., et al., *Serum autotaxin levels are correlated with hepatic fibrosis and ballooning in patients with non-alcoholic fatty liver disease*. World journal of gastroenterology, **2018**. 24, 1239.
- [23] Yamazaki, T., et al., *Association of Serum Autotaxin Levels with Liver Fibrosis in Patients with Chronic Hepatitis C*. Scientific reports, **2017**, 7, 46705.
- [24] Ando, W., et al., *Serum Autotaxin Concentrations Reflect Changes in Liver Stiffness and Fibrosis After Antiviral Therapy in Patients with Chronic Hepatitis C*. Hepatology communications, **2018**. 2, 1111.
- [25] Joshita, S., et al., *Serum autotaxin is a useful liver fibrosis marker in patients with chronic hepatitis B virus infection*. Hepatol Res, **2018**. 48, 275.
- [26] Kaffe, E., et al., *Hepatocyte autotaxin expression promotes liver fibrosis and cancer*. Hepatology, **2017**. 65, 1369.
- [27] Bain, G., et al., *Selective Inhibition of Autotaxin Is Efficacious in Mouse Models of Liver Fibrosis*. J Pharmacol Exp Ther, **2017**. 360, 1.
- [28] Baader, M., et al., *Characterization of the properties of a selective, orally bioavailable autotaxin inhibitor in preclinical models of advanced stages of liver fibrosis*. Br J Pharmacol, **2018**. 175, 693.
- [29] Keune, W.-J., et al., *Rational Design of Autotaxin Inhibitors by Structural Evolution of Endogenous Modulators*. Journal of Medicinal Chemistry, **2017**. 60, 2006.
- [30] Kedziora, K.M., et al., *Rapid Remodeling of Invadosomes by Gi-coupled Receptors: DISSECTING THE ROLE OF Rho GTPases*. J Biol Chem, **2016**. 291, 4323.
- [31] Akcora, B.O., G. Storm, and R. Bansal, *Inhibition of canonical WNT signaling pathway by beta-catenin/CBP inhibitor ICG-001 ameliorates liver fibrosis in vivo through suppression of stromal CXCL12*. Biochim Biophys Acta Mol Basis Dis, **2018**. 1864, 804.
- [32] Seki, E. and R.F. Schwabe, *Hepatic inflammation and fibrosis: functional links and key pathways*. Hepatology, **2015**. 61, 1066.
- [33] Zhang, C.Y., et al., *Liver fibrosis and hepatic stellate cells: Etiology, pathological hallmarks and therapeutic targets*. World J Gastroenterol, **2016**. 22, 10512.
- [34] He, L., et al., *Expression of hepatic stellate cell activation-related genes in HBV-, HCV-, and nonalcoholic fatty liver disease-associated fibrosis*. PLoS One, **2020**. 15, e0233702.
- [35] Gurvich, O.L., et al., *Transcriptomics uncovers substantial variability associated with alterations in manufacturing processes of macrophage cell therapy products*. Sci Rep, **2020**. 10, 14049.
- [36] Wang, Z., et al., *Autotaxin stimulates LPA2 receptor in macrophages and exacerbates dextran sulfate sodium-induced acute colitis*. J Mol Med (Berl), **2020**. 98, 1781.
- [37] Rahman, S.M., et al., *CCAAT/enhancing binding protein β deletion in mice attenuates inflammation, endoplasmic reticulum stress, and lipid accumulation in diet-induced nonalcoholic steatohepatitis*. Hepatology, **2007**. 45, 1108.

- [38] Corin K.A. and Gibson L.J. *Cell contraction forces in scaffolds with varying pore size and cell density*. *Biomaterials*. 2010 Jun;31(18):4835-45.
- [39] F. Salgado-Polo, A. Fish, M.-T. Matsoukas, T. Heidebrecht, W.-J. Keune, A. Perrakis, *J Biol Chem*, **2018**. 293, 14312.
- [40] Hiroshi Nishimasu 1, Shinichi Okudaira, Kotaro Hama, Emiko Mihara, Naoshi Dohmae, Asuka Inoue, Ryuichiro Ishitani, Junichi Takagi, Junken Aoki, Osamu Nureki, *Nat Struct Mol Biol*, **2011**. 18, 205.
- [41] Nicolas Desroy, Christopher Housseman, Xavier Bock, Agnès Joncour, Natacha Bienvenu, Laëtitia Cherel, Virginie Labeguere, Emilie Rondet, Christophe Peixoto, Jean-Marie Grassot, Olivier Picolet, Denis Annoot, Nicolas Triballeau, Alain Monjardet, Emanuelle Wakselman, Veronique Roncoroni, Sandrine LeTallec, Roland Blanque, Celine Cottereaux, Nele Vandervoort, Thierry Christophe, Patrick Mollat, Marieke Lamers, Marielle Auberval, Boska Hrvacic, Jovica Ralic, Line Oste, Ellen van der Aar, Reginald Brys, Bertrand Heckmann, *J Med Chem*. **2017**, 60, 3580.
- [42] Yulia A Nevzorova, Zoe Boyer-Diaz, Francisco Javier Cubero, Jordi Gracia-Sancho, *J Hepatol*, **2020**. 73, 423.
- [43] Brandon, J. A., Kraemer, M., Vandra, J., Halder, S., Ubele, M., Morris, A. J., & Smyth, S. S., *PLOS ONE*, **2019**. 14, e0208099.



Chapter A7

Autotaxin facilitates selective LPA receptor signaling

Fernando Salgado-Polo,^{1,2} Razvan Borza,^{1,2} Minos-Timotheos Matsoukas,³ Florence Marsais,⁴ Catherine Jagerschmidt,⁴ Ludovic Waeckel,⁴ Wouter H. Moolenaar,¹ Paul Ford,⁵ Bertrand Heckmann,⁴ and Anastassis Perrakis^{1,2,*}

Affiliations:

- ¹ Division of Biochemistry, The Netherlands Cancer Institute, Amsterdam, Plesmanlaan 121, 1066 CX Amsterdam, The Netherlands.
 - ² Oncode Institute, The Netherlands.
 - ³ Department of Biomedical Engineering, University of West Attica, 12243, Athens, Greece.
 - ⁴ Galapagos SASU, 102 Avenue Gaston Roussel, 93230 Romainville, France.
 - ⁵ Galapagos NV, Generaal De Wittelaan L11 A3, 2800 Mechelen, Belgium.
- * Correspondence: a.perrakis@nki.nl.

Intended for publication on *Cell Chemical Biology*.

Abstract

Autotaxin (ATX; ENPP2) produces the lipid mediator lysophosphatidic acid (LPA) that signals through disparate EDG (LPA₁₋₃) and P2Y (LPA₄₋₆) G protein-coupled receptors. ATX/LPA promotes several (patho)physiological processes, including in pulmonary fibrosis, thus serving as an attractive drug target. However, it remains unclear if clinical outcome depends on how different ATX inhibitors modulate the ATX/LPA signaling axis. Here, we show that inhibitors binding to the ATX “tunnel” specifically abrogate key aspects of ATX/LPA signaling. We find that the tunnel is essential for signaling efficacy and dictates cellular responses independent of ATX catalytic activity, with a preference for activation of P2Y LPA receptors. These responses are abrogated more efficiently by tunnel-binding inhibitors, such as ziritaxestat (GLPG1690), compared to inhibitors that exclusively target the active site, as shown in primary lung fibroblasts and a murine model of radiation-induced pulmonary fibrosis. Our results uncover a receptor-selective signaling mechanism for ATX, implying clinical benefit for tunnel-targeting ATX inhibitors.

Introduction

Lysophosphatidic acid (LPA; mono-acyl-*sn*-glycero-3-phosphate) is a lipid mediator that signals through specific G protein-coupled receptors (GPCRs) to regulate multiple biological processes^{[1], [2]}. Six LPA receptors (LPARs), belonging to two unrelated families, have been identified. LPA₁₋₃ belong to the so-called EDG family, together with the receptors for sphingosine-1-phosphate (S1PR1-5), whereas LPA₄₋₆ are P2Y (purinergic-type) GPCRs^[3]. Strikingly, structural studies have revealed different modes of ligand (LPA) entry for the prototypic receptor, LPA₁ (EDG2) versus that for LPA₆ (P2Y5). LPA₁ accepts its LPA ligand from the extracellular space (water phase), whereas LPA₆ is thought to receive LPA by lateral diffusion, following insertion into the outer lipid bilayer^{[4], [5]}.

All LPARs activate diverse effector pathways by coupling to distinct heterotrimeric G proteins. The LPAR expression pattern and G protein coupling repertoire in a given cell type largely determine the signaling output, which includes proliferation and survival via AKT and ERK pathways, and migration and invasion via Rho-family small GTPases^[6]. LPA signaling is restrained by the action of cell-associated lipid-phosphate phosphatases (LPP1-3)^[7] that dephosphorylate LPA to non-signaling mono-acylglycerol.

LPA is produced by autotaxin (ATX or ENPP2), a secreted lyso-phospholipase D (lysoPLD) that hydrolyzes extracellular lysophosphatidylcholine (LPC) and other lysophospholipids into their bioactive products. ATX is secreted by diverse cell types and is present in body fluids; it is the only member of the ectonucleotide pyrophosphatase/phosphodiesterase family (ENPP) with lysoPLD activity^[8]. The ATX–LPAR signaling axis regulates numerous biological activities, including embryonic development and postnatal organ function^{[9], [10]}, and has been implicated in life-threatening diseases, particularly pulmonary fibrosis and cancer^{[11], [12]}. For this reason, ATX has attracted considerable interest as a drug target.

ATX is a compact, multi-domain glycoprotein consisting of a central bimetallic catalytic phosphodiesterase (PDE) domain flanked by two N-terminal somatomedin B-like domains and a C-terminal inactive nuclease-like domain^{[13], [14]}. The PDE domain has a tripartite binding site that has been the focus of drug discovery and development^[15]. This tripartite site is composed of (i) a catalytic bimetallic site next to a hydrophilic shallow groove that accommodates the glycerol moiety of lipid substrates, (ii) a hydrophobic pocket that binds acyl chains, and (iii) a partially hydrophobic tunnel in a T-junction leading to the other side of the PDE domain^{[13], [14]}. Importantly, the tunnel binds LPA^[14], as well as steroid molecules^[16], and has been proposed to serve as an ‘exit channel’ that might also modulate catalytic efficiency^{[14], [17]}.

ATX interacts with cell-surface integrins^[18] and/or heparan sulfate proteoglycans^[19], and

has been speculated to directly interact with LPARs, although evidence for the latter notion is lacking^{[3],[20]}. Through interaction with the cell surface, ATX may facilitate delivery of LPA to its cognate GPCRs in a highly localized manner^[21]. Recent studies have revealed ATX/LPA as a T-cell repellent and suggested that ATX secreted by tumor cells functions as an LPA-producing 'chaperone' that protects LPA from rapid degradation^[22].

During the last decades, many small-molecule ATX inhibitors have been developed that show different ATX binding modes with respect to occupying the catalytic site and the hydrophobic pocket together (type I), or the pocket alone (type II), or the tunnel alone (type III)^[15]. The first ATX inhibitor to enter clinical trials for idiopathic pulmonary fibrosis (IPF), the clinical candidate ziritaxestat (GLPG1690) designed by Galapagos NV (Mechelen, Belgium), is a hybrid molecule that occupies both the hydrophobic pocket and the tunnel and was defined as a type IV inhibitor. Subsequent ATX inhibitors to enter clinical trials for fibrotic diseases and tumor progression are either of type III or type IV. It remains unclear whether the ATX binding mode of the different inhibitor types determines physiological outcome and, particularly, the function of ATX's unique tunnel therein.

Here, we address these questions by showing that only tunnel-blocking ATX inhibitors are capable of inhibiting the full spectrum of LPA-mediated signaling responses. Furthermore, we demonstrate that an intact tunnel is essential for this effect. Strikingly, ATX/LPA-mediated signaling shows a strong preference for P2Y family GPCRs (LPA₆), which accept the LPA ligand from the lipid bilayer. Finally, we validate these findings in lung fibroblasts and in a murine model of radiation-induced pulmonary fibrosis^[23]. Taken together, our results show that the ATX tunnel is essential for transport and delivery of LPA to LPARs, resulting in enhanced and selective signaling outputs. Thus, by virtue of the ATX tunnel, ATX-bound LPA functions as a 'biased' receptor agonist. These findings bring a new perspective in our understanding of the ATX–LPA signaling axis and highlight the clinical benefit of targeting the ATX tunnel to block LPA signaling.

Results

Different types of ATX inhibitors modulate select signaling events

We analyzed two highly potent compounds inhibiting LPC hydrolysis: a newly developed type I inhibitor, termed Compound A (CpdA), and the type IV inhibitor ziritaxestat (GLPG1690). The crystal structures of CpdA and ziritaxestat bound to rat ATX confirmed their expected binding modes. CpdA is a classic competitive type I inhibitor, occupying the active site and hydrophobic pocket and forming several hydrogen bonding interactions, while ziritaxestat is a type IV inhibitor binding the tunnel, mostly by van der Waals interactions, as previously shown in complex with murine ATX (Fig. 1A-C, Fig. S1A-C)^[24].

As the tunnel is a secondary binding site for LPA, which can modulate LPC hydrolysis^[17], we confirm that ziritaxestat, but not CpdA, competes with LPA for tunnel occupancy (Fig. S1D).

Having verified the structural binding mode for both compounds, we examined whether these distinct inhibitors behave differently in a cellular context. The effects of CpdA and ziritaxestat, in addition to PF8380 (type I inhibitor)^[25] and Cpd17 (type IV inhibitor)^[26], were therefore assessed. Type I compounds were more efficient in inhibiting ATX catalytic activity *in vitro* ($IC_{50} < 10$ nM) than type IV compounds ($IC_{50} > 25$ nM) (Fig. 1D). However, type I and type IV compounds were equally proficient in inhibiting ATX signaling in cell culture ($EC_{50} \sim 1$ μ M), as measured by Western blot analysis of AKT activation in human BJeH skin fibroblasts (Fig. 1D). The lack of correlation between inhibition of catalytic efficiency *in vitro* and cellular outcome suggests that occupying the ATX tunnel could determine biological outcome.

To corroborate these findings, we wanted to examine the effect of ATX in an ATX-free extracellular environment. Therefore, we evaluated ATX expression (by quantitative polymerase chain reaction [qPCR]) and secretion (by Western blotting) in several cell lines (Fig. 1E, Fig. S1E). As NIH-3T3 fibroblasts were found to lack detectable ATX expression, as reported previously^[27], these cells were used in subsequent experiments.

Cells were stimulated using recombinant ATX, with or without LPC substrate, alone or with ATX inhibitors CpdA or ziritaxestat. Phosphorylation of AKT and ERK was more strongly inhibited by ziritaxestat than CpdA (Fig. 1F). We note that p-AKT or p-ERK were reduced in absolute levels (normalized to total actin) and in comparison to total AKT or ERK levels (in subsequent experiments only normalized values are reported). Moreover, ziritaxestat markedly abrogated RhoA activation, whereas the impact of CpdA was limited (Fig. 1G). ATX-induced transwell cell migration was increased by LPC (18:1) and was more efficiently reduced by ziritaxestat than by CpdA (Fig. 1H).

The feature that distinguishes ziritaxestat from CpdA is not its potency in inhibiting LPC hydrolysis, but its occupancy of the LPA-binding tunnel. This suggests that specific LPA signaling functions may be mediated through LPA binding to the ATX tunnel. We therefore examined if ATX can act as an LPA chaperone, independent of its catalytic activity.

ATX is a dual-function protein that acts as an LPA chaperone in LPA signaling

LPA is known to activate AKT, ERK, and RhoA through distinct G protein–effector pathways. Of note, in all subsequent experiments, we used FAF albumin (a known LPA carrier) at a concentration of 7.5 μ M (0.05% w/v) - much higher than the concentration

of recombinant ATX (20 nM). Albumin-bound LPA efficiently activated ERK in NIH-3T3 cells, but only marginally activated AKT and RhoA (Fig. 2A,B). Addition of recombinant ATX alone activated AKT, RhoA, and, to a lesser extent, ERK (Fig. 2A,B). It therefore appears that both LPA in the presence of albumin and ATX alone (without added LPA) activate complementary pathways. Further, ATX preincubated with LPA (ATX-bound LPA) significantly enhanced the activation of AKT and RhoA when compared to stimulation with LPA or ATX alone (Fig. 2A,B, Fig. S2A,B); notably, that was not observed for ERK activation. In cell migration assays, NIH-3T3 cells failed to respond to albumin-bound LPA, but did respond to ATX-bound LPA (Fig. 2C). Similar results were obtained using ATX-deficient MDA-MB-231 breast carcinoma cells (Fig. S2C). However, in ATX-secreting RAT-1 and BJeH fibroblasts, albumin-bound LPA was sufficient to activate both AKT and ERK; this activation was not enhanced by adding ATX (Fig. 2D, Fig. S2D).

Next, we examined if the effect of exogenously added ATX could be recapitulated by enforced ATX expression in NIH-3T3 cells. Transient ATX expression enabled LPA-induced activation of AKT, but reduced ERK activation in this setting (Fig. 2E); that recapitulated the effect of LPA observed in BJeH and RAT-1 cells, which are endogenously expressing ATX.

This suggests that ATX is needed for specific aspects of LPA signaling. As binding of ziritaxestat to the tunnel was important for abrogating the activation of AKT, ERK, and RhoA in the context of ATX-mediated LPC hydrolysis, we asked if ziritaxestat or CpdA affect the action of ATX-bound LPA. Ziritaxestat, but not CpdA, inhibited AKT and ERK activation by ATX-bound LPA (Fig. 2F, Fig. S2E). Consistently, ziritaxestat showed a stronger effect than CpdA on LPAR-driven RhoA activation (Fig. 2G). Both compounds affected NIH-3T3 cell migration, with ziritaxestat exerting a more pronounced effect (Fig. 2H).

Figure 1. Different ATX inhibitors differentially modulate cellular signaling. (A,B) Schematic of (A) type I and (B) type IV modes of binding. Binding pose of CpdA and ziritaxestat at the ATX tripartite site from co-crystal structures (PDB ID 7Z3K, 7Z3L) are shown on the right. (C) Surface representation of the ATX tripartite site. The binding poses of CpdA (in green) and ziritaxestat (in orange) in each co-crystal structure have been superimposed. (D) LysoPLD activity of ATX (20 nM), measured by choline release from LPC(18:1) (150 μ M), and the inhibitory effect of four different ATX inhibitors, indicated as IC_{50} values, measured at 0.05% w/v (7.5 μ M) fatty acid-free (FAF) bovine serum albumin (BSA). The effect of type I (CpdA) and type IV (ziritaxestat) inhibition on ATX-mediated LPC(18:1) hydrolysis in BJeH human skin fibroblasts was examined using Western blot analysis of p-AKT, and is indicated as cell-based EC_{50} values. Data represent the mean value of triplicate measures \pm SEM (error bars). (E) Relative qPCR expression patterns of ATX (*ENPP2*) and *LPAR1-6* in the indicated cell lines. Results are shown as a heat map where Ct values were normalized to cyclophilin and presented in logarithmic scale. ATX secretion is quantified in **Fig. S1C**. (F) Murine NIH-3T3 cells were treated with ATX, preincubated for 30 min with LPC (1 μ M) and for 5 min in the presence or absence of CpdA (5 μ M)

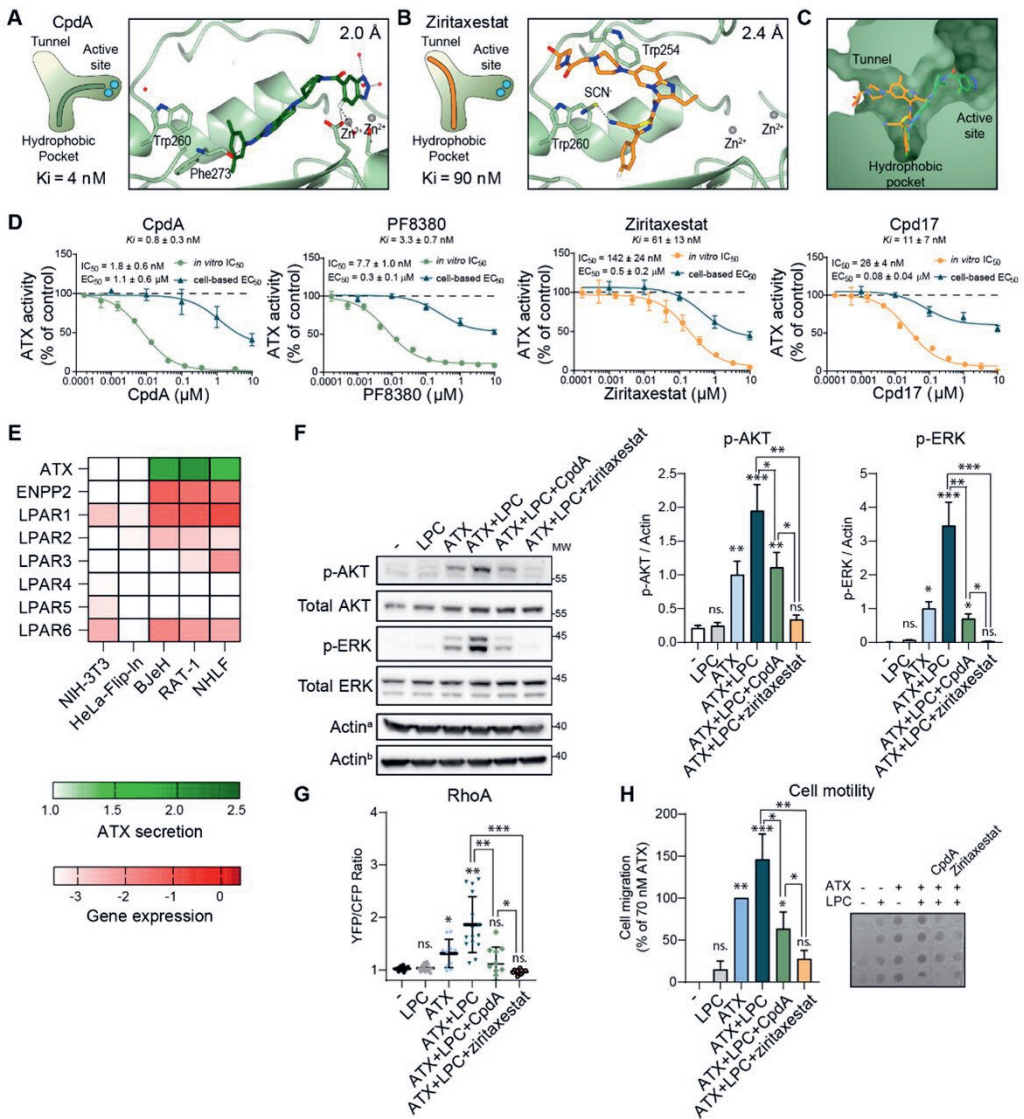


Figure 1. Different ATX inhibitors differentially modulate cellular signaling.

or ziritaxestat (5 μM), then analyzed by Western blotting. Left panel, representative Western blots of AKT and ERK activation (total AKT, total ERK, and actin are shown as loading controls); right panels, quantitation of p-AKT and p-ERK from three independent experiments using actin as a loading control. Data represent the average value of triplicate biological measures ± SEM (error bars). ^aactin from p-AKT and p-ERK blot, ^bactin from total AKT and total ERK blot; *p<0.05, **p<0.01, ***p<0.001; ns, not significant (when not specified, tested versus negative control) (one-way ANOVA, Dunnett's post-hoc test). (G) Activation of RhoA in NIH-3T3 cells, measured as yellow/green fluorescent protein

(YFP/CFP) fluorescence ratio, upon stimulation by ATX, preincubated for 30 min with LPC (1 μ M) and for 10 min in the presence or absence of CpdA (5 μ M) or ziritaxestat (5 μ M). Data depict median \pm IQR of 20 fields containing at least 10 cells. * p <0.05, ** p <0.01, *** p <0.001; ns, not significant (when not specified, tested versus negative control) (one-way ANOVA, Dunnett's post-hoc test). **(H)** Transwell migration of NIH-3T3 cells in response to albumin- or ATX-bound (20 nM) LPC (1 μ M) in the lower chamber upon 4 h. ATX was allowed to hydrolyze LPC into LPA where it was not inhibited by CpdA (5 μ M) or ziritaxestat (5 μ M). Left panel, quantitation of stimulant-dependent cell migration; right panel, representative filter containing fixed cells. Data represent the average value of triplicate biological measures \pm SEM (error bars). * p <0.05, ** p <0.01, *** p <0.001; ns, not significant (when not specified, tested versus negative control) (one-way ANOVA, Dunnett's post-hoc test).

Taken together, these results suggest that type IV inhibitors occupying the ATX tunnel do more than inhibit LPA production. According to this scenario, ATX is a dual-function protein that acts as an LPA-producing chaperone with functional specificity.

LPA delivery by ATX requires a structurally intact tunnel

To decouple the catalytic activity of ATX from its chaperone signaling function, we performed a series of mutations (Fig. 3A): the catalytic nucleophile Thr210 was mutated to alanine to abrogate ATX lysoPLD activity; residue Gly257 was mutated into a lysine to bring a positive charge and a long side chain hampering entry of LPA molecules from the back of the tunnel; and residue Trp255 located in the middle of the LPA-binding ATX tunnel was mutated to an alanine, removing such potential aromatic-aliphatic interactions which have been observed with LPA^[17], oxysterols^[16] and inhibitors^[26]. While both ATX(T210A) and ATX(W255A) mutants rendered ATX catalytically inactive *in vitro*, ATX(G257K) retained ~30% of the catalytic activity (Fig. 3B).

We then asked if the tunnel mutants would affect LPA binding. To assess this we performed a series of molecular dynamics (MD) simulations on wildtype ATX and the three mutants, as described previously^[17]. The observed LPA binding events in the tunnel were reduced in all three mutants, compared to wildtype (Fig. 3C). Whereas LPA binding in the tunnel was observed in 50% of the simulations on wildtype ATX, ATX(T210A) showed binding in 20% of the simulations and ATX(G257K) in 10% of the cases. No binding events were observed for ATX(W255A). Thus, we have created (i) a catalytically inactive mutant that has a compromised but functioning tunnel (T210A), (ii) a mutant that retains catalytic activity but has a compromised tunnel (G257K), and (iii) a mutant that lacks both catalytic activity and a functional tunnel (W255A). We then assessed these mutants in cell-based assays to better understand the importance of an intact tunnel for downstream LPA signaling.

Preincubating all ATX variants (wildtype, T210A, G257K, W255A) with LPA resulted in significantly increased AKT activation by wildtype ATX, ATX(T210A) and ATX(G257K), but

not by ATX(W255A) (Fig. 3D, Fig. S2A, Fig. S3A–D), compared to LPA alone. ERK activation was not significantly different in the presence of wildtype ATX or any of the mutants (Fig. 3D, Fig. S3A–D). Catalytically inactive ATX(T210A) activated RhoA, albeit to a lesser extent than wildtype ATX; by contrast, the ATX(G257A) and ATX(W255A) tunnel mutants failed to activate RhoA (Fig. 3E, S3E). Additionally, in NIH-3T3 cell migration assays, both wildtype ATX and ATX(T210A), ATX(W255A), induced chemotactic activity when preincubated with LPA (Fig. 3F). ATX(G257A) showed an intermediate phenotype and required higher LPA concentrations to cause cell response. These results indicate that the ATX tunnel is key for specific signaling functions dependent on ATX and are not coupled to catalytic activity.

We then asked if endogenously secreted ATX could recapitulate the signaling outcome triggered by recombinant protein. Transient transfection of the respective ATX variants in NIH-3T3 cells led to ATX secretion and enabled LPA-induced AKT activation (Fig. 3G). While ATX(T210A) has a similar effect to that of wildtype ATX, the two tunnel mutants did not significantly increase the activation of AKT with respect to LPA alone. However, none of the overexpressed ATX variants resulted in a significant increase of ERK activation.

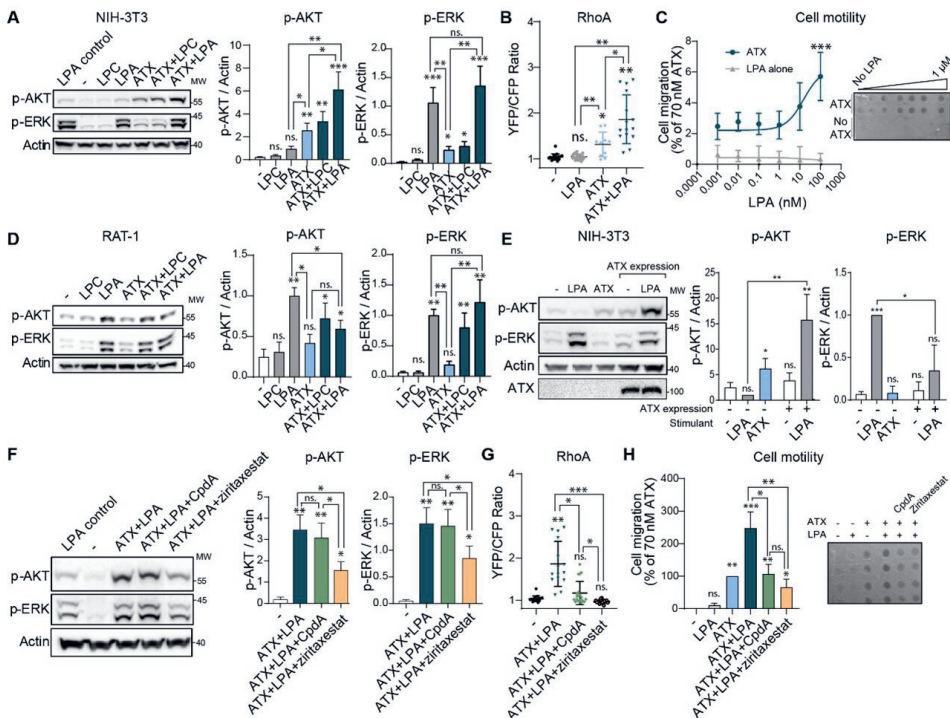


Figure 2. Role of ATX in LPA-mediated signaling and effect of distinct ATX inhibitors.

Functional selectivity of ATX: preference for P2Y-type LPA₆ over EDG-type LPA₁

Given that LPA₁₋₃ and LPA₄₋₆ are evolutionarily distinct receptors and use different ligand entry modes (Fig. 4A), we asked whether ATX/LPA shows LPAR selectivity. Since HeLa-Flp-In cells exhibited very low (or undetectable) expression of ATX and LPA₁₋₆ (Fig. 1D), we used these cells to reconstitute inducible expression of EDG LPA₁ and P2Y LPA₆ (C-terminally HA-tagged) and to analyze ATX/LPAR signaling. We confirmed that both LPA₁ and LPA₆ were expressed at similar levels, as shown by qPCR and Western blot analyses (Fig. S4A,B), and were localized to the plasma membrane, as shown by confocal microscopy (Fig. S4C).

We used these cell lines to examine receptor activation in response to ATX, LPA, and ATX preincubated with LPA. As a readout, we used agonist–receptor internalization and quantified cytoplasmic LPAR-containing vesicles by confocal imaging. LPA₁ was internalized in response to albumin-bound LPA and ATX-bound LPA, but to a lesser extent in response to ATX alone (Fig. 4B). By contrast, LPA₆ did not exhibit detectable internalization upon LPA stimulation, but responded more strongly to ATX and to ATX preincubated with LPA (Fig. 4C). This suggests that the non-catalytic effects of ATX are preferentially mediated by the P2Y-type LPARs than by EDG-type LPARs.

Figure 2. Role of ATX in LPA-mediated signaling and effect of distinct ATX inhibitors. (A) Role of ATX as an LPA carrier driving activation of AKT and ERK in NIH-3T3 cells. Cells were serum starved for 16 h and stimulated for 5 min with albumin-bound LPC (1 μ M) or LPA (1 μ M), with ATX alone (20 nM) or with ATX preincubated for 30 min with LPC or LPA. Albumin-bound LPA was used as a control for NIH-3T3 cells after a 2.5-min stimulation and was used for normalization. Left panel, representative Western blot; right panels, quantitation of AKT and ERK activation. Three independent experiments were quantified, shown as the mean \pm SEM. * p <0.05, ** p <0.01, *** p <0.001; ns, not significant (when not specified, tested versus negative control) (one-way ANOVA, Dunnett's post-hoc test). (B) RhoA activation in NIH-3T3 cells in response to the indicated stimulants. The response amplitude was quantitated (see Fig. S2 for complete time course). Data depict median \pm IQR of 20 fields containing at least 10 cells. * p <0.05, ** p <0.01; ns, not significant (when not specified, tested versus negative control) (one-way ANOVA, Dunnett's post-hoc test). (C) Boyden chamber NIH-3T3 cell migration assay performed in serum-free media, using a gradient of albumin- or ATX-bound LPA(18:1) as stimulant, where the concentrations of the carriers remained constant. Left panel, quantitation of LPA-dependent cell migration depending on the carrier; right panel, representative filter containing fixed cells. Albumin alone does not suffice to enable LPA-mediated cell migration. Data represent the average value of triplicate biological measures \pm SEM (error bars). *** p <0.001, tested versus 100 nM LPA in the absence of ATX (one-way ANOVA, Dunnett's post-hoc test). (D) Role of ATX as an LPA carrier driving activation of AKT and ERK in NIH-3T3 cells. Cells were serum starved for 16 h and stimulated for 5 min with albumin-bound LPC (1 μ M) or LPA (1 μ M), with ATX alone (20 nM) or with ATX preincubated for 30 min with LPC or LPA. Note the contrasting pattern of p-AKT to

that of panel (A). Left panel, representative Western blot; right panels, quantitation of AKT and ERK activation. Quantitation of three independent experiments, shown as the mean \pm SEM. * $p < 0.05$, ** $p < 0.01$; ns, not significant (one-way ANOVA, Dunnett's post-hoc test). (E) Need of endogenous ATX production for AKT activation in NIH-3T3 cells. Cells were serum starved and transfected with 1 μg ATX cDNA for 24 h. Left panel, representative Western blot; right panels, quantitation of AKT and ERK activation. Three independent experiments were quantified, shown as the mean \pm SEM. * $p < 0.05$, ** $p < 0.01$, *** $p < 0.001$; ns, not significant (when not specified, tested versus negative control) (one-way ANOVA, Dunnett's post-hoc test). (F) The ability of CpdA and ziritaxestat to compete with LPA for binding to ATX was tested in NIH-3T3 cells. Cells were treated with ATX-bound LPA for 5 min in the presence or absence of CpdA (5 μM) or ziritaxestat (5 μM) and compared to albumin-bound LPA (control). Left panel, representative Western blot; right panels, quantitation of AKT and ERK activation. Quantitation of three independent experiments, shown as the mean \pm SEM. * $p < 0.05$, ** $p < 0.01$; ns, not significant (when not specified, tested versus negative control) (one-way ANOVA, Dunnett's post-hoc test). (G) RhoA activation in NIH-3T3 cells in response to ATX-bound LPA for 10 min in the presence or absence of CpdA (5 μM) or ziritaxestat (5 μM). Data depict median \pm IQR of 20 fields containing at least 10 cells. * $p < 0.05$, ** $p < 0.01$, *** $p < 0.001$; ns, not significant (when not specified, tested versus negative control) (one-way ANOVA, Dunnett's post-hoc test). (H) Transwell migration of NIH-3T3 cells in response to albumin- or ATX-bound (20 nM) LPA (1 μM) in the lower chamber. The ATX chaperone function was hampered by CpdA (5 μM) or ziritaxestat (5 μM). Left panel, quantitation of stimulant-dependent cell migration; right panel, representative filter containing fixed cells. Data represent the average value of triplicate biological measures \pm SEM (error bars). * $p < 0.05$, ** $p < 0.01$, *** $p < 0.001$; ns, not significant (when not specified, tested versus negative control) (one-way ANOVA, Dunnett's post-hoc test).

Consistent with this, LPA₁-expressing HeLa cells responded to albumin-bound LPA, as shown by activation of AKT, ERK, and RhoA, irrespective of ATX presence (Fig. 4D,E, Fig. S4D,E). In marked contrast, LPA₆-expressing cells showed much stronger AKT/ERK/RhoA activation responses to ATX-bound LPA than to albumin-bound LPA (but weaker than to ATX alone) (Fig. 4F,G, Fig. S4D,E).

Finally, we examined if CpdA and ziritaxestat differentially affected LPA₁- versus LPA₆-mediated signaling in induced HeLa cells. We focused on the dual function of ATX, using ATX preincubated with LPA. In LPA₁-expressing cells, both CpdA and ziritaxestat reduced the internalization of LPA₁ and activation of RhoA (Fig. 4H,I). In LPA₆-expressing cells, both compounds reduced LPA₆ internalization (Fig. 4J), but ziritaxestat was a more efficient inhibitor of RhoA activation (Fig. 4K). The efficacy of CpdA and ziritaxestat in these assays can be explained on the basis that the LPA chaperone function of ATX not only requires the tunnel (exclusively blocked by ziritaxestat), but also the orthosteric binding site (targeted by both CpdA and ziritaxestat).

Collectively, these findings suggest that ATX-bound LPA signaling shows preference for P2Y LPARs. Given the specific effect of ziritaxestat and its therapeutic potential for lung fibrosis, we aimed to corroborate the above mechanism in primary human lung fibroblasts.

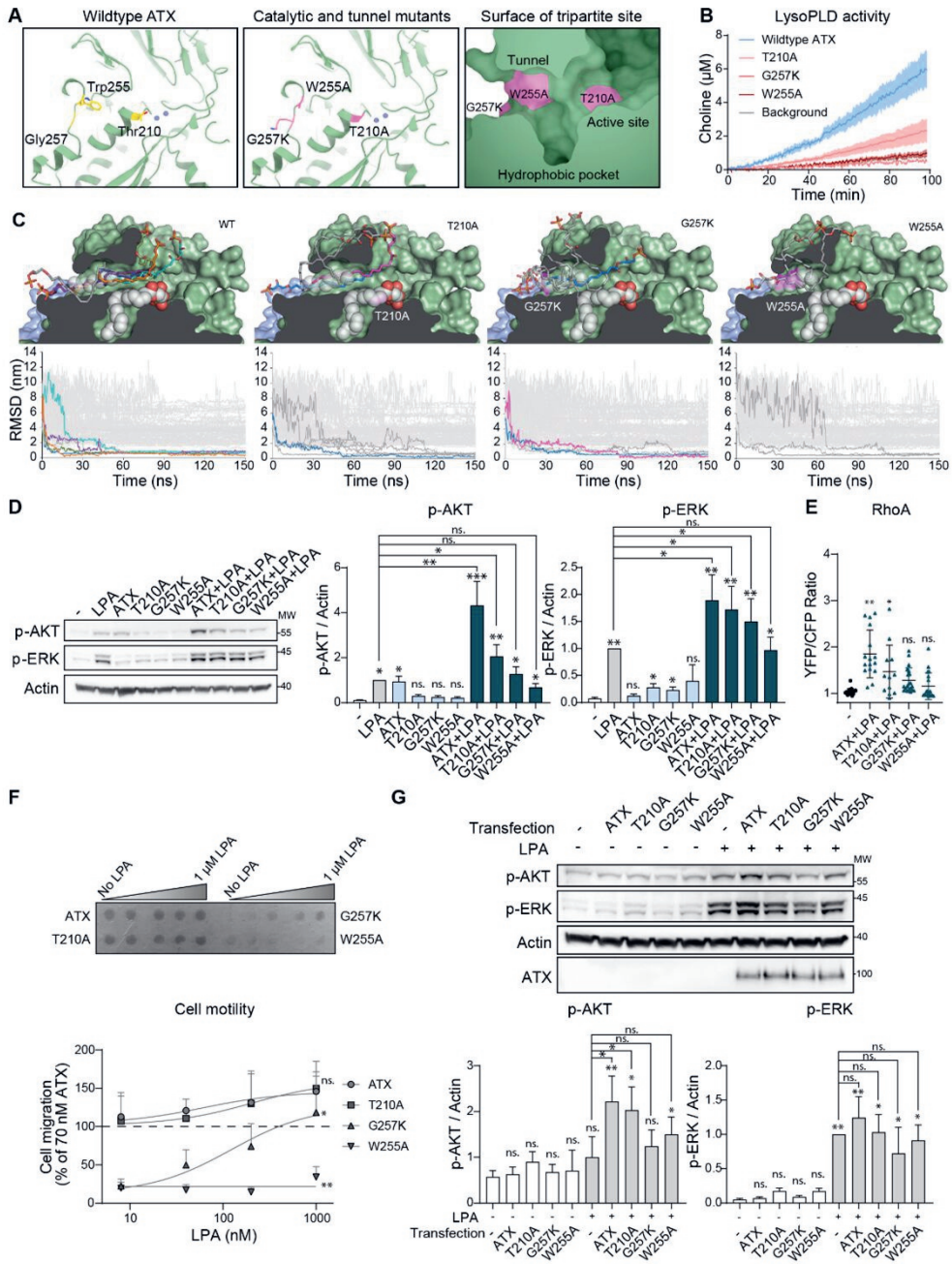


Figure 3. LPA delivery as a catalysis-independent event that requires an intact ATX tunnel.

Figure 3. LPA delivery as a catalysis-independent event that requires an intact ATX tunnel.

(A) Ribbon and surface structure of the ATX tripartite site, showing the location of the mutation series: catalytically inactive ATX(T210A), catalytically active tunnel mutant ATX(G257K), and inactive tunnel mutant ATX(W255A). Left panel, the wildtype residues are depicted in yellow; central panel, the mutated residues are shown in pink; right panel, the residues to be mutated are indicated as pink patches on the surface of the ATX tripartite site. (B) Choline release assays of wildtype ATX, catalytically inactive ATX(T210A), catalytically active tunnel mutant ATX(G257K), and inactive tunnel mutant ATX(W255A). Data represent the average of three different experiments \pm SD. (C) MD simulations of LPA binding to the tunnel of wildtype and mutant ATX. Top panels, representation of the binding modes of LPA(18:1) molecules to the tunnel. Bottom panels, the lipid molecules that entered and remained in the tunnel during the MD simulations of wildtype, T210A, G257K and W255A are shown in stick representations and colors corresponding to RMSD graph colors (top panels). The mutation site, where visible, is highlighted in magenta surface color. The carbon atoms used for the RMSD calculations are shown in white transparent spheres, and the LPA molecule occupying the hydrophobic pocket is shown in a white nontransparent sphere representation. The surface of the protein is color-coded as follows: PDE domain in light green, NUC domain in blue, and the lasso loop in orange. RMSD values of the hydrophobic lipid tail (carbon atoms C10–C18) to the reference atoms from the refined 3NKP crystal structure. Colored lines represent the LPA molecules that entered the tunnel cavity of ATX, whereas gray lines represent the remaining LPA molecules (except the one in the hydrophobic pocket) of the system. (D) AKT and ERK activation in NIH-3T3 cells in response to albumin-bound LPA (1 μ M), 20 nM ATX, catalytically inactive ATX(T210A), or tunnel mutant ATX(W255A), or LPA-bound to ATX, ATX(T210A), or ATX(W255A). Stimulants were preincubated for 30 min and cells were stimulated for a total of 5 min. Left panel, representative Western blot; right panels, quantitation of activated AKT and ERK. Three independent experiments were quantified, shown as the mean \pm SEM. * p <0.05, ** p <0.01, *** p <0.001; ns, not significant (when not specified, tested versus negative control) (one-way ANOVA, Dunnett's post-hoc test). (E) RhoA activation in NIH-3T3 cells in response to 20 nM wildtype ATX, ATX(T210A), or ATX(W255A). The response amplitude was quantitated (see **Fig. S3E** for complete time course). Data depict median \pm IQR of 20 fields containing at least 10 cells. * p <0.05, ** p <0.01; ns, not significant to negative control (one-way ANOVA, Dunnett's post-hoc test). (F) Transwell NIH-3T3 cell migration assay performed in serum-free medium, using recombinant ATX, ATX(T210A), or ATX(W255A) (20 nM) in the presence or absence of 1 μ M LPA as stimulants. Upper panel, representative filter containing fixed cells; lower panel, quantitation of LPA-dependent cell migration. Data represent the average value of triplicate biological measures \pm SEM (error bars). * p <0.05, ** p <0.01; ns, not significant to 70 nM ATX in the absence of LPA (one-way ANOVA, Dunnett's post-hoc test). (G) NIH-3T3 cells were serum starved and transiently transfected with 1 μ g ATX, ATX(T210A), or ATX(W255A) cDNA for 24 h, then analyzed by Western blotting. Upper panel, representative Western blot of AKT and ERK activation; lower panels, quantitation of activated AKT and ERK. Quantitation of three independent experiments, shown as the mean \pm SEM. * p <0.05, ** p <0.01; ns, not significant to negative control (one-way ANOVA, Dunnett's post-hoc test).

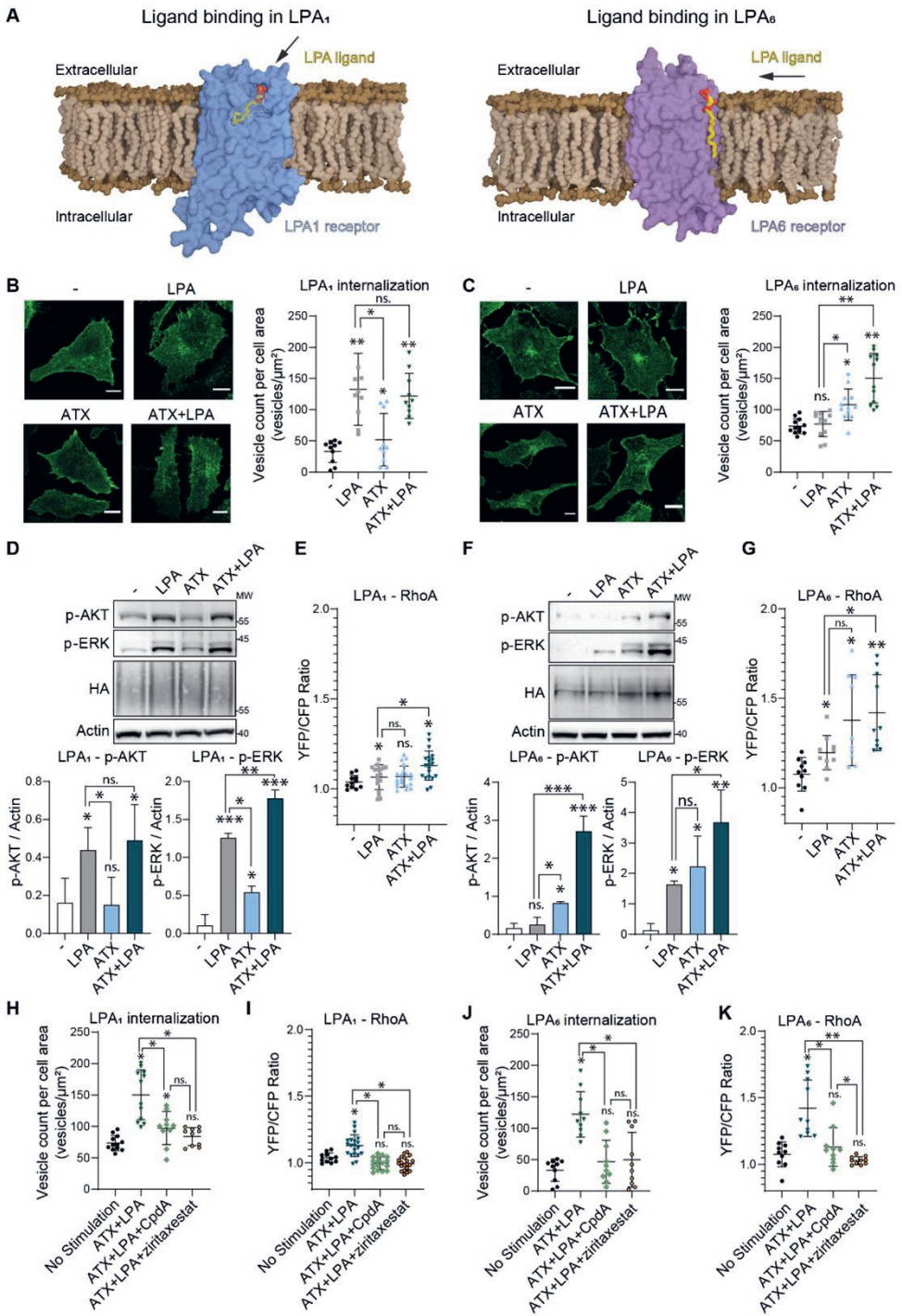


Figure 4. ATX shows a preference for P2Y-type LPA₆ over EDG-type LPA₁.

Figure 4. ATX shows a preference for P2Y-type LPA₆ over EDG-type LPA₁. (A) Surface representation of the differing entry modes of LPA(18:1) into the binding pockets of LPA₁ (left) and LPA₆ (right). UCSF ChimeraX 1.2.5 was used to generate surfaces. Membranes with bound LPARs were created and rendered using Blender 2.93.5.PDB codes. The structures were retrieved from the AlphaFold database (AF-Q92633-F1 [LPA₁] and AF-P43657-F1 [LPA₆]^{[28], [29]}). (B, C) Representative images and quantitation of the internalization of (B) LPA₁-HA and (C) LPA₆-HA in HeLa-Flp-In cells upon stimulation with albumin-bound LPA (1 μM), ATX (20 nM), or ATX-bound LPA for 15 min. Left panels, representative confocal images used for vesicle quantitation; right panel, calculation of the number of internalized vesicles. Data represent the average value ± SEM (error bars) of triplicate experiments where at least 20 fields were analyzed. *p<0.05, **p<0.01; ns, not significant (when not specified, tested versus negative control) (one-way ANOVA, Dunnett's post-hoc test). (D) Activation of AKT and ERK in LPA₁-HA-expressing HeLa cells. Stimulation of LPA₁-HA in HeLa-Flp-In cells that were starved overnight with 0.5% serum-containing medium, where receptor expression was also induced. Top panel, representative Western blot; bottom panels, quantitation of AKT and ERK activation. Quantitation of three independent experiments, shown as the mean ± SEM. *p<0.05, ***p<0.001; ns, not significant (when not specified, tested versus negative control) (one-way ANOVA, Dunnett's post-hoc test). (E) RhoA activation in response to albumin-bound LPA (1 μM), ATX (20 nM), and ATX-bound LPA in HeLa-Flp-In cells (YFP/CFP fluorescence ratio) mediated by LPA₁-HA. The response amplitude was quantitated (see Fig. S4 for full time course). Data depict median ± IQR of 20 fields containing at least 10 cells. *p<0.05; ns, not significant (when not specified, tested versus negative control) (one-way ANOVA, Dunnett's post-hoc test). (F) Activation of AKT and ERK in LPA₆-HA-expressing HeLa cells. Stimulation of LPA₆-HA in HeLa-Flp-In cells that were starved overnight with 0.5% serum-containing medium, where receptor expression was also induced. Top panel, representative Western blot; bottom panels, quantitation of AKT and ERK activation. Quantitation of three independent experiments, shown as the mean ± SEM. *p<0.05, **p<0.01, ***p<0.001; ns, not significant (when not specified, tested versus negative control) (one-way ANOVA, Dunnett's post-hoc test). (G) RhoA activation in response to albumin-bound LPA (1 μM), ATX (20 nM), and ATX-bound LPA in HeLa-Flp-In cells (YFP/CFP fluorescence ratio) mediated by LPA₆-HA. The response amplitude was quantitated (see Fig. S4 for full time course). Data depict median ± IQR of 20 fields containing at least 10 cells. *p<0.05, **p<0.01; ns, not significant (when not specified, tested versus negative control) (one-way ANOVA, Dunnett's post-hoc test). (H) Induction of internalization of LPA₁-HA in HeLa-Flp-In cells by ATX-bound LPA (20 nM, 1 μM) with or without CpdA (5 μM) or ziritaxestat (5 μM). Intracellular vesicle count upon a 15-min stimulation in the presence of serum-free Dulbecco's Modified Eagle Medium (DMEM) containing 0.05% FAF-BSA. Data show the average value ± SEM (error bars) of triplicate experiments where at least 20 fields were analyzed. *p<0.05; ns, not significant (when not specified, tested versus negative control) (one-way ANOVA, Dunnett's post-hoc test). (I) RhoA activation in LPA₁-HA-expressing HeLa-Flp-In cells (shown as a YFP/CFP fluorescence ratio) upon stimulation with ATX-bound LPA for 10 min in the presence or absence of CpdA (5 μM) or ziritaxestat (5 μM). Data depict median ± IQR of 20 fields containing at least 10 cells. *p<0.05; ns, not significant (when not specified, tested versus negative control) (one-way ANOVA,

Dunnett's post-hoc test). (J) Induction of the internalization of LPA₆-HA in HeLa-Flp-In cells by ATX-bound LPA (20 nM, 1 μM) with or without CpdA (5 μM) or ziritaxestat (5 μM). Intracellular vesicle count upon a 15-min stimulation in the presence of serum-free DMEM containing 0.05% FAF-BSA. Note that CpdA and ziritaxestat abolish vesicle internalization in LPA₆-HA-expressing cells. Data represent the average value ± SEM (error bars) of triplicate experiments where at least 20 fields were analyzed. *p<0.05; ns, not significant (when not specified, tested versus negative control) (unpaired t-test). (K) RhoA activation in LPA₆-HA-expressing HeLa-Flp-In cells (shown as a YFP/CFP fluorescence ratio) upon stimulation with ATX-bound LPA for 10 min in the presence or absence of CpdA (5 μM) or ziritaxestat (5 μM). Data depict median ± IQR of 20 fields containing at least 10 cells. *p<0.05; **p<0.01; ns, not significant (when not specified, tested versus negative control) (one-way ANOVA, Dunnett's post-hoc test).

ATX-mediated LPA delivery in human lung fibroblasts

Normal human lung fibroblasts (NHLFs) express and secrete ATX and express high levels of EDG receptors LPA₁ and LPA₃, and P2Y receptor LPA₆ (Fig. 1D).

Treatment of NHLFs with albumin-bound LPA resulted in weak activation of AKT, but activated ERK (Fig. 5A, S5A). Even though non-activated NHLFs secrete ATX (Fig. 1E), the response of activated NHLFs to LPA resembles more the ATX-free NIH-3T3 cells (Fig. S5A). ATX alone, ATX plus LPC, and ATX-bound LPA activated both AKT and ERK. This is in agreement with the results from NIH-3T3 cells (Fig. 2A). Stimulation with catalytically inactive ATX(T210A) resulted in AKT activation, whereas stimulation with the tunnel mutant ATX(W255A) failed to do so (Fig. S5B). CpdA did not significantly inhibit AKT or ERK activation (Fig. 5B), and only affected the RhoA response to ATX-bound LPA to a low extent (Fig. 5C, Fig. S5C). By contrast, tunnel-binding ziritaxestat abrogated AKT and RhoA activation, confirming that our results extend to early-passage NHLFs.

As all cell-based assays confirmed that ATX is a dual-function protein, and that ziritaxestat (but not CpdA) inhibits its activity as an LPA chaperone with functional specificity (Fig. 5D), we then examined the relative efficacy of ziritaxestat and CpdA *in vivo*, in a murine model of pulmonary fibrosis.

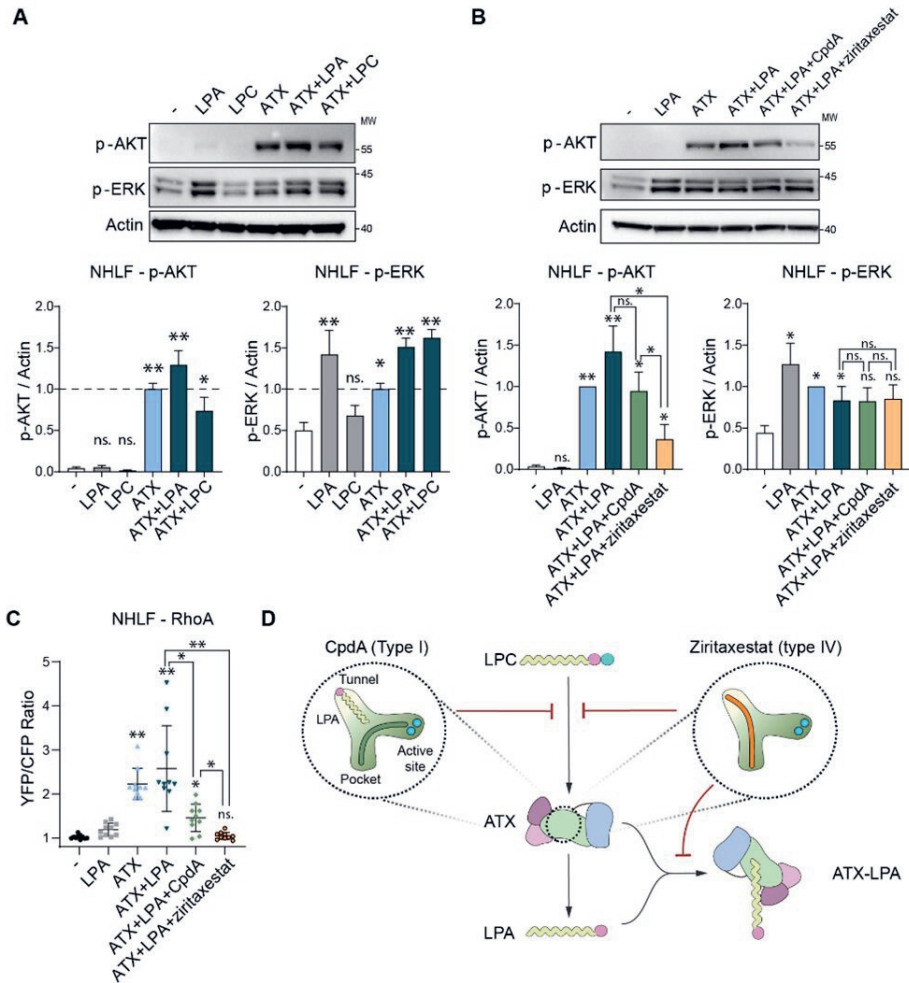


Figure 5. ATX-mediated LPA delivery and signaling in human lung fibroblasts.

Figure 5. ATX-mediated LPA delivery and signaling in human lung fibroblasts. (A) Stimulation of NHLFs with LPA or LPC in the presence or absence of ATX. Top panel, representative Western blot; bottom panels, quantitation of AKT and ERK activation. Quantitation of three independent experiments, representing the average value of triplicate biological measures \pm SEM (error bars). * $p < 0.05$, ** $p < 0.01$, ns, not significant (when not specified, tested versus negative control) (one-way ANOVA, Dunnett's post-hoc test). (B) Stimulation of NHLFs with LPA, ATX, or ATX-LPA preincubated for 30 min with or without CpDdA (5 μ M) or ziritaxestat (5 μ M). Top panel, representative Western blot; bottom panels, quantitation of AKT and ERK activation. Quantitation of three independent experiments, representing the average value of triplicate biological measures \pm SEM (error bars). * $p < 0.05$, ** $p < 0.01$, ns, not significant (when not specified, tested versus negative control) (one-way ANOVA, Dunnett's post-hoc test). (C) RhoA activation in response to albumin-bound LPA, ATX, or

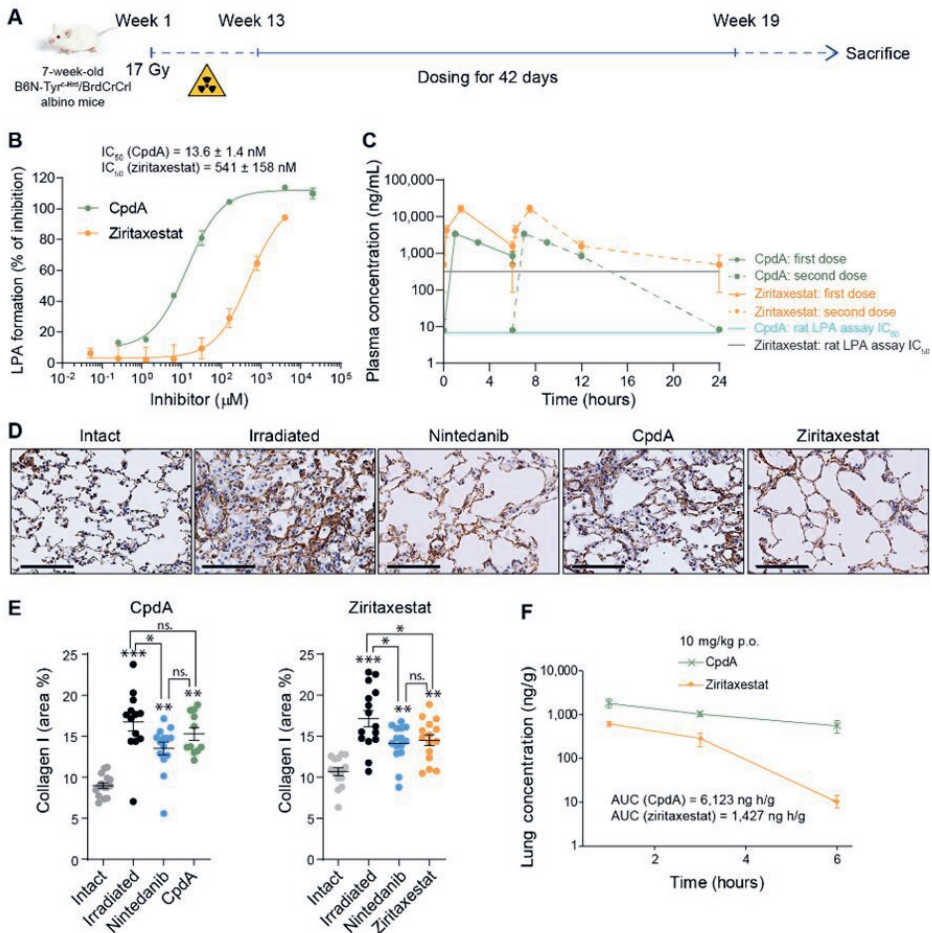
ATX-bound LPA for 10 min in the presence or absence of CpdA (5 μ M) or ziritaxestat (5 μ M). The response amplitude was quantitated (see **Fig. S5** for full time course). Data depict median \pm IQR of 20 fields containing at least 10 cells. * $p < 0.05$, ** $p < 0.01$, ns, not significant (when not specified, tested versus negative control) (one-way ANOVA, Dunnett's post-hoc test). **(D)** Schematic representation of secreted ATX with its tripartite site, LPA binding in the ATX tunnel, and the binding modes of ATX inhibitors CpdA and ziritaxestat. LPA₁ accepts LPA from the water phase, whereas LPA₆ accepts LPA from the lipid bilayer (**Fig. 4A**), with ATX serving as an LPA-producing chaperone.

Tunnel-blocking ziritaxestat, but not CpdA, reverses pulmonary fibrosis in mice

Ziritaxestat and CpdA were evaluated in a model of radiation-induced pulmonary fibrosis, a serious adverse effect of radiotherapy for patients with lung cancer with few treatment options^{[30], [31]}, and relevant for progressive lung fibrosis in a therapeutic setting (Fig. 6A)^[30]. The beneficial outcome of ziritaxestat on radiotherapy has been assessed in previous work^[32]; in this mouse model both compounds were evaluated in two separate experiments, where the doses were selected based on the compounds' potency in rat plasma LPA assays (Fig. 6B). Drug exposure was measured at steady-state in rat plasma LPA assays, which confirmed the similar target coverage and respective IC₅₀ values of the compounds (541 nM for ziritaxestat and 13.6 nM for CpdA) (Fig. 6B, Table S1). When assayed above their IC₅₀ values, CpdA was more efficient than ziritaxestat in inhibiting LPA production (Fig. 6C).

As fibrotic areas are characterized by increased secretion of extracellular matrix proteins, including type I and III collagen, we quantitated the effect of CpdA and ziritaxestat on reducing pulmonary collagen I levels. Irradiation induced a significant increase in collagen I levels after 19 weeks compared with the non-treated control, which was reduced in both experiments by treatment with nintedanib, a clinically approved drug for the treatment of IPF (Fig. 6D,E)^{[33], [34]}. While CpdA treatment did not decrease collagen I levels significantly ($p = 0.59$), ziritaxestat treatment showed some attenuation of collagen I secretion ($p = 0.048$) (Fig. 6D,E). Pharmacokinetic analysis of lung exposure after single oral administration of both compounds (at 10 mg/kg) showed that the values for the area under the concentration–time curve from 0 to 6 hours (AUC_{0-6h}) were five-fold higher for CpdA than for ziritaxestat (6,123 ng.h/g versus 1,427 ng.h/g) (Fig. 6F). As such, the lack of CpdA therapeutic activity was not due to lower pulmonary exposure.

In summary, targeting the ATX tunnel and the related non-catalytic ATX activities is important both *in vitro* and *in vivo*, highlighting the therapeutic potential of ATX inhibitors that block the tunnel and its chaperone function.



A7

Figure 6. Ziritaxestat, but not Cpda, reverses pulmonary fibrosis *in vivo*. (A) Radiation-induced fibrosis model. Irradiated lung was treated with Cpda (10 mg/kg b.i.d.), ziritaxestat (30 mg/kg b.i.d.), or nintedanib, a clinically approved drug for the treatment of IPF (positive control; 60 mg/kg q.d.). (B) Percentage of reduction in 18:2 LPA formation from *ex vivo* rat plasma samples upon incubation with Cpda or ziritaxestat, as determined by liquid chromatography–mass spectrometry. The percentage of inhibition was calculated by normalization of data to LPA levels after a 2-h incubation at 37°C in the absence of the compounds. The resulting IC_{50} values (\pm SEM) are shown. (C) Mean (\pm SEM) steady-state plasma concentrations of Cpda and ziritaxestat after a p.o. administration at 10 mg/kg b.i.d. and 30 mg/kg b.i.d., respectively, shown on logarithmic scale. (D,E) Analysis of collagen I levels in the murine model of radiation-induced fibrosis. (D) Representative images of collagen I staining. (E) Surface area quantitation of collagen I levels of Cpda- or ziritaxestat-treated mice after 19 weeks. *p<0.05, **p<0.01, ***p<0.001; ns, not significant (when not specified, tested versus intact mouse group) (one-way ANOVA, Dunnett’s post-hoc test). (F) Lung tissue exposure of Cpda and ziritaxestat after a single p.o. administration at 10 mg/kg.

Discussion

Here we have addressed this question by examining how type I and type IV ATX inhibitors affect specific LPAR-mediated signaling events. We find that type IV compounds are more efficient in inhibiting AKT activation, RhoA activation, cell migration, and receptor internalization. Strikingly, our data suggest that ATX is not only needed for LPA production, but that it can also act as an LPA chaperone. It is this specific chaperone activity that can be targeted by type III or type IV compounds, which occupy the ATX tunnel. We corroborate these findings in fibroblast cell lines, LPA₁- and LPA₆-expressing HeLa cells, NHLFs, and in a murine model of radiation-induced pulmonary fibrosis.

A further novel finding of this study is that the chaperone function of ATX shows high specificity for LPA₆ over LPA₁, at least in the context of our reconstituted system, which is supported by receptor expression patterns in tested cell lines. This observation poses the question of whether this selectivity is related to how EDG and P2Y LPARs recognize and accept LPA ligands. This could happen due to the distinct binding modes of LPA₁^[4] and LPA₆^[5] (further discussed in **Chapter A9**). Nonetheless, our results suggest that EDG LPARs are preferentially activated by albumin-bound LPA^[42], whereas P2Y LPARs prefer ATX-bound LPA. Interestingly, during early embryogenesis, ATX signals through P2Y LPA₄ and LPA₆, with no apparent role for EDG-type LPARs^{[9], [10]}. P2Y receptors LPA₅ and LPA₆ also play unique roles in anti-tumor immunity, regulating T cell receptor function and mediating ATX-induced repulsion of tumor-infiltrating T cells, respectively^{[22], [43]}.

The relevance of EDG family LPA₁ in IPF and systemic sclerosis has been established using *Lpar1* knockout mice; these animals are protected from fibrosis in models of lung and dermal fibrosis^{[44], [45]}. ATX expression is increased in the fibrotic skin of patients with systemic sclerosis and in a bleomycin mouse model of systemic sclerosis^[46]. Increased ATX and LPA levels have also been found in lung tissue and bronchoalveolar lavage fluid, respectively, of patients with IPF^{[47], [48]}. Ziritaxestat has been trialed as a treatment for IPF and systemic sclerosis^[49]; however, phase 3 trials in patients with IPF were discontinued because the benefit-risk profile of the drug no longer supported continuation. Our present data suggest that physiological effects of ziritaxestat, which showed promise in phase IIb trials, can be attributed to its ATX binding mode occupying the ATX tunnel and thereby inhibiting specific signaling events including RhoA-mediated cytoskeletal reorganization. At first sight, this appears at odds with the role of EDG LPARs in IPF, as ziritaxestat shows functional preference for the prototypic P2Y LPAR, LPA₆. Based on the mouse studies discussed above, the phenotype we assess is mainly an effect of LPA₁ EDG-mediated signaling. LPA₁ function is affected by both CpdA and ziritaxestat, and mediates therapeutic efficacy. We suggest that while abrogating ATX catalytic activity is a major component of the physiological function of ATX inhibitors, type IV inhibitors like

ziritaxestat bring in play additional features that are delineated in this study, specifically targeting P2Y LPA-mediated signaling. Additionally, that the therapeutic effect of ATX type IV inhibitors in fibrotic diseases, but also in cancer, must be viewed also in the context of an interplay with the immune system; for example, P2Y-type LPA₆ is most highly expressed in immune cells^[22].

Future structural and functional studies should help to elucidate the mechanism of ATX-mediated transfer of bound LPA to the membrane outer leaflet. The involvement of biased signaling, or the role of other ATX co-receptors such as integrins, could be explored. This might also advance our broader understanding of how lipid mediators, such as LPA, regulate biological functions in a receptor-selective manner and thus suggest new therapeutic opportunities. In a more general context, this study highlights how structural and mechanistic insights may translate into the (pre)clinical efficacy of inhibitors blocking the ATX tunnel. Several inhibitors that occupy the ATX tunnel are currently in clinical trials; this work provides a rationale for their mode of action, targeting both the enzymatic and the chaperone function of ATX.

A7

Limitations of the study

Our study shows that the ATX tunnel functions as an LPA chaperone, facilitating receptor-selective signaling and implying a clinical benefit for tunnel-targeting ATX inhibitors, like ziritaxestat. Ziritaxestat, significantly reduced collagen I levels in irradiated mouse lungs and ameliorated murine disease outcome. However, the current experimental setting does not allow further comparison between ziritaxestat and CpdA (an inhibitor that does not target the ATX tunnel and, thus, the LPA chaperone function), as the *in vivo* studies were performed in two different experiments. We cannot exclude that this experimental design results in considerable variation within the different groups, thereby hampering a direct comparison to the same reference groups.

Experimental Procedures

Crystallographic methods. Rat ATX for structural studies was overexpressed and purified as described previously^[35]. For the crystallization studies, ATX was incubated with each screened compound at a 1:10 (protein:compound) ratio for at least 30 min. Crystals were grown for at least 7 days in a 24-well optimization screen (18–20% PEG 3350, 0.1–0.4 M NaSCN, and 0.1–0.4 M NH₄I). In all cases, the best diffracting crystals were obtained at RT by mixing 1 μ L of the protein:compound solution and 1 μ L of reservoir solution. All crystals were vitrified in cryoprotectant, which consisted of reservoir solution with the

addition of 20% (v/v) glycerol. Other solvent:protein ratios tested per condition were 1:2 and 2:1.

The X-ray diffraction data for the ATX–inhibitor complexes were collected at SLS on beamline PXIII^[36] at 100 K, and were recorded on a PILATUS 2M-F detector to high resolution. All data were processed and integrated with XDS^[36]. CpdA and ziritaxestat were processed on site, using the SLS automated processing pipeline, and scaled with AIMLESS^[37]. The structures were determined by molecular replacement using MOLREP^[38], with the structure of ATX (PDB 2XR9) as the search model. Model building and subsequent refinement were performed iteratively with COOT^[39], REFMAC5^[40], and PDB_REDO^[41]. Structure validation was carried out by MolProbity^[42]. The structure models and experimental diffraction data of CpdA and ziritaxestat were deposited at the Protein Data Bank under the codes 7Z3K and 7Z3L, respectively (Supplemental Table 2).

Biochemical assays and modeling of kinetic data. The biochemical studies of ATX lysoPLD activity were performed with ATX. Activity was measured by a coupled reaction with 1 U ml⁻¹ choline oxidase and 2 U ml⁻¹ horseradish peroxidase (HRP) and 2 mM homovanillic acid (HVA) (all from Sigma-Aldrich). For the assays, 14:0, 16:0, 18:1 20:0 LPC (Avanti polar Lipids Inc.) was incubated with 20 nM ATX, reaching a final volume of 100 µl buffer, which contained 50 mM Tris, 0.01%, 50 mM CaCl₂, Triton X-100, pH 7.4. Steady-state choline release was measured at 37 °C by HVA fluorescence at $\lambda_{ex} / \lambda_{em} = 320/460$ nm in Corning® 96- or 384-well OptiPlate (Sigma-Aldrich) and with a PHERAstar plate reader (BMG Labtech)^[16]. To determine the IC₅₀ for the different inhibitors on ATX activity, the velocity of the reaction was monitored for each compound as a function of time and the linear phase of the kinetics was taken from 60 min after the addition of ATX to the reaction buffer. The resulting fluorescence intensity signal over time was used to model all inhibitor concentrations simultaneously using the following formula, where v_{max} and v_{min} were fitted for the minimum and maximum relative velocity, and c_i corresponds to the inhibitor concentration for each assay^[16]:

$$V = \frac{v_{max} - v_{min}}{(1 + c_i / IC_{50})} + v_{min} \quad (\text{Equation 1})$$

Competition with LPA allostery. The activation assays using LPA were performed in a similar way as those done for the inhibitors. In this case, LPA was dissolved in Ethanol: H₂O (1:1), 0.01% TX-100 and was added to the reaction buffer. The presence of ethanol was taken into account and controls in the absence of ATX and/or LPC were employed to correct the kinetic data. ATX was incubated for 30 min with different concentrations of inhibitors and subsequently added to the reaction buffer containing 150 µM 18:1 LPC and different starting concentrations of 18:1 LPA. The slopes were calculated from at least 60 min after the addition of ATX. The percentage of LPA-driven activation was normalized

to ATX in the absence of LPA and inhibitors, which represented 100% activity. Lastly, the activation constant or AC_{50} was obtained from the following equation:

$$V = \frac{v_{max} - v_{min}}{(1 + c_i / AC_{50})} + v_{min} \quad (\text{Equation 2})$$

Cell-based assays. Human ATX used in cell-based studies was overexpressed and purified as described previously^[35].

AKT and ERK phosphorylation. A total of 100,000 BJeH or 50,000 HeLa cells were seeded in 12-well tissue culture plates and allowed to grow for 24 h in DMEM (Gibco, Life Technologies) containing 10% fetal calf serum (FCS) (Thermo Scientific, USA) and 100 U mL⁻¹ streptomycin/penicillin (Gibco, Life Technologies). In the case of NIH-3T3, 300,000 cells were plated on 6-well plates. Next, the cells were washed twice with phosphate buffer solution (PBS) and serum starved overnight. ATX (20 nM) was incubated with inhibitors, LPC or LPA, for 30 min in serum-free medium containing 0.05% (w/v) FAF-BSA (total volume 1 mL). Medium from the 12-well plates was removed and replaced with 1 mL of the ATX-inhibitor mixture. Cells were stimulated for 15 min, after which the medium was removed and the plates immediately frozen on dry ice and stored at -80 °C. For Western blotting, cells were washed with cold PBS, lysed in RIPA buffer, supplemented with protease inhibitors and protein phosphatase inhibitors (20 mM NaF and 1 mM orthovanadate; Pierce), and centrifuged. Protein concentration was measured using a BCA protein assay kit (Pierce), after which LDS sample buffer (NuPAGE, Invitrogen) and 1 mM dithiothreitol (DTT) were added to the lysate. SDS-PAGE pre-cast gradient gels (4–12% NuPAGE Bis-Tris, Invitrogen) were loaded with 20 µg of total protein, followed by transfer to nitrocellulose membrane. Non-specific protein binding was blocked by 5% BSA in PBS-Tween (0.1%); primary antibodies (D9L: phospho-AKT [Ser473], 1:1,000; 4370S: phospho-ERK1/2 [Thr202/Tyr204], 1:1,000; Cell Signaling Technology) were incubated overnight at 4 °C in PBS-Tween with 5% BSA containing 0.1% NaN₃. Horseradish peroxidase-conjugated secondary antibodies (DAKO, Glostrup, Denmark) were incubated for 1 h (RT; 293 K) in PBS-Tween with 2.5% BSA and developed using ECL Western blot reagent.

Rho GTPase biosensor. A fluorescence resonance energy transfer (FRET) pair consisting of RhoA-Cerulean3 and PKN fused to circularly permuted Venus was used^[58]. The HR1 region of PKN was used as the effector domain for activated RhoA. Experiments were performed in phenol red-lacking DMEM medium at 37 °C. Cells were allowed to adhere overnight on uncoated coverslips, after which they were serum starved and transfected with the biosensor for 24 h. Next, the coverslips were placed on a thermostat-controlled (37 °C) inverted Nikon Diaphot microscope and excited at 425 nm. Donor and acceptor emission were detected simultaneously with two photomultipliers, using a 505-nm beam splitter and optical filters: 470 ± 20 nm (CFP channel) and 530 ± 25 nm (YFP channel). The

Supplemental Table 2. Crystallographic details.

Data Collection	CpdA (7Z3K)	GLPG1690 (7Z3L)
Wavelength (Å)	1.0000	1.0000
Resolution (Å)	2.00	2.40
Space group	P1	P12 ₁
Unit cell a b c (Å), β (deg)	53.7 62.5 63.6 104.2 98.6 93.2	62.8 88.7 77.0 90.0 102.8 90.0
Data quality statistics ^a		
CC _{1/2}	0.985 (0.437)	0.996 (0.766)
R _{merge}	0.137 (0.798)	0.081 (0.752)
<I/ σ >	5.6 (1.3)	8.2 (1.6)
Completeness (%)	98.0 (96.9)	99.8 (99.5)
Redundancy	3.1 (3.2)	3.4 (3.5)
Refinement		
No. atoms	7130	6676
protein	6404	6348
ligand/metal/glycan	173	204
water/iodine	553	124
R _{work} /R _{free} (%)	20.2/24.2	24.4/25.9
Validation		
rsmsd/rmsZ bond lengths (Å)	0.0027/ 0.196	0.0017/0.128
rsmsd/rmsZ bond angles (deg)	1.218/ 0.719	1.194/0.690
Ramachandran preferred/outliers (%)	95.68/0.00	94.24/0.26
Ramachandran Z score	-0.86	-2.21
Rotamers preferred (%)	95.68	93.81
MolProbity/Clash score (%ile)	96/99	100/100

^aHigh resolution shell in parentheses.

emission data were analyzed using the Fiji software and normalized to control cells. At least three independent experiments were analyzed for every condition (20 fields of view/condition, 3–5 cells/field of view, >50 cells/condition). FRET was expressed as the ratio between acceptor and donor signals, set at 1 at the onset of the experiment.

Cell migration assays. Cell migration was measured using 48-well chemotaxis chambers (Neuro Probe, Inc.) equipped with 8 mm-pore polycarbonate membranes, coated with fibronectin (20 mg/mL). Cells (4.8×10^6 /mL) were added to the upper chamber. FAF-BSA (0.5 mg/mL) was used as a lysophospholipid carrier. For NIH-3T3 cells, migration was allowed for 4 h at 37 °C in humidified air containing 5% CO₂. Migrated cells were fixed in Diff-Quik Fix and stained using Diff-Quik II. Migration was quantified by color intensity measurements using Adobe Photoshop.

MD simulations. Models of human wildtype autotaxin (Uniprot code Q13822) and mutants T210A, G257K and W255A in complex with 18:1 LPA were constructed on the basis

of our previously reported crystal structures of rat autotaxin (PDB codes 5DLW and 5DLT)^[16] as templates (94% sequence identity) as previously described^[17]. All MD simulations were performed using the GROMACS software version 2021.5.^[59] Each ATX (wildtype or mutant) - 18:1 LPA molecule complex contained 10 extra 18:1 LPA molecules at random positions with a minimum distance of 40 Å to the tunnel, ~58,500 water molecules, and Na⁺ ions (for total charge equilibrium) in a 12.5 x 12.5 x 12.5-nm simulation box (total number of ~189,000 atoms), and was minimized and equilibrated until 10 independent 150 ns MD trajectories were produced in a process we have described previously^[17]. The total simulation time for the four complexes and replicas was added up to a total of 6.0 μs.

Production of LPAR-expressing HeLa-Flp-In cells. cDNA containing human *LPAR1*, *LPAR2*, *LPAR3*, and *LPAR6* was amplified by PCR to remove its stop codon and add the restriction sites for BamHI and XhoI (or NotI for *LPAR6*), after which it was subcloned in an in-house produced pDNA5.1-HA vector. Codon-optimized gene blocks for *LPAR4* and *LPAR5* were ordered to facilitate amplification and cloning strategies, which included the addition of restriction sites for BamHI and XhoI (or NotI for *LPAR5*). For plasma membrane localization, the signal peptide of neuronal acetylcholine receptor subunit alpha-7 was added at the N-terminus of P2Y LPARs; 0.2 μg of the resulting vectors and 1.8 μg pOG44 Flp-Recombinase Expression Vector (Invitrogen) were incubated with 6 μL FuGENE 6 (Invitrogen) in 200 μL Opti-MEM (Gibco) for 30 minutes, after which the mix was added to previously produced HeLa-Flp-In cells. Cell medium was refreshed 24 h later, and selection with 1 μg/mL puromycin was started and maintained with resistant cells.

Real-time quantitative PCR. Cells were allowed to grow to almost complete confluency on 10-cm dishes in 10% FCS-containing DMEM. Total RNA was extracted using the GeneJET purification kit (Fermentas). cDNA was synthesized by reverse transcription from 5 μg RNA using First Strand cDNA Synthesis Kit (Thermo Scientific). RTqPCR was performed on a 7500 Fast System (Applied Biosystems) as follows: 95 °C for 2 min, 95 °C for 0 min, 60 cycles at 95 °C for 15 s, followed by 60 °C for 1 min for annealing and extension. The final reaction mixtures (12 μL) consisted of diluted cDNA, 16SYBR Green Supermix (Applied Biosystems), 200 nM forward primer, and 200 nM reverse primer. Reactions were performed in 384-well plates, with three independent biological replicas. As a negative control, the cDNA was replaced by MilliQ water. Cyclophilin was used as reference gene. Each sample was analyzed in triplicate and the normalized expression (NE) data were calculated using the equation $NE = 2^{-(Ct_{\text{target}} - Ct_{\text{reference}})}$.

Detection of rat LPA plasma levels. Whole blood was collected from rats in sodium heparin tubes. The samples were centrifuged at 3,000 rpm for 15 min at 4 °C to separate the plasma, which was stored at -80 °C. CpdA and ziritaxestat were serially diluted in dimethyl sulfoxide (DMSO) and 0.5 μL of the dilutions dispensed into 96-well plates placed on ice;

plasma was thawed on ice. Next, 49.5 μL of plasma were added to wells containing 0.5 μL of ziritaxestat or CpdA (1% final DMSO concentration). The plates were covered with a polypropylene lid and incubated for 2 h at 37 °C in humidified air containing 5% CO_2 , with gentle shaking (except for the control samples, which were stored at -20 °C). The control samples were thawed on ice, then transferred to the incubated plates before liquid chromatography–mass spectrometry analysis. For the analysis, 10 μL of plasma proteins from the incubated plates were precipitated with an excess of methanol containing the internal standard 17:0 LPA (Cat# 857127, Avanti Polar Lipids, Inc.). The samples were centrifuged and the supernatants injected onto a C18 column. Analytes were eluted off the column under isocratic conditions. An API5500 QTRAP mass spectrometer (ABSciex™) was used for the detection of 18:2 LPA. Relative quantities were calculated based on the peak area.

Radiation-induced fibrosis mice model. Procedure and drug-naïve seven-week-old female B6 albino (B6N-Tyr^{c-Brd}/BrdCrCrI) mice (16–18 grams) from Charles River (France) were delivered at the Plateforme de Radiothérapie Expérimentale in Institut Curie (Orsay, France). After a 7-day acclimatization period, they were identified using the micro-tattoo Aramis system. Mice were anesthetized with isoflurane, placed in holders, and irradiated with a single 17-Gy dose in the thorax area (Week 1)^[60]. All mice survived after irradiation. The week after irradiation, mice were shipped to Galapagos Animal Facilities (Romainville, France), where they were housed 10 per cage after individual identification using microchip (Biolog-id, Boulogne-Billancourt, France). They were maintained at 22 °C on a 12-h light/dark cycle (07:00–19:00); food and water were provided *ad libitum*. The study was performed according to the Animal Institutional Care and Use Committee of Galapagos, ethical guidelines of animal experimentation, and the guidelines for welfare of animals in experimentation. At Week 13, fur was removed on the thorax of the anesthetized mice (using a shaving razor, then hair removing cream). *In vivo* imaging using a proprietary collagen near-infrared fluorescent probe was used to exclude mice presenting liver fibrosis ($\approx 15\%$), and to allocate them to each experimental group according to their lung fibrosis level. Treatment with ziritaxestat (30 mg/kg b.i.d) or CpdA (10 mg/kg b.i.d) was assayed by oral route, in comparison to nintedanib (60 mg/kg q.d). Treatment was initiated 13 weeks after irradiation and lasted for 6 weeks. On Week 17, 4 weeks after initiation of dosing, steady-state pharmacokinetics were assessed, with sampling at four time points: 0, 1, 3, and 6 h (assuming 24 h is $t=0$ h). Plasma was prepared and kept at -20 °C until quantification using liquid chromatography–mass spectrometry. At Week 19, mice were killed by elongation. Entire lungs were removed, rinsed with PBS, and weighed. Lobes of the lungs were separated and fixed in formaldehyde for 48 h before paraffin embedding. For every lung, 4- μm thick sections were immunostained with anti-collagen I antibody. The immunohistochemistry samples were processed automatically using the immunostainer BOND-RX (Leica). The stained sections were scanned (NanoZoomer, Hamamatsu Photonics

K.K.) before quantification by image analysis (CaloPix, Tribun Health). Data were expressed as percentage of collagen I area per area of lung tissue devoid of the main constitutive collagen in vessels and bronchi.

Acknowledgements

High resolution mass spectral data were obtained at the EPSRC Mass Spectrometry facility at the University of Swansea, UK. X-ray diffraction data were collected at the European Synchrotron Radiation Facility (ESRF) and the Swiss Light Source (SLS). This work benefited from access to the NKI Protein Facility at Instruct-NL, an Instruct-ERIC center. We thank Elisa Matas-Rico and Willem-Jan Keune for help in establishing cell-based experiments, and Kees Jalink for discussions, ideas, and signaling reagents. This study was partially funded by Galapagos NV (Mechelen, Belgium). Editorial support was provided by Iain Haslam, PhD (Aspire Scientific, Bollington, UK), funded by Galapagos NV. This research was supported by an institutional grant of the Dutch Cancer Society and of the Dutch Ministry of Health, Welfare and Sport.

Supplemental information

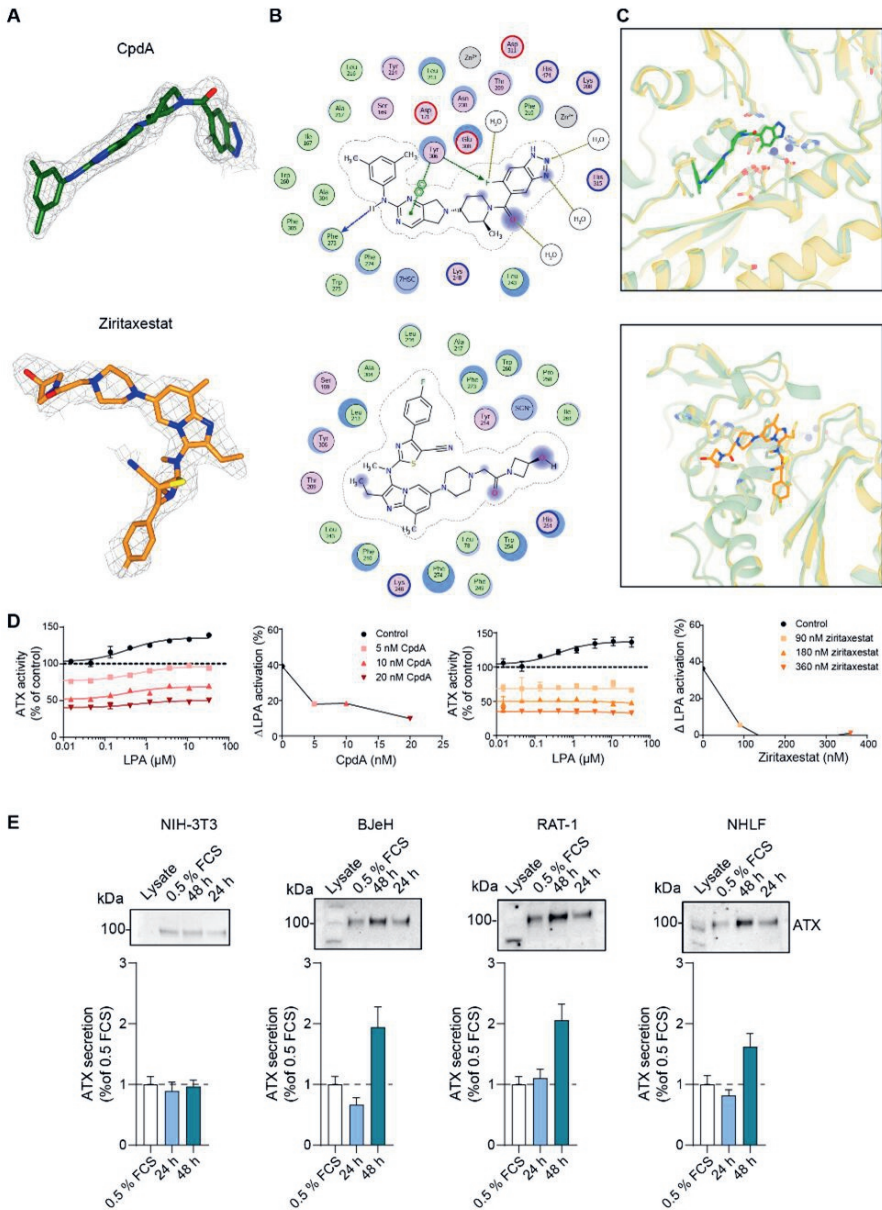


Figure S1. Different types of ATX inhibitors modulate specific signaling events. (A) Fit of CpdA (left) and ziritaxestat (right) model (carbon in orange; nitrogen in blue; oxygen in red; sulfur in yellow) to the 2mFo–DFc electron density map after refinement. **(B)** Interaction of CpdA (upper panel) and ziritaxestat (lower panel) with ATX, shown in a two-dimensional interaction network generated by Lidia software on WinCoot. Side- and main-chain hydrogen bonds are indicated in

green and blue arrows, respectively; hydrogen bonds with water molecules are represented in gold. SCN⁻; thiocyanate; 7HSC, 7 α -hydroxycholesterol. **(C)** Comparison of the two-dimensional structural elements in the ATX co-crystals with CpdA and ziritaxestat. Top panel, the co-crystal structure of ATX-CpdA is shown in green, both for protein and compound, and superimposed to the structure of ATX (orange) co-crystallized with ziritaxestat. Bottom panel, the co-crystal structure of ATX-ziritaxestat is shown in orange, both for protein and compound, and superimposed to the structure of ATX (green) co-crystallized with CpdA. **(D)** Ability of CpdA (upper panels) and ziritaxestat (lower panels) to block the ATX tunnel, determined by the abolition of LPA allostery while retaining residual, slow-turnover ATX catalysis. The dashed horizontal line represents the time of cell stimulation. Data represent the average value of triplicate measures \pm SEM (error bars). **(E)** Secretion of ATX by the cell lines evaluated in this study. Data represent the average value of triplicate measures \pm SEM (error bars).

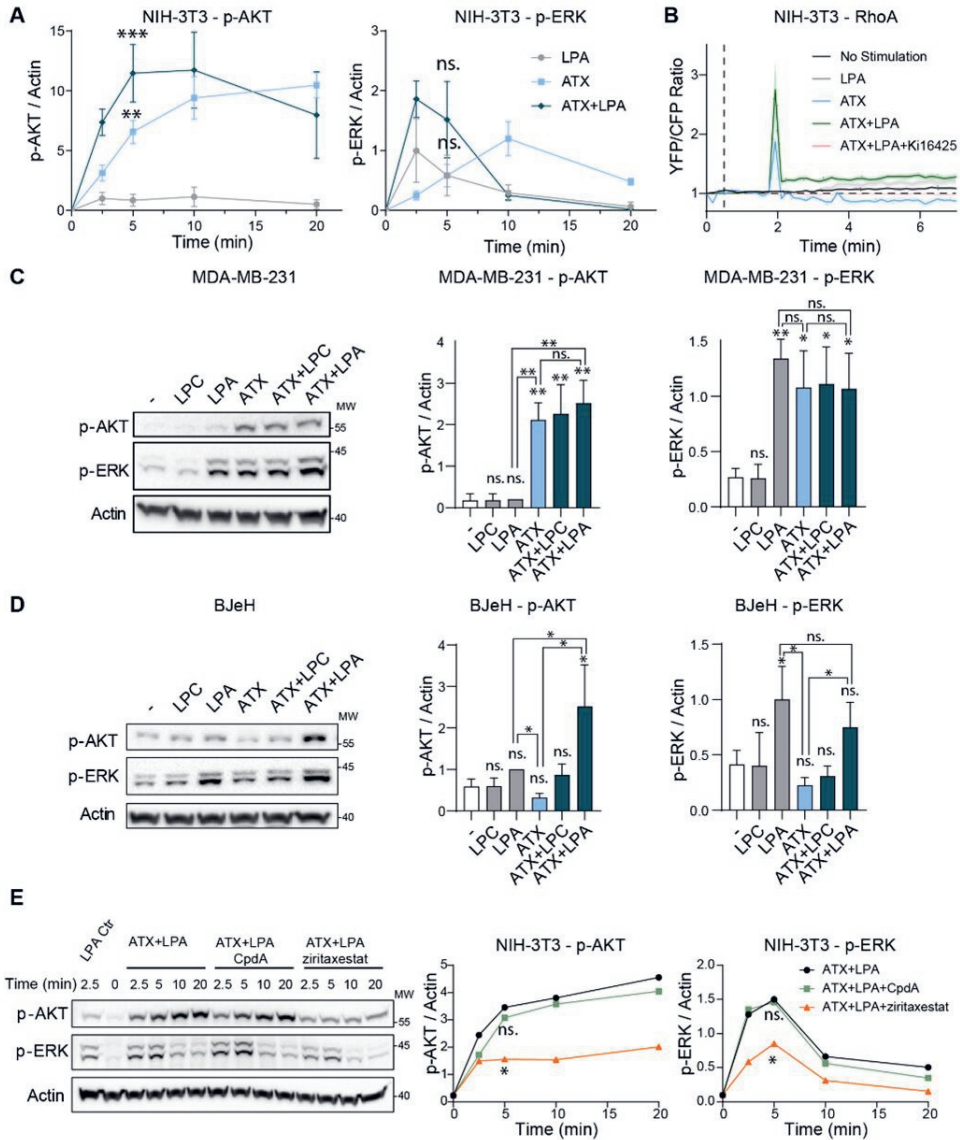


Figure S2. ATX is crucial for triggering LPA signaling. (A) Kinetics of NIH-3T3 cell responses through AKT and ERK activation normalized to LPA control after a 2.5-min stimulation. Quantitation of three independent experiments, shown as the mean \pm SEM. ** $p < 0.01$; *** $p < 0.001$; ns, not significant to 5-min response to LPA alone (one-way ANOVA, Dunnett's post-hoc test). (B) Raw data behind the YFP/CFP fluorescence ratio shown in **Fig. 2B**. The dashed vertical line represents the time of cell stimulation. The ratio was calculated upon time-course stimulation of NIH-3T3 cells with LPA, ATX, or ATX-bound LPA for 10 min in the presence or absence of 5 μ M CpdA or ziritaxestat. (C,D) Activation of AKT and ERK in response to LPC, LPA, ATX, and the combination thereof in (C) MDA-MB-231 and (D) BJeH cells. ATX was preincubated with LPC or LPA for at least 30 min. Quantitation

of three independent experiments, shown as the mean \pm SEM. * $p < 0.05$; ** $p < 0.01$; ns, not significant (when not specified, tested versus negative control) (one-way ANOVA, Dunnett's post-hoc test). (E) Blockade of the activation of AKT and ERK over time by 5 μ M CpdA and ziritaxestat in NIH-3T3 cells. Quantitation of three independent experiments, shown as the mean \pm SEM. * $p < 0.05$; ns, not significant to 5-min response to ATX+LPA (one-way ANOVA, Dunnett's post-hoc test).

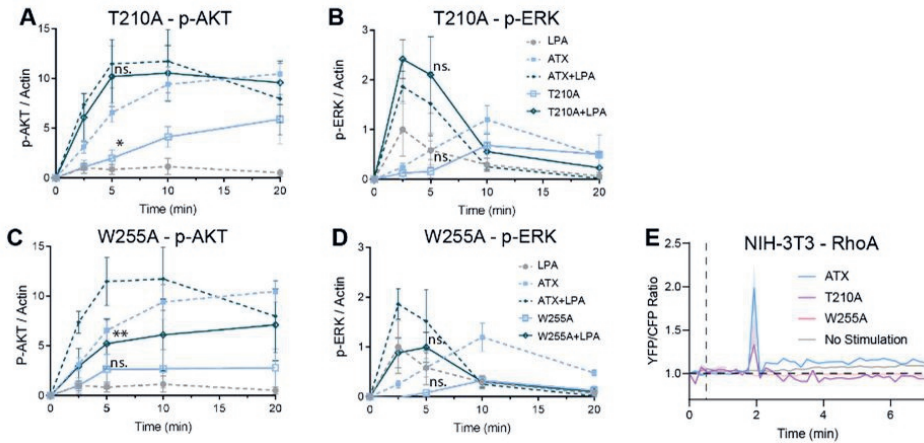


Figure S3. LPA delivery is catalysis independent and requires an intact ATX tunnel. (A–D) Activation of AKT and ERK in NIH-3T3 cells over time upon stimulation with LPA and (A,B) ATX(T210A) or (C,D) ATX(W255A), or LPA bound to each mutant. Quantitation of three independent experiments, shown as the mean \pm SEM. * $p < 0.05$; ** $p < 0.01$; ns, not significant to 5-min response to wildtype ATX bound or unbound to LPA (dashed line, plotted in Fig. S2A) (one-way ANOVA, Dunnett's post-hoc test). (E) Complete time course measure of RhoA activation as YFP/CFP fluorescence ratio from quantitation in Fig. 3. The dashed vertical line represents the time of cell stimulation.

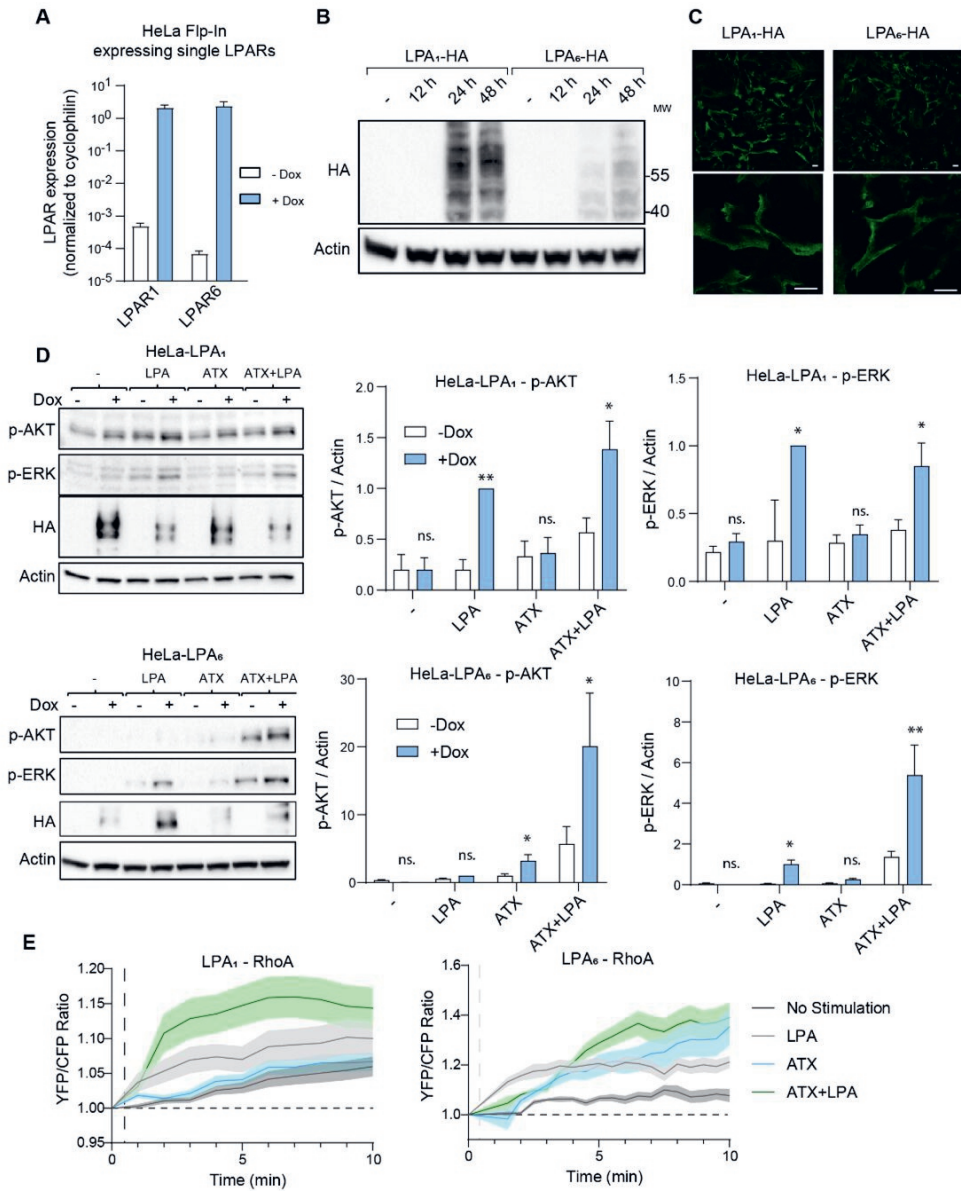


Figure S4. ATX-mediated signaling favors P2Y LPA₆ receptor. (A) qPCR expression of induced HA-tagged LPARs compared with that of uninduced HeLa-Flp-In cells. Ct values were normalized to cyclophilin and presented in logarithmic scale. (B) Representative Western blots and quantitation of uninduced and induced LPA₁-HA- and LPA₆-HA-expressing HeLa-Flp-In cells. (C) Representative confocal microscopy images of LPAR induction and subcellular localization at the plasma membrane. Scale bar represents 10 μ m. (D) Stimulation of HeLa-Flp-In cells that were starved overnight with 0.5% serum-containing medium, where receptor expression was also induced. Left panels, representative

Western blots of AKT and ERK activation; center and right panels, quantitation of p-AKT and p-ERK from three independent experiments, shown as the mean \pm SEM. * $p < 0.05$, ** $p < 0.01$; ns, not significant to non-induced controls (white boxes) (one-way ANOVA, Dunnett's post-hoc test). (E) Complete time-course measure of RhoA activation as YFP/CFP fluorescence ratio from quantitation in **Fig. 4**. The dashed vertical line represents the time of cell stimulation.

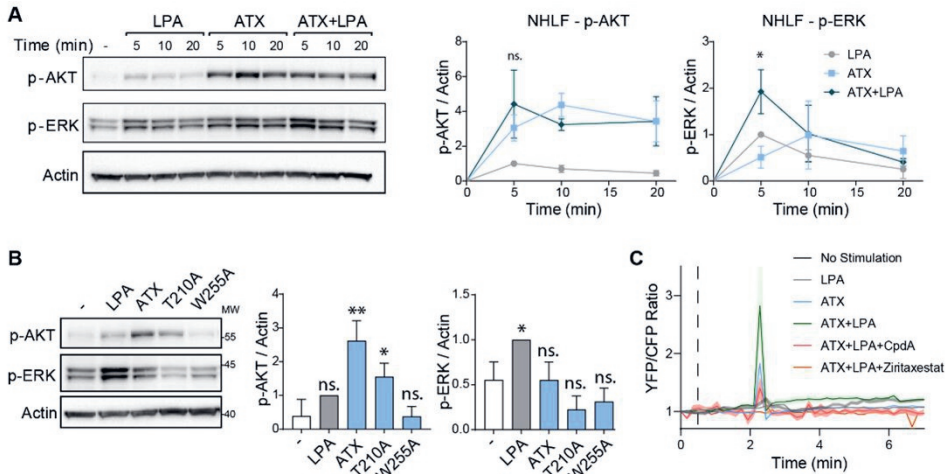


Figure S5. ATX-mediated LPA delivery and signaling in primary lung fibroblasts. (A) NHLFs were serum starved for 16 h and stimulated at different times with LPA (1 μ M), ATX (20 nM), or a mixture of both. Upper panel, representative Western blot; right-hand panels, fold-change of AKT and ERK activation kinetics. Quantitation of three independent experiments, representing the average value of triplicate biological measures \pm SEM (error bars). * $p < 0.05$; ns, not significant to 5-min response to LPA alone (one-way ANOVA, Dunnett's post-hoc test). (B) NHLFs were stimulated with LPA, ATX, catalytically inactive ATX(T210), and tunnel mutant ATX(W255A), and analyzed by Western blotting. Left panel, representative Western blots of AKT and ERK activation (total AKT, total ERK, and actin are shown as loading controls); right panels, quantitation of p-AKT and p-ERK from three independent experiments, representing the average value of triplicate biological measures \pm SEM (error bars). * $p < 0.05$, ** $p < 0.01$; ns, not significant to negative control (one-way ANOVA, Dunnett's post-hoc test). (C) Complete time-course measure of RhoA activation as YFP/CFP fluorescence ratio from quantitation in **Fig. 5**. The dashed vertical line represents the time of cell stimulation.

Table S1. Ziritaxestat, but not CpdA, reverses pulmonary fibrosis *in vivo*. Steady-state pharmacokinetic parameters of CpdA and ziritaxestat.

Steady state Pharmacokinetic parameters

Plasma parameters		Ziritaxestat	CpdA
Female albino C57BL/6J mice		30 mg/kg p.o. b.i.d. MC 0.5 %	10 mg/kg p.o. b.i.d. PEG400/MC 0.5% (20/80)
C_{max}	(ng/mL)	16,600	3,430
T_{max}	(h)	1.5	1
C_{last}	(ng/mL)	488	8.37
AUC (0-6h)	(ng h/mL)	42,400	11,000
AUC (0-18h)	(ng h/mL)	53,500	13,200
AUC (0-24h)	(ng h/mL)	95,900	24,200
Rat LPA assay IC₅₀	(nM)	541	13.6
	(ng/mL)	318	7

AUC(0-24 h) = AUC(0-6 h)+AUC(0-18 h)

References

- [1] K. Yanagida, Y. Kurikawa, T. Shimizu, S. Ishii, *Biochim. Biophys. Acta - Mol. Cell Biol. Lipids*, **2013**, 1831, 33.
- [2] Y. C. Yung, N. C. Stoddard, J. Chun, *J. Lipid Res.*, **2014**, 55, 1192.
- [3] V. A. Blaho, J. Chun, *Trends Pharmacol. Sci.*, **2018**, 39, 953.
- [4] J. E. Chrencik, C. B. Roth, M. Terakado, H. Kurata, R. Omi, Y. Kihara, D. Warshaviak, S. Nakade, G. Asmar-Rovida, M. Mileni, H. Mizuno, M. T. Griffith, C. Rodgers, G. W. Han, J. Velasquez, J. Chun, R. C. Stevens, M. A. Hanson, *Cell*, **2015**, 161, 1633.
- [5] R. Taniguchi, A. Inoue, M. Sayama, A. Uwamizu, K. Yamashita, K. Hirata, M. Yoshida, Y. Tanaka, H. E. Kato, Y. Nakada-Nakura, Y. Otani, T. Nishizawa, T. Doi, T. Ohwada, R. Ishitani, J. Aoki, O. Nureki, *Nature*, **2017**, 548, 356.
- [6] Y. Kihara, M. Maceyka, S. Spiegel, J. Chun, *Br. J. Pharmacol.*, **2014**, 171, 3575.
- [7] a. J. Morris, S. S. Smyth, *J. Lipid Res.*, **2014**, 55, 2195.
- [8] R. Borza, F. Salgado-Polo, W. H. Moolenaar, A. Perrakis, *J. Biol. Chem.*, **2022**, 298, 101526.
- [9] L. A. van Meeteren, P. Ruurs, C. Stortelers, P. Bouwman, M. A. van Rooijen, J. P. Pradere, T. R. Pettit, M. J. O. Wakelam, J. S. Saulnier-Blache, C. L. Mummery, W. H. Moolenaar, J. Jonkers, *Mol. Cell Biol.*, **2006**, 26, 5015.
- [10] D. Yasuda, D. Kobayashi, N. Akahoshi, T. Ohto-Nakanishi, K. Yoshioka, Y. Takuwa, S. Mizuno, S. Takahashi, S. Ishii, *J. Clin. Invest.*, **2019**, 129, 4332.
- [11] I. Ninou, C. Magkrioti, V. Aidinis, *Front. Med.*, **2018**, 5, 1.
- [12] E. Kaffe, C. Magkrioti, V. Aidinis, *Cancers (Basel)*, **2019**, 11
- [13] J. Hausmann, S. Kamtekar, E. Christodoulou, J. E. Day, T. Wu, Z. Fulkerson, H. M. H. G. H. G. Albers, L. A. Van Meeteren, A. J. S. S. Houben, L. Van Zeijl, S. Jansen, M. Andries, T. Hall, L. E. Pegg, T. E. Benson, M. Kasiem, K. Harlos, C. W. V. Vander Kooi, S. S. Smyth, H. Ovaa, M. Bollen, A. J. Morris, W. H. Moolenaar, A. Perrakis, L. A. Van Meeteren, L. Van Zeijl, S. Jansen, M. Andries, T. Hall, L. E. Pegg, T. E. Benson, M. Kasiem, K. Harlos, C. W. V. Vander Kooi, S. Susan, H. Ovaa, M. Bollen, A. J. Morris, W. H. Moolenaar, A. Perrakis, *Nat. Struct. Mol. Biol.*, **2011**, 18, 198.
- [14] H. Nishimasu, S. Okudaira, K. Hama, E. Mihara, N. Dohmae, A. Inoue, R. Ishitani, J. Takagi, J. Aoki, O. Nureki, *Nat. Struct. Mol. Biol.*, **2011**, 18, 205.
- [15] F. Salgado-Polo, A. Perrakis, *Cancers*, 11. 11101577., 2019.
- [16] W.-J. Keune, J. Hausmann, R. Bolier, D. Tolenaars, A. Kremer, T. Heidebrecht, R. P. Joosten, M. Sunkara, A. J. Morris, E. Matas-Rico, W. H. Moolenaar, R. P. Oude Elferink, A. Perrakis, *Nat. Commun.*, **2016**, 7, 11248.
- [17] F. Salgado-Polo, A. Fish, M.-T. Matsoukas, T. Heidebrecht, W.-J. Keune, A. Perrakis, *J. Biol. Chem.*, **2018**, 293, jbc. RA118.004450.
- [18] Z. Fulkerson, T. Wu, M. Sunkara, C. Vander Kooi, A. J. Morris, S. S. Smyth, *J. Biol. Chem.*, **2011**, 286, 34654.
- [19] A. J. S. Houben, X. M. R. Van Wijk, L. A. Van Meeteren, L. Van Zeijl, E. M. A. Van De Westerlo, J. Hausmann, A. Fish, A. Perrakis, T. H. Van Kuppevelt, W. H. Moolenaar, *J. Biol. Chem.*, **2013**, 288, 510.
- [20] S. A. Jethwa, E. J. Leah, Q. Zhang, N. A. Bright, D. Oxley, M. D. Bootman, S. A. Rudge, M. J. O. Wakelam, *J. Cell Sci.*, **2016**, 129, 3948.
- [21] A. Perrakis, W. H. Moolenaar, *J. Lipid Res.*, **2014**, 55, 1010.

- [22] E. Matas-Rico, E. Frijlink, I. van der Haar Àvila, A. Menegakis, M. van Zon, A. J. Morris, J. Koster, F. Salgado-Polo, S. de Kivit, T. Lança, A. Mazzocca, Z. Johnson, J. Haanen, T. N. Schumacher, A. Perrakis, I. Verbrugge, J. H. van den Berg, J. Borst, W. H. Moolenaar, *Cell Rep.*, **2021**, 37
- [23] S. Bickelhaupt, C. Erbel, C. Timke, U. Wirkner, M. Dadrich, P. Flechsig, A. Tietz, J. Pföhler, W. Gross, P. Peschke, L. Hoeltgen, H. A. Katus, H. J. Gröne, N. H. Nicolay, R. Saffrich, J. Debus, M. D. Sternlicht, T. W. Seeley, K. E. Lipson, P. E. Huber, *J. Natl. Cancer Inst.*, **2017**, 109, 1.
- [24] N. Desroy, C. Housseman, X. Bock, A. Joncour, N. Bienvenu, L. Cherel, V. Labeguere, E. Rondet, C. Peixoto, J. Grassot, O. Picolet, D. Annoot, N. Triballeau, A. Monjardet, E. Wakselman, V. Roncoroni, S. Le Tallec, R. Blanque, C. Cottreaux, N. Vandervoort, T. Christophe, P. Mollat, M. Lamers, M. Auberval, B. Hrvacic, J. Ralic, L. Oste, E. van der Aar, R. Brys, B. Heckmann, *J. Med. Chem.*, **2017**, 60, 3580..
- [25] J. Gierse, A. Thorarensen, K. Beltey, E. Bradshaw-pierce, L. Cortes-burgos, T. Hall, A. Johnston, M. Murphy, O. Nemirovskiy, S. Ogawa, L. Pegg, M. Pelc, M. Prinsen, M. Schnute, J. Wendling, S. Wene, R. Weinberg, A. Wittwer, B. Zweifel, J. Masferrer, *J. Pharmacol. Exp. Ther.*, **2010**, 2, 310.
- [26] W.-J. Keune, F. Potjewyd, T. Heidebrecht, F. Salgado-Polo, S. J. F. Macdonald, L. Chelvarajan, A. Abdel Latif, S. Soman, A. J. Morris, A. J. B. Watson, C. Jamieson, A. Perrakis, *J. Med. Chem.*, **2017**, 60, 2006.
- [27] S. W. Nam, T. Clair, C. K. Campo, H. Y. Lee, L. A. Liotta, M. L. Stracke, *Oncogene*, **2000**, 19, 241.
- [28] J. Jumper, R. Evans, A. Pritzel, T. Green, M. Figurnov, O. Ronneberger, K. Tunyasuvunakool, R. Bates, A. Žídek, A. Potapenko, A. Bridgland, C. Meyer, S. A. A. Kohl, A. J. Ballard, A. Cowie, B. Romera-Paredes, S. Nikolov, R. Jain, J. Adler, T. Back, S. Petersen, D. Reiman, E. Clancy, M. Zielinski, M. Steinegger, M. Pacholska, T. Berghammer, S. Bodenstein, D. Silver, O. Vinyals, A. W. Senior, K. Kavukcuoglu, P. Kohli, D. Hassabis, *Nature*, **2021**, 596, 583.
- [29] M. Varadi, S. Anyango, M. Deshpande, S. Nair, C. Natassia, G. Yordanova, D. Yuan, O. Stroe, G. Wood, A. Laydon, A. Žídek, T. Green, K. Tunyasuvunakool, S. Petersen, J. Jumper, E. Clancy, R. Green, A. Vora, M. Lutfi, M. Figurnov, A. Cowie, N. Hobbs, P. Kohli, G. Kleywegt, E. Birney, D. Hassabis, S. Velankar, *Nucleic Acids Res.*, **2022**, 50, D439.
- [30] H. Jin, Y. Yoo, Y. Kim, Y. Kim, J. Cho, Y. S. Lee, *Cancers (Basel)*, **2020**, 12, 1.
- [31] N.-H. Ding, J. J. Li, L.-Q. Sun, *Curr Drug Targets*, **2013**, 14, 1347..
- [32] X. Tang, M. Wuest, M. G. K. Benesch, J. Dufour, Y. Zhao, J. M. Curtis, A. Monjardet, B. Heckmann, D. Murray, F. Wuest, D. N. Brindley, *Mol. Cancer Ther.*, **2020**, 19, 63.
- [33] K. Mross, M. Stefanic, D. Gmehling, A. Frost, F. Baas, C. Unger, R. Strecker, J. Henning, B. Gaschler-Markefski, P. Stopfer, L. de Rossi, R. Kaiser, *Clin. cancer Res. an Off. J. Am. Assoc. Cancer Res.*, **2010**, 16, 311.
- [34] T. Eisen, Y. Shparyk, N. Macleod, R. Jones, G. Wallenstein, G. Temple, Y. Khder, C. Dallinger, M. Studeny, A.-B. Loembe, I. Bondarenko, *Invest. New Drugs*, **2013**, 31, 1283.
- [35] J. K. Fleming, T. R. Glass, S. J. Lackie, J. M. Wojciak, *J. Lipid Res.*, **2016**, 57, 1737.
- [36] D. Mathew, K. N. Kremer, P. Strauch, G. Tigyi, R. Pelanda, R. M. Torres, *Front. Immunol.*, **2019**, 10

- [37] M. Funke, L. Knudsen, D. Lagares, S. Ebener, C. K. Probst, B. A. Fontaine, A. Franklin, M. Kellner, M. Kühnel, S. Matthieu, R. Grothausmann, J. Chun, J. D. J. Roberts, M. Ochs, A. M. Tager, *Am. J. Respir. Cell Mol. Biol.*, **2016**, 55, 105.
- [38] F. V. Castelino, J. Seiders, G. Bain, S. F. Brooks, C. D. King, J. S. Swaney, D. S. Lorrain, J. Chun, A. D. Luster, A. M. Tager, *Arthritis Rheum.*, **2011**, 63, 1405.
- [39] F. V. Castelino, G. Bain, V. A. Pace, K. E. Black, L. George, C. K. Probst, L. Goulet, R. Lafyatis, A. M. Tager, *Arthritis Rheumatol.*, **2016**, 68, 2964.
- [40] I. Nikitopoulou, I. Ninou, N. Manitsopoulos, I. Dimopoulou, S. E. Orfanos, V. Aidinis, A. Kotanidou, *Intensive care Med. Exp.*, **2021**, 9, 12.
- [41] A. M. Tager, P. LaCamera, B. S. Shea, G. S. Campanella, M. Selman, Z. Zhao, V. Polosukhin, J. Wain, B. A. Karimi-Shah, N. D. Kim, W. K. Hart, A. Pardo, T. S. Blackwell, Y. Xu, J. Chun, A. D. Luster, *Nat. Med.*, **2008**, 14, 45.
- [42] E. Helmer, A. Willson, C. Brearley, M. Westerhof, S. Delage, I. Shaw, R. Cooke, S. Sidhu, *Clin. Pharmacol. drug Dev.*, **2022**, 11, 246.
- [43] J. Hausmann, E. Christodoulou, M. Kasiem, V. De Marco, L. A. Van Meeteren, W. H. Moolenaar, D. Axford, R. L. Owen, G. Evans, A. Perrakis, *Acta Crystallogr. Sect. F Struct. Biol. Cryst. Commun.*, **2010**, 66, 1130.
- [44] W. Kabsch, *Acta Crystallogr. Sect. D Biol. Crystallogr.*, **2010**, 66, 133.
- [45] P. R. Evans, *Acta Crystallogr. Sect. D Biol. Crystallogr.*, **2011**, 67, 282.
- [46] A. Vagin, A. Teplyakov, *Acta Crystallogr. Sect. D Biol. Crystallogr.*, **2010**, 66, 22.
- [47] P. Emsley, B. Lohkamp, W. G. Scott, K. Cowtan, *Acta Crystallogr. Sect. D Biol. Crystallogr.*, **2010**, 66, 486.
- [48] G. N. Murshudov, P. Skubák, A. A. Lebedev, N. S. Pannu, R. A. Steiner, R. A. Nicholls, M. D. Winn, F. Long, A. A. Vagin, *Acta Crystallogr. Sect. D Biol. Crystallogr.*, **2011**, 67, 355.
- [49] R. P. Joosten, F. Long, G. N. Murshudov, A. Perrakis, *IUCr*, **2014**, 1, 213.
- [50] V. B. Chen, W. B. Arendall, J. J. Headd, D. A. Keedy, R. M. Immormino, G. J. Kapral, L. W. Murray, J. S. Richardson, D. C. Richardson, *Acta Crystallogr. Sect. D Biol. Crystallogr.*, **2010**, 66, 12.
- [51] K. M. Kedziora, D. Leyton-Puig, E. Argenzio, A. J. Boumeester, B. Van Butselar, T. Yin, Y. I. Wu, F. N. Van Leeuwen, M. Innocenti, K. Jalink, W. H. Moolenaar, *J. Biol. Chem.*, **2016**, 291, 4323.



Chapter A8

Additional publications on autotaxin



Structure-activity relationships of small molecule autotaxin inhibitors with a discrete binding mode

Lisa M. Miller, Willem-Jan Keune, Diana Castagna, Louise C. Young, Emma L. Duffy, Frances Potjewyd, Fernando Salgado-Polo, Paloma Engel García, Dima Semaan, John M. Pritchard, Anastassis Perrakis, Simon J. F. Macdonald, Craig Jamieson, and Allan J. B. Watson

Abstract

Autotaxin (ATX) is a secreted enzyme responsible for the hydrolysis of lysophosphatidylcholine (LPC) to the bioactive lysophosphatidic acid (LPA) and choline. The ATX-LPA signaling pathway is implicated in cell survival, migration, and proliferation; thus, the inhibition of ATX is a recognized therapeutic target for a number of diseases including fibrotic diseases, cancer, and inflammation, amongst others. Many of the developed synthetic inhibitors for ATX have resembled the lipid chemotype of the native ligand; however, a small number of inhibitors have been described that deviate from this common scaffold. Herein, we report the structure-activity relationships (SAR) of a previously reported small molecule ATX inhibitor. We show through enzyme kinetics studies that analogues of this chemotype are noncompetitive inhibitors, and using a crystal structure with ATX we confirm the discrete binding mode.

Published on *Journal of Medicinal Chemistry*. 2017, 60(2): 722-748.

In this project, I contributed to structure-activity relation experiments and data analysis of novel type III autotaxin inhibitors. Their potency was determined by activity assays measuring the hydrolysis rate of lysophosphatidylcholine, autotaxin's physiological substrate. Their binding mode was confirmed to be non-competitive, which was of use in developing the ideas presented in Chapter A2.

Rational design of autotaxin inhibitors by structural evolution of endogenous modulators

Willem-Jan Keune, Frances Potjewyd, Tatjana Heidebrecht, Fernando Salgado-Polo, Simon J. F. Macdonald, Lakshman Chelvarajan, Ahmed Abdel Latif, Sony Soman, Andrew J. Morris, Allan J. B. Watson, Craig Jamieson, and Anastassis Perrakis

Abstract

Autotaxin produces the bioactive lipid lysophosphatidic acid (LPA) and is a drug target of considerable interest for numerous pathologies. We report the expedient, structure-guided evolution of weak physiological allosteric inhibitors (bile salts) into potent competitive Autotaxin inhibitors that do not interact with the catalytic site. Functional data confirms that our lead compound attenuates LPA mediated signaling in cells and reduces LPA synthesis *in vivo*, providing a promising natural product derived scaffold for drug discovery.

Published on *Journal of Medicinal Chemistry*. 2017, 60(5): 2006-2017.

This study presented the synthesis and potency of the first-in-class tunnel-hydrophobic pocket hybrid inhibitors targeting autotaxin. I contributed to their development by means of activity assays and data analysis for the cleavage of lysophosphatidylcholine by autotaxin, which confirmed biochemically that type IV compounds act as competitive inhibitors. This project resulted in the nanomolar-affinity Compound 17 (Cpd17), used in Chapter A2 during hypothesis validation to establish the role of the allosteric tunnel in substrate hydrolysis.

LAHMA: structure analysis through local annotation of homology matched amino acids

Bart van Beusekom, George Damaskos, Maarten L. Hekkelman, Fernando Salgado-Polo, Yoshitaka Hiruma, Anastassis Perrakis and Robbie P. Joosten

Abstract

Comparison of homologous structure models is a key step in analyzing protein structure. With a wealth of homologous structures, comparison becomes a tedious process, and often only a small (user-biased) selection of data is used. A multitude of structural superposition algorithms are then typically used to visualize the structures together in 3D and to compare them. Here, the Local Annotation of Homology-Matched Amino acids (LAHMA) website (<https://lahma.pdb-redo.eu>) is presented, which compares any structure model with all of its close homologs from the PDB-REDO databank. LAHMA displays structural features in sequence space, allowing users to uncover differences between homologous structure models that can be analyzed for their relevance to chemistry or biology. LAHMA visualizes numerous structural features, also allowing one-click comparison of structure-quality plots (for example the Ramachandran plot) and 'in-browser' structural visualization of 3D models.

Published on *Acta Crystallographica D: Structural Biology*. 2021, 77(Pt 1): 28-40.

In this collaboration, I made use of the LAHMA web-based server to analyze novel features of autotaxin, which became apparent through systematic comparison with related homologous structures. Firstly, LAHMA showed that the glycosylation sites Asn53 and Asn410 in autotaxin's sequence did not appear to be glycosylated in all structures, suggesting that this modification may not be essential for protein folding. Secondly, the analysis of co-crystal inhibitor-bound autotaxin structures unveiled that Phe275 acts as a rail switch for accessing the allosteric tunnel. This is achieved by two rotamer groups that differently stabilize molecules occupying the allosteric tunnel, or those spanning both the tunnel and hydrophobic pocket.

Autotaxin impedes anti-tumor immunity by suppressing chemotaxis and tumor infiltration of CD8⁺ T cells

Elisa Matas-Rico, Elselien Frijlink, Irene van der Haar Àvila, Apostolos Menegakis, Maaïke van Zon, Andrew J Morris, Jan Koster, Fernando Salgado-Polo, Sander de Kivit, Telma Lança, Antonio Mazzocca, Zoë Johnson, John Haanen, Ton N Schumacher, Anastassis Perrakis, Inge Verbrugge, Joost H van den Berg, Jannie Borst, Wouter H Moolenaar

Abstract

Autotaxin (ATX; ENPP2) produces lysophosphatidic acid (LPA) that regulates multiple biological functions via cognate G protein-coupled receptors LPAR1-6. ATX/LPA promotes tumor cell migration and metastasis via LPAR1 and T cell motility via LPAR2, yet its actions in the tumor immune microenvironment remain unclear. Here, we show that ATX secreted by melanoma cells is chemorepulsive for tumor-infiltrating lymphocytes (TILs) and circulating CD8⁺ T cells ex vivo, with ATX functioning as an LPA-producing chaperone. Mechanistically, T cell repulsion predominantly involves Gα12/13-coupled LPAR6. Upon anti-cancer vaccination of tumor-bearing mice, ATX does not affect the induction of systemic T cell responses but, importantly, suppresses tumor infiltration of cytotoxic CD8⁺ T cells and thereby impairs tumor regression. Moreover, single-cell data from melanoma tumors are consistent with intratumoral ATX acting as a T cell repellent. These findings highlight an unexpected role for the pro-metastatic ATX-LPAR axis in suppressing CD8⁺ T cell infiltration to impede anti-tumor immunity, suggesting new therapeutic opportunities.

Published on *Cell Reports*. 2021, 37(7): 110013.

This interdisciplinary project explained critical aspects of the function of autotaxin as a lipid chaperone, relating to Chapter A7, where this function is further unraveled. During the characterization of the secretion of autotaxin by relevant cell lines, I performed activity assays and analysis. This allowed the validation of the engineered autotaxin-expressing TC-1 lung epithelial tumor cell line prior to in vivo experiments.

Structure and function of the ecto-nucleotide pyrophosphatase/phosphodiesterase (ENPP) family: Tidying up diversity

Razvan Borza, Fernando Salgado-Polo, Wouter H Moolenaar, Anastassis Perrakis

Abstract

Ecto-nucleotide pyrophosphatase/phosphodiesterase (ENPP) family members (ENPP1-7) have been implicated in key biological and pathophysiological processes, including nucleotide and phospholipid signaling, bone mineralization, fibrotic diseases, and tumor-associated immune cell infiltration. ENPPs are single-pass transmembrane ecto-enzymes, with notable exceptions of ENPP2 (Autotaxin) and ENNP6, which are secreted and glycosylphosphatidylinositol (GPI)-anchored, respectively. ENNP1 and ENNP2 are the best characterized and functionally the most interesting members. Here, we review the structural features of ENPP1-7 to understand how they evolved to accommodate specific substrates and mediate different biological activities. ENPPs are defined by a conserved phosphodiesterase (PDE) domain. In ENPP1-3, the PDE domain is flanked by two N-terminal somatomedin B-like domains and a C-terminal inactive nuclease domain that confers structural stability, whereas ENPP4-7 only possess the PDE domain. Structural differences in the substrate-binding site endow each protein with unique characteristics. Thus, ENPP1, ENPP3, ENPP4, and ENPP5 hydrolyze nucleotides, whereas ENPP2, ENPP6, and ENNP7 evolved as phospholipases through adaptations in the catalytic domain. These adaptations explain the different biological and pathophysiological functions of individual members. Understanding the ENPP members as a whole advances our insights into common mechanisms, highlights their functional diversity, and helps to explore new biological roles.

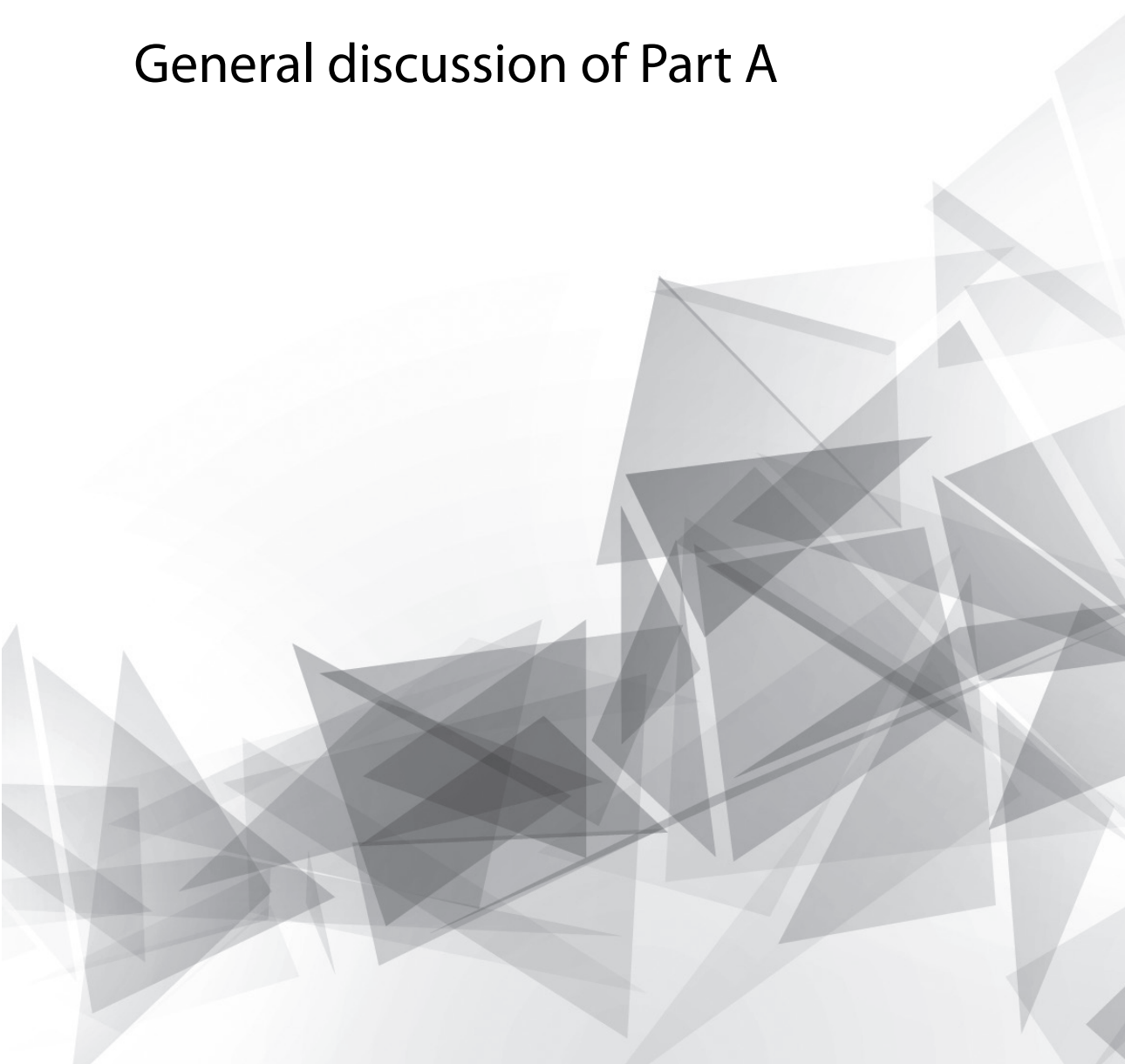
Published on *Journal of Biological Chemistry*. 2022, 298(2): 101526.

This review compared the seven members of the ENPP protein family from a structural perspective. I noticed the "literature gap" in the field, and I suggested writing this review, which I helped R.B. to kick-start and organize, during his start as a PhD student in "Covid-19 times".



Chapter A9

General discussion of Part A



The previous chapters on autotaxin were presented according to the conceptual evolution during the development of Part A of this thesis. However, these advances in the field were only achieved by combining individual contributions from separate chapters.

For this reason, in this chapter I will evaluate the implications of my research following a non-linear approach. First, the advances in understanding autotaxin's catalysis will be analyzed (**Chapter A2**). Second, the novel role of autotaxin as a signaling lipid chaperone will be discussed with a focus on the main future research perspectives (**Chapter 2, 7**). Next, the evolution of the autotaxin inhibitor family, the current pharmacological status, and the related results in this thesis will be discussed (**Chapters 4, 5, 7, 8**). Lastly, the main implications of this thesis in disease treatment will be presented (**Chapters 3, 6, 7**).

Catalytic functions of autotaxin

Autotaxin has long been established as the lysophospholipase D that converts LPC into LPA, but the exact catalytic mechanism remained a subject of study and debate. The first complete characterization of ATX catalysis showed that LPC binding was slow and rate limiting, and offered clear evidence for a model where catalysis first results in choline release, which is followed by the slow release of NBD-LPA (tens of seconds)^[1].

While it is widely accepted that LPA can inhibit hydrolysis of artificial substrates, the literature disagreed on the role of LPA in LPC hydrolysis. An initial study over a decade ago, showed some LPA product inhibition^[2], which has later been disputed^[3]. **Chapter A2** shows that the actual mechanism goes in the opposite direction: several LPA species can increase ATX activity on different natural LPC substrates. This was apparent in the alleviation of the 10-min lag phase in time-course measurements of ATX activity when external LPA was added.

The discovery of the modulation by the allosteric tunnel^[4] offered an opportunity to extend the previous kinetic model. We expanded the classical catalytic cycle with two LPA hydrolysis rates, $k_{cat\ fast}$ and $k_{cat\ slow}$, which defined the lag phase in ATX kinetics. As our results established that the binding of LPA at the tunnel takes place with low affinity ($\sim 1\ \mu\text{M}$), the faster rate is only observed when LPA accumulates (or is added exogenously) and is bound to the tunnel while an LPC binds in the catalytic orthosteric site ($\text{ATX:LPA}_a\text{:LPC}$). Binding of LPA at the ATX tunnel is consistent with earlier results^[5] that attributed residual electron density to (16:0, 18:0, 18:1, 18:3 and 22:6) LPA bound in crystallographic structures of mouse autotaxin.

In **Chapter A2**, another important aspect of this extended kinetic model is presented:

specific LPC/LPA species pairs in the orthosteric and allosteric sites result in different degrees of ATX activity increase. This reflects the *in vivo* situation, where the presence of short LPA species could accelerate the hydrolysis of long LPC species, and *vice versa*. This may create fascinating positive feedback loops between different ATX substrates and products, resulting in still unknown regulatory mechanisms.

Non-catalytic functions of autotaxin

The findings presented in **Chapter A7** support the view that ATX acts as a dual-function protein that can activate signaling pathways by virtue of its unique tunnel, independent of its catalytic activity. The LPA chaperone role has unique characteristics, but also analogies to other lipid chaperones. Albumin is the primary and most abundant LPA chaperone, showing high LPA binding affinity. In our experiments, the albumin concentration was $\sim 8 \mu\text{M}$. The chaperone function of ATX was prominent at as low as 20 nM, in the presence of albumin as a ‘competitor’ for LPA recruitment. Analogies with the S1P lysolipid chaperone are thus apparent. Serum albumin binds S1P, but with lower affinity than HDL-associated apolipoprotein M (ApoM), which serves as the major circulatory S1P chaperone^{[6],[7]}. It has been shown that the ApoM/S1P complex evokes S1PR1-mediated biological responses in a selective manner, distinct from those evoked by albumin-bound S1P. ApoM/S1P thus serves as a ‘biased agonist’ for S1PR1. Unlike ApoM-bound S1P, albumin-bound S1P is short-lived in plasma and activates S1PR1 in a manner distinct from that of ApoM-S1P^[8]. The present results for LPA and ATX point to a similar mechanism, with the distinct peculiarity of the dual enzymatic and chaperone role of ATX.

The additional role of ATX mediating LPA delivery involves specific LPA binding to the ATX tunnel, which is in agreement with a previous hypothesis^[5], and with biochemical evidence and molecular dynamics simulations indicating that the tunnel acts as a secondary binding site (**Chapter A2**). Moreover, LPA binds to and is released from the orthosteric site with $t_{1/2} \approx 0.1 \text{ s}$ and from the tunnel with $t_{1/2} \approx 0.01 \text{ s}$, suggesting that LPA is more readily transferred from the tunnel for delivery to its cognate receptors^[9]. Thus, based on the available evidence, both the tunnel and the hydrophobic LPC/LPA-binding pocket can deliver receptor-active LPA. However, our experiments suggest that an intact tunnel is necessary for this to occur.

A recent study showed that active ATX can bind to the surface of secreted exosomes and carry LPA^[10]. Such an event could lead LPA-bound ATX to the cell surface, after which ATX would release LPA and activate LPARs. Indeed, the authors indicated that it was by this mechanism that ATX yielded activation of LPA₁ and LPA₃ in the employed *in vitro* experimental setup^[10]. However, molecular dynamics simulations and kinetic modelling

presented in **Chapter A2** argue that the presence of LPA in the ATX allosteric tunnel is an independent event, which does not represent an exit pathway of produced LPA by LPC hydrolysis in the adjacent orthosteric site.

A novel finding of **Chapter A7** is that ATX shows greater specificity for LPA₆ over LPA₁ when acting as a lipid chaperone, at least in the context of our reconstituted system, which is supported by receptor expression patterns in tested cell lines. Is this selectivity related to the binding mode of EDG and P2Y LPARs to LPA ligands? The crystal structures of LPA₁^[11] and LPA₆^[12] have suggested two distinct entry modes for LPA: EDG family receptors bind LPA in a well-defined pocket facing the extracellular milieu, while for P2Y family receptors, a pocket is open towards the lateral membrane. It therefore appears likely that ATX binding to the plasma membrane enables efficient LPA transfer to LPA₆ via the lipid bilayer. Another possible explanation is an indirect interaction between LPA-bound ATX and P2Y LPARs, mediated by cell-surface integrins^[13]. Such a pathway could involve β -arrestin-mediated 'biased' signaling, as exemplified by the ApoM-S1PR1 signaling axis^{[6]-[8]}.

Taken together, the evidence is consistent with the role of ATX as an LPA carrier, transporting LPA to distal locations from those where LPC can be taken. LPC is present in the blood at high concentrations (100–200 μM ^[14]); most of it is bound to serum albumin and cannot be "extracted" by ATX because of their similar affinities (approximately 1 μM)^[15], while a small fraction (about 1 μM) is free and can be recognized by ATX^[16].

Autotaxin inhibitors

Following its implication in tumor progression and pulmonary fibrosis, ATX has attracted considerable interest as a drug target from pharmaceutical companies and academic researchers. Structural studies demonstrated that ATX inhibitors exhibit different binding modes. ATX inhibitors entering clinical trials in patients with pulmonary fibrosis or cancer include ziritaxestat, which progressed to phase 3. BBT-877 (Bridge Biotherapeutics Inc., Pangyo, South Korea), IOA-289 (iOnctura SA, Geneva, Switzerland), and cudetaxestat (Blade Therapeutics Inc., South San Francisco, USA) are now in phase 1 or 2 trials and are also type IV (or perhaps, for some, type III) inhibitors, displaying the common characteristic of occupying the ATX tunnel. None of the numerous potent type I orthosteric ATX inhibitors occupy the tunnel^{[17]-[20]}, and none have entered clinical trials, to the best of our knowledge. These data raise the intriguing questions of whether and how the specific drug binding mode determines the physiological outcome of ATX/LPA signaling, both *in vitro* and *in vivo*. Moreover, the efficacy of type V (**Chapter A4** and **A5**) and type VI (**Chapter A5** and **A8**) compounds should be addressed in the context of blocking the role of ATX as an LPA chaperone to further validate the relevance of the ATX tunnel in this mechanism.

In **Chapter A7**, we have addressed this question by examining how type I and type IV ATX inhibitors affect specific LPA receptor-mediated signaling events. We find that type IV compounds are more efficient in inhibiting AKT activation, RhoA activation, cell migration, and receptor internalization. Strikingly, as discussed before, our data suggest that ATX is not only needed for LPA production, but that it can also act as an LPA chaperone. It is this specific chaperone activity that can be targeted by type III or type IV compounds, which occupy the ATX tunnel.

It is worth noting that, even though Ziritaxestat has been trialed as a treatment for IPF and systemic sclerosis, phase 3 trials in patients with IPF were discontinued because the benefit-risk profile of the drug no longer supported continuation. Our present data suggest that the physiological effects of ziritaxestat, which showed promise up onto phase 2b trials, are attributable to its ATX binding mode occupying the ATX tunnel and thereby inhibiting specific signaling events including RhoA-mediated cytoskeletal reorganization. At first sight, this appears at odds with the role of EDG LPARs in IPF, as ziritaxestat shows functional preference for the prototypic P2Y LPAR, LPA₆. However, ziritaxestat also affects LPA₁-mediated signaling, which will contribute to its therapeutic effect. LPA₆ is also present in lung fibroblasts^[21]. Additionally, the therapeutic effect of LPA receptor antagonists in fibrotic diseases, but also in cancer, must be viewed in the context of an interplay with the immune system; LPA₆ is most highly expressed in immune cells, as indicated in **Chapter A8**^[22].

Pathophysiology of autotaxin

Historically, LPA had been identified as a growth factor in serum that could induce motility in fibroblasts and cancer cells through G protein-coupled receptors (GPCRs)^{[26], [27]}. Subsequent research identified specific LPA GPCRs (LPA₁₋₆), which have distinct expression patterns^[28]. Deregulation of the ATX/LPA signaling axis has been linked to different diseases, such as fibrosis^[29], pruritus^[30], multiple sclerosis^[31], inflammation, cancer^{[32], [33]}, and in the initiation and progression of liver disease^[20-25].

In **Chapter A3**, we showed the successful synthesis of fluorinated ATX inhibitors based on the clinical drug candidate, GLPG1690. Biochemical and crystallographic analysis of the most promising candidates for radiofluorination confirmed the compounds' binding mode as type IV inhibitors. [¹⁸F]**20** was the best performing labeled compound in *in vivo* PET studies, and *ex vivo* biodistribution, which encouraged its use in a mouse model of LPS-treated liver injury and inflammation, showing excellent binding specificity. This is one of the first works identifying ¹⁸F-labeled ATX-targeted PET type IV ligands. Its preliminary application in a mouse model of liver injury could serve as an excellent entry point for

further development of clinical applications.

In **Chapter A6**, we showed significant upregulation of ATX gene and protein expression in human liver NASH and cirrhosis patients, which we recapitulated in CCl₄-induced liver injury and MCD diet-induced NASH mouse models. Having confirmed and strengthened the connection between ATX and liver disease, we showed that two different ATX inhibitors, PF8380 (type I) and Cpd17 (type IV) have an effect in a variety of *in vitro* assays in hepatocytes, pro-inflammatory macrophages and activated HSCs. The inhibitors ameliorated the effect of different external stimuli that lead to the induction of fibrotic and inflammatory markers. Among these, we showed a decrease in collagen I contraction of HSCs upon ATX inhibition, a measure of functional cellular activation^[38], and decreased migration of activated HSCs and macrophages. Further cell-based studies shed light on the relevant downstream signaling cascades affected by ATX inhibitor treatment: the RhoA pathway, which relates to cytoskeletal organization and thus to fibrotic phenotypes, and the MAPK/ERK and AKT/PKB pathways, influencing inflammation and fibrogenesis. Moreover, this study showed that Cpd17 has a notably more beneficial potential in treating fibrotic phenotypes, compared to PF8380, which had already shown effectiveness in attenuating CCl₄-induced liver cirrhosis in a previous study^[26].

The excellent *in vitro* and *in vivo* efficacy of Cpd17 in liver disease models, together with GLPG1690 efficacy in treating IPF up to phase 2b trials, and the potential related radiolabeled PET probes, argue that Type IV compounds are promising in treating fibrosis and likely other pathologies related to the LPA/ATX axis. Finally, these results also suggest it worth exploring the role of the ATX/LPA axis and the effect of its inhibition in models of liver cancer, with potential therapeutic opportunities for HCC. This is an ongoing project at the NKI that stems from the conclusions presented in **Chapters 6 and 7**.

References

- [1] L. P. Saunders, W. Cao, W. C. Chang, R. a Albright, D. T. Braddock, E. M. De La Cruz, *J. Biol. Chem.*, **2011**, 286, 30130.
- [2] L. A. Van Meeteren, P. Ruurs, E. Christodoulou, J. W. Goding, H. Takakusa, K. Kikuchi, A. Perrakis, T. Nagano, W. H. Moolenaar, *J. Biol. Chem.*, **2005**, 280, 21155.
- [3] M. G. K. Benesch, Y. Y. Zhao, J. M. Curtis, T. P. W. McMullen, D. N. Brindley, *J. Lipid Res.*, **2015**, 56, 1134.
- [4] W. Keune, J. Hausmann, R. Bolier, D. Tolenaars, A. Kremer, T. Heidebrecht, R. Joosten, M. Sunkara, A. Morris, E. Matas-Rico, W. Moolenaar, R. Oude Elferink, A. Perrakis, *Nat. Commun.*, **2016**, 7, 11248.
- [5] H. Nishimasu, S. Okudaira, K. Hama, E. Mihara, N. Dohmae, A. Inoue, R. Ishitani, J. Takagi, J. Aoki, O. Nureki, *Nat. Struct. Mol. Biol.*, **2011**, 18, 205.
- [6] C. Christoffersen, H. Obinata, S. B. Kumaraswamy, S. Galvani, J. Ahnström, M. Sevvana, C. Egerer-Sieber, Y. A. Muller, T. Hla, L. B. Nielsen, B. Dahlbäck, *Proc. Natl. Acad. Sci. U. S. A.*, **2011**, 108, 9613.
- [7] A. Cartier, T. Hla, *Science*, 366. American Association for the Advancement of Science, Oct. 18, 2019.
- [8] S. Galvani, M. Sanson, V. A. Blaho, S. L. Swendeman, H. Conger, B. Dahlbäck, M. Kono, R. L. Proia, J. D. Smith, T. Hla, *Sci. Signal.*, **2015**, 8, ra79.
- [9] A. Tokumura, J. Sinomiya, S. Kishimoto, T. Tanaka, K. Kogure, T. Sugiura, K. Satouchi, K. Waku, K. Fukuzawa, *Biochem. J.*, **2002**, 365, 617.
- [10] S. A. Jethwa, E. J. Leah, Q. Zhang, N. A. Bright, D. Oxley, M. D. Bootman, S. A. Rudge, M. J. O. Wakelam, *J. Cell Sci.*, **2016**, 129, 3948.
- [11] J. E. Chrencik, C. B. Roth, M. Terakado, H. Kurata, R. Omi, Y. Kihara, D. Warshaviak, S. Nakade, G. Asmar-Rovida, M. Mileni, H. Mizuno, M. T. Griffith, C. Rodgers, G. W. Han, J. Velasquez, J. Chun, R. C. Stevens, M. A. Hanson, *Cell*, **2015**, 161, 1633.
- [12] R. Taniguchi, A. Inoue, M. Sayama, A. Uwamizu, K. Yamashita, K. Hirata, M. Yoshida, Y. Tanaka, H. E. Kato, Y. Nakada-Nakura, Y. Otani, T. Nishizawa, T. Doi, T. Ohwada, R. Ishitani, J. Aoki, O. Nureki, *Nature*, **2017**, 548, 356.
- [13] Z. Fulkerson, T. Wu, M. Sunkara, C. Vander Kooi, A. J. Morris, S. S. Smyth, *J. Biol. Chem.*, **2011**, 286, 34654.
- [14] J. Aoki, A. Taira, Y. Takanezawa, Y. Kishi, K. Hama, T. Kishimoto, K. Mizuno, K. Saku, R. Taguchi, H. Arai, *J. Biol. Chem.*, **2002**, 277, 48737.
- [15] A. E. A. Thumser, D. C. Wilton, *Biochem. J.*, **1995**, 307, 305.
- [16] M. Umezu-Goto, Y. Kishi, A. Taira, K. Hama, N. Dohmae, K. Takio, T. Yamori, G. B. Mills, K. Inoue, J. Aoki, H. Arai, *J. Cell Biol.*, **2002**, 158, 227.
- [17] F. Salgado-Polo, A. Perrakis, *Cancers*, 11. 11101577., 2019.
- [18] Y. Jia, Y. Li, X.-D. Xu, Y. Tian, H. Shang, *Pharmaceuticals*, **2021**, 14, 1203.
- [19] S. Mulholland, H. Adamali, S. L. Barratt, *Clin. Pharmacol. Adv. Appl.*, **2020**, 12, 97.

- [20] iOnctura, 2021. <https://www.ionctura.com/admin/resources/ioa-289sitc-results-9-11final.pdf>
- [21] M. Uhlén, L. Fagerberg, B. M. Hallström, C. Lindskog, P. Oksvold, A. Mardinoglu, Å. Sivertsson, C. Kampf, E. Sjöstedt, A. Asplund, I. M. Olsson, K. Edlund, E. Lundberg, S. Navani, C. A. K. Szigartyo, J. Odeberg, D. Djureinovic, J. O. Takanen, S. Hober, T. Alm, P. H. Edqvist, H. Berling, H. Tegel, J. Mulder, J. Rockberg, P. Nilsson, J. M. Schwenk, M. Hamsten, K. Von Feilitzen, M. Forsberg, L. Persson, F. Johansson, M. Zwahlen, G. Von Heijne, J. Nielsen, F. Pontén, *Science (80-.)*, **2015**, 347
- [22] E. Matas-Rico, E. Frijlink, I. van der Haar Àvila, A. Menegakis, M. van Zon, A. J. Morris, J. Koster, F. Salgado-Polo, S. de Kivit, T. Lança, A. Mazzocca, Z. Johnson, J. Haanen, T. N. Schumacher, A. Perrakis, I. Verbrugge, J. H. van den Berg, J. Borst, W. H. Moolenaar, *Cell Rep.*, **2021**, 37
- [23] L. D. Baker, Y. Fujiwara, K. Pigg, R. Tsukahara, S. Kobatashi, H. Murofushi, A. Uchiyama, K. Murakami-Murofushi, E. Murph, G. B. Mills, G. Tigyi, *J Biol Chem*, **2006**, 281, 22786.
- [24] H. Zhang, X. Xu, J. Gajewiak, R. Tsukahara, Y. Fujiwara, J. Liu, J. I. Fells, D. Perygin, A. L. Parrill, G. Tigyi, G. D. Prestwich, *Cancer Res.*, **2009**, 69, 5441.
- [25] R. Gupte, R. Patil, J. Liu, Y. Wang, S. C. Lee, Y. Fujiwara, J. Fells, A. L. Bolen, K. Emmons-Thompson, C. R. Yates, A. Siddam, N. Panupinthu, T. C. T. Pham, D. L. Baker, A. L. Parrill, G. B. Mills, G. Tigyi, D. D. Miller, *ChemMedChem*, **2011**, 6, 922.
- [26] E. van Corven, A. Groenink, K. Jalink, T. Eichholtz, W. Moolenaar, *Cell*, **1989**, 59, 45.
- [27] K. Jalink, E. J. Van Corven, W. H. Moolenaar, *J. Biol. Chem.*, **1990**, 265, 12232..
- [28] J. Wang, Y. Sun, J. Qu, Y. Yan, Y. Yang, H. Cai, *Expert Rev. Mol. Diagn.*, **2016**, 16, 1103.
- [29] A. M. Tager, P. LaCamera, B. S. Shea, G. S. Campanella, M. Selman, Z. Zhao, V. Polosukhin, J. Wain, B. A. Karimi-Shah, N. D. Kim, W. K. Hart, A. Pardo, T. S. Blackwell, Y. Xu, J. Chun, A. D. Luster, *Nat. Med.*, **2008**, 14, 45.
- [30] A. E. Kremer, J. J. W. W. Martens, W. Kulik, F. Ruëff, E. M. M. Kuiper, H. R. van Buuren, K. J. van Erpecum, J. Kondrackiene, J. Prieto, C. Rust, V. L. Geenes, C. Williamson, W. H. Moolenaar, U. Beuers, R. P. J. Oude Elferink, *Gastroenterology*, **2010**, 139, 1018.e1.
- [31] K. Thirunavukkarasu, B. Tan, C. A. Swearingen, G. Rocha, H. H. Bui, D. J. McCann, S. B. Jones, B. H. Norman, L. A. Pfeifer, J. K. Saha, *J. Pharmacol. Exp. Ther.*, **2016**, 359, 207.
- [32] E. Barbayiannia, E. Kaffeb, V. Aidinisb, G. Kokotos, *Prog. Lipid Res.*, **2015**, 58, 76..
- [33] M. G. K. Benesch, X. Tang, G. Venkatraman, R. T. Bekele, D. N. Brindley, *J. Biomed. Res.*, **2016**, 30, 272.



Part B

Glycerophosphodiester
phosphodiesterases (GDPD)





Chapter B1

Introduction to
glycerophosphodiester
phosphodiesterases (GDPDs)



GPI-anchored proteins

Glycosylphosphatidylinositol (GPI)-anchored proteins at the plasma membrane are involved in the regulation of many vital biological functions, including signal transduction, cell adhesion, intercellular communication and differentiation. GPI anchoring is a complex post-translational modification that tethers membrane proteins, via their C-terminus, to a glycosylated phosphatidylinositol (PI) core in the outer leaflet of the plasma membrane, particularly at lipid raft nanodomains^{[1]-[3]}. Since they lack a transmembrane domain, GPI-anchored proteins cannot transmit signals by themselves but must interact with transmembrane effectors or cellular adhesion pathways to achieve signaling competence. Importantly, GPI anchoring confers a unique property to membrane proteins, namely susceptibility to phospholipase attack. Indeed, GPI-linked proteins can be released from their anchors and detected as soluble proteins in culture medium and body fluids. However, identification of the responsible phospholipase(s) and their biological function has long been elusive.

The GDPD protein family

Recent studies have identified members of the glycerophosphodiester phosphodiesterase (GDPD) family^[4], notably GDE2 and GDE3 (also known as GDPD5 and GDPD2, respectively), as unique GPI-specific phospholipases that cleave select GPI-anchored proteins and thereby alter cell phenotype^{[5]-[7]}. GDE2 is by far the best studied family member and, along with GDE3 and GDE6 (GDPD4), is characterized by six transmembrane helices, a catalytic ectodomain and intracellular N- and C-terminal tails (Fig. 1). GDE2 acts in a phospholipase D (PLD)-like manner, as inferred from its ability to release choline from glycerol-3-phosphocholine *in vitro*^[8]. GDE2 was originally found to drive neuronal maturation and survival in the developing spinal cord^{[9], [10]} through cleavage of GPI-anchored RECK, a Notch ligand regulator, leading to Notch inactivation and induction of neurogenesis in adjacent neural progenitors^[6]. Also in the nervous system, GDE2 promotes neuronal differentiation in a cell-autonomous manner through *cis*-cleavage of glypican-6 (GPC6)^[5]. In this way, GDE2 thus acts in a non-cell-autonomous manner. In marked contrast to GDE2, its close relative GDE3 functions as GPI-specific phospholipase C (PLC) and shows different substrate preference from GDE2, the structural basis of which remains unclear^[7]. In the brain, GDE2 is mainly expressed in neurons and oligodendrocytes, whereas GDE3 expression is restricted to astrocytes, indicative of cell type-specific signaling functions (https://web.stanford.edu/group/barres_lab/brain_rnaseq.html).

Pathophysiology of GDE2

The cleavage of GPC6 by GDE2 was reported by our collaborators at the NKI Elisa Matas-Rico and Wouter Moolenaar, connecting GDE2 activity to the glypican protein family. Glypicans (GPC1–GPC6) are GPI-anchored heparan sulfate proteoglycans (HSPGs) that play key roles in morphogenesis, and can influence signaling cascades and biological functions via various mechanisms, including growth factor recruitment or direct binding to transmembrane receptors such as type-II receptor protein phosphatases (RPTPs)^{[11]–[13]}. Enforced GDE2 expression led to altered Rho GTPase signaling, upregulation of neuronal differentiation markers, neurite outgrowth and resistance to neurite retraction through an as-yet-unknown transmembrane effector pathway^[5]. Moreover, *GDE2* expression strongly correlated with positive clinical outcome in neuroblastoma^[5], an often lethal neurodevelopmental malignancy characterized by impaired differentiation^[14]. Importantly, *Gde2*-knockout in mice leads to progressive neurodegeneration with pathologies reflecting human neurodegenerative disease, which was accompanied by reduced glypican release, implicating dysregulated GPI-anchored protein activity in neurodegeneration^[15]. Finally, GDE2 depletion in zebrafish embryos resulted in motility defects and impaired pancreas differentiation, as shown by reduced insulin expression, which was attributed in part to altered Notch regulation^[16]. Expression of human GDE2 restored insulin expression in these embryos, indicating functional conservation between zebrafish and human GDE2^[16]. Taken together, these results underscore the need for tight control of GDE2 surface expression and activity *in vivo*. However, it remains unknown how GDE2 is regulated.

B1

Scope of Part B of this thesis

Even though some of the biological and phenotypical functions of GDE2 have been characterized, it remains a mystery how its function on the cell surface is regulated. In **Chapter B2**, we wanted to understand how the uniquely long C-terminal tail of GDE2 is important for constitutive endocytosis, and whether this related to surface activity over GPI-anchored proteins. Moreover, as this protein relates to a favorable outcome in neuroblastoma, we wanted to assess how this process affects phenotypical differentiation in model cell lines.

The complementary brain expression patterns of GDE2 (mostly located in motor neurons) and GDE3 (mainly present in glial cells) caught our interest, and drove us to investigate whether these proteins play a role in the development and regulation of glioblastoma. In the preliminary work presented in **Chapter B3**, we wanted to understand whether contactins, key GPI-anchored proteins involved in this brain malignancies, can be recognized as

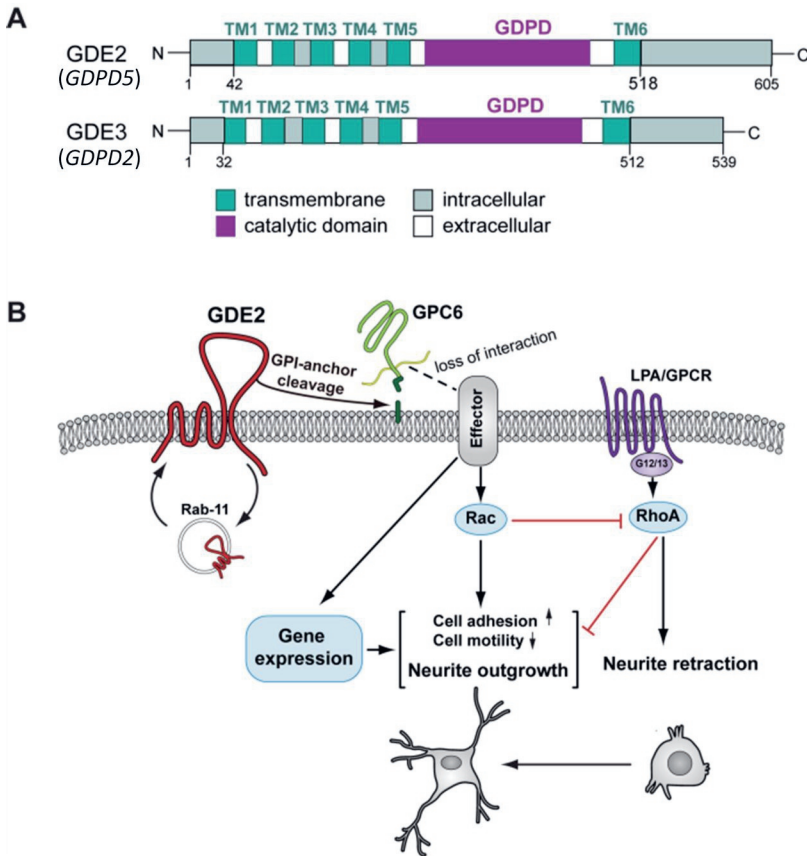


Figure 1. Domain structure and signaling function of GDE2 and GDE3. (A) GDE2 and GDE3 are composed of six transmembrane helices, a catalytic ectodomain responsible for GPI-anchor cleavage, and intracellular N- and C-terminal tails. **(B)** Cleavage of GPC6 by GDE2 in neuroblastoma cells indirectly promotes cell differentiation markers, decreasing tumoral potential. Figure adapted from Matas-Rico et al., 2018^[16].

substrates by GDE2 or GDE3. Additionally, we aimed to evaluate the phenotypical effect of GDE2 expression in glioblastoma invasiveness using an immortalized cell model.

Finally, the findings, implications and future research directions of Part B of this thesis are discussed in **Chapter B4**.

References

- [1] M. A. J. Ferguson, G. W. Hart, T. Kinoshita, A. Varki, R. D. Cummings, J. D. Esko, P. Stanley, G. W. Hart, M. Aebi, A. G. Darvill, T. Kinoshita, N. H. Packer, J. H. Prestegard, R. L. Schnaar, and P. H. Seeberger, *Cold Spring Harbor Laboratory Press*, **2015**, 137.
- [2] M. Fujita, T. Kinoshita, *FEBS Lett.*, **2010**, 584, 1670.
- [3] M. G. Paulick, C. R. Bertozzi, *Biochemistry*, **2008**, 47, 6991.
- [4] D. Corda, M. G. Mosca, N. Ohshima, L. Grauso, N. Yanaka, S. Mariggi?, *FEBS Journal*, **2014**, 281, 998.
- [5] E. Matas-Rico, M. van Veen, D. Leyton-Puig, J. van den Berg, J. Koster, K. M. Kedziora, B. Molenaar, M. J. A. Weerts, I. de Rink, R. H. Medema, B. N. G. Giepmans, A. Perrakis, K. Jalink, R. Versteeg, W. H. Moolenaar, *Cancer Cell*, **2016**, 30, 986.
- [6] S. Park, C. Lee, P. Sabharwal, M. Zhang, C. L. F. Meyers, S. Sockanathan, *Science*, **2013**, 339, 324.
- [7] M. Van Veen, E. Matas-Rico, K. van de Wetering, D. Leyton-Puig, K. M. Kedziora, V. de Lorenzi, Y. Stijf-Bultsma, B. van den Broek, K. Jalink, N. Sidenius, A. Perrakis, W. H. Moolenaar, *Elife*, **2017**, 6, 1.
- [8] M. Gallazzini, J. D. Ferraris, M. B. Burg, *Proc. Natl. Acad. Sci. U. S. A.*, **2008**, 105, 11026.
- [9] M. Rao, S. Sockanathan, *Science (80-.)*, **2005**, 309, 2212.
- [10] P. Sabharwal, C. Lee, S. Park, M. Rao, S. Sockanathan, *Neuron*, **2011**, 71, 1058.
- [11] M. Capurro, T. Izumikawa, P. Suarez, W. Shi, M. Cydzik, T. Kaneiwa, J. Garipey, L. Bonafe, J. Filmus, *J. Cell Biol.*, **2017**, 216, 2911.
- [12] I. Farhy-Tselnicker, A. C. M. van Casteren, A. Lee, V. T. Chang, A. R. Aricescu, N. J. Allen, *Neuron*, **2017**, 96, 428.
- [13] J. S. Ko, G. Pramanik, J. W. Um, J. S. Shim, D. Lee, K. H. Kim, G.-Y. Chung, G. Condomitti, H. M. Kim, H. Kim, J. de Wit, K.-S. Park, K. Tabuchi, J. Ko, *Proc. Natl. Acad. Sci. U. S. A.*, **2015**, 112, 1874.
- [14] N. Ratner, G. M. Brodeur, R. C. Dale, N. F. Schor, *Ann. Neurol.*, **2016**, 80, 13.
- [15] C. Cave, S. Park, M. Rodriguez, M. Nakamura, A. Hoke, M. Pletnikov, S. Sockanathan, *Mol. Neurodegener.*, **2017**, 12, 8.
- [16] M. van Veen, L. A. Mans, E. Matas-Rico, J. van Pelt, A. Perrakis, W. H. Moolenaar, A.-P. G. Haramis, *Int. J. Biochem. Cell Biol.*, **2018**, 94, 71.



Chapter B2

Sequence-dependent trafficking and activity of GDE2, a GPI-specific phospholipase promoting neuronal differentiation

Fernando Salgado-Polo,¹ Michiel van Veen,² Bram van den Broek,² Kees Jalink², Daniela Leyton-Puig,² Anastassis Perrakis,¹ Wouter H. Moolenaar,^{1,*} and Elisa Matas-Rico^{1,*}

Affiliations:

¹Division of Biochemistry, The Netherlands Cancer Institute, Plesmanlaan 121, 1066 CX Amsterdam, The Netherlands.

²Division of Cell Biology, The Netherlands Cancer Institute, Plesmanlaan 121, 1066 CX Amsterdam, The Netherlands.

*Correspondence: w.moolenaar@nki.nl; e.matas@nki.nl.

Based on:

Journal of Cell Science. 2020, 133(3): jcs235044.

Abstract

GDE2 (also known as GDPD5) is a multispanning membrane phosphodiesterase with phospholipase D-like activity that cleaves select glycosylphosphatidylinositol (GPI)-anchored proteins and thereby promotes neuronal differentiation both in vitro and in vivo. GDE2 is a prognostic marker in neuroblastoma, while loss of GDE2 leads to progressive neurodegeneration in mice; however, its regulation remains unclear. Here, we report that, in immature neuronal cells, GDE2 undergoes constitutive endocytosis and travels back along both fast and slow recycling routes. GDE2 trafficking is directed by C-terminal tail sequences that determine the ability of GDE2 to cleave GPI-anchored glypican-6 (GPC6) and induce a neuronal differentiation program. Specifically, we define a GDE2 truncation mutant that shows aberrant recycling and is dysfunctional, whereas a consecutive deletion results in cell-surface retention and gain of GDE2 function, thus uncovering distinctive regulatory sequences. Moreover, we identify a C-terminal leucine residue in a unique motif that is essential for GDE2 internalization. These findings establish a mechanistic link between GDE2 neuronal function and sequence-dependent trafficking, a crucial process gone awry in neurodegenerative diseases.

Introduction

Glycerophosphodiester phosphodiesterase (GDE)2 (GDPD5) and GDE3 (GDPD2) are members of the glycerophosphodiester phosphodiesterase (GDPD) family^[1] that act as glycosylphosphatidylinositol (GPI)-specific phospholipases, yielding release of their targeted GPI-anchored proteins off the plasma membrane. As GPI-anchored proteins are involved in regulating cell signaling, adhesion, communication and differentiation, cleavage by GDE2 or GDE3 results in phenotypic alteration^{[2]-[4]}.

GDE2 and GDE3 are multi-pass membrane proteins that present six transmembrane helices, a conserved catalytic ectodomain and intracellular N- and C-terminal tails of unknown functions (Fig. 1A,B). In neuronal cell lines, high GDE2 expression has been associated with favorable outcome in neuroblastoma, the third most common type of cancer in children^[2]. *In vivo*, GDE2 knockout mice suffer from late-onset neuronal degeneration in the spinal cord, a phenotype reminiscent of human neurodegenerative disease (ALS)^[5]. Behavioral motor deficits have also been observed in GDE2-depleted zebrafish embryos^[6]. These intriguing results suggest that enforcing GDE2 surface expression and activity could be a therapeutic strategy for neuroblastoma and neurodegenerative disease. However, little is known how GDE2 surface localization is regulated.

Here, we report that, in undifferentiated neuronal cells, GDE2 is regulated by membrane trafficking under control of its long C-terminal tail. Membrane trafficking is of vital importance for cellular homeostasis and numerous signaling processes, particular in the nervous system, and its dysregulation can lead to disease. We identify distinctive C-terminal sequences that govern GDE2 exocytosis, endocytosis and recycling preference, and thereby modulate GDE2 biological activity both positively and negatively. In particular, through consecutive truncations, GDE2 recycling preference and cell-surface expression can be manipulated to render GDE2 either dysfunctional or hyperactive. Importantly, we discover a leucine residue in a non-canonical sorting motif that is key for GDE2 endocytosis and ensuing recycling. Together, our results reveal the sequence determinants of GDE2 trafficking and activity, thus providing mechanistic insight into cell-intrinsic GPI-anchor cleavage and its (neuro)biological outcome. Since membrane trafficking is impaired in neurodegenerative diseases, while GDE2 protects against neurodegeneration in mice, our findings may have pathophysiological implications, as will be discussed.

Results

GDE2 trafficking – constitutive endocytosis and recycling

Initial pilot studies showed that in undifferentiated neuronal cells, GDE2 is enriched

in recycling endosomes, strongly suggesting regulation by membrane trafficking^[2]. We analyzed GDE2 trafficking in SH-SY5Y and N1E-115 neuronal cells, which resemble immature sympathetic neurons and express very low levels of endogenous GDE2^[2]. GDE2 [tagged with HA, GFP or mCherry (mCh)] was detected in discrete microdomains or clustered nanodomains, as revealed by super-resolution microscopy^[2]; Fig. 1C). Intracellularly, GDE2 was particularly abundant in perinuclear vesicles (Fig. 1C). Of note, untagged GDE2 showed similar subcellular localization to tagged versions of GDE2 in both neuronal cell lines (Fig. S1A). GDE2–GFP-containing vesicles in single SH-SY5Y cells were highly mobile and show rapid bi-directional movement towards and from the neurite ending, as shown by live-imaging (Movie 1). Treatment with the dynamin inhibitor dynasore resulted in GDE2 accumulation at the plasma membrane with almost complete loss of GDE2-positive vesicles (Fig. S1B). Furthermore, we confirmed that GDE2 colocalized with the endogenous transferrin receptor (TfR), a prototypic cargo of the clathrin-dependent endocytosis route (Fig. S1C). From these results, we conclude that GDE2 undergoes classical clathrin- and dynamin-mediated internalization^[7]. GDE2 internalization via a parallel clathrin-independent pathway cannot formally be excluded, but is unlikely to make a substantial contribution since more than 90% of the earliest detectable endocytic vesicles in mammalian cells arise from clathrin-coated pits^[8]. Finally, it is worth noting that endosomal GDE2 lacks signaling activity as its catalytic ectodomain is exposed to the vesicle lumen, not to the cytoplasm.

Rab GTPases are highly specific master regulators of membrane trafficking and play key roles in maintaining neuronal function^{[9], [10]}. In both neuronal cell lines, GDE2–GFP colocalized with the early endosome marker Rab5–mCh (Fig. 1D; Fig. S2A), but the majority of intracellular GDE2 was detected in the Rab4- and Rab11-regulated recycling routes, known as the ‘fast’ and ‘slow’ routes, respectively (Fig. 1D; Fig. S2A). Rab4 (Rab4a and Rab4b)-mediated fast recycling involves a half-time of a few minutes, whereas Rab11 (Rab11a and Rab11b) regulates slow recycling with a half-time of >10 min^[11]. A small proportion of GDE2 was detected in Rab7-positive (Rab7⁺; Rab7a and Rab7b) late endosomes, which deliver cargo to lysosomes for degradation, and a small fraction of GDE2 was indeed found in LAMP1-positive lysosomes (Fig. S3). Quantification of the results from both neuronal cell lines showed that GDE2 predominantly localized to Rab11⁺ endosomes (mean ~60%), somewhat less to Rab5⁺ and Rab4⁺ endosomes (mean 30–45%, depending on the cell line), and much less to Rab7⁺ late endosomes and lysosomes (Fig. 1D; Fig. S3). In support of the colocalization results, biochemical studies using co-transfected HEK293 cells showed GDE2 formed a complex with Rab4, Rab5, Rab7 and Rab11 (Fig. S2B).

We measured GDE2 internalization and recycling in both neuronal cell lines using a biotin labeling procedure, in which biotinylated GDE2–HA was allowed to internalize at 37°C in the presence or absence of serum. The biotin moiety was then removed from the

cell-surface GDE2 pool using the membrane-impermeant reducing agent MESNa at 4°C. Internalized GDE2 was triggered to recycle back by a temperature shift from 4°C to 37°C (Fig. 1E). As shown in Fig. 1F and Fig. S2C, internalized GDE2 was found to travel back to the plasma membrane within 15 to 30 min in both SH-SY5Y and N1E-115 cells, independent of serum stimulation. We therefore conclude that GDE2 endocytosis and recycling is a constitutive process and insensitive to serum factors.

C-terminal tail truncations uncover unique regulatory sequences

To explore the sequence determinants of GDE2 endocytosis and recycling, we focused on the long C-terminal tail [amino acids (aa) 518–605] (Fig. 2A). Motif searching did not reveal canonical tyrosine-based or acidic dileucine-based endocytic motifs^{[12], [13]}, nor known protein interaction motifs. It is noteworthy that the distal C-terminal region (aa 570–605) of GDE2 shows marked sequence divergence among vertebrates (Fig. 2A), suggesting that these last 35 residues are not of major importance for GDE2 function but rather may play a species-specific role.

We made consecutive truncations in the C-terminal tail of GDE2 (Fig. 2A) and analyzed their colocalization with Rab5, Rab4 and Rab11 in N1E-115 cells. GDE2(Δ C570) showed the same subcellular localization as full-length GDE2, confirming that the last 35 residues are dispensable for proper GDE2 localization (Fig. 2B). GDE2(Δ C560) showed reduced surface expression (see also Fig. 4A,B below) and less colocalization with Rab11; remarkably, it accumulated preferentially in Rab4⁺ fast recycling endosomes at the expense of Rab11 colocalization (Fig. 2B–F). This suggests that the aa 561–570 region contains signaling information for balanced endocytic recycling of GDE2 (i.e. Rab4⁺ versus Rab11⁺ routing). GDE2(Δ C550), which has a further consecutive 10-aa truncation, is retained at the plasma membrane with no evidence of endosomal GDE2 (Fig. 2C–E), suggesting that the aa 551–560 stretch contains an essential endocytosis signal. Upon further truncation (at aa 540 or 530), GDE2 remained trapped intracellularly as aggregates (Fig. 2B–F), with GDE2(Δ C530) accumulating in lysosomes (Fig. S3). The respective GDE2–Rab protein colocalization results are quantified in Fig. 2F. We conclude that the aa 530–550 juxtamembrane region is required for proper GDE2 expression and exocytosis, while the aa 551–570 stretch contains all relevant trafficking information.

Sequence determinants of GDE2 trafficking and cell surface expression

To determine the sequence determinants of GDE2 trafficking in further detail, we turned to SH-SY5Y cells stably expressing doxycycline (Dox)-inducible GDE2^[2]. GDE2, its deletion mutants and catalytically dead GDE2(H233A) showed maximal expression after 24–48 h of Dox treatment; we also found that GDE2(Δ C540) and GDE2(Δ C530) were very poorly expressed (Fig. S4A). GDE2 trafficking was monitored during 30 min. in the presence of 10% serum using the biotin-labeling procedure (cf. Fig. 1E). As shown in Fig. 3A,B, GDE2-FL

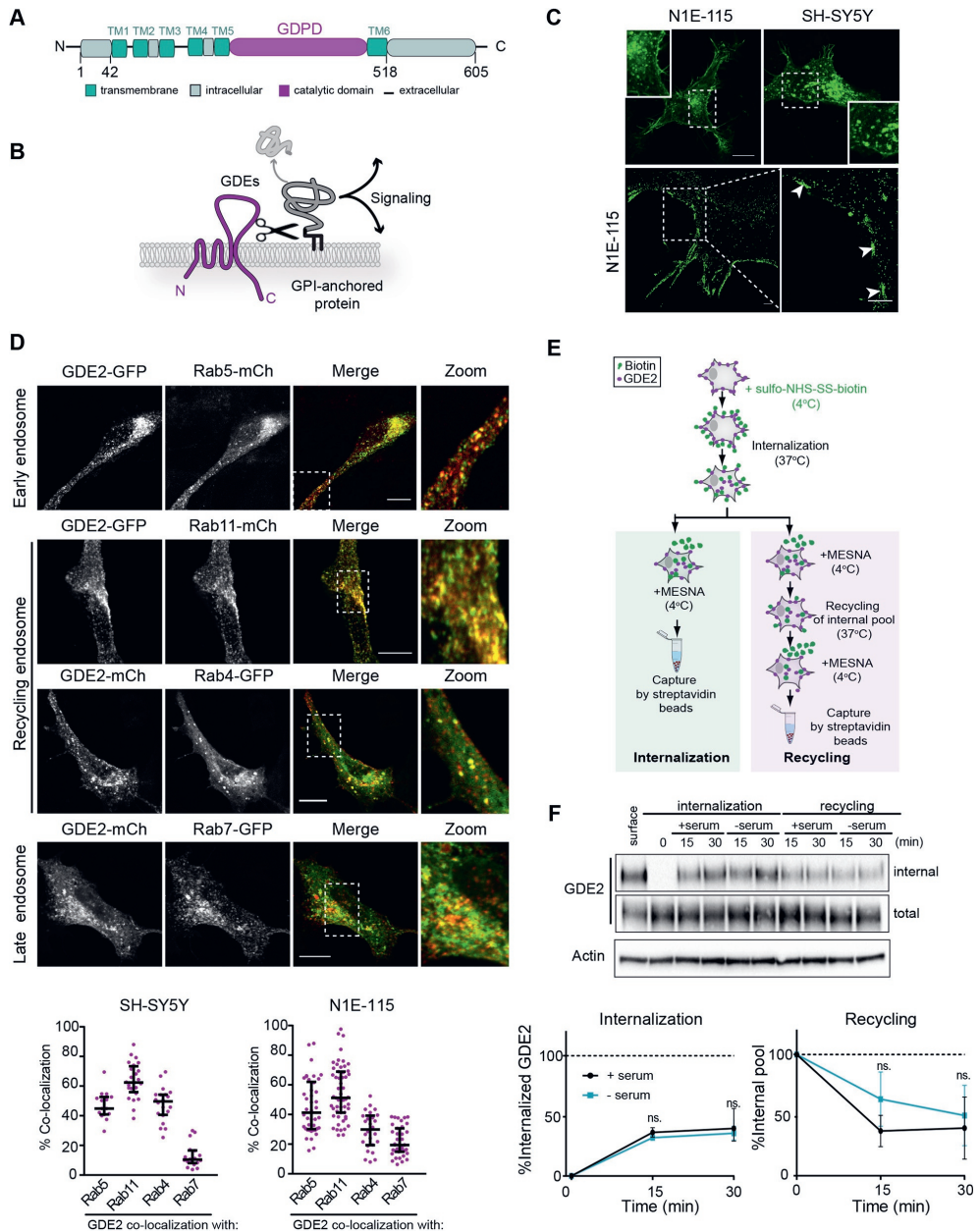


Figure 1. GDE2 localization and endocytic trafficking routes. (A) Domain structure of GDE2 showing six transmembrane (TM) domains, a GDPD ectodomain and intracellular N- and C-terminal tails. (B) GDE2 cleaves and sheds GPI-anchored proteins resulting in activation of signaling cascades. (C) GDE2 subcellular localization. Top, confocal images showing GDE2-GFP in membrane microdomains and intracellular vesicles in N1E-115 and SH-SY5Y cells. Bottom, super-resolution images of N1E-115 cells expressing GDE2-GFP. White arrows point to membrane microdomains. (D) GDE2-GFP co-localization with various Rab proteins in different endosomal compartments. (E) Schematic of GDE2 internalization and recycling. (F) Western blot and line graph showing GDE2 internalization and recycling. 'ns.' indicates no significant difference.

Scale bars: 10 μm (top), 1 μm (bottom). See also^[2]. (D) Confocal images of GDE2 in early, recycling and late endosomes (Rab5-, Rab11-, Rab4- and Rab7-positive, respectively), in SH-SY5Y cells. Scale bars: 10 μm . Bottom panels show quantification of GDE2 colocalization with the indicated Rab GTPases, expressed as the percentage of yellow versus red pixels (≥ 25 cells from three independent experiments). Data represent the median \pm interquartile range of colocalization. (E) Schematic illustration of the internalization and recycling assay using biotin labeling. Cells expressing GDE2-mCh were surface-labeled with NHS-S-S-Biotin. Internalization proceeded for 15 and 30 min at 37°C in presence or absence of 10% FBS. Surface biotin was reduced with MesNa at 4°C, and the cells were shifted to 37°C for the indicated time periods to trigger recycling of the internal pool. (F) The amount of internalized and total biotin-labeled GDE2 in SH-SY5Y cells was determined by immunoblotting using anti-HA antibody. Actin was used as loading control. SH-SY5Y cells inducibly expressing GDE2-HA were surface-labeled with NHS-S-S-Biotin. Labeled GDE2 was allowed to internalize or recycle in the presence or absence of 10% FBS, as indicated. Representative western blots are shown as well as quantified band density from three independent experiments. Internalization was normalized to surface GDE2, and recycling to the internalized pool after 30 min. Data represent the mean \pm s.e.m. Results were not significantly different (ns) between with or without serum (one-way ANOVA). Similar results were obtained in N1E-115 cells (Fig. S2C).

and GDE2(Δ C570) showed similar internalization and recycling kinetics, whereas recycling of the GDE2(Δ C560) internal pool was strongly reduced. By contrast, GDE2(Δ C550) underwent negligible internalization with no recycling. These results fully support those obtained in N1E-115 cells (Fig. 2).

After Dox treatment, the GDE2 truncation mutants showed a differential distribution between plasma membrane and endocytic vesicles that was very similar to that in N1E-115 cells (Fig. 4A). Quantitative microscopic analysis (Fig. 4B) showed that full-length GDE2 (GDE2-FL) and GDE2(Δ C570) displayed similar surface-to-cytoplasm ratios, while GDE2(Δ C550) showed a much higher ratio, in agreement with its retention at the plasma membrane. GDE2(Δ C560) showed a reduced ratio, as it preferentially accumulates in fast recycling endosomes (Fig. 4B). GDE2(Δ C530) showed virtually no expression at the plasma membrane, while catalytically dead GDE2(H233A) showed a surface-to-cytoplasm ratio identical to wild-type, confirming that GDE2 trafficking and surface expression are independent of catalytic activity^[2].

To quantify the relative surface expression levels, we biotin labeled cell surface GDE2-HA, which was then immunoprecipitated and detected by western blot. Analysis of the ratio of surface expression over total protein expression confirmed that GDE2 (Δ C570) behaved like GDE2-FL while GDE2(Δ C560) surface levels were strongly decreased when compared to GDE2-FL (Fig. 4C,D). Finally and consistent with the above results, cell surface expression of endocytosis-incompetent GDE2(Δ C550) was strongly enriched.

We also measured the expression of GDE2 truncation mutants by flow cytometry (FACS) (Fig. 5A), using catalytically dead GDE2(H233A) as control (Fig. S4B). In agreement with the biotin-labeling results, GDE2-FL and GDE2(Δ C570) showed similar cell surface levels while GDE2(Δ C560) expression was reduced (Fig. 5A, left panel). However, this analysis did not reveal enhanced plasma membrane expression of GDE2(Δ C550), which we attribute to limitations inherent to FACS.

Sequence-dependent trafficking determines GPC6-shedding activity of GDE2

To assess how GDE2 trafficking relates to activity, we used the above FACS conditions to measure GDE2 catalytic activity towards endogenous GPC6, a preferred GPI-anchored substrate of GDE2 in neuronal cells^[2] (Fig. 5A; Fig. S4B). Catalytic activity of GDE2 and its truncation mutants towards GPC6 correlated with their respective surface levels. However, GDE2(Δ C560) was dysfunctional, as it failed to cause shedding GPC6 from SH-SY5Y cells (Fig. 5A, left panel). Interestingly, this apparent loss of GPC6-shedding activity correlates with the preference of GDE2(Δ C560) for fast recycling in combination with its reduced expression at the plasma membrane. Our efforts to detect GDE2-induced GPC6 accumulation in the medium were unsuccessful because of high background levels of GPC6 in SH-SY5Y cells.

We therefore used a different method to measure GDE2-induced GPC6 accumulation release in the medium. For this, we used transiently transfected HeLa cells co-expressing mutant GDE2-HA and GPC6-GFP (Fig. S5). HeLa cells express low levels of endogenous GPC6 and show similar subcellular localizations of GDE2-HA and its mutants to that observed in neuronal cells (Fig. S5A). Cell lysates and supernatants were analyzed for GPC6-GFP by western blotting (Fig. S5B). The quantified results (Fig. S5C) indicate that endocytosis-incompetent GDE2(Δ C550) now showed a nearly two-fold higher GPC6-shedding efficacy than GDE2-FL, indicative of 'hyperactivity' and in agreement with its greater abundance on the plasma membrane. On the other hand, GDE2(Δ C560) was not completely dysfunctional towards GPC6 shedding under these alternate assay conditions.

GDE2 regulation of neuronal differentiation genes

GDE2 regulates a neural differentiation transcriptional program, as shown by overexpression and knockdown studies^[2]. Building on those results, we investigated how GDE2 truncation affects the expression of select neuronal differentiation marker genes, including those encoding key transcription factors (SOX2, PAX6, NEUROD1), neurotrophin receptors (NGFR, NTRK2 and SLITRK6), presynaptic t-SNARE protein SNAP25, GPI-anchored neurotrimin (NTM), neuron-specific enolase (NSE) and cytoskeletal proteins (NES, MAP2 and TUJ1) and others. Induction of these genes by the respective GDE2 truncation mutants mirrored the induction of GPC6 release, albeit to varying degrees

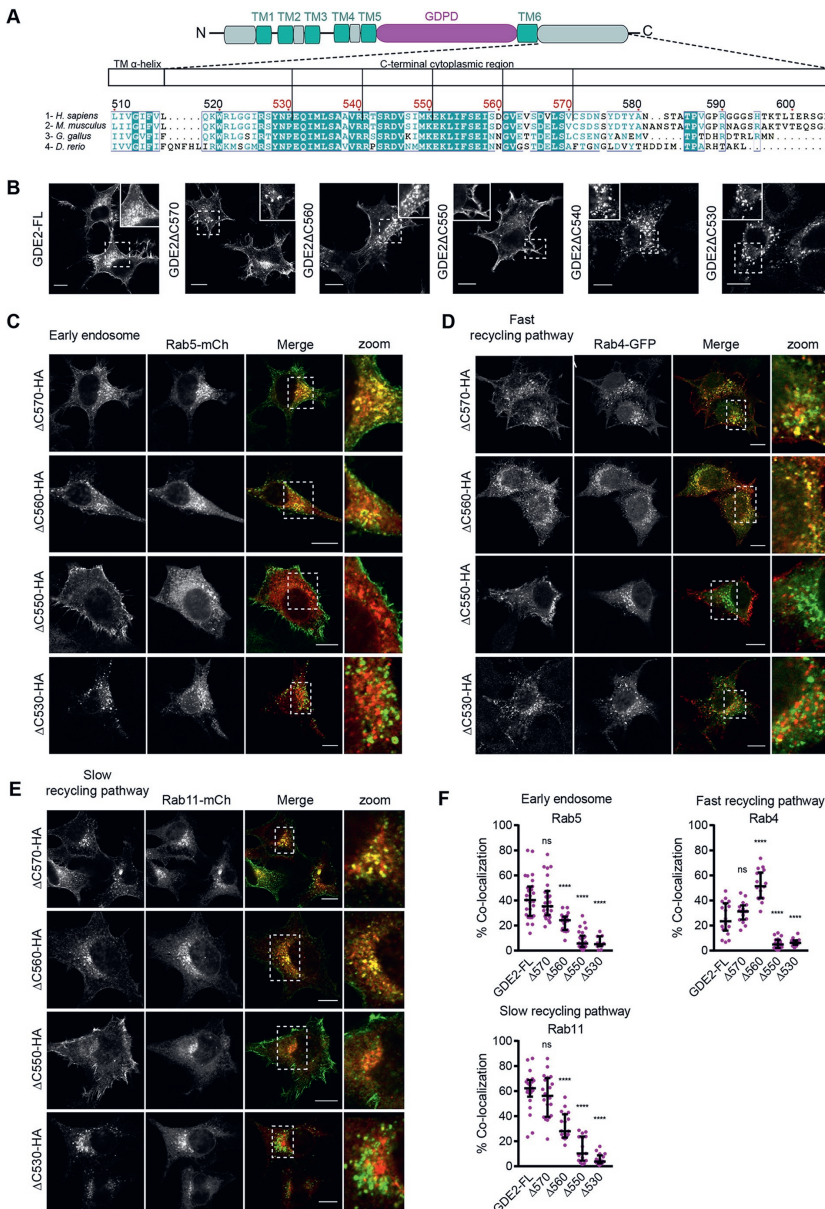


Figure 2. C-terminal tail truncations uncover unique regulatory sequences. (A) C-terminal sequence alignments of human, mouse, chicken and zebrafish GDE2, and a diagram of the truncation mutants in human GDE2 used in this paper. Note poor sequence conservation in the very C-terminal residues. (B) Subcellular localization of GDE2-HA and its truncation mutants in N1E-115 cells. (C–E) Confocal images of N1E-115 cells co-expressing the indicated GDE2 C-terminal truncations, and Rab5-mCh (C), Rab4-GFP (D) and Rab11-mCh (E). (F) Quantification of GDE2-Rab colocalization (percentage of yellow versus red pixels for ≥ 25 cells from three independent experiments). Data represent the median \pm interquartile range of colocalization. ****P<0.0001; ns, not significant (one-way ANOVA). Scale bars: 10 μ m.

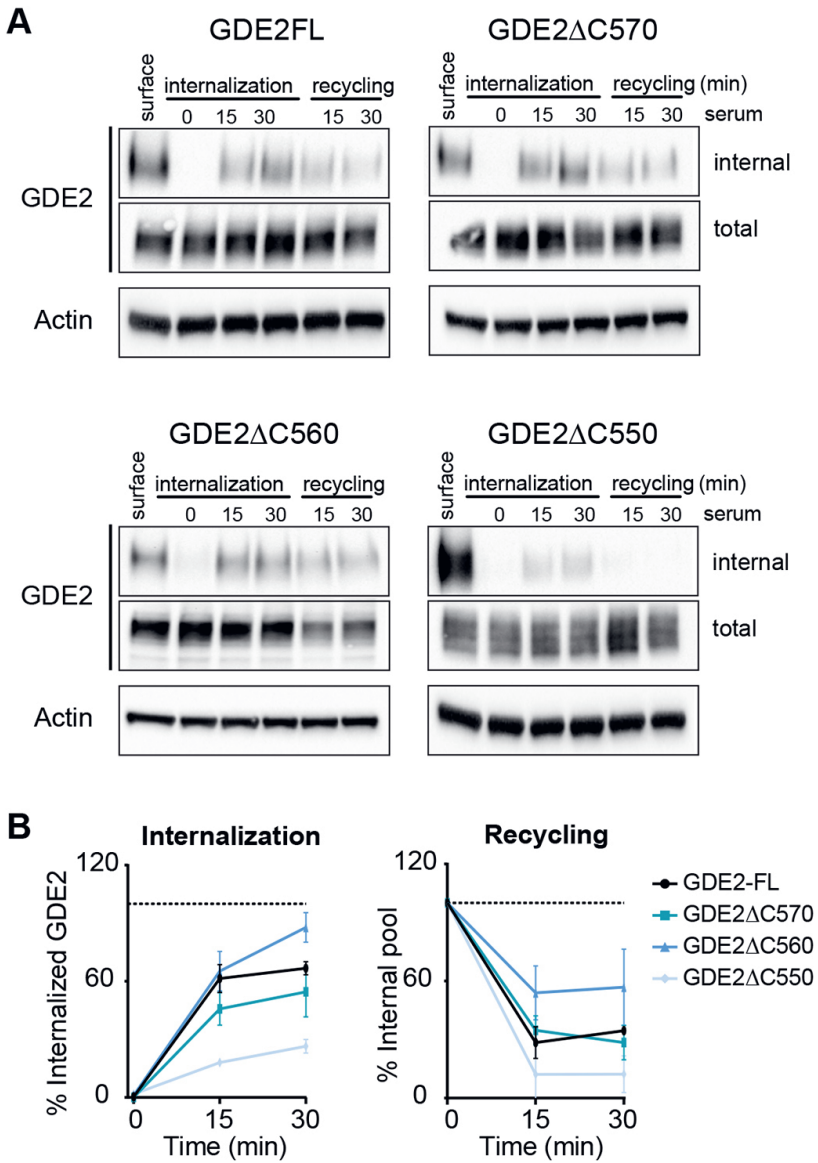


Figure 3. C-terminal truncations impair internalization and recycling of GDE2. (A) Internalization and recycling of GDE2-FL and its C-terminal truncations was followed during 30 min. SH-SY5Y cells inducibly expressing GDE2-HA (Fig. S4A) were surface-labeled with NHS-S-S-Biotin. Labeled GDE2 was allowed to internalize or recycle in the presence of 10% FBS as indicated. Representative western blots are shown. (B) Quantification of band density from three independent experiments. Internalization was normalized to surface GDE2, and recycling to the internalized pool after 30 min. Data represent the mean±s.e.m.

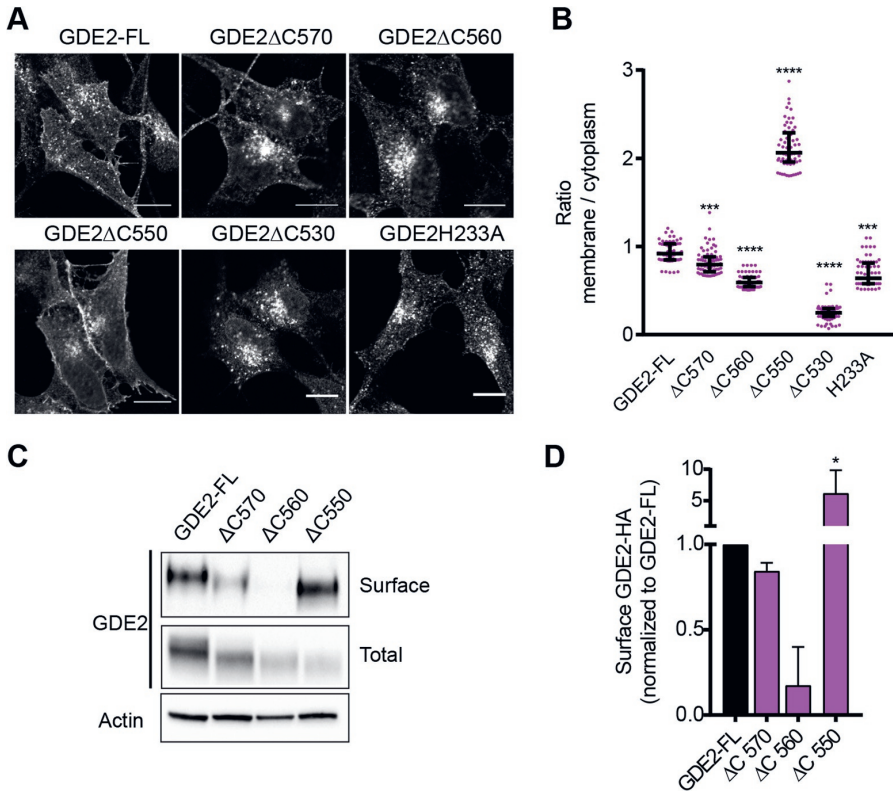


Figure 4. Localization and trafficking of GDE2 and its C-terminal truncations. (A) Localization of GDE2 and the indicated C-terminal truncation construct in Dox-treated SH-SY5Y cells (48 h). See also Fig. S4A. (B) Quantification of GDE2 surface versus cytosol localization in inducible SH-SY5Y cells (24 h). At least 20 cells from three independent preparations were segmented and analysed by ImageJ to calculate the membrane:cytoplasmic signal ratio (median \pm interquartile range); *** P <0.001, **** P <0.0001 (one-way ANOVA). (C) SH-SY5Y cells inducibly expressing GDE2-HA were surface-labeled with NHS-S-S-Biotin, immunoprecipitated with streptavidin beads and analyzed by western blotting. (D) Quantification of band density for surface expression normalized to GDE2-FL (median \pm s.e.m.); * P <0.05 (one-way ANOVA).

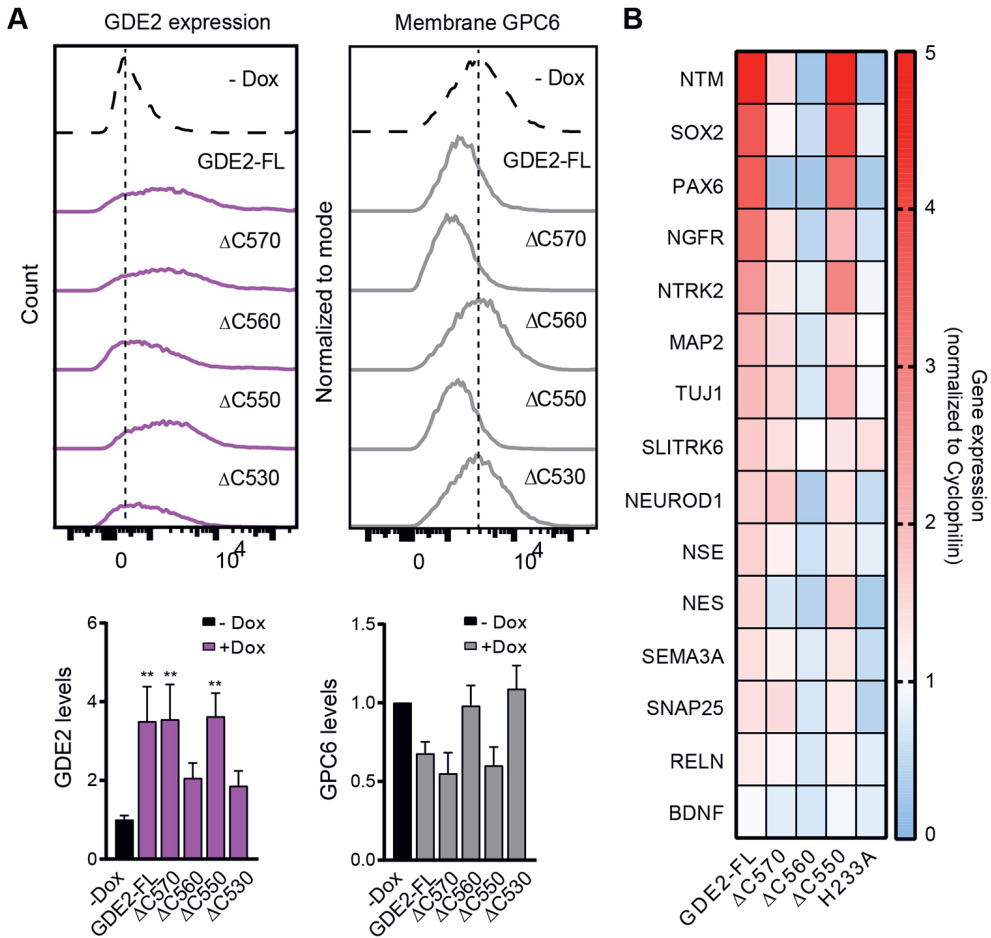


Figure 5. Sequence-dependent trafficking determines GDE2 biological activity. (A) Left panel, surface expression of GDE2–HA and its truncated mutants upon Dox-induced (48 h) expression, as detected by flow cytometry. Right panel, GPC6 surface levels as a function of GDE2–HA expression compared to that in GDE2-deficient cells (–Dox), as detected by flow cytometry using an anti-GPC6 antibody. In both cases, representative histograms from the same experiment are shown. Lower panels, quantifications (mean \pm s.e.m.) of the above FACS data from three independent experiments. ** $P < 0.001$ (one-way ANOVA). (B) Induction of neuronal differentiation marker genes upon Dox-induced expression of the indicated GDE2 constructs as determined by RT-qPCR and shown in a heat map. For quantification see Fig. S4C.

(Fig. 5B; Fig. S4C). GDE2($\Delta C570$) lacked full signaling activity, although it showed wild-type trafficking behavior and activity towards GPC6. Remarkably, however, GDE2($\Delta C560$) showed again loss-of-function as it failed to induce significant gene transcription similar to that seen with catalytically dead GDE2(H233A) (Fig. 5B; Fig. S4C). Finally, GDE2($\Delta C550$) showed virtually wild-type activity towards the differentiation markers, indicating full

recovery of function that was lost in GDE2(Δ C560). The signaling pathways that lead from GDE2 surface activity to gene transcription remain to be explored.

Residue Leu553 dictates GDE2 endocytosis and cell surface expression

We next set out to determine what is unique about the aa 551–570 region that confers endocytosis and recycling on GDE2. Sequence inspection revealed a potential trafficking determinant, namely residue Leu-553, located in a putative non-canonical LI-based sorting motif (Fig. 6A). Canonical dileucine motifs are acidic and contain six amino acids (consensus [D/E]xxxL[L/I]), and mediate endocytosis of transmembrane proteins via direct interaction with the clathrin adaptor complex AP-2^{[12]–[15]}. Mutating Leu-553 to a serine residue in GDE2(Δ C560) or GDE2-FL [which may have a more prominent effect than a leucine to alanine mutation in this case^[16]] led to strongly disrupted internalization and enhanced accumulation on the cell surface (Fig. 6A,B), and showed reduced colocalization with Rab5, Rab4 and Rab11 (Fig. 6B–D). Hence, Leu-553 is a key endocytosis regulatory residue that directs GDE2 into early endosomes (Rab5⁺) and ensuing recycling routes. Interestingly, the putative 6-aa LI-based endocytic motif (MKEKLI) is basic rather than acidic (Fig. 7A) and highly conserved among vertebrates (Fig. 2A). Mutating residues adjacent to Leu-553 should disclose the nature of this intriguing putative LI-based sorting motif.

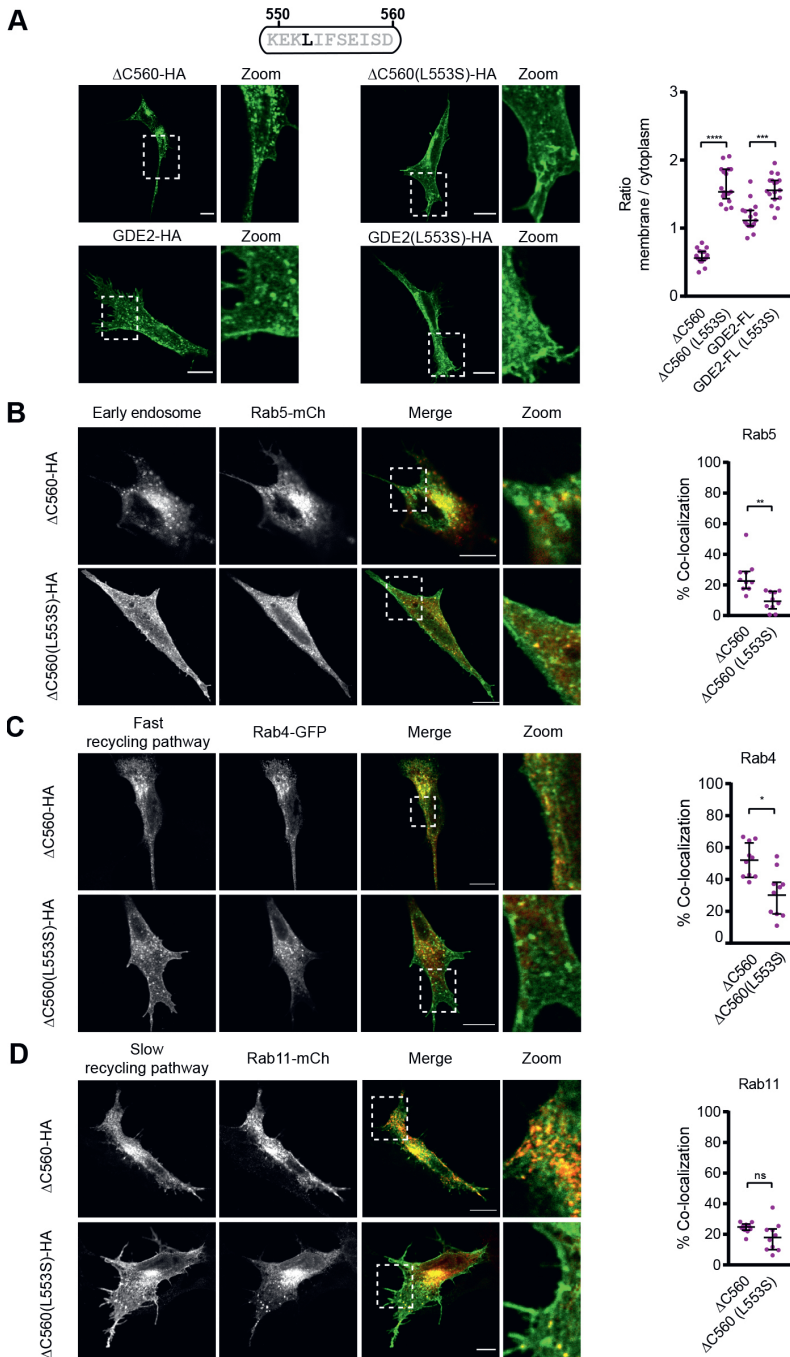


Figure 6. Residue Leu-553 dictates endocytosis and cell-surface expression of GDE2(Δ 560) and GDE2-FL. (A) Left panel, mutating Leu-553 in GDE2(Δ 560) and GDE2-FL leads to increased plasma membrane localization in SH-SY5Y cells. Right panel, quantification of surface versus

cytosol localization the mutated (L533S) and non-mutated GDE2 constructs in SH-SY5Y cells; 15 cells were segmented and analyzed with ImageJ to calculate the membrane:cytoplasmic signal ratio (median±interquartile range). ***P<0.001, ****P<0.0001 (one-way ANOVA). (B–D) Left panels, confocal images of SH-SY5Y cells co-expressing the indicated GDE2 mutants and Rab5–mCh (B), Rab4–GFP (C) and Rab11–mCh (D). Right panels, quantification of GDE2–Rab colocalization (percentage of yellow versus red pixels for 10 cells). Data represent the median±interquartile range of colocalization. *P<0.05, **P<0.01 (one-way ANOVA). Scale bars: 10 μm.

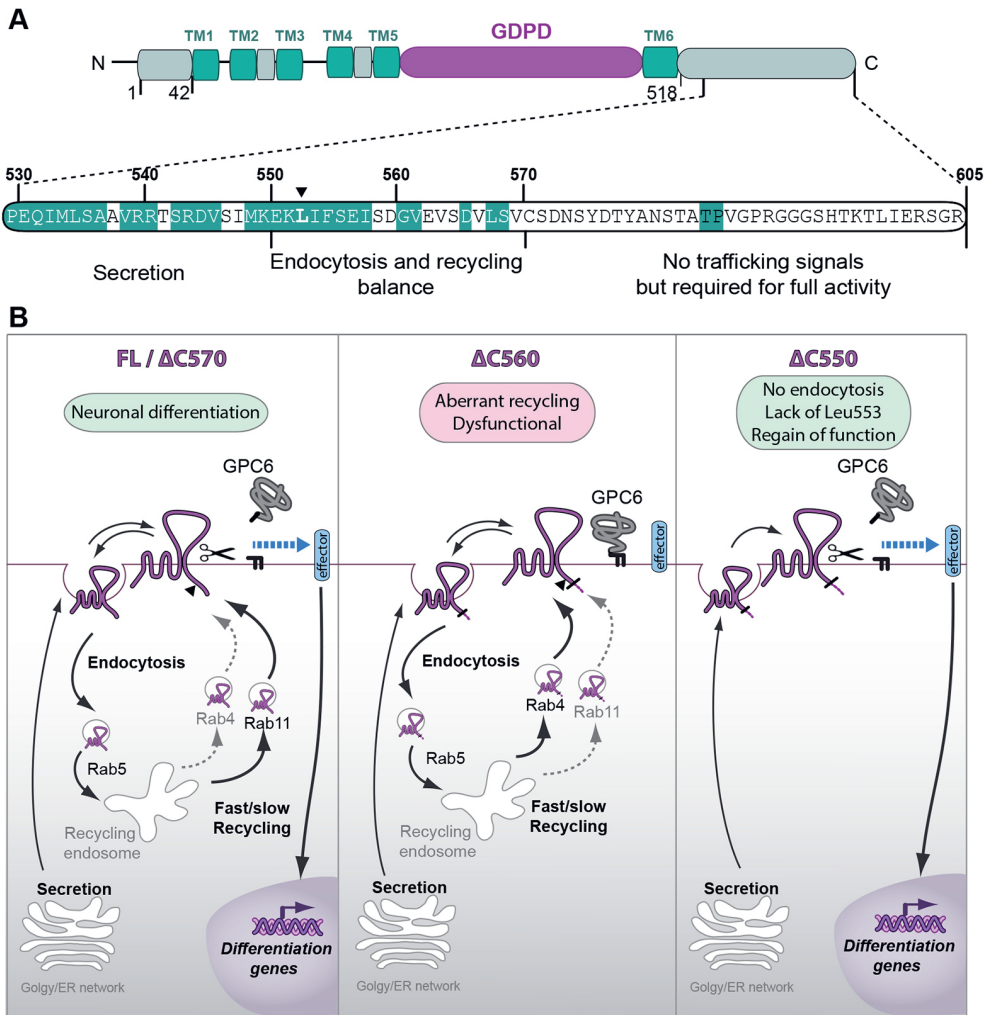


Figure 7. Sequence determinants of GDE2 trafficking and biological activity. (A) The C-terminal region (aa 530–550 or 541–550) is essential for proper expression, secretion and membrane insertion. The sequence from aa 551–560 determines endocytosis (with a key role for residue Leu-553, indicated by an arrowhead) and Rab4 fast recycling preference, but negatively regulates GDE2 function. Sequence from aa 561–570 is required for proper GDE2 recycling and function.

Residues in white are not conserved between mammalian, chicken and/or zebrafish GDE2 (cf. Fig. 2A). (B) Scheme of membrane trafficking, localization and biological output of GDE2 and the indicated truncation mutants, acting in a cell-autonomous manner through GPC6 cleavage and an as-yet-unknown transmembrane effector. GDE2 is constitutively internalized while the majority of endocytosed GDE2 recycles along Rab4⁺ and Rab11⁺ routes in a sequence-dependent manner. A small percentage of internalized GDE2 is sorted to Rab7⁺ late endosomes and lysosomes (not illustrated). GDE2(Δ C570) shows wild-type trafficking behavior and GPC6-releasing activity, yet is not fully signaling competent. GDE2(Δ C560) shows preference for Rab4-driven fast recycling and is dysfunctional, whereas GDE2(Δ C550) is retained at the cell surface with regain of function. The endocytosis regulatory residue Leu-553 is indicated by a black arrowhead. Signaling efficacy is inferred from GPC6 shedding and induction of neuronal differentiation marker genes. See text for further details.

Discussion

In this study, we have uncovered C-terminal tail sequences that regulate the trafficking and activity of GDE2, a unique GPI-specific phospholipase that promotes neuronal differentiation and, furthermore, is implicated in pancreas development. Moreover, we have identified a C-terminal leucine residue that is essential for GDE2 internalization. In neuronal cells, GDE2 undergoes constitutive endocytosis and recycling, independently of its catalytic activity or the presence of serum factors. GDE2 is internalized in a Dynasore-sensitive manner and co-traffics with the transferrin receptor. Hence, we conclude that GDE2 follows the classical clathrin-mediated endocytosis route^[7], supported by the fact that clathrin-independent endocytosis plays only a minor role in mammalian cells^[8]. GDE2 is then routed to Rab5⁺ early endosomes where sorting decisions are made. The large majority of GDE2 is recycled back to the cell surface along two distinct pathways, the fast (Rab4⁺) and slow (Rab11⁺) route, respectively. In general, constitutive recycling serves to generate a highly dynamic internal pool of membrane receptors or ecto-enzymes that is critical for their cell surface expression, signaling fidelity and ensuing cellular responses^[13]. In case of GDE2, its constant recycling may serve to probe the cell surface for specific GPI-anchored substrates, such as GPC6, in a highly dynamic manner.

The C-terminal determinants of GDE2 trafficking, surface expression and activity were inferred from Rab GTPase colocalizations, GPC6 shedding and induction neural differentiation markers, respectively. Our major findings are summarized in Fig. 7. In brief, the last 35 C-terminal residues – which are poorly conserved among vertebrates (Fig. 2A) – are dispensable for GDE2 trafficking and enzymatic activity towards GPC6, yet the GDE2(Δ C570) mutant is not fully signaling competent in terms of biological activity. This suggests that the very C-terminal region contains trafficking-unrelated signaling

information that is possibly species specific. Strikingly, upon two further 10-aa truncations, the resulting GDE2(Δ C560) mutant is redirected from slow (Rab11⁺) to fast (Rab4⁺) recycling with virtual loss of function, whereas GDE2(Δ C550) shows endocytosis failure, cell surface retention and (re)gain of function, as illustrated in the schemes of Fig. 7B. Finally, the juxta-membrane region at aa 518–550 appears to be required for GDE2 biosynthesis and export, as the Δ C540 and Δ C530 mutants are detected as aggregates and fail to enter the secretory pathway.

The most relevant regulatory sequence emerging from our analysis is the 20-amino-acid region at aa 551–570, as it contains all the signaling information essential for GDE2 endocytosis, proper recycling and activity. Of special importance is our identification of Leu-553 as key residue essential for GDE2 endocytosis and ensuing recycling. It is located in a highly conserved LI-based sequence (549-MKEKLIFSEI-558) (Fig. 7A) that does not conform to the consensus dileucine sorting motif, [D/E]xxxL[L/I]^{[12],[13],[17]}. Mutating Leu-553 to a serine residue led to marked disruption of GDE2 internalization, with strongly reduced Rab GTPase colocalizations, and accumulation on the plasma membrane. In other words, mutating Leu-553 shifts the GDE2(Δ C560) phenotype to that of GDE2(Δ C550) (Fig. 7B).

We need to understand why GDE2(Δ C560) is dysfunctional in terms of defective GPC6 shedding and impaired induction of neuronal differentiation markers. Owing to its preferred fast recycling, in combination with reduced cell surface expression, GDE2(Δ C560) may be misdirected to membrane nanodomains that are short of GPI-anchored substrates, particularly GPC6. Alternatively, accelerated recycling of GDE2(Δ C560) could entail a relatively short residence time at the plasma membrane with loss of effective GDE2–substrate interaction. For the ease of mechanistic reasoning, aberrant recycling and dysfunction of GDE2(Δ C560) is restored by adding another 10 residues to generate GDE2(Δ C570). In other words, GDE2(Δ C560) undergoes endocytosis because of Leu-533 but it lacks signals for balanced recycling and proper surface activity, which makes the adjacent 561–570 region particularly important in terms of regulation, even though this stretch is not well conserved among vertebrates (Figs 2A and 7A).

B2

Experimental procedures

Cells. SH-SY5Y, N1E-115 and HEK293 cells (obtained from the ATCC) were grown in Dulbecco's modified Eagle's medium (DMEM) supplemented with 10% fetal bovine serum (FBS) at 37°C under 5% CO₂. Antibodies used were against HA (3F10 from Roche Diagnostics; 1:1000); β -actin (AC-15 from Sigma; 1:10,000); mCherry (16D7 from Thermo Fisher Scientific; 1:1000); LAMP-1 (ab2900 from Abcam; 1 μ g/ml) and GPC6 (LS-C36518 from LifeSpan Bioscience; 1:100). Allophycocyanin (APC)-conjugated anti-HA epitope tag

antibody (cat. no. 901523, Biolegend, 1:200); EZ-Link™ Sulfo-NHS-biotin and Streptavidin–agarose resins were from Pierce, and GFP or mCherry Trap® beads were from ChomoTek; Eugene 6 from Invitrogen.

Plasmids and transfections. Human GDE2 cDNA was subcloned in pcDNA3.1 as described previously^[2]. Truncated versions of GDE2 were generated by amplification of full-length GDE2–HA or GDE2–mCherry using reverse primers for the last residues of each truncation. This was followed by a digestion with **BamHI** and **EcoRV**, after which the amplified inserts were cloned into digested and gel-purified pcDNA3.1, and selected with ampicillin. GDE2 point mutants were generated by site-directed mutagenesis using two complementary oligonucleotides with the desired mutated bases at the center of their sequences. A temperature gradient from 55 to 60°C was used during the PCR amplifications. The PCR products were digested with **DpnI** and transformed into DH5- α competent bacteria and screened for the expected mutated bases.

Confocal and super-resolution microscopy. Cells cultured on 24 mm, #1.5 coverslips were washed and fixed with 4% paraformaldehyde (PFA), permeabilized with 0.1% Triton X-100 and blocked with 5% BSA for 1 h. Incubation with primary antibodies was done for 1 h, followed by incubation with Alexa-conjugated antibodies for 45 min at room temperature. For confocal microscopy, cells were washed with PBS, mounted with Immuno-Mount™ (Thermo Fisher Scientific) and visualized on a LEICA TCS-SP5 confocal microscope (63 \times objective). Super-resolution imaging was done using an SR-GSD Leica microscope equipped with an oxygen scavenging system, as previously described^[2]. In short, 15,000 frames were taken in TIRF or EPI mode at 10 ms exposure time. Movies were analyzed and corrected using the ImageJ plugin Thunderstorm (<http://imagej.nih.gov/ij/>), followed by correction with an ImageJ macro using the plugin Image Stabilizer.

Live imaging. Live-cell imaging of GDE2–GFP in SH-SY5Y cells was undertaken on a Leica TCS SP5 confocal microscope equipped with 63 \times oil immersion lens (NA 1.4; Leica, Mannheim, Germany). Coverslips were mounted on a metal ring system and exposed to buffer solution (140 mM NaCl, 5 mM KCl, 1 mM MgCl₂, 1 mM CaCl₂, 10 mM HEPES pH 7.2 and 10 mM glucose). Excitation was at 488 nm and emission was collected between 510 and 580 nm. Images were collected every 7.8 s for 40 min. For display as a movie, the image was cropped and displayed with the Fire LUT using open source Fiji software, version 1.52p.

GDE2 plasma membrane localization. We performed image analysis for plasma membrane localization of HA-tagged GDE2 constructs by using Fiji/ImageJ. In brief, confocal images stained for GDE2–HA were segmented and analyzed using Fiji software and a macro that automated the process. First, images were thresholded with the

MaxEntropy algorithm to delimit single cells and filtered by Gaussian Blur (radius=2) and smoothed for segmentation with a median radius of two. Using the Region of Interest manager on Fiji, the background was delimited by using the Li algorithm for thresholding. The cytoplasmic regions were selected by subtracting the plasma membrane thickness (fixed to 0.5 μm , but adjustable from a 0.2–5.0 range) and eroded with a pixel width of one to avoid having empty membranes in segmented cells. Next, the plasma membrane region was obtained by subtracting the background to the cytoplasmic region. Finally, the ratio of the membrane to cytoplasmic signals was calculated from the median value of these regions.

Western blotting. For western blotting, cells were washed with cold PBS, lysed in NP-40 buffer (50 mM Tris-HCl pH 7.4, 150 mM NaCl, 2 mM EDTA, 1% NP-40, 0.25% sodium deoxycholate) supplemented with protease inhibitors and centrifuged (20,000 g for 15 min). Protein concentration was measured using a BCA protein assay kit (Pierce) and LDS sample buffer (NuPAGE, Invitrogen) was added to the lysate or directly to the medium. Equal amounts were loaded on SDS-PAGE pre-cast gradient gels (4–12% Nu-Page Bis-Tris, Invitrogen), followed by transfer to nitrocellulose membrane. Non-specific protein binding was blocked by 5% skimmed milk in TBST followed by incubation with primary antibodies overnight at 4°C in TBST with 2.5% skimmed milk, and then secondary antibodies conjugated to horseradish peroxidase (DAKO, Glostrup, Denmark) for 1 h at room temperature. Proteins were detected using ECL western blot reagent.

Biotin labeling. For quantification of GDE2 internalization and recycling, we used a biotin-labeling assay. GDE2–mCh-expressing N1E-115 cells were serum starved for 1 h, transferred to ice, washed in ice-cold PBS, and surface labeled at 4°C with 0.2 mg/ml NHS-SS-biotin (Pierce). For GDE2 internalization, cells were exposed to serum-free medium at 37°C for the indicated time periods. Cells were transferred to ice and washed with PBS, the remaining surface biotin was reduced with sodium 2-mercaptoethane sulfonate (MesNa), and the reaction was quenched with iodoacetamide (IAA) prior to cell lysis. For recycling assays, cells were labeled with biotin as above, and incubated in serum-free medium at 37°C for 30 min to allow internalization of GDE2. Cells were returned to ice, washed with PBS, and biotin was reduced using MesNa. Recycling of the internal GDE2 pool was induced by a temperature shift to 37°C for 0–30 min. Cells were returned to ice, washed with PBS and surface biotin was reduced by MesNa. MesNa was quenched by IAA and the cells were lysed. Biotin-labeled GDE2 was detected using Streptavidin beads and anti-mCh antibody.

Immunoprecipitation. For co-immunoprecipitation of GDE2 and Rabs, HEK293T cells were plated on plastic dishes of 10 cm diameter and transient co-transfected with GDE2–mCh or GDE2–GFP, and Rab4a–GFP, Rab5a–mCh, Rab7a–GFP or Rab11a–mCh. Rab constructs

were provided by Coert Margadant (Dept. Molecular and Cellular Hemostasis, Sanquin, the Netherlands) and Jacques Neefjes (Dept. Chemical Immunology, University of Leiden, the Netherlands). After 24 h cells were lysed using RIPA buffer. Protein concentration was determined using Protein BCA protein assay kit (Pierce). Immunoprecipitation was carried out incubating 500 µg–1 mg cytoplasmic extracts with GFP or mCherry Trap® beads (ChromoTek) at 4°C for 1 h. Beads were washed three times and eluted by boiling in SDS sample buffer for 10 min at 95°C. Supernatants were applied onto an SDS gel and subjected to immunoblot analysis.

Inducible GDE2 expression. SH-SY5Y cells with inducible expression of GDE2 constructs were generated using the Retro-X™ Tet-On® Advanced Inducible Expression System (Clontech), as described previously^[2]. After retroviral transduction, the cells were placed under selection with G418 (800 mg/ml) supplemented with puromycin (1 µg/ml) for 10 days. GDE2 induction (in the presence of 1 µg/ml doxycycline) was verified by western blotting and confocal microscopy. Transient transfection was performed with Fugene 6 reagent (Invitrogen) according to the manufacturer's instructions.

Flow cytometry. For GPC6 and GDE2–HA surface expression analysis, cells were grown in complete medium with 10% FCS with or without doxycycline. Cells were trypsinized into single-cell suspensions and then $\sim 8 \times 10^5$ cells were incubated with 5 µl of anti-GPC6 antibody LS-C36518 (LifeSpan Bioscience) and in 4 µl of APC-conjugated anti-HA antibody (BioLegend). Bound GPC6 antibody were detected by incubating with a 1:200 dilution of goat Alexa-Fluor-488-conjugated anti-mouse-IgG secondary antibody in 2% BSA for 45 min on ice. Fluorescence measurements were performed using BD LSRFORTESSA and using FlowJo software.

GDE2 enzymatic activity assays. GDE2 activity assays were carried out in HEK293 cells, essentially as described by Matas-Rico et al.^[2]. HeLa cells were seeded on six-wells plates and co-transfected with expression vectors for human HA-tagged GDE2 or its truncations together with GFP-tagged GPC6. At 24 h after transfection with FuGENE® 6, cells were incubated for an additional 24 h in DMEM with 0.1% FCS. The conditioned medium was removed and cell lysates were prepared using NP-40/NaDOC lysis buffer (50 mM Tris-HCl pH 7.4, 150 mM NaCl, 2 mM EDTA, 1% NP-40, 0.25% NaDOC and 5% glycerol) supplemented with protease inhibitor cocktail. The amount of substrate proteins in the medium and cell lysates was analyzed by western blotting.

Induction of neural differentiation marker genes. Total RNA was extracted using the GeneJET purification kit (Fermentas). cDNA was synthesized by reverse transcription from 5 µg RNA using the First Strand cDNA Synthesis Kit (Thermo Fisher Scientific). Real-time quantitative PCR (RT-qPCR) was performed on a 7500 Fast System (Applied Biosystems)

as follows: 95°C for 2 min, 95°C for 0 min, 60 cycles at 95°C for 15 s followed by 60°C for 1 min for annealing and extension. The final reaction mixtures (12 µl) consisted of diluted cDNA, 16SYBR Green Supermix (Applied Biosystems), 200 nM forward primer and 200 nM reverse primer. Reactions were performed in 384-well plates with three independent biological replicas. The primers used are listed in Table S1. As a negative control, the cDNA was replaced by milliQ water. Cyclophilin was used as reference gene. Each sample was analyzed in triplicate and the normalized expression (NE) data were calculated with the equation $NE = 2^{-(Ct_{target} - Ct_{reference})}$.

Acknowledgements

We thank the reviewers for insightful comments, especially those on dileucine-based endocytosis.

Supplemental Information

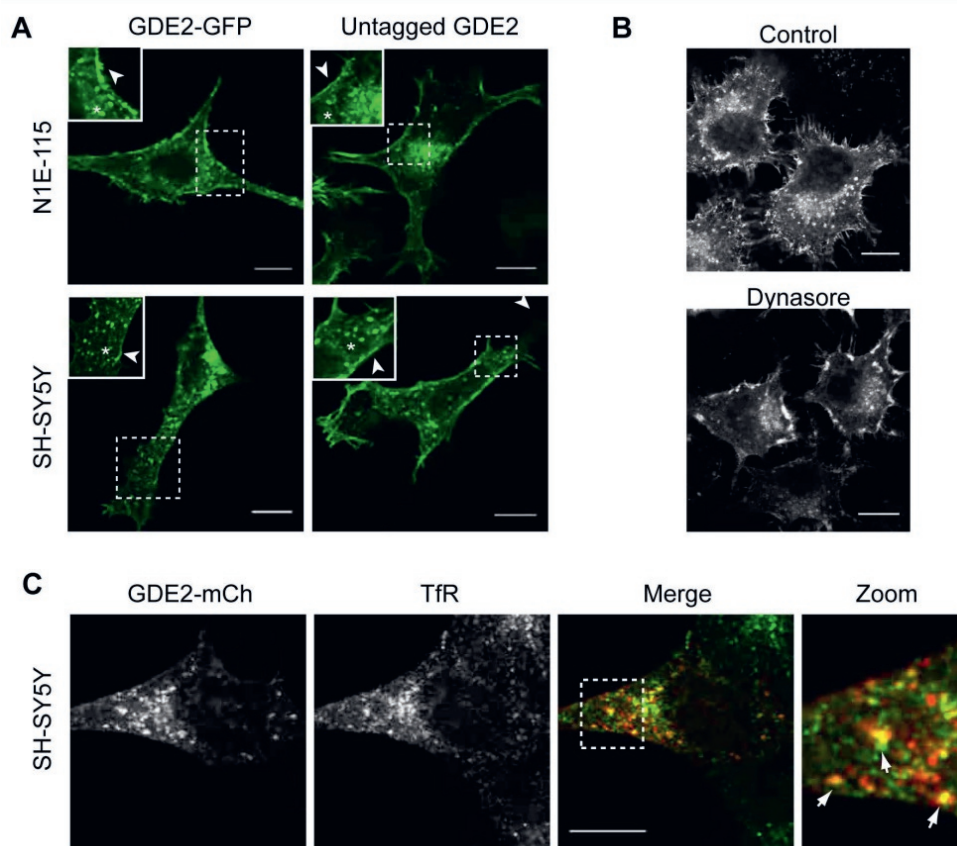


Figure S1. GDE2 subcellular localization and endocytic routes. **A.** Confocal images showing GDE2-GFP and untagged GDE2 localization in membrane microdomains and intracellular vesicles in N1E-115 and SH-SY5Y cells. White arrows point to microdomains at the plasma membrane and asterisk to intracellular vesicles. Bar, 10 μ m. **B.** GDE2 accumulates at the cell surface with loss of GDE2-positive vesicles in N1E-115 cells treated with the dynamin inhibitor Dynasore (80 μ M). Bar, 10 μ m. **C.** GDE2 co-localizes with endogenous transferrin receptor. SH-SY5Y cells were transiently transfected with GDE2-mCherry, fixed, and endogenous transferrin receptor (TfR) detected with an anti-TfR antibody. The zoom panel shows a magnified view of the area outline by the dashed square. White arrows point to GDE2- and TfR-positive vesicles. Bar 10 μ m.

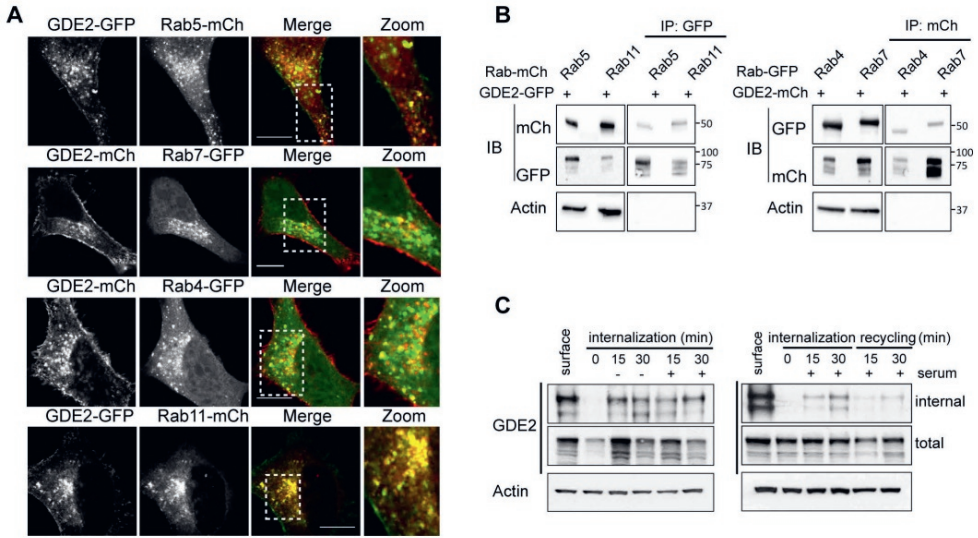


Figure S2. GDE2 colocalizes with Rab GTPases. **A.** GDE2 co-localizes with the indicated Rab GTPases in N1E-115 cells. Bar, 10 μ m. **B.** GDE2 (fused to GFP or mCh) associates with the indicated Rab GTPases in HEK293T cells. GDE2 was immunoprecipitated (IP) and subjected to immunoblotting (IB) using either anti-GFP or anti-mCherry antibody. **C.** N1E-115 cells expressing GDE2-mCh were surface-labelled with NHS-S-S-Biotin. Internalization proceeded for 15 and 30 min at 37°C in presence or absence of 10% FBS. Surface biotin was reduced with MesNa at 4°C, and the cells were shifted to 37°C for the indicated time periods to trigger recycling of the internal pool. The amount of internalized and total biotin-labelled GDE2 determined by immunoblotting using anti-mCh antibody. Actin was used as loading control.

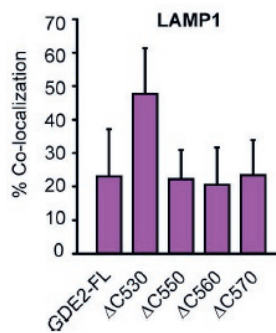
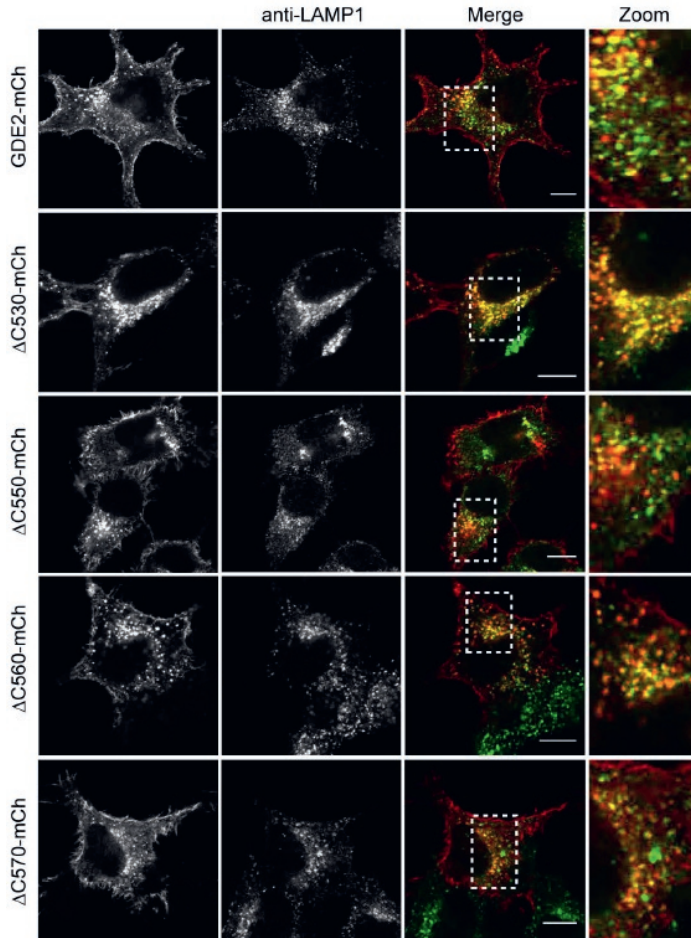


Figure S3. Lysosomal localization of GDE2 and its truncation mutants. N1E-115 cells expressing the indicated GDE2-mCh constructs were immunostained for LAMP1, using LAMP1-specific antibody. Bar, 10 μ m. Lower panel, quantification of GDE2-LAMP1 co-localization. Data represent the median \pm SEM (error bars) of co-localization.

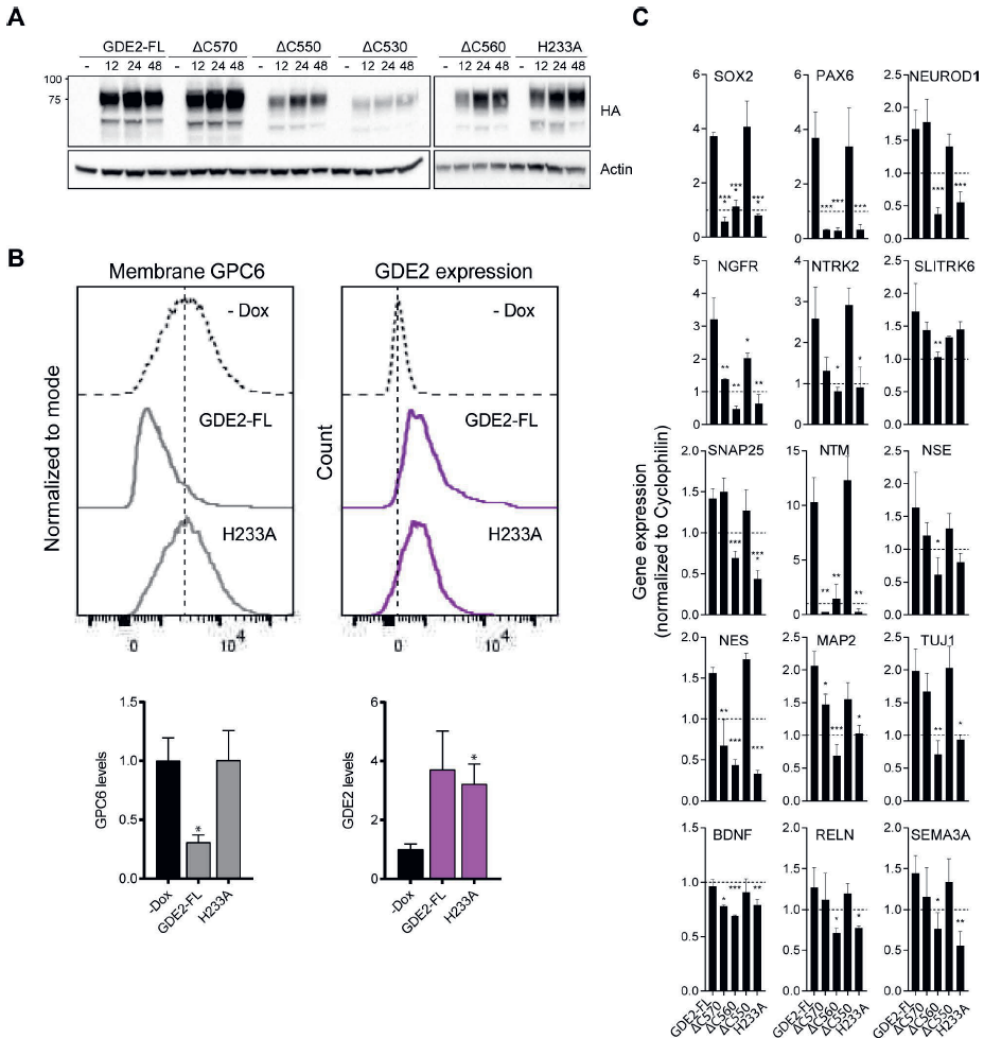


Figure S4. Expression and localization of GDE2 and truncation mutants in Dox-treated SH-SY5Y cells. **A.** Western blots showing expression of the indicated GDE2-HA constructs after 24 and 48 hrs of Dox treatment. Actin was used as loading control. See also **Fig. 3A**. **B.** Control experiment showing that GDE2(H233A) at the cell surface is inactive towards GPC6. Cell surface expressions were determined by FACS. Data show the median \pm SEM (error bars) from triplicate measurements taken from two independent experiments. * $p < 0.05$, paired t test. See also **Fig. 3C**. **C.** Induction of neuronal differentiation genes upon Doxycycline induction (48 hrs) of the indicated GDE2 constructs, as determined by qPCR. Data represent the average value of triplicate biological measures \pm SEM (error bars). * $p < 0.05$, ** $p < 0.01$, *** $p < 0.001$, **** $p < 0.0001$ by unpaired t test. See also **Fig. 3D**.

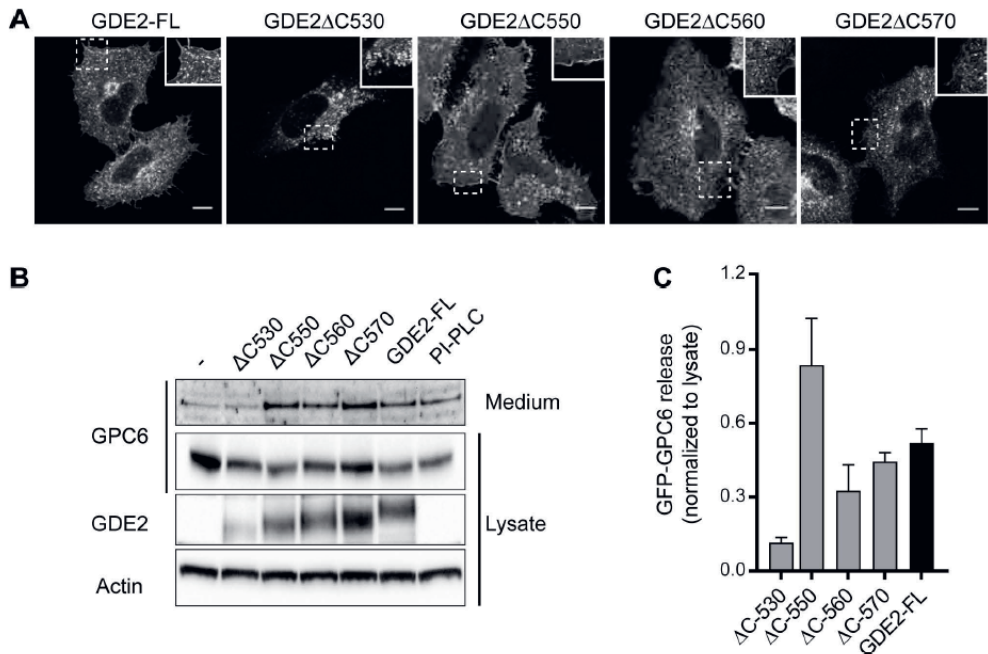


Figure S5. GDE2-induced GPC6 shedding in HeLa cells. **A.** Localization of GDE2-HA and its truncation mutants in HeLa cells. Subcellular localizations were similar to those in neuronal cells. Bar, 10 μ m. **B.** HeLa cells were co-transfected with GFP-GPC6 and GDE2-HA. After 24 hrs, cells were serum-starved and GPC6 was allowed to accumulate in the medium. Bacterial PI-PLC was used as control. **C.** Quantitated bands of released GPC6 normalized to its total expression in the cell lysate.

Movie 1. Live-imaging of GDE2 intracellular trafficking in SH-SY5Y cells. A single cell expressing eGFP-tagged GDE2 was imaged on a Leica SP8 confocal microscope using a 63x oil immersion objective at \sim 8 frames per min. Note the rapid motility of vesicular GDE2 and its bi-directional movement towards and from the neurite ending. Scale bar and timing as indicated. Image size, 81 x 33 μ m.

Table S1. Primers used for qPCR

Gene	Forward primer 5'-3'	Reverse primer 5'-3'
BDNF	TGGCTGACACTTTCGAACAC	GGACCCTCATGGACATGTTT
Cyclophilin	CATCTGCACTGCCAAGACTGA	TTGCCAAACACCACATGCTT
MAP2	CCAATGGATTCCCATACAGG	TCCTTGACAGACCTCTCT
NES	AGGTGGCCACGTACAGGAC	TCTCAAGGGTAGCAGGCAAG
NEUROD1	CCGACAGAGCCCAGATGTAGTTCTT	GCCCCAGGGTTATGAGACTATCACT
NGFR	GGGCCTCGTGTTCTCCTG	CAGGGATCTCCTCGCACTC
NSE	CTGATGCTGGAGTTGGATGG	CCATTGATCACGTTGAAGGC
NTM	GTCTCTCAGGCTGCTGTTC	ATCCAGGCACCACTTGTTCAT
NTRK2	CGAATCTCCAACCTCAGACC	CCCCATTGTTTCATGTGAGTG
PAX6	CAGCTCGGTGGTGTCTTTGT	ACTTGAAGTGGAACTGACAC
RELN	CCACAGGCCTTAATACAACAACAG	GGGTCTGAATAACTAAAGCGACATGA
SEMA3A	TTGTCTGTCTTTTCTGGGGAGT	TGTGATCCTTTGCTCCAACA
SLITRK6	AATAACCCATCCATGCCAAC	AACCACTATCCCTGCAGCAC
SNAP25	AGTTGGCTGATGAGTCGCTG	TGAAAAGGCCACAGCATTTT
SOX2	ATGGGTTCGGTGGTCAAGT	GGTAGTGCTGGGACATGTGA
TUJ1	CCTGGAACCCGGAACCAT	AGGCCTGAAGAGATGTCCAAG

References

- [1] D. Corda, M. G. Mosca, N. Ohshima, L. Grauso, N. Yanaka, S. Mariggiò, *FEBS Journal*, **2014**, 281, 998.
- [2] E. Matas-Rico, M. van Veen, D. Leyton-Puig, J. van den Berg, J. Koster, K. M. Kedziora, B. Molenaar, M. J. A. Weerts, I. de Rink, R. H. Medema, B. N. G. Giepmans, A. Perrakis, K. Jalink, R. Versteeg, W. H. Moolenaar, *Cancer Cell*, **2016**, 30, 986.
- [3] S. Park, C. Lee, P. Sabharwal, M. Zhang, C. L. F. Meyers, S. Sockanathan, *Science*, **2013**, 339, 324.
- [4] M. Van Veen, E. Matas-Rico, K. van de Wetering, D. Leyton-Puig, K. M. Kedziora, V. de Lorenzi, Y. Stijf-Bultsma, B. van den Broek, K. Jalink, N. Sidenius, A. Perrakis, W. H. Moolenaar, *Elife*, **2017**, 6, 1.
- [5] C. Cave, S. Park, M. Rodriguez, M. Nakamura, A. Hoke, M. Pletnikov, S. Sockanathan, *Mol. Neurodegener.*, **2017**, 12, 8.
- [6] M. van Veen, L. A. Mans, E. Matas-Rico, J. van Pelt, A. Perrakis, W. H. Moolenaar, A.-P. G. Haramis, *Int. J. Biochem. Cell Biol.*, **2018**, 94, 71.
- [7] M. Mettlen, P.-H. Chen, S. Srinivasan, G. Danuser, S. L. Schmid, *Annu. Rev. Biochem.*, **2018**, 87, 871.
- [8] V. Bitsikas, I. R. J. Corrêa, B. J. Nichols, *Elife*, **2014**, 3, e03970.
- [9] M. L. Mignogna, P. D'Adamo, *Small GTPases*, **2018**, 9, 145.
- [10] A. Wandinger-Ness, M. Zerial, *Cold Spring Harb. Perspect. Biol.*, **2014**, 6, a022616.
- [11] F. R. Maxfield, T. E. McGraw, *Nat. Rev. Mol. Cell Biol.*, **2004**, 5, 121.
- [12] J. S. Bonifacino, L. M. Traub, *Annu. Rev. Biochem.*, **2003**, 72, 395.
- [13] P. J. Cullen, F. Steinberg, *Nat. Rev. Mol. Cell Biol.*, **2018**, 19, 679.
- [14] C. M. Guardia, R. De Pace, R. Mattera, J. S. Bonifacino, *Curr. Opin. Neurobiol.*, **2018**, 51, 103.
- [15] B. T. Kelly, A. J. McCoy, K. Späte, S. E. Miller, P. R. Evans, S. Höning, D. J. Owen, *Nature*, **2008**, 456, 976.
- [16] K. Denzer, B. Weber, A. Hille-Rehfeld, K. V. Figura, R. Pohlmann, *Biochem. J.*, **1997**, 326 (Pt 2, 497.
- [17] A. Sanger, J. Hirst, A. K. Davies, M. S. Robinson, *J. Cell Sci.*, **2019**, 132



Chapter B3

Contactins are specifically cleaved by GDE3: new implications in glioblastoma

This chapter is based on experiments performed together with Loraine Cahn, whom I supervised during her master internship.

Abstract

Two members of the Glycerophosphodiester phosphodiesterase (GDPD) family, GDE2 and GDE3, are transmembrane enzymes reported to cleave Glycosylphosphatidylinositol (GPI)-anchored proteins (GPI-APs) at the plasma membrane of mammalian cells. GPI-APs are known to regulate a plethora of cellular processes, and their cleavage and subsequent shedding by GDE2 and GDE3 has been shown to modulate several processes, including survival in neuroblastoma and breast cancer. However, none of these GDEs have been extensively studied and much remains unknown about the identity of their potential GPI-anchored substrates. The contactin (CNTN) protein family are cell adhesion molecules anchored by GPI; thus, they represent potential GDE substrates. CNTNs are predominantly expressed in the brain, and have been involved in cancer. CNTNs show high expression in glioblastoma, a cancer type with poor clinical outcome. We investigated if GDE2 and GDE3 could cleave contactins, as this could have interesting applications in glioblastoma, and showed that GDE3 is responsible for cleaving both CNTN4 and CNTN6. In addition, we show that GDE2 induces a reduction in the expression of a number of invasiveness-related genes in U-87 cells, suggesting a role for GDE2 in glioblastoma invasion. To conclude, by identifying new GDE-specific substrates and GDE-induced changes in gene-expression, this study opens up the path towards clinical implications of GDEs in glioblastoma treatment.

Introduction

Glycosylphosphatidylinositol (GPI)-anchored proteins (GPI-APs) are a class of proteins containing a glycolipid anchor composed of phosphatidylinositol and a sugar core. This anchor is added to the C-terminus of the protein in the endoplasmic reticulum as a post-translational modification, allowing the GPI-AP to localize to the external leaflet of the plasma membrane. GPI-APs are expected to account for approximately 0.5% of total proteins in Eukaryotes and over 150 mammalian variants have been identified. By associating to other membrane-bound proteins, they regulate a wide variety of cellular functions. Processes regulated by GPI-APs include, but are not limited to: enzymatic activity, signal transduction, cell adhesion, cellular communication, neuritogenesis, and immune response. As a consequence of the variety of processes they regulate, GPI-APs are essential for normal cellular functioning, as well as the development of diseases, including several types of cancer. Importantly, an elevation of GPI-AP shedding has been found in the plasma of patients suffering from several types of cancers and has been reported to be a marker of malignancy^[1].

The regulating activities of GPI-APs are in turn controlled by two members of the glycerophosphodiester phosphodiesterase (GDPDs) protein family: glycerophosphodiester phosphodiesterase 2 (GDE2) and 3 (GDE3). Both consist of six transmembrane domains and a large catalytic ectodomain that is capable of inactivating GPI-AP-related functions by cleaving the phosphodiester bond in the GPI-anchor. By doing so, GDE2 and GDE3 have been shown to have potential anti-cancer implications. More specifically, GDE2 has been shown to cleave reversion-inducing cysteine-rich protein with kazal motifs (RECK)^[2] and glypican-6 (GPC6)^[3], resulting in an inhibition of proliferation, drug-resistance and cell motility, as well as an induction of differentiation in neuroblastoma cells. In addition, GDE2 has been reported to correlate to favorable clinical outcome for neuroblastoma patients^[3]. Expression of GDE3, on the other hand, correlates to favorable clinical outcome for breast cancer patients and has been shown to inhibit tissue remodeling, cell adhesion, migration and invasiveness in breast cancer cells by cleaving urokinase receptor (uPAR)^[4]. This evidence suggests that GDE2 and GDE3 may have future implications in therapeutic strategies against these and possibly other types of cancer. However, none of these GDEs have been extensively studied and much about their functions remains unknown. Considering the abundance of GPI-APs within the mammalian proteasome, it is likely that both GDE2 and GDE3 have many other substrates and, therefore, various unidentified functions. Identifying these substrates and functions is an important step towards the explanation of the biological role of GDE2 and GDE3 and would be essential knowledge to investigate their potential as an anti-cancer therapy.

Western blot-based activity assay was used to assess whether GDE2 and/or GDE3 cleave

the GPI-APs Contactin 4 (CNTN4) and Contactin 6 (CNTN6). Both GPI-APs are members of the six-membered contactin subgroup of the immunoglobulin cell adhesion molecule superfamily (IgCAMs). Predominantly expressed in the brain, collective evidence implies that both contactins are involved in the pathogenesis of neurodevelopmental disorders, as well as several types of cancer. Specifically, contactin 4 is associated with malignant behavior in Pheochromocytomas and Paragangliomas^[5] and can decrease the response of neuroblastoma cells to differentiating agents^[6]. Contactin 6, on the other hand, is a Notch ligand and promotes differentiation of neural progenitor cells into oligodendrocytes, a subset of glia cells^[7].

As a next step in this study, the effect of GDE2 and GDE3 on cancer-related phenotypes in glioblastoma was examined. Although being the most common primary brain tumor in adults, glioblastoma has very poor prognosis and high mortality rates due to little effective therapeutic options. As contactins are highly expressed in glioblastoma, the possibility of several GDE-induced phenotypic alterations were examined using a U-87 cell line

Results

CNTN4 and CNTN6 are cleaved by GDE3

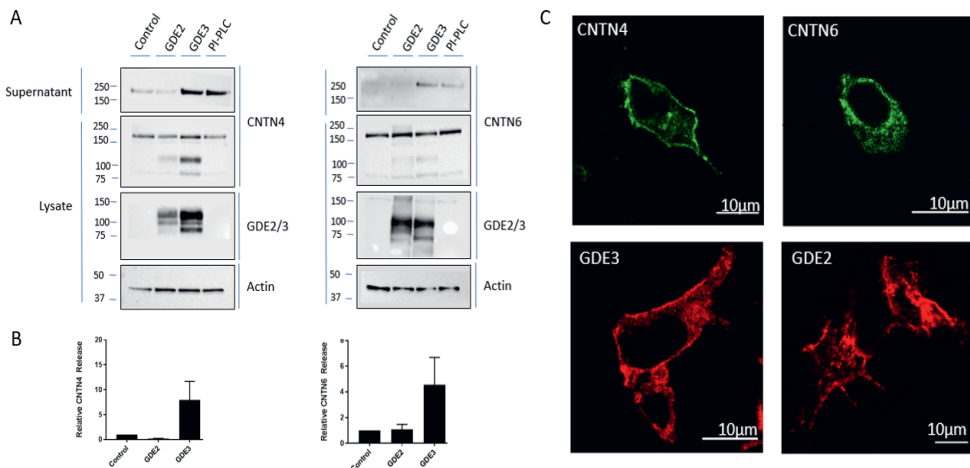


Figure 1. Activity Assay and Confocal Microscopy showing that CNTN4 and CNTN6 Localize to the Plasma Membrane and are Cleaved by GDE3. (A) Western blots of CNTN4 (left) and CNTN6 (right). CNTN4 and CNTN6 are cleaved by GDE3. (B) Quantification of three technical replicates \pm SEM. CNTN4 is cleaved by GDE3 to a higher extent than CNTN6. (C) Analysis of the localization of CNTN4, CNTN6, GDE2 and GDE3 in HEK293 cells by confocal microscopy. Both CNTNs and GDEs localize to the cell membrane predominantly.

To examine if CNTN4 and CNTN6 are cleaved from the plasma membrane by GDE2 or GDE3, an activity assay was performed. HEK293 cells were transfected with GFP-tagged CNTN4 or CNTN6 and co-transfected with mCherry-tagged GDE2 or GDE3, or an empty vector, which was used as a negative control. A subset of cells co-transfected with empty vector was treated with Phosphoinositide phospholipase C (PI-PLC), a protein known to cleave all GPI-APs, which was regarded as a positive control. As shown in Figure 1, only with the presence of GDE3 both Contactin 4 and Contactin 6 accumulate in the supernatant to a higher extent than in the negative control and to a similar extent as in the positive control. Therefore, it can be concluded that both Contactins are cleaved from the plasma membrane by GDE3 and not by GDE2. Interestingly, CNTN4 is cleaved by GDE3 more than CNTN6. Concluding from the similar acquired signal for contactins, GDEs and loading control (actin) in the lysates, equal amounts of protein was present in all samples and co-transfection was successful. By performing confocal microscopy upon 24 hours of transfection, it is shown that both contactins and GDEs localize to the plasma membrane. Interestingly, CNTN4 localizes to the plasma membrane to a higher extent than CNTN6.

Production of GDE2- and GDE3-inducible U-87 cell lines

For further phenotypic examination upon stable GDE expression in glioblastoma cells, GDE2- and GDE3-inducible U-87 cell lines were produced. Three doxycycline-inducible systems were obtained using retroviral transduction: two GDE2-inducible (HA- and mCherry-tagged) and one GDE3-inducible (GFP-tag). To test whether the systems were functioning properly, the levels of GDE were quantified after 0, 8, 24, or 48 hours of doxycycline treatment by Western blot. In addition, confocal microscopy was used to analyze the localization of the GDEs after 48 hours of doxycycline treatment. To this end, immunofluorescence was performed on the system with GDE2-HA. GDE3-GFP was visible neither on the Western blot nor by confocal microscopy (results not shown). Sequencing of the GDE3-GFP plasmid DNA pointed out that no GFP or GDE3 was present. As a consequence, this system could not be trusted and was not used in further experiments. Conversely, both inducible systems for GDE2 were detectable by Western blot, by which it was seen that the signal was the strongest after 48 hours of doxycycline induction, as depicted in Figure 2. In addition, both GDE2-HA and GDE2-mCherry became visible in the confocal microscopy analysis, where they showed to localize to the plasma membrane, as well as to intracellular recycling vesicles.

Invasion capacity related genes are downregulated upon GDE2 expression

To study the possibility of GDE2 being related to invasion capacity in glioblastoma, five genes were quantified by quantitative polymerase chain reaction (qPCR) analysis upon GDE2 induction: Alpha-crystallin B chain (CRYAB), Adenylate kinase isoenzyme 5 (AK5), Fibrinogen C domain-containing protein 1 (FIBCD1), Insulin-like growth factor (IGF)-

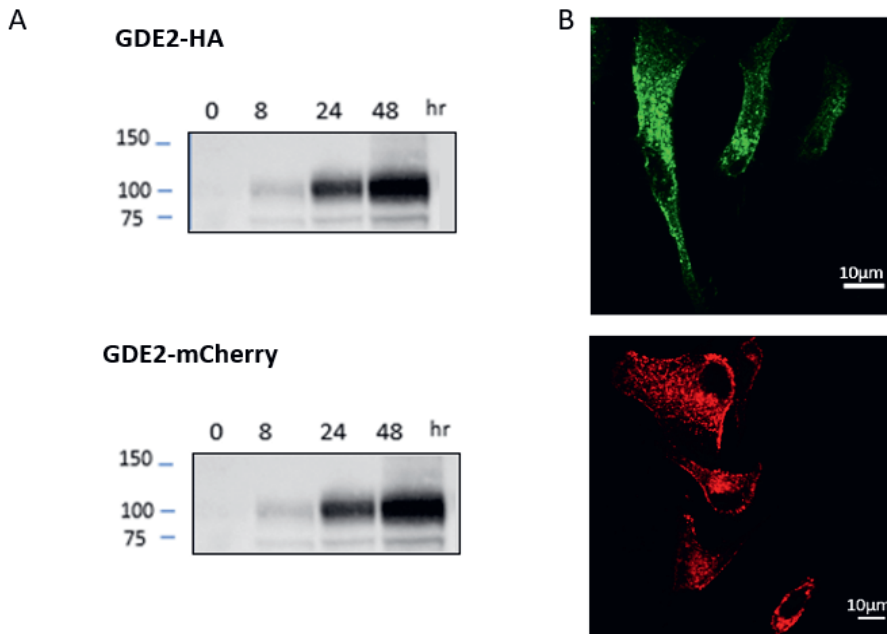


Figure 2. Activity Assay and Confocal Microscopy showing Successful Production of GDE2- and GDE3-inducible U-87. (A) Western blots showing an increase of GDE2-HA (top) and GDE2-mCherry (bottom) concentration over time. (B) Confocal microscopy analysis of localisation of GDE2-HA (top) and GDE2-mCherry (bottom). Both localize to the plasma membrane and intracellular recycling vesicles.

binding protein 4 (IGFBP4) and H3 and cysteine-rich domain-containing protein 2 (STAC2). These five genes have been previously shown to be significantly upregulated in invasive subclones of U-87 cells as compared to non-invasive subclones (Pencheva et al., 2017). As an additional validation of the proper functioning of the inducible systems, the GDE2 gene was simultaneously quantified. As shown in Figure 3, four out of five invasion-related marker genes: AK5, FIBCD1, IGFBP4 and STAC2, showed a 2-4 fold reduction in expression levels upon GDE2 induction. CRYAB expression remained similar upon induction of GDE2-HA, but had a 2-fold higher expression upon induction of GDE2-mCherry. Interestingly, induction of GDE2-HA was stronger than induction of GDE2-mCherry. However, both systems yielded similar results, indicating that a maximum effect was already reached by induction of GDE2-mCherry.

Differentiation state and random motility

To examine the possibility of GDE2 being related to differentiation state and random motility in glioblastoma, two pilot assays were performed. Upon 24 hours of GDE2-induction, differentiation state was measured by quantification of neurite outgrowth.

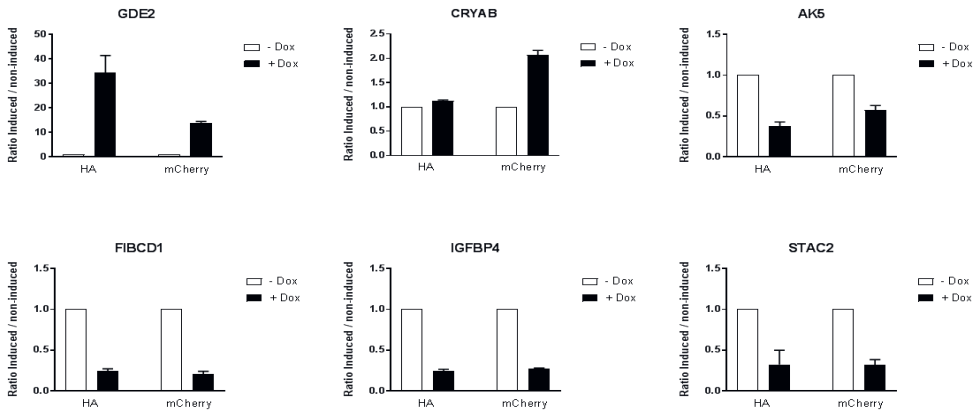


Figure 3. qPCR Analysis Revealing the Upregulation of Genetic Markers of Invasiveness in Glioblastoma. Quantification of genes related to invasion capacity in U87 cells by qPCR, average of three technical replicates \pm SEM upon 48-hour treatment with doxycycline. Both inducible systems express high levels of GDE2.

From Figure 4, no difference of neurite outgrowth can be observed in the quantification or visual evaluation. For the quantification of random motility, cells were tracked for 15 hours and the average travelled distance over 30 minutes was measured. Concluding from Figure 5, a higher random motility was observed upon GDE2-induction.

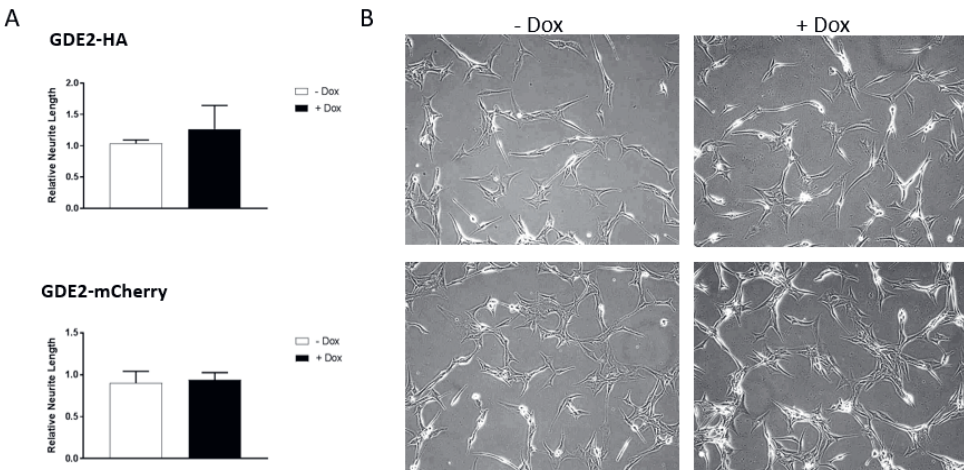


Figure 4. Induction of GDE2 does not Alter Differentiation State of U-87 Cells. (A) Differentiation state of cells expressing GDE2-HA (up) and GDE2-mCherry (down) quantified by neurite length (μm) after 24 hours of exposure to doxycycline (average \pm SEM, $n=10$). (B) Life images captures after 24 hours, showing no observable differences in neurite outgrowth.

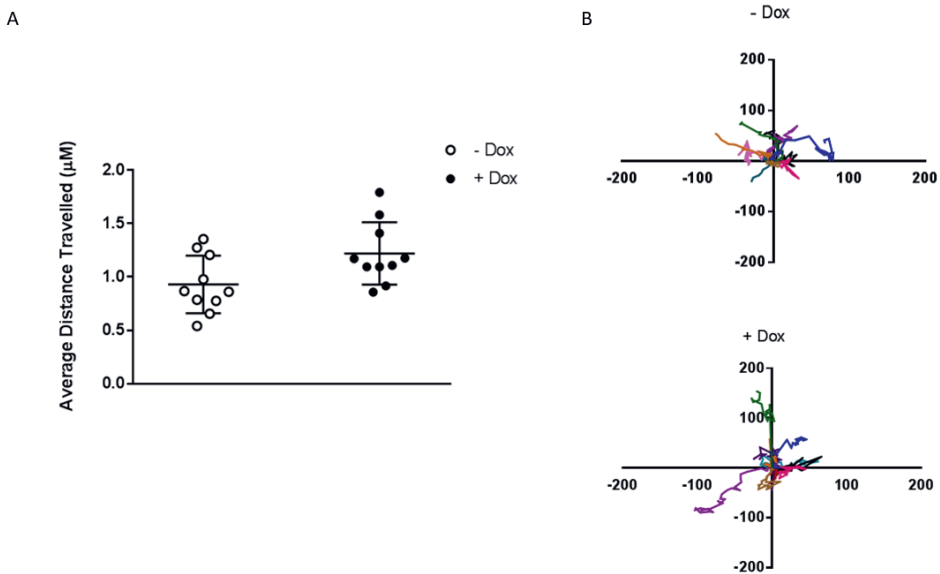


Figure 5. Induction of GDE2 Increases Random Capacity of U-87 Cells. Random motility of U87 cells expressing GDE2-HA after 15 hours of doxycycline induction (average \pm SEM, $n=10$). (A) random motility measured by the average distance travelled every 30 minutes (μm), showing that induced cells travel more than uninduced cells. (B) Total distance travelled by cells after 15 hours on an x/y-plane.

PRNP, NTNG1 and CDH13 are highly expressed in U-87 cells

To be able to understand how phenotypic changes may occur in U-87 cells, screening for highly expressed GPI-APs is a relevant next step. Using qPCR, the expression of a number of cancer-related GPI-AP genes was screened for in U-87 cells. To obtain samples with a higher state of differentiation, a subset of cells was serum-starved. As shown in Figure 6, a high expression of cellular prion protein (PRNP), Netrin-G1 (NTNG1) and T-cadherin (CDH13) was found. All three genes showed to have lower expression upon serum starvation-induced differentiation, indicating a correlation of the expression of these genes to differentiation state.

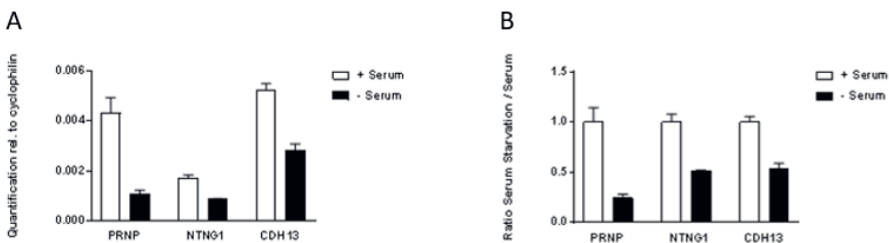


Figure 6. qPCR Analysis Revealing Highly Expressed Genes in U-87 Cells. Specific amplification

of PRNP, NTNG1 and CDH13 in U-87 cells of three technical replicates (average \pm SEM). (A) expression normalized to cyclophilin. (B) expression normalized to serum-containing medium. Upon serum starvation, expression levels decrease by 2-fold approximately.

Discussion and research outlook

This study takes the first step in assessing the involvement of GDE2 and GDE3 in glioblastoma. Here we show that CNTN4 and CNTN6 are novel target substrates for GDE3's enzymatic activity. Taking into account the cancer-stimulating effects of CNTN4 in brain cancers, GDE3 may have future therapeutic implications in these cancer types. Furthermore, CNTN6 is a ligand for Notch, an important regulator of cell self-renewal. Thus, future research should focus on the involvement of GDE3 in relevant cancer types through the cleavage of CNTN4 and CNTN6. As CNTNs primarily function as cell adhesion molecules, the direct impact of their cleavage should be validated in the context of cell motility and invasion capacity.

These results suggest that three other members in the CNTN family are potential GDE2 or GDE3 substrates: CNTN1, CNTN2 and CNTN3. While CNTN1 and CNTN3 are the least studied family members, only reported as candidate tumor suppressor genes with potential prognostic value in glioblastoma^{[8], [9]}, CNTN2 has been shown to inhibit proliferation of U-87 cells^[10]. Thus, examining GDE-specific cleavage of CNTN1, CNTN2 and CNTN3 is a necessary future direction to elucidate the additional role and mechanism of action of GDE3 in glioblastoma and its treatment.

The use of GDE2-inducible U-87 cells allowed examining the effect of GDE2-induction on the expression of five genes related to cell invasion: AK5, FIBCD1, IGFBP4 and STAC2. Our results indicate that GDE2 overexpression causes a downregulation of all five genes, suggestion an indirect role for GDE2 in reducing the scope of cell invasion in glioblastoma cells.

To understand how a reduction in cell invasion can be achieved, it is critical to determine which cell-surface substrates are targeted by GDE activity in glioblastoma cells. An initial assessment in this study reports three highly expressed GPI-APs in U-87 cells: netrin G-1 (NTNG1), T-cadherin (CDH13) and cellular prion protein (PRNP). Notably, CDH13 is a cell adhesion protein involved in cell migration and invasion. Given their potential involvement in the hallmarks of glioblastoma, it should be determined if these proteins can be recognized as substrates by GDE2 or GDE3. Lastly, it is worth considering an involvement of these proteins in differentiation state as well. This is especially the case for PRNP, for it controls stem cell-like properties of human glioblastoma tumor-initiating

cells^[11]. Thus, it would be relevant to perform assays on U-87-derived inducible systems to evaluate if GDE-mediated shedding of PRNP influences differentiation status.

Experimental procedures

Cell culture. HEK293, U-87 and Phoenix cells were grown in Dulbecco's modified Eagle's medium (DMEM) supplemented with 10% fetal bovine serum (FBS), 2 mM L-glutamine, 100 units/mL penicilline G and 100 µg/mL streptomycin at 37°C under 5% CO₂.

Retroviral transduction of U-87 cells. U-87 cells with inducible expression of GDE2 and GDE3 constructs were generated using the Retro-X™ Tet-On® Advanced Inducible Expression System (ClonTech). Phoenix Amphi cells were transfected overnight with 0,5 µg/mL pRetrox-Tet-On DNA using Fugene 6 reagent (Invitrogen). Medium was removed and filtered with a 0.45 µm filter and 5 µg/mL polybrene was added to the medium. All was transferred to U-87 cells followed by 5 hours of incubation. The transduction step was then repeated. After 24 hours, cells were placed under selection with G418 (200 µg/ml). When selection was complete, the protocol was repeated using pRetrox-GDE2-HA, pRetrox-GDE2-mCherry, and pRetrox-GDE3-GFP DNA, upon which selection was supplemented with puromycin (2 µg/ml). GDE2-HA, GDE-mCherry and GDE3-GFP were induced by adding 1 µg/ml doxycycline.

Cloning of GFP-tagged CNTN4 and CNTN6, and mCherry-tagged GDE2 and GDE3.

To obtain CNTN4 and CNTN6 for transfection, restriction cloning was performed. Primers with restriction sites were designed to amplify the CNTN4 and CNTN6 genes from cDNA by PCR. cDNA was obtained from the neuroblastoma cell line SH-SY5Y. The forward primer contained an *Apal* (CNTN4) or *Xmal* (CNTN6) restriction site, and the reverse primer contained a *NotI* restriction site. The amplified product was cleaved with restriction enzymes for *Apal/Xmal* and *NotI* from New England BioLabs inc[®]. On gel purification of the cleaved product was performed, cutting out a fragment of approximately 1.250kb. The vector pDisplay IgK-GFP-GPC6 was digested making use of the same restriction enzymes, thereby removing the in-built GPC6. The cut-empty vector was dephosphorylated using Antarctic phosphatase and on-gel purification was performed, cutting out a fragment of 5.7kb. Contactin and vector were ligated in a 3:1 ratio. Transformation was performed inserting a total of 160ng DNA in DH5-alpha competent *E. coli* bacteria by heat-shock and cultures were kept in selection by ampicillin.

Human GDE2 and GDE3 cDNA was subcloned as previously described^[3].

Activity assay and transient transfection. A total of 150,000 cells/well of HEK293

cells were plated on a Polyethylenimine- (PEI)-coated 6-well plate. After an overnight incubation, cells were co-transfected with previously cloned CNTN4 or CNTN6, and GDE2-mCherry, GDE3-mCherry or an empty vector (pDisplay IgK-GFP-GPC6), using Fugene 6 reagent (Invitrogen) in a 1:3 ratio in Opti-MEM medium. 24 hours after transfection, the medium was replaced by 1.2 mL serum-free DMEM. After 24 hours, PI-PLC (1:1,000) was added to one well containing cells co-transfected with empty vector. Next, the cells were analyzed by Western blotting.

Western blotting. Both the activity assays and the assessment of the functioning of the doxycycline-inducible systems were performed by Western blot. After 24-hour co-transfection or 48-hour doxycycline induction, cell supernatants were collected and centrifuged at 4,500 rpm for 45 min. Simultaneously, cells were washed with cold PBS and lysed in NP-40 buffer supplemented with protease inhibitors. The cell lysates were collected by scraping the wells' surface and they were centrifuged at 14,000 rpm for 15 min. Next, protein concentration was measured and normalized using the BCA protein assay kit (Pierce) and DTT and LDS sample buffer (NuPAGE, Invitrogen) was added. Lysate samples were loaded on an SDS-PAGE pre-cast gradient gel (4–12% Nu-Page Bis-Tris, Invitrogen) containing approximately 20 µg of total protein as well as a maximal amount of sample containing supernatant (28 µL). Protein was transferred to a nitrocellulose membrane. Non-specific protein binding was then blocked by 5% skimmed milk in TBST. Primary antibodies against actin, GFP, mCherry and HA were incubated in TBST with 2.5% skimmed milk, supplemented with 0.1% sodium azide. Antibodies against HA, GFP and mCherry were incubated overnight at 4°C, antibody against actin was incubated for 30 minutes at room temperature. Secondary antibodies conjugated to horseradish peroxidase (DAKO, Glostrup, Denmark) were incubated for 1 hour in 2.5% milk at room temperature, upon which protein was detected using ECL Western blot reagent.

Immunofluorescence. To prepare GDE2-HA for confocal microscopy, immunofluorescence staining was performed. Cells cultured on a 24-mm coverslip were washed with PBS and fixed using 4% paraformaldehyde in PBS (pH 7.4). Cells were permeabilized using 0.1% Triton X-100 and unspecific antibody binding was blocked using 2% BSA in PBS for 1 hour. A primary antibody against HA and an Alexa488-conjugated secondary antibody were subsequently incubated for 1 hour at room temperature in 2% BSA in PBS. Finally, the cells were mounted on a coverslip with mounting medium (Immu-Mount, Thermo Scientific).

Confocal microscopy. For assessing the subcellular localization of CNTN4, CNTN6, GDE2 and GDE3, confocal microscopy was performed. Cells were cultured on a 24-mm coverslip, fixed and mounted as previously described. Samples were visualized on a LEICA TCS-SP5 confocal microscope (63x objective).

qPCR analysis. Total RNA of U-87 cells was obtained using the GeneJET purification kit (Fermentas). Subsequently, cDNA was synthesized by reverse transcription from 5 µg RNA using a First Strand cDNA Syntesis Kit (Thermo Scientific). Real Time qPCR was performed on a 7500 Fast System (Applied Biosystems). Annealing and extension was performed (2 minutes at 95°C, 15 seconds at 95°C, 40 cycles, 1 minute at 60°C for annealing and extension), followed by dissociation. The final reaction mixtures (12 µl) consisted of diluted cDNA, SYBR Green Supermix (Applied Biosystems), 10 µM forward primer and 10 µM reverse primer. Reactions were performed in triplicates in 96-well plates. The primers used are depicted in Table 1. As a negative control, cDNA was replaced by nuclease-free water. Cyclophilin was used as a reference gene. The normalized expression (NE) data were calculated by the equation $NE = 2^{-(Ct_{target} - Ct_{reference})}$.

Random motility and differentiation assay. Inducible GDE2-HA- and GDE2-mCherry-expressing cells were counted and a total of 60,000 cells/well were plated in a 12-well plate. After 24 hours, they were washed with PBS, serum-free DMEM was added and doxycycline induction was started. Live imaging was performed using a Leica CCD3 microscope and images were captured every 30 minutes for 48 hours. Differentiation was measured by quantifying neurite length after 24 hours using the software ImageJ. Random motility was determined by tracking a total number of 10 cells for 15 hours, localizing cells every 30 minutes using the manual tracking function on ImageJ.

Table 5. Primers used for qPCR analysis.

Gene	Forward Primer 5'-3'	Reversed Primer 5'-3'
CRYAB	CCGACGTCTACTTCCCTGAG	CCATGCACCTCAATCACATC
AK5	CAGTGTGAAAAGCTGGTGGA	GGATAGCCGTCATCAGGAA
FIBCD1	TGGCTAGGGCTCAAGAGGAT	CAGTGCCGGAATAGTCAGC
IGFBP4	GAGGAGCTGGTGCGAGAG	CTGGATGGCCTCGATCTC
STAC2	GAAACTCCAAACAGGGCTTG	CAGTGGGTGGGGACTCTTT
GDE2	TCCTGGAACTGAGTGTGAA	GATGAGGGTGAAGGAGACCA
NTNG2	TTACACACACGGGACTGTGG	CACCCCTTCTTCTCTCCTC
CDH13	GGTCTCGAGCCCATACTTCA	AAGGAGCCCTGGATGTCTTT
PRNP	ACAAC TTTGTGCACGACTGC	TGGAGAGGAGAAGAGGACCA

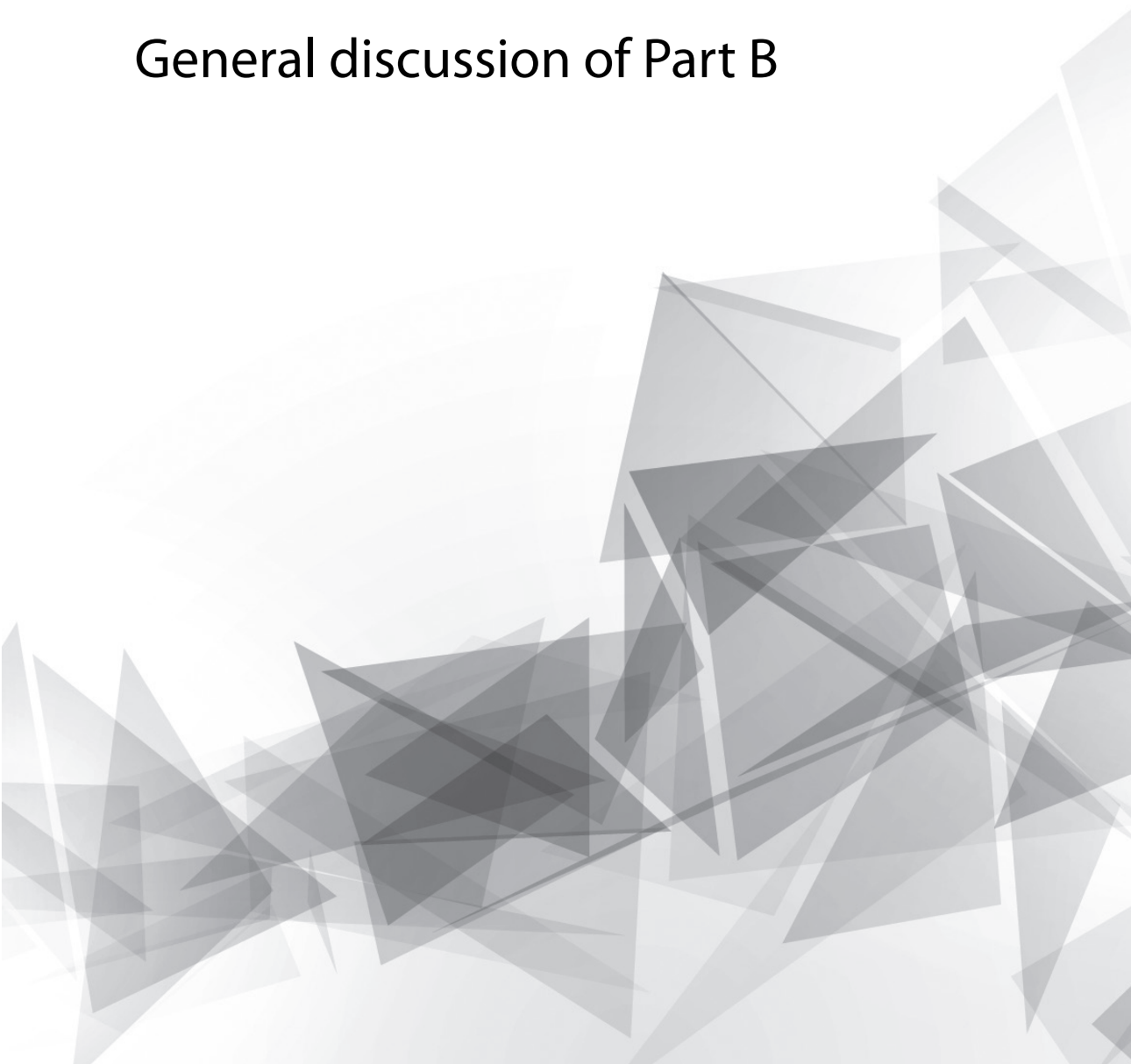
References

- [1] S. Dolezal, S. Hester, P. S. Kirby, A. Nairn, M. Pierce, K. L. Abbott, *Cancer Biomark.*, **2014**, 14, 55.
- [2] S. Park, C. Lee, P. Sabharwal, M. Zhang, C. L. F. Meyers, S. Sockanathan, *Science (80-)*, **2013**, 339, 324.
- [3] E. Matas-Rico, M. van Veen, D. Leyton-Puig, J. van den Berg, J. Koster, K. M. Kedziora, B. Molenaar, M. J. A. Weerts, I. de Rink, R. H. Medema, B. N. G. Giepmans, A. Perrakis, K. Jalink, R. Versteeg, W. H. Moolenaar, *Cancer Cell*, 30. 986., 2016.
- [4] M. Van Veen, E. Matas-Rico, K. van de Wetering, D. Leyton-Puig, K. M. Kedziora, V. de Lorenzi, Y. Stijf-Bultsma, B. van den Broek, K. Jalink, N. Sidenius, A. Perrakis, W. H. Moolenaar, *Elife*, **2017**, 6, 1.
- [5] L. Evenepoel, F. H. van Nederveen, L. Oudijk, T. G. Papatomas, D. F. Restuccia, E. J. T. Belt, W. W. de Herder, R. A. Feelders, G. J. H. Franssen, M. Hamoir, D. Maiter, H. K. Ghayee, J. W. Shay, A. Perren, H. J. L. M. Timmers, S. van Eeden, L. Vroonen, S. Aydin, M. Robledo, M. Vikkula, C. R. de Krijger, W. N. M. Dinjens, A. Persu, E. Korpershoek, *J. Clin. Endocrinol. Metab.*, **2018**, 103, 46.
- [6] L. M. Hansford, S. A. Smith, M. Haber, M. D. Norris, B. Cheung, G. M. Marshall, *Cytogenet. Genome Res.*, **2003**, 101, 17.
- [7] X.-Y. Cui, Q.-D. Hu, M. Tekaya, Y. Shimoda, B.-T. Ang, D.-Y. Nie, L. Sun, W.-P. Hu, M. Karsak, T. Duka, Y. Takeda, L.-Y. Ou, G. S. Dawe, F.-G. Yu, S. Ahmed, L.-H. Jin, M. Schachner, K. Watanabe, Y. Arsenijejevic, Z.-C. Xiao, *J. Biol. Chem.*, **2004**, 279, 25858.
- [8] H. Nord, C. Hartmann, R. Andersson, U. Menzel, S. Pfeifer, A. Piotrowski, A. Bogdan, W. Kloc, J. Sandgren, T. Olofsson, G. Hesselager, E. Blomquist, J. Komorowski, A. von Deimling, C. E. G. Bruder, J. P. Dumanski, T. Díaz de Ståhl, *Neuro. Oncol.*, **2009**, 11, 803.
- [9] Y.-F. Zhu, Y.-B. Guo, H.-Y. Zhang, P. Yang, D.-F. Wei, T.-T. Zhang, B.-R. Pan, L. Liu, *Oncol. Lett.*, **2019**, 18, 1863.
- [10] Y. Guo, P. Zhang, H. Zhang, P. Zhang, R. Xu, *Onco. Targets. Ther.*, **2017**, 10, 791.
- [11] A. Corsaro, A. Bajetto, S. Thellung, G. Begani, V. Villa, M. Nizzari, A. Pattarozzi, A. Solari, M. Gatti, A. Pagano, R. Würth, A. Daga, F. Barbieri, T. Florio, *Oncotarget*, **2016**, 7, 38638.



Chapter B4

General discussion of Part B



GDE2 intracellular trafficking

Chapter B2 uncovers the C-terminal tail sequences modulating the constitutive intracellular trafficking of GDE2. The experiments in neuronal cells showed how GDE2 vesicle trafficking follows the classical clathrin-mediated endocytosis route^[1], and is then routed to Rab5⁺ early endosomes for sorting. Most GDE2 returns to the cell surface through two recycling pathways: the fast (Rab4⁺) and slow (Rab11⁺) routes. As GDE2 is an ecto-enzyme, proper cell surface localization is crucial for ensuring its catalytic function^[2]. It can be argued that GDE2's constitutive cellular trafficking may be used to dynamically encounter specific GPI-anchored substrates, such as GPC6.

This mechanism of vesicle internalization is enabled by a C-terminal leucine residue. Dileucine-based motifs in the cytosolic tails of transmembrane proteins bind to the prototypical AP-2 clathrin adaptor complex that associates with the cytosolic face of the plasma membrane to mediate endocytosis^[3], with a strong requirement for inositol phospholipids^[4]. Adaptor protein (AP) complexes such as AP-2 are particularly important for polarized sorting in neuronal cells, given their extreme morphological asymmetry^[5], while AP dysfunction underlies a range of neurological pathologies^{[4], [6]}. Further studies are needed to define the exact sequence of this putative LI-based sorting motif and its possible interaction with the AP-2 complex.

To gain further mechanistic insight it will be essential to identify adaptors and other binding partners of the GDE2 tail that not only drive the recycling machinery but may also regulate GDE2 activity independently of its trafficking behavior. In this respect, subcellular localization of GDE2 mediated by its transmembrane domains warrants further study^[7], as does its possible interaction with regulatory transmembrane proteins, such as, for example, the tetraspanins that associate with the ADAM10 ecto-protease to regulate its trafficking and substrate specificity^[8]. Post-translational modifications might also modulate GDE2 trafficking and function, as exemplified by the finding that under oxidative conditions, disulfide bonding disrupts GDE2 exocytosis and cell-surface expression^[9]. However, we did not find evidence for GDE2 ubiquitylation or phosphorylation playing an important role in determining GDE2 subcellular localization [F.S.P., E.M.-R. and Roy Baas (Division of Biochemistry, The Netherlands Cancer Institute, Amsterdam), unpublished results].

Aside from tightly regulated trafficking, the biological outcome of GDE2 activity will critically depend on the local availability of GPI-anchored protein substrates and their spatiotemporal regulation in a given cell type. Determination of the substrate specificity for GDE2 and its structural basis therefore has a high priority. From a signaling point of view, another key question concerns the intracellular signaling routes by which GDE2-induced GPI-anchor cleavage triggers gene expression and neuronal differentiation

cell autonomously. One attractive scenario implicates type-II receptor protein tyrosine phosphates (RPTPs) as candidate effectors, some of which exhibit high-affinity interactions with glypicans and might initiate new signaling events upon GDE2-included glypican cleavage^{[10], [11]}.

Pathophysiological implications of GDE2 and GDE3

GDE2 deficiency has implications in the development of neurodegeneration in mice with motor neuron pathologies analogous to those in human disease^{[12], [13]}. This raises the possibility that the GDE2 dysfunction described in **Chapter B2** may underlie aspects of neurodegenerative disease and/or contribute to the pathophysiology of neuroblastoma. However, to our knowledge, disease-associated GDE2 deficits have not been documented to date, neither in neurodegenerative disease nor in malignant neuroblastoma. Given the present findings, however, GDE2 dysfunction could well result from defective endocytic trafficking rather than from loss-of-function mutations. As impaired membrane trafficking is a hallmark of neurodegenerative diseases, unraveling the trafficking mechanisms of GDE2 – and those of its GPI-anchored substrates – should help better understand the regulation of GDE2 activity and its (patho)physiological implications in the nervous system and beyond.

Chapter B3 involves GDE2 and GDE3 in glioblastoma for the first time. On the one hand, GDE2 was able to reduce invasion markers using an immortalized glioblastoma cell line in a preliminary analysis. However, further phenotypical characterization should be performed. On the other hand, we show that GDE3 cleaves two proteins belonging to the contactin family: CNTN4 and CNTN6^{[14], [15]}. These cell-adhesion molecules that are highly expressed in glioblastoma and have previously been shown to be involved in the development of several other brain cancers. As GDE3 highly expresses in glial cells (https://web.stanford.edu/group/barres_lab/brain_rnaseq.html), its cleavage of CNTN4 and CNTN6, among other GPI-anchored proteins, is an intriguing regulatory mechanism that requires further research.

References

- [1] M. Mettlen, P.-H. Chen, S. Srinivasan, G. Danuser, S. L. Schmid, *Annu. Rev. Biochem.*, **2018**, 87, 871.
- [2] P. J. Cullen, F. Steinberg, *Nat. Rev. Mol. Cell Biol.*, **2018**, 19, 679.
- [3] B. T. Kelly, A. J. McCoy, K. Späte, S. E. Miller, P. R. Evans, S. Höning, D. J. Owen, *Nature*, **2008**, 456, 976.
- [4] A. Sanger, J. Hirst, A. K. Davies, M. S. Robinson, *J. Cell Sci.*, **2019**, 132
- [5] J. S. Bonifacino, *J. Cell Biol.*, **2014**, 204, 7.
- [6] C. M. Guardia, R. De Pace, R. Mattera, J. S. Bonifacino, *Curr. Opin. Neurobiol.*, **2018**, 51, 103.
- [7] P. Cosson, J. Perrin, J. S. Bonifacino, *Trends Cell Biol.*, **2013**, 23, 511.
- [8] A. L. Matthews, J. Szyroka, R. Collier, P. J. Noy, M. G. Tomlinson, *Biochem. Soc. Trans.*, **2017**, 45, 719.
- [9] Y. Yan, C. Wladyka, J. Fujii, S. Sockanathan, *Nat. Commun.*, **2015**, 6, 7006.
- [10] C. H. Coles, E. Y. Jones, A. R. Aricescu, *Semin. Cell Dev. Biol.*, **2015**, 37, 98.
- [11] J. S. Ko, G. Pramanik, J. W. Um, J. S. Shim, D. Lee, K. H. Kim, G.-Y. Chung, G. Condomitti, H. M. Kim, H. Kim, J. de Wit, K.-S. Park, K. Tabuchi, J. Ko, *Proc. Natl. Acad. Sci. U. S. A.*, **2015**, 112, 1874.
- [12] C. Cave, S. Park, M. Rodriguez, M. Nakamura, A. Hoke, M. Pletnikov, S. Sockanathan, *Mol. Neurodegener.*, **2017**, 12, 8.
- [13] E. Matas-Rico, M. van Veen, D. Leyton-Puig, J. van den Berg, J. Koster, K. M. Kedziora, B. Molenaar, M. J. A. Weerts, I. de Rink, R. H. Medema, B. N. G. Giepmans, A. Perrakis, K. Jalink, R. Versteeg, W. H. Moolenaar, *Cancer Cell*, 30. 986., 2016.
- [14] L. Evenepoel, F. H. van Nederveen, L. Oudijk, T. G. Papathomas, D. F. Restuccia, E. J. T. Belt, W. W. de Herder, R. A. Feelders, G. J. H. Franssen, M. Hamoir, D. Maiter, H. K. Ghayee, J. W. Shay, A. Perren, H. J. L. M. Timmers, S. van Eeden, L. Vroonen, S. Aydin, M. Robledo, M. Vikkula, R. R. de Krijger, W. N. M. Dinjens, A. Persu, E. Korpershoek, *J. Clin. Endocrinol. Metab.*, **2018**, 103, 46.
- [15] X.-Y. Cui, Q.-D. Hu, M. Tekaya, Y. Shimoda, B.-T. Ang, D.-Y. Nie, L. Sun, W.-P. Hu, M. Karsak, T. Duka, Y. Takeda, L.-Y. Ou, G. S. Dawe, F.-G. Yu, S. Ahmed, L.-H. Jin, M. Schachner, K. Watanabe, Y. Arsenijevic, Z.-C. Xiao, *J. Biol. Chem.*, **2004**, 279, 25858.



Addendum



Interview: First person – Fernando Salgado-Polo

Based on:

Interview published on *Journal of Cell Science* on 10 February 2020.

Abstract

First Person is a series of interviews with the first authors of a selection of papers published on *Journal of Cell Science*, helping early-career researchers promote themselves alongside their papers. Fernando Salgado-Polo is first author on 'Sequence-dependent trafficking and activity of GDE2, a GPI-specific phospholipase promoting neuronal differentiation', published on JCS. Fernando is a PhD student in the lab of Anastassis Perrakis at The Netherlands Cancer Institute, Amsterdam, The Netherlands, investigating the biochemical characterization of (lyso)phospholipases and their biological roles in cell signaling.



How would you explain the main findings of your paper in lay terms?

Neuroblastoma is one of the most common cancer types in children, and happens when some motor neurons keep dividing uncontrollably. Glypican 6, among many other proteins on the surface of the cell, can get messages across telling cells to keep dividing. In our lab, we identified that a protein on the cell membrane, called GDE2, can shed glypican 6 off the cell surface, making cells less cancerous. In this work, we aimed to explain why GDE2 is sometimes found on the cell surface, where it is active, and some other times in vesicles inside the cell, where it would be inactive. To figure this out, we chopped off pieces of GDE2, and we discovered a sequence that forces GDE2 to leave the cell surface and go inside the cell. Eventually, we saw that this related to more glypican 6 being present on the surface, making neuroblastoma cells divide more. In the future, we will explore which other proteins take part in making GDE2 go into vesicles. This will help us get a better picture of its role in neuroblastoma and, possibly, neurodegenerative diseases.

Were there any specific challenges associated with this project? If so, how did you overcome them?

When we performed experiments to determine if the GDE2 truncations caused distinct phenotypes, our unanimously agreed least-favorite was the quantitation of internalization and recycling rates by biotin labeling. As part of the revision of the paper, we had to first optimize a working protocol with a cell line, as well as get technically reproducible results,

which meant my co-author Elisa Matas-Rico and I had to work for very long hours in the lab for a couple of months. Eventually, we managed to get it all to work and fulfill the reviewers' expectations. Going through this made me recall once again how gratifying science is when hard work has its reward.

When doing the research, did you have a particular result or 'eureka' moment that has stuck with you?

I think our shared 'eureka' moment was the time we observed the subcellular localization of each truncation when using inducible stably transfected cells. Upon taking a first glimpse on the microscope, it was clear to both of us that the 'trend' we were seeing with transient transfections was in fact a real phenotypic difference (Fig.1).

Why did you choose Journal of Cell Science for your paper?

The Journal of Cell Science appealed to us because of its focus on fundamental research in the field of cell biology, which is why we thought our story would be a fit. Moreover, JCS is published by a not-for-profit organization with an interdisciplinary audience, which warrants a broad audience.

What motivated you to pursue a career in science, and what have been the most interesting moments on the path that led you to where you are now?

Contrary to what most people would respond to this question, biology was admittedly one of the subjects I liked the least in high school – age 12–15. However, it was around this time when my uncle, who worked as a biotechnologist, passed away in an unexpected way. I think this was one important factor that made me focus my attention on biochemistry and physics in the coming years. Regarding milestones that shaped me professionally, I would say that moving to The Netherlands to take my master's degree has arguably had the biggest effect on my career in science. In large part because this allowed me to get out of my comfort zone and work in two well-known Dutch research institutes with an international and multidisciplinary environment. Our article in JCS is a very good example of this, since it mainly involved cell biology and microscopy techniques that I had no experience with as an undergraduate student. Honestly, I believe having a change of scene and research groups can only enrich your training and education as a scientist, and I highly recommend people who are unsure about it to take that chance and go for it.

Who are your role models in science? Why?

I was studying biochemistry at the Complutense University of Madrid when the European financial crisis started to damage science in Spain. During my university years, I admired many motivated scientists who were and are still passionate about biochemistry and molecular biology despite the lack of resources they face. One such example is Dr Cristina

Casals, who kindly hosted me as an undergraduate student. Her passion both in lectures and in the lab was contagious and made research really appeal to me up to this day. This further confirmed to me that my research path should always include protein biophysics and lipid research as constants, since that is what I truly love doing.

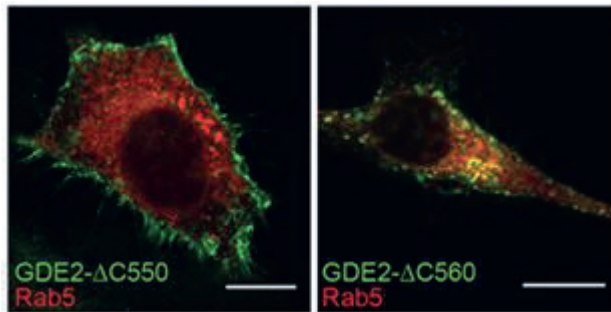


Figure 1. C-terminal tail truncations uncover unique regulatory sequences. Confocal images of N1E-115 cells co-expressing the indicated GDE2 C-terminal truncations and Rab5-mCh as a marker for early endosomes. Scale bars: 10 μ m.

What's next for you?

In the short/medium term I will be working on finishing up other projects as part of my PhD. I expect to finish by the second half of 2021 (let's see if my prediction stands by then!), after which I would like to take up a job as a postdoctoral researcher and continue my career trying to combine structural biology and cell biochemistry – since I can't make up my mind which one I prefer.

Tell us something interesting about yourself that wouldn't be on your CV

Beyond all doubt, learning languages is one of my passions in life, which has held true ever since I was in middle school. I really enjoy knowing what the logic behind a language is, what sounds people use to communicate, and how culture has shaped dialects and accents into what they are nowadays. Of course, I will take any chance to practice with a native speaker, which is easy in such an international and friendly environment like the Netherlands Cancer Institute. However, sometimes this means I will try to think in five different languages while doing experiments at work... Aside from this, I enjoy having beers after work on Fridays (borrelen in Dutch), going clubbing with friends, and traveling. The latter has been partly restricted to Madrid lately, since I became the proud uncle of a gorgeous baby boy last May.

Reference

Salgado-Polo, F., van Veen, M., van den Broek, B., Jalink, K., Leyton-Puig, D., Perrakis, A., Moolenaar, W. H. and Matas-Rico, E. (2020). Sequence-dependent trafficking and activity of GDE2, a GPI-specific phospholipase promoting neuronal differentiation. *J. Cell Sci.* 133, 235044. <https://doi.org/10.1242/jcs.235044>

List of publications

- Salgado-Polo, F.; Borza, R.; Marsais, F.; Jagerschmidt, C.; Waeckel, L.; Moolenaar, W. H.; Ford, P.; Heckmann, B.; Perrakis, A. Autotaxin facilitates selective LPA receptor signaling. *Under review for Cell Chemical Biology*.
- Booijink, R.; Salgado-Polo, F.; Jamieson, C.; Perrakis, A.; Bansal, R. A novel type IV autotaxin inhibitor ameliorates acute liver injury and nonalcoholic steatohepatitis. *EMBO Mol. Med.* **2022**, 14 (9), e16333. doi: 10.15252/emmm.202216333.
- Clark, J. M.*; Salgado-Polo, F.*; Macdonald, S. J. F.; Barrett, T. N.; Perrakis, A.; Jamieson, C. Structure-Based Design of a Novel Class of Autotaxin Inhibitors Based on Endogenous Allosteric Modulators. *J. Med. Chem.* **2022**, 65 (8), 6338–6351. doi: 10.1021/acs.jmedchem.2c00368.
- Borza, R.; Salgado-Polo, F.; Moolenaar, W. H.; Perrakis, A. Structure and Function of the Ecto-Nucleotide Pyrophosphatase/Phosphodiesterase (ENPP) Family: Tidying up Diversity. *J. Biol. Chem.* **2022**, 298 (2), 101526. doi: 10.1016/j.jbc.2021.101526.
- Matas-Rico, E.; Frijlink, E.; van der Haar Àvila, I.; Menegakis, A.; van Zon, M.; Morris, A. J.; Koster, J.; Salgado-Polo, F.; de Kivit, S.; Lança, T.; Mazzocca, A.; Johnson, Z.; Haanen, J.; Schumacher, T. N.; Perrakis, A.; Verbrugge, I.; van den Berg, J. H.; Borst, J.; Moolenaar, W. H. Autotaxin Impedes Anti-Tumor Immunity by Suppressing Chemotaxis and Tumor Infiltration of CD8(+) T Cells. *Cell Rep.* **2021**, 37 (7), 110013. doi: 10.1016/j.celrep.2021.110013.
- Deng, X.*; Salgado-Polo, F.*; Shao, T.*; Xiao, Z.; Van, R.; Chen, J.; Rong, J.; Haider, A.; Shao, Y.; Josephson, L.; Perrakis, A.; Liang, S. H. Imaging Autotaxin In Vivo with (18)F-Labeled Positron Emission Tomography Ligands. *J. Med. Chem.* **2021**, 64 (20), 15053–15068. doi: 10.1021/acs.jmedchem.1c00913.
- van Beusekom, B.; Damaskos, G.; Hekkelman, M. L.; Salgado-Polo, F.; Hiruma, Y.; Perrakis, A.; Joosten, R. P. LAHMA: Structure Analysis through Local Annotation of Homology-Matched Amino Acids. *Acta Crystallogr. Sect. D, Struct. Biol.* **2021**, 77 (Pt 1), 28–40. doi: 10.1107/S2059798320014473.
- Salgado-Polo, F.; van Veen, M.; van den Broek, B.; Jalink, K.; Leyton-Puig, D.; Perrakis, A.; Moolenaar, W. H.; Matas-Rico, E. Sequence-Dependent Trafficking and Activity of GDE2, a GPI-Specific Phospholipase Promoting Neuronal Differentiation. *J. Cell Sci.* **2020**, 133 (3). doi: 10.1242/jcs.235044.
- Salgado-Polo, F.; Perrakis, A. The Structural Binding Mode of the Four Autotaxin Inhibitor Types That Differentially Affect Catalytic and Non-Catalytic Functions. *Cancers (Basel)*. **2019**, 11 (10). doi: 10.3390/cancers11101577.
- Salgado-Polo, F.; Fish, A.; Matsoukas, M.-T.; Heidebrecht, T.; Keune, W.-J.; Perrakis, A. Lysophosphatidic Acid Produced by Autotaxin Acts as an Allosteric Modulator of Its Catalytic Efficiency. *J. Biol. Chem.* **2018**, 293 (37), 14312–14327. doi: 10.1074/jbc.RA118.004450.
- Keune, W.-J.; Potjewyd, F.; Heidebrecht, T.; Salgado-Polo, F.; Macdonald, S. J. F.; Chelvarajan, L.; Abdel Latif, A.; Soman, S.; Morris, A. J.; Watson, A. J. B.; Jamieson, C.; Perrakis, A. Rational Design of Autotaxin Inhibitors by Structural Evolution of Endogenous Modulators. *J. Med. Chem.* **2017**, 60 (5), 2006–2017. doi: 10.1021/acs.jmedchem.6b01743.

Miller, L. M.; Keune, W.-J.; Castagna, D.; Young, L. C.; Duffy, E. L.; Potjewyd, F.; Salgado-Polo, F.; Engel García, P.; Semaan, D.; Pritchard, J. M.; Perrakis, A.; Macdonald, S. J. F.; Jamieson, C.; Watson, A. J. B. Structure-Activity Relationships of Small Molecule Autotaxin Inhibitors with a Discrete Binding Mode. *J. Med. Chem.* **2017**, *60* (2), 722–748. doi: 10.1021/acs.jmedchem.6b01597.

* these authors contributed equally to this publication.

Curriculum vitae (English)

Fernando Salgado Polo was born on the 28th of April 1993 in Cáceres, Extremadura, Spain. He graduated in Biochemistry at the Complutense University of Madrid, Spain, in 2015. He then moved to Amsterdam, the Netherlands, to follow the master's degree in Biomolecular Sciences at the VU University, which he finished with honors in 2017. At this stage, he performed a first internship at the Netherlands Cancer Institute (NKI) in the group of prof. dr. A. Perrakis, studying the biochemical regulation of autotaxin. Next, he followed a longer second placement at the Academic Medical Center (AMC) in Amsterdam in the group of prof. dr. T. van der Poll, where he studied macrophage differentiation in connection to endotoxin tolerance. After this, he returned to the NKI for his PhD, where he took part in numerous research projects related to autotaxin and the GDPD protein family.

Curriculum vitae (español)

Fernando Salgado Polo nació el 28 de abril de 1993 en la ciudad española de Cáceres, Extremadura. En 2015, se graduó en Bioquímica en la Universidad Complutense de Madrid, tras lo cual se mudó a Ámsterdam, Países Bajos, a fin de realizar sus estudios de máster en Ciencias Biomoleculares en la Universidad Libre de Ámsterdam (*Vrije Universiteit*). En esta etapa formativa, realizó una primera estancia en prácticas en el grupo de investigación del catedrático Anastassis Perrakis, donde estudió la regulación bioquímica de la proteína *autotaxina*. A continuación, llevó a cabo un segundo periodo de prácticas en el Centro Médico Académico (AMC) de Ámsterdam en el grupo del catedrático Tom van der Poll, donde investigó el proceso de diferenciación de macrófagos en relación con la tolerancia a toxinas bacterianas. Finalmente, concluyó sus estudios de máster con matrícula de honor y regresó al NKI para su doctorado, en el que tomó parte en un gran número de proyectos de investigación que implicaron a la autotaxina y las proteínas de la familia GTPD.

Summary

Enzymes allow for essential chemical reactions that make life possible. They are the cell's catalysts, binding to a *substrate* and turning it into a *product*. Enzymes can be found in many shapes: single proteins that help digest our food, protein complexes that enable the replication of our genetic material, and RNA-based enzymes that ensure the proteins synthesis.

All these functions need enzymes to be active or inactive in the right place at the right time; thus, they have to be regulated. This can simply be driven by the amount of substrate they come across, which pushes their reactions forward, or by the amount of product that has already built up, which slows their reactions down. More sophisticated mechanisms exist, like the binding of a molecule or modulator somewhere in the enzyme's structure (known as an allosteric site), or a humanmade drug that binds to an enzyme in a way that no more product can be made.

If conditions allow and an enzyme manages to make a product, it will typically carry out a biological function, such as keeping our metabolisms running or activating a so-called cell signaling pathway. Signaling within or between our cells is necessary to sense what happens around them and answer important questions: "Can I take up enough oxygen?", "Is there enough sugar in the blood?", "Is it daytime or nighttime?", "Should I divide or die?".

The focus of this thesis is on enzymes called phospholipases, which make cuts at specific places in phospholipids. Lipids, are not only the basic building blocks of our cells' membranes, but they are also potent cell signaling molecules, modulating pathways that determine a cell's fate.

In **Part A**, I study the phospholipase called **autotaxin** (or **ATX**), an essential enzyme that cleaves a specific lipid type: lysophospholipids. When coming across a lysophospholipid with a polar headgroup, autotaxin will cleave this headgroup off, leaving behind a new lysolipid. The most physiologically relevant products of autotaxin is a series of lipids called lysophosphatidic acids (**LPAs**). There are various types of LPA (with *e.g.* different acyl chain lengths or number of unsaturated bonds) even if we often refer to all these as LPA. LPAs are necessary for many life processes, such as embryonic development and blood vessel growth, but are also the driver for many diseases, as it can trigger cancer metastasis, inflammation and fibrosis, among others.

In **Chapter A1**, I give a general introduction to autotaxin, which covers relevant biochemical knowledge since its discovery, as well as a brief overview of drug development efforts to block its function. The crystal structure of autotaxin, previously determined in my home

lab, had revealed a triple interconnected binding site: the **tripartite site** (artistically depicted in the cover of this thesis). This site within autotaxin encompasses the catalytic active site, where the enzymatic reaction takes place; the hydrophobic pocket, which accommodates the lipid chain, and the allosteric site, the so-called **tunnel**.

Chapter A2 explores the role of the tunnel. Here, I unveil a new and striking regulatory mechanism, where the LPA product accelerates its own synthesis by binding to the tunnel. I show this by a combination of biophysical techniques, molecular dynamics simulations and transient and steady state kinetic analyses, which concludes in a comprehensive model of the low- and high-activity states of autotaxin's function.

Many inhibitors have been designed over the last two decades to block autotaxin's activity. Seeing that the tunnel is so important for the regulation of its activity, my home lab had collaborated in the production of a new compound that blocks both the tunnel and the hydrophobic pocket (type IV). In **Chapter A3**, similar compounds have been synthesized to allow labeling them to enable positron emission tomography (PET), in hopes that it can be used for non-invasive detection of autotaxin. Here, we first analyze the binding mode of this drug to autotaxin, to then validate its effectiveness in tracking autotaxin in *in vivo* liver disease models.

In **Chapter A4**, I describe the collaborative discovery, optimization and function of a new hybrid series of autotaxin inhibitors designed to bind at both the tunnel and the active site (type V). This represents a complementary mode of action to that of the tunnel-hydrophobic pocket hybrids (type IV), which could prove clinically significant in the future.

The existence of different inhibitory mechanisms at autotaxin's tripartite site eventually enabled their classification of all inhibitors developed so far, into the six distinct binding modes. In **Chapter A5**, I review the available compounds' structures and site of binding within autotaxin, in light of their structures.

Out of these diverse modes of binding, to date only compounds that bind at the tunnel have progressed to clinical trials for the treatment of fibrotic diseases. **Chapter A6** focuses on the potential application of autotaxin inhibitors in liver disease. Motivated by the insights we had in the previous chapters, we contrast the compounds PF8380 (type I) and Cpd17 (type IV) in relevant hepatic cell lines, where we describe the signaling pathways that get activated. As Cpd17 decreased most *in vitro* hallmarks of liver disease significantly more than PF8380, we decided to study the effectiveness of Cpd17 in animal models for liver disease. This study showed a great reduction of plasma levels of important biomarkers, such as triglycerides, cholesterol and transaminases, suggesting that inhibition of autotaxin by type IV compounds can be important for treatment of fibrotic liver disease.

The observation that tunnel-binding type IV Cpd17 performed better than type I PF8380 *in vitro* raised an important question: are type IV autotaxin inhibitors mechanistically different from type I compounds? To address this, we teamed up with the Belgo-Dutch company Galapagos NV to compare their effect on CpdA (type I) and the phase 3 clinical candidate GLPG1690 (type IV). **Chapter A7** delves into the biochemical and cell biological one-to-one comparison of these two types of drugs, and unveiling an overlooked function of autotaxin as a signaling molecule: autotaxin ensures the selective transport of LPA to its cell surface receptors. We conclude this study by an *in vivo* comparison of CpdA and GLPG1690 in primary lung fibroblasts and in a pulmonary fibrosis animal model, which support our previous results.

Additionally, my work on autotaxin resulted in five more collaborative publications in diverse aspects, ranging from inhibitor design to their immunotherapeutic applications. My contributions to these works are briefly commented in **Chapter A8**.

In **Chapter A9** I discuss how we now view the enzymatic and non-enzymatic functions of autotaxin. I also examine how clinical success of drug candidates targeting autotaxin depends on binding the **tunnel**, which inhibits the catalysis-independent signaling functions that I uncovered in my research.

In **Part B** of this thesis, I research another family of phospholipases: the glycerophosphodiester phosphodiesterase (or **GDPD**) family. Much like autotaxin, GDPDs will look for phospholipids, which they will cleave at specific sites. In this case, GDPDs recognize a very complex lipid that cells attach to some proteins so that these proteins stay in the cell surface. Cleavage of this *anchor* (called glycosylphosphatidylinositol or **GPI**) by the GDPDs will shed a specific protein off the cell surface into, for instance, the blood, where it can have a specific function, or be used as a biomarker for cancer. The emerging picture in this relatively new field is that the activity of specific GDPDs relates to a positive prognosis of breast cancer and neuroblastoma, among others.

In **Chapter B1**, I introduce the most important aspects of GPI anchors, as well as the established biology of two members of the GDPD protein family: GDE2 and GDE3. Even though these proteins are both inserted in the plasma membrane, GDE2 does not always remain there. This protein actually goes into vesicles inside the cell, where it cannot carry out its function. As regulation of cellular location is crucial for enzymatic activity, in **Chapter B2** I studied the determinants of this behavior by removing different stretches of GDE2's C-terminal amino acid sequence. We then analyzed the impact of altered intracellular trafficking on neuroblastoma cell lines. Given the accumulated evidence of the role of GDE2 and GDE3 in malignant cancers, I also ventured to identify new clinically relevant substrates they may recognize and cleave. A preliminary step in this direction

is taken in **Chapter B3**, where we show that contactins are an attractive and unstudied protein family recognized by GDE3, but not GDE2. This finding may become relevant towards better treatments for glioblastoma. Lastly, in **Chapter B4** I discuss the main findings and implications of my work on the GDPD protein family, emphasizing on future research directions.

Nederlandse samenvatting

Enzymen voeren essentiële chemische reacties uit, die het leven mogelijk maken. Ze zijn de katalysatoren van de cel, die zich aan een *substraat* binden om het in een *product* om te zetten. Enzymen kunnen in veel verschillende vormen worden aangetroffen: afzonderlijke eiwitten die ons voedsel helpen verteren, eiwitcomplexen die de replicatie van ons genetisch materiaal mogelijk maken, en zelfs RNA-enzymen die de eiwitten van ons lichaam maken.

Voor al deze functies zijn enzymen nodig die op het juiste moment en op de juiste plaats actief of juist inactief zijn; ze moeten dus worden gereguleerd. Hun activiteit is eenvoudig te beïnvloeden door de hoeveelheid substraat die de enzymen tegenkomen. Hierdoor worden hun reacties bevorderd, of, als de hoeveelheid product zich reeds heeft opgehoopt, worden hierdoor hun reacties vertraagd. Er bestaan ook meer verfijnde mechanismen, zoals de binding van een molecuul of *modulator* in de structuur van het enzym (bekend als een allosterische bindingsplaats), of een door de mens gemaakt geneesmiddel dat zich aan een enzym bindt zodat er geen product meer kan worden gemaakt.

Als de omstandigheden het toelaten en een enzym erin slaagt een product te maken, voert dit meestal een biologische functie uit, zoals het op gang houden van onze stofwisseling of het activeren van een zogenaamde celsignaleringsroute. Celsignaling binnen of tussen onze cellen is nodig om aan te voelen wat er om hen heen gebeurt en belangrijke vragen te beantwoorden: “Kan ik genoeg zuurstof opnemen?”, “Is er suiker in het bloed?”, “Is het dag of nacht?”, “Moet ik sterven of mag ik me delen?”.

In dit proefschrift ligt de nadruk op fosfolipasen, die op specifieke plaatsen in fosfolipiden knippen. Lipiden zijn niet alleen de basisbouwstenen van de membranen van onze cellen, maar ze zijn ook krachtige moleculen voor celsignaling, waarbij celsignaleringsroutes geactiveerd worden die het lot van een cel bepalen.

In **Deel A** bestudeer ik het fosfolipase **autotaxine** (of **ATX**), een essentieel enzym dat een specifiek type lipide knipt: de lysofosfolipiden. Wanneer een lysofosfolipide met een polaire kopgroep wordt aangetroffen, kan autotaxine de kopgroep afsplitsen, waarbij een nieuwe lysolipide achterblijft. De fysiologisch meest relevante producten van autotaxine zijn een type lipiden die lysofosfatidezuren (**LPA's**) worden genoemd. LPA is noodzakelijk voor veel levensprocessen, zoals de embryonale ontwikkeling en de groei van bloedvaten, maar te veel of juist te weinig kan ook leiden tot veel ziekten, waar het onder meer kankermetastase, ontsteking en fibrose kan veroorzaken.

In **Hoofdstuk A1** geef ik een algemene inleiding van autotaxine, waarin de relevante

biochemische kennis sinds zijn ontdekking wordt behandeld, evenals de ontwikkeling van medicijnen om de functie te blokkeren. De kristalstructuur van autotaxine onthulde een drie onderling verbonden bindingsplaatsen: de **tripartiete bindingsplaats** (artistiek afgebeeld op de omslag van dit proefschrift). Deze plaats in autotaxine omvat de katalytische actieve bindingsplaats, waar de enzymatische reactie plaatsvindt; de hydrofobe *pocket*, die de lipideketen herbergt, en de allosterische bindingsplaats, de zogenaamde **tunnel**.

Hoofdstuk A2 gaat dieper in op de rol van de tunnel. Hier onthul ik een nieuw en opvallend regulatiemechanisme, waarbij ATX zijn eigen activiteit versnelt door binding van LPA aan de tunnel. Dit toon ik aan door een combinatie van biofysische technieken, moleculaire dynamicsimulaties en kinetische analyses, wat naar een uitgebreid model leidt van de lage- en hoge-activiteitstoestanden van autotaxine.

In de afgelopen twee decennia zijn er veel inhibitoren ontworpen om de activiteit van autotaxine te blokkeren. Omdat de tunnel zo belangrijk is voor de regulatie van zijn activiteit, had mijn lab bij het NKI meegewerkt aan de productie van een nieuw geneesmiddel dat allebei de tunnel en de hydrofobe *pocket* blokkeert (type IV). In **Hoofdstuk A3** werden vergelijkbare geneesmiddelen gemaakt en radioactief gelabeld om het door positronemissietomografie (PET) te onderzoeken, in de hoop dat het gebruikt kan worden voor niet-invasieve detectie van autotaxine. Hier analyseren we eerst de bindingsmodus van dit geneesmiddel aan autotaxine, om vervolgens zijn effectiviteit te valideren door het opsporen van autotaxine in muizenmodellen voor leverziekte.

In **Hoofdstuk A4** beschrijf ik de ontdekking, de optimalisatie en de functie van een nieuwe hybride serie autotaxine inhibitoren die ontworpen zijn om zowel de tunnel als de actieve bindingsplaats (type V) te blokkeren. Dit is een aanvullend mechanisme op dat van de inhibitoren die de tunnel en hydrofobe *pocket* blokkeren (type IV) en zou dat in de toekomst van groot klinisch belang zou kunnen zijn.

Het combineren van verschillende inhibitoren die op diverse manieren in de tripartiete bindingsplaats van autotaxine binden heeft geleid tot zes verschillende types inhibitoren. In **Hoofdstuk A5** bespreek ik de structuur van de beschikbare geneesmiddelen en hun bindingsplaats binnen autotaxine in het licht van hun kristalstructuren.

Van deze zes verschillende types inhibitoren, zijn tot op heden alleen geneesmiddelen met een tunnel-bindingsplaats getest in klinische proeven tegen fibrotische ziekten. Aangezien leverziekten vaak door ontsteking en fibrose ontstaan, richt **Hoofdstuk A6** zich op de toepassing van de inhibitoren voor autotaxine voor de behandeling van leverziekten. Na de positieve resultaten van de voorbije hoofdstukken zetten we de geneesmiddelen

PF8380 (type I) en Cpd17 (type IV) tegenover elkaar in relevante levercellijnen, waarbij we de geactiveerde celsignaleringsroutes beschrijven. Aangezien Cpd17 beter is om de kenmerken van leverziekte in cellijnen te verminderen dan PF8380, besloten wij het effect van Cpd17 te bestuderen in twee muizenmodellen voor fibrotische leverziekte. In deze proeven kon het geneesmiddel Cpd17 een grote vermindering veroorzaken van plasmaspiegels van belangrijke *biomarkers*, zoals triglyceriden, cholesterol en transaminasen.

Doordat type IV (tunnelbindende) Cpd17 beter presteerde dan type I (niet-tunnelbindende) PF8380 wilden we antwoord geven op een belangrijke vraag: zijn type IV inhibitoren voor autotaxine mechanistisch anders dan die van type I? Om dit te kunnen beantwoorden hebben we samengewerkt met het Belgisch-Nederlandse bedrijf Galapagos NV. **Hoofdstuk A7** gaat in op de biochemische en celbiologische één-op-één vergelijking tussen CpdA (type I) en fase 3 klinische kandidaat GLPG1690 (type IV). Dit werk onthult dat autotaxine een functie heeft als een signaalmolecule. Ik laat zien dat het zorgt voor het selectieve transport van LPA naar zijn receptoren op het celoppervlak. We sluiten deze studie af met een vergelijking van CpdA en GLPG1690 in een muizenmodel voor longfibrose dat onze eerdere resultaten ondersteunt.

Daarnaast heeft mijn werk aan autotaxine naar nog vijf gezamenlijke publicaties geleid in diverse aspecten, inclusief het ontwerp van inhibitoren en hun toepassingen in immunotherapie. Mijn bijdraag aan deze projecten worden kort toegelicht in **Hoofdstuk A8**.

In **Hoofdstuk A9** bespreek ik hoe we nu tegen de enzymatische en niet-enzymatische functies van autotaxine aankijken. Hier ga ik ook in op hoe het klinische succes van de geneesmiddelen gericht tegen autotaxine afhankelijk is van het binden in de **tunnel** en het blokkeren van de katalyse-onafhankelijke signaleringsfuncties die door mijn onderzoek naar voren zijn gebracht.

In **Deel B** van dit proefschrift onderzoek ik een andere familie fosfolipasen: de glycerophosphodiester phosphodiesterase (of **GDPD**) familie. Net als autotaxine gaan GDPD's op zoek naar fosfolipiden om ze op specifieke plaatsen te knippen. In dit geval herkennen GDPD's een zeer complexe lipide die sommige eiwitten aan de cellen verankeren, zodat deze op het celoppervlak vast blijven zitten. Door het afknippen van dit *anker* (glycosylfosfatidylinositol of **GPI**) door de GDPD's kunnen specifieke eiwitten van het celoppervlak worden losgemaakt en bijvoorbeeld in het bloed terechtkomen, waar ze als *biomarker* voor kanker zou kunnen worden gevolgd. Dit is zo omdat sommige GDPD's eiwitten van het celoppervlak afknippen die cellen steeds opnieuw laten delen; de activiteit van dit type GDPD's houdt dus verband met een positieve prognose van

onder andere borstkanker en neuroblastoom.

In **Hoofdstuk B1** introduceer ik de belangrijkste aspecten van GPI-ankers, evenals de gevestigde biologie van twee leden van de GDPD eiwitfamilie: GDE2 en GDE3. Hoewel deze twee eiwitten in het plasmamembraan zitten, blijft GDE2 niet altijd op het celoppervlak aanwezig. Dit eiwit wordt door de cel naar binnen gevouwen in kleine blaasjes. Deze blaasjes binnenin de cel zorgen ervoor dat GDE2 zijn functie niet kan uitvoeren. Omdat de regulatie van cellulaire locatie cruciaal is voor enzymatische activiteit, bestudeer ik in **Hoofdstuk B2** welke onderdelen van GDE2 essentieel zijn voor het maken van deze blaasjes, door verschillende stukken van de aminozuursequentie van GDE2 weg te halen. Vervolgens analyseren we de rol van deze afgeknotte eiwitten en hun fenotypische effecten op neuroblastoom cellijnen. Gezien de vele bewijzen voor de rol van GDE2 en GDE3 in kwaadaardige kankers, ik heb me ook gewaagd aan de identificatie van nieuwe klinisch relevante substraten die ze kunnen herkennen en knippen. Een eerste stap in deze richting wordt gezet in **Hoofdstuk B3**, waar we laten zien dat contactines een aantrekkelijke en onbestudeerde eiwitfamilie zijn die wel door GDE3, maar niet door GDE2 herkend worden. Deze bevinding kan van belang zijn voor betere behandelingen van glioblastoma. Tenslotte bespreek ik in **Hoofdstuk B4** de belangrijkste bevindingen en implicaties van mijn werk aan de GDPD eiwitfamilie, met de nadruk op toekomstige onderzoeksrichtingen.

Resumen en español

Las enzimas llevan a cabo reacciones químicas esenciales para la vida; son los catalizadores de las células, que se unen a un *sustrato* para convertirlo en un *producto*. Las enzimas aparecen de muchas formas distintas: como proteínas individuales que ayudan a digerir los alimentos, como complejos proteicos que permiten la replicación de nuestro material genético o como enzimas basadas en ARN que permiten la producción de las proteínas.

Para cumplir todas estas funciones, las enzimas tienen que estar activas o inactivas dónde y cuándo sea necesario, por lo que requieren de una gran regulación que ocurre según la cantidad de sustrato que encuentren -lo que acelera las reacciones químicas- o en función de la cantidad de producto que ya se ha acumulado -para evitar que se forme más-. Hay mecanismos más sofisticados, como las moléculas o *moduladores* que se unen en la estructura de la enzima (conocido como sitio alostérico) o los fármacos que se unen a una enzima para evitar que se forme más producto.

Si las condiciones son las adecuadas y una enzima dada consigue generar un producto, este cumplirá una función biológica, como puede ser mantener el metabolismo en funcionamiento o activar una de las llamadas *ruta de señalización celular*. La señalización celular ocurre dentro de una célula o entre varias y les permite percibir lo que ocurre a su alrededor y para que den respuesta a preguntas acuciantes: «¿Hay suficiente oxígeno para respirar?», «¿Cuánta azúcar hay en la sangre?», «¿Es de día o de noche?», «¿Me multiplico o muero?».

Esta tesis se centra en las enzimas denominadas fosfolipasas, que realizan cortes en lugares específicos de los fosfolípidos. Estos lípidos se conocen comúnmente como los componentes básicos de las membranas de nuestras células, pero también son potentes moléculas de señalización celular, que modulan rutas para determinar el destino de una célula.

En la **Parte A** de esta tesis, estudio la fosfolipasa llamada **autotaxina (ATX)**, una enzima esencial que corta un tipo específico de lípidos: los lisofosfolípidos. De esta forma, cuando la autotaxina se encuentra con un lisofosfolípido que tiene una cabeza polar, la autotaxina lo separa y deja un nuevo lisolípido: los ácidos lisofosfatídicos (**LPA**). Existen varios tipos de LPA -con diferentes longitud de ácidos grasos o grado de insaturación- y todos ellos son necesarios para distintos procesos vitales, como son el desarrollo embrionario y la expansión de los vasos sanguíneos. No obstante, el LPA es la causa de muchas enfermedades, pues puede provocar la metástasis del cáncer, la inflamación y la fibrosis, entre otras patologías.

En el **Capítulo A1**, ofrezco una introducción general a la autotaxina, que abarca los conocimientos bioquímicos pertinentes desde su descubrimiento, así como un breve resumen de los diferentes fármacos que se han desarrollado para inactivarla. Mi laboratorio resolvió la estructura de la autotaxina hace una década, lo que reveló la existencia de un sitio triple para unión de moléculas: el **sitio tripartito** (representado artísticamente en la portada de esta tesis). Este sitio se encuentra dentro de la autotaxina y abarca el sitio activo donde tiene lugar la reacción enzimática; el bolsillo hidrofóbico, que aloja la cadena lipídica, y el sitio alostérico, el llamado **túnel**.

El **Capítulo A2** explora el papel del túnel y desvela un novedoso mecanismo de regulación, por el que el LPA producido acelera su propia síntesis tras unirse al túnel. Mediante una combinación de técnicas biofísicas, simulaciones de dinámica molecular y análisis cinéticos, concluyo el capítulo con un modelo completo de los estados de baja y alta actividad con los que funciona la autotaxina.

En las últimas dos décadas, se han diseñado muchos inhibidores para bloquear la actividad de la autotaxina. Al ver que el túnel es tan importante para la regulación de su actividad, mi laboratorio colaboró en la producción de un nuevo compuesto para bloquear tanto el túnel como el bolsillo hidrofóbico (tipo IV). En el **Capítulo A3**, presento como la síntesis de compuestos parecidos sirve para poder marcarlos radiactivamente, con el fin de emplearlos para tomografía por emisión de positrones (PET), es decir, para detectar de forma no invasiva la autotaxina en el cuerpo. En este proyecto, primero analizo el modo de unión de este fármaco a la autotaxina, para, a continuación, validar la eficacia del seguimiento por PET en modelos de enfermedad hepática.

En el **Capítulo A4**, describo el descubrimiento, la optimización y el funcionamiento de una nueva serie de inhibidores para la autotaxina que ocupan tanto el túnel como al sitio activo (tipo V). Esto representa un modo de acción complementario al de los compuestos que se unen al túnel y al bolsillo hidrofóbico (tipo IV) y que podría ser relevante para la clínica en el futuro.

Con el tiempo, se han producido inhibidores que se unen a partes distintas dentro del sitio tripartito, lo que permite clasificarlos en seis modos de unión distintos. En el **Capítulo A5**, reviso las estructuras de todos los compuestos disponibles, así como el sitio de unión que ocupan dentro de la autotaxina.

Teniendo en cuenta todos los modos de unión posibles, hasta la fecha sólo los compuestos que se unen al túnel han sido lo suficientemente eficaces como que se empleen en ensayos clínicos para el tratamiento de enfermedades fibróticas. Por ello, el **Capítulo A6** se centra en la posible aplicación de los inhibidores de la autotaxina en las enfermedades hepáticas.

Partiendo de los resultados prometedores que obtuvimos en los capítulos anteriores, decidí contrastar los compuestos PF8380 (tipo I) y Cpd17 (tipo IV) en líneas celulares hepáticas, para describir qué rutas de señalización se activan. Como Cpd17 disminuyó la mayor parte de los marcadores de enfermedad hepática -y en mayor medida que PF8380-, decidimos estudiar la eficacia de Cpd17 en modelos animales para enfermedad hepática. En este estudio, observamos una gran reducción de los niveles de triglicéridos, colesterol y transaminasas, lo que sugiere que la inhibición de la autotaxina por los compuestos de tipo IV puede ser relevante para el tratamiento de enfermedades hepáticas.

Puesto que en el capítulo anterior confirmamos que Cpd17 (tipo IV) funcionó mejor que PF8380 (tipo I), decidimos dar respuesta a una pregunta importante: ¿los inhibidores de tipo IV funcionan de forma distinta a los compuestos de tipo I? Para resolver esta incógnita, trabajamos con la empresa belgo-holandesa Galapagos NV para comparar los efectos de CpdA (tipo I) y el candidato clínico de fase 3 GLPG1690 (tipo IV). Así, el **Capítulo A7** se refiere a la comparación bioquímica y celular de estos dos tipos de fármacos, lo que desvela una función desconocida hasta el momento: la autotaxina permite el transporte selectivo del LPA a sus receptores en la superficie celular. Concluimos este estudio con una comparación de CpdA y GLPG1690 en modelos animales para fibrosis pulmonar, que respaldan nuestros resultados anteriores.

Además, mi trabajo sobre la autotaxina dio lugar a otras cinco publicaciones en colaboraciones de diversa índole que van desde el diseño de inhibidores hasta sus aplicaciones en inmunoterapia; estos trabajos de investigación se comentan brevemente en el **Capítulo A8**.

En el **Capítulo A9**, analizo la visión actual de las funciones enzimáticas y no enzimáticas de la autotaxina. Asimismo, examino cómo el éxito clínico de ciertos fármacos contra la autotaxina depende de su unión al túnel, pues este proceso inhibe las funciones de señalización celular descubiertas en mi investigación.

En la **Parte B** de esta tesis, investigo otra familia de fosfolipasas: la familia de las *fosfodiesterasas de glicerofosfodiésteres* (o **GDPD**). Al igual que la autotaxina, las GDPD buscan fosfolípidos para realizar cortes en sitios específicos; no obstante, las GDPD reconocen un lípido muy complejo presente en algunas proteínas a modo de *ancla* para que permanezcan sobre la superficie celular. La ruptura de este *anclaje* (llamado *glucosilfosfatidilinositol* o **GPI**) por parte de las GDPDs hace que una proteína específica se desprenda de la superficie celular para que viaje, por ejemplo, a la sangre, donde puede cumplir una función específica o emplearse como biomarcador del cáncer. Pese a que este campo de investigación es relativamente nuevo, la actividad de ciertas GDPDs se ha relacionado con un pronóstico positivo en el cáncer de mama y el neuroblastoma, entre

otros.

En el **Capítulo B1**, presento los aspectos más importantes de los anclajes por GPI, así como el conocimiento actual sobre dos miembros de la familia de proteínas GDPD: GDE2 y GDE3. Aunque ambas proteínas se insertan en la membrana plasmática, GDE2 no siempre permanece allí, pues puede pasar a vesículas dentro de la célula, donde no puede desempeñar su función. Como la regulación de la localización celular es vital para la actividad enzimática, en el **Capítulo B2** estudio los determinantes de este comportamiento por medio de la truncación de distintos tramos de la secuencia de aminoácidos C-terminal de la proteína GDE2. A continuación, analizamos el impacto que esto tiene en el tráfico intracelular en líneas celulares de neuroblastoma. Teniendo en cuenta la gran cantidad de información sobre el papel de la GDE2 y la GDE3 en los cánceres malignos, también me aventuré a identificar nuevos sustratos que pudieran ser clínicamente relevantes. Un paso preliminar en esta dirección se da en el **Capítulo B3**, donde muestro que las contactinas son una familia de proteínas muy interesante, pero poco estudiada, que son reconocidas por la GDE3, pero no por la GDE2. Este hallazgo puede ser relevante para mejorar los tratamientos de glioblastoma. Por último, en el **Capítulo B4** discuto las principales conclusiones e implicaciones de mi trabajo sobre la familia de proteínas GDPD, y hago hincapié en el enfoque que debería llevar esta investigación en el futuro.

Acknowledgements / Agradecimientos

To wrap it all up, here's the section most of you will read first 😊. Working at the NKI was a very important part of my life, both professionally and personally. Thanks to the lab, I grew a lot (some may even say "aged"), and built many new friendships with lots of nice people from very different backgrounds. In these next pages, I'll try to thank all of those who laughed and partied with me in the good times. I'll try to keep it short, but I'm a Spaniard, *i.e.* passionate.

I will start by thanking the person that gave me a chance when I was a naïve internship student. My promoter **Tassos**. Κύριε Πεπράκη, I really appreciate that you accepted me in your lab for the past six/seven years. Although you first offered me a six-month project that spectacularly failed within the first four weeks. You made sure I would not get demotivated and allowed me to collaborate with Frankie and Lisa on two different types of autotaxin's inhibitors. Through this you made me one of the proud discoverers of Compound 17. Later on you offered me a PhD position and patiently waited for me to come back from the dark side (in this case, immunology). During my PhD, you were nice enough to give me a main project (#1) that was also killed; this time, after two years, but made sure I could still fall back on the "safer" autotaxin projects. You were so active in starting up collaborations that I added a brand new project to my list for several weeks in a row, tallying up to a whopping 19 projects – including some secret ones. I'm very fortunate you spotted my scientific curiosity and allowed me to fly solo in many of my projects, and gave me plenty of freedom to simply explore science. I know you worry about my "I want to leave academia" thing now, but I'm sure that academia will always be a great place with promoters like you. I am confident you'll have the same effect on the next students. Σας ευχαριστώ για όλα αυτά τα χρόνια, κύριε Πεπράκη.

Natuurlijk moet ik **Willem** ook bedanken voor al de tijd die hij aan mijn stage besteedde. Ik geef toe dat ik je wetenschappelijke passie bewonderde, met het gevolg dat ik naar meer zou streven in mijn onderzoek, zowel toen als nu nog steeds. Verder kan ik je beloven dat mijn schrijven veel beter is geworden dan wat je op de eerste versie van mijn verslag moest lezen! On the same note, I wouldn't have known my way around an Äkta™ without the help of **Tati**. You were very instructive and made everything so clear that I still remember several of your do's and don'ts while working in the lab. Thank you as well for all the crystal fishing! **Sasha**, it was partly thanks to you that I joined the NKI after hearing you explain all the biophysics equipment in the lab during my master's. Your help and enthusiasm during my internship and PhD made difficult things seem straightforward. Thanks a lot for that and for all the interesting conversations we've had on all possible topics!

There were two people who really helped me get off to a good start in my PhD. **Elisa**, además de nuestro mutuo apoyo emocional, todas tus explicaciones sobre el trabajo en el laboratorio y en biología celular fueron de un valor incalculable en el resto de mi doctorado. Todo el mundo lo sabe, pues me encuentro diciendo «según Elisa» bastante a menudo. ¡Gracias por el tiempo que invertiste en mí! **Wouter**, ik waardeer al je hulp met schrijven en met bedenken van experimenten. Verder heb je aan mij heel veel kennis overgebracht. Dankzij jou kon ik zonder twijfel beter op de hoogte blijven van wat nieuw was in onze gezamenlijke projecten, daarvoor ben ik je erg dankbaar.

During my PhD I had the privilege to supervise three talented people in the lab. **Jen**, it was a pleasure to collaborate with you. I learned a lot about the organic chemists' perspective, and I have to say that I'm still in awe by how fast you grasped the basics of cell biology in our lab. **Loraine**, ik ben heel trots dat ik je begeleider tijdens je masterstage kon zijn. Ik waardeerde dat je een heel globaal overzicht over meerdere projecten wilde hebben; van je vragen heb ik ook veel geleerd. Ik ben heel bij dat je stage met mij jou heeft geholpen om besluiten te nemen over je carrière. Heel veel succes gewenst in je PhD! **Răzvan**, I enjoyed working and troubleshooting with you. I am sure you'll find that *harder project* you're looking for, and you'll make it work. It feels like I'm passing the baton to you, so make Tassos proud! *Mult noroc!*

Ik wil graag **Titia**, **Kees** en **Arnoud** bedanken voor hun inzicht en steun tijdens mijn voortgangsevaluaties. Samen met Wouter gaven jullie mij het gevoel dat ik op jullie kon vertrouwen in geval dat het nodig zou zijn. Verder hebben jullie op verschillende manieren bijgedragen aan mijn projecten met nieuwe ideeën, reagentia en contactpersonen voor samenwerkingen, dus heel erg bedankt daarvoor.

Besides the people who actively helped me get my PhD, there were plenty of colleagues in my department who kept me going. They made this possible through group outings, escape rooms, trips, Friday *borrels*, and many, many coffee breaks (usually without coffee).

I want to start by thanking three very special PhD students in the department. **Susanita**, sharing these past years with you as an officemate have been simply *großartig*. You're somehow both a very knowledgeable scientist and a party animal in the same being, so it's always nice to have you around, even when you're a little bossy ;-). Also, you're many attempts to get me to use a bike will not be forgotten! **Jitskita**, je bent aan de beurt! Toen ik je voor het eerst zag dacht ik: "Oh, jeetje. Nu moet ik midden in een pandemie mijn kantoortje delen met iemand die de hele dag aan het hoesten en niezen is". Gelukkig zag ik snel veel meer dan hooikoorts in jou, en ik moet zeggen dat het echt een eer was om samen met zo'n slimme, grappige en inzichtelijke persoon te werken als jij. Ik wens je heel veel succes met de rest van je PhD. Zorg goed op ons kantoortje! En nu, wat kan ik zeggen

over **Bart**? Je verliet het lab al een tijdje geleden (meer dan de helft van mijn PhD...), maar voor een lange tijd was je mijn onafscheidelijke maat bij de borrels. Ik merkte echter pas hoe goed ik jou kende ik in jouw afscheidsfilm de hoofdrol moest spelen. ¡Muchas gracias por haberme hecho sentir en casa desde el primer día!

There have also been three very friendly (student) technicians in the lab that made forget about my negativity. **Foteini** (Φωτεινούλα), I don't know how you did it, but you were happy even while being exhausted. You made me enjoy the beginning of my PhD a lot, through festivals or by telling each other how much we liked our clothes almost every day. I am very lucky to have kept a friend like you for all these years! **Justina** (Justinita), I love how similar we are and how we can count on each other for many things, be it science, job applications or personal advice. I wish you, Arvydas and Rikis all the best, but don't worry, I'll come visit you again in Alphen very soon! **María** (Μαράκι), even though lockdown was in the way, we had so much fun with the peeps from Louweshoek (and Gian-Luca) at *borrels*, at Macumba, in Zeeland or simply exploring Amsterdam. And how nice was it to learn Dutch from me with Justina?! I hope you're still practising it in Greece!

Moreover, there are a few postdocs that made my life at the NKI more enjoyable. **Andrea**, thanks for all your good advice, and the many *borrels* we shared. **Xiaohu**, thanks for the Chinese food and the introduction to Cryo-EM! **Torben** (Torbie, an honorary postdoc in my mind), congrats on your (upcoming) wedding! Thanks for all the bad movies, the dirty jokes and for keeping everything running. **Gian-Luca** Joseph McLelland, c'était toujours amusant de faire des choses avec toi en écoutant tes commentaires politiquement incorrects. De plus, merci de m'avoir rapproché de la culture québécoise à travers Jérôme 50, parmi d'autres. **Shun**, danke schön, dass du mir ein bisschen geholfen hast, Deutsch zu sprechen. Ich hoffe, dass das letzte Jahr deines Postdocs sehr produktiv sein wird. Wenn ich weiß, wohin ich als Nächstes gehe, lade ich dich ein! And to all of you, best of luck in the future!

I also want to single out two people without whom the lab would break into pieces. **Mirna**, je bent een waanzinnige secretaresse. Ik heb weinig personen ontmoet die zo efficiënt voor zo veel verschillende mensen kunnen werken. Bedankt dat je alles zo gemakkelijk hebt gemaakt. **Yvette**, min of meer geldt hetzelfde voor jou. Je droeg veel bij aan mijn projecten door te adviezen voor kloneren, celkweek en IP's. Dankzij jou blijft het lab, tot nu toe, in één stuk.

I also want to thank all the other B8 members that I had the pleasure to get to know. From the **Perrakis/Sixma/Protein facility** ensemble: Robbie, Ida, Ren, Maarten, George, Yoshi, Will, Wouter, Elli, Misbha, Hans (Wienk and Janssen), Robbert, Sanket, Nina, Luca, Doreth, Niels, Anu, Shreya, Farid, Roy, Patrick, Magda, John, Danique, Pim & Herrie, Boğaç,

Ismail, Jan, Ivette, Lisa (Engelhardt), Michael, Lois and Bas. From the **Brummelkamp** group: Thijn, Lisa (van den Hengel and Landskron), Abdel, Astrid, Danielle, Nicolaas, Marta, Peter, Vincent, Joppe, Jacqueline, Markus, Matthijs, Elmer and Lucas. Lastly, I wanted to thank **Mohammed**, for keeping the lab and the offices clean, and for always practising his Spanish with me.

However nice everyone at my department clearly was, there have been many fun people close to me elsewhere at the NKI, but I'd like to highlight **Felipe** (Felipito, Pipes), **Nils**, **Mila** and **Heta**. Though in different groups of friends, I had lots of fun with you all and felt at home whenever I was with you. So thanks a lot for being there for each other during our PhDs! I also wanted to thank everyone that I met and had fun with at the NKI *borrel*. It was very nice to meet all of you and I'm sure we'll stay in touch!

Some (brilliant) people have described the NKI as being my wife. Well, in many ways this is true: I've shared most workdays and weekends with it, and I've had an emotional attachment to it. However, there have been two constant pillars in my life in Amsterdam that stood the test of time. **Nathalie** and **Vanessa**, we three started our journey in Amsterdam at the same time, and what a ride it's been. We've changed a lot, had our ups and downs, but we always find a way to meet up and have fun. I love how our plans evolved from chasing Nat in Antwerp and going on a *sprps.me* trip to Poland, to housewarming and 30th birthday parties. We still manage to party all night long, so there are no problems at sight! Other very nice people I've had lots of fun with these past years in Amsterdam are: Jose, Alba, Yike, Lisette, Frederique, Juliette, Oli, Elmo, Sandra, Julian, Selina, Tes, Dani, Dani, Onur, Graham, Pia and Nick.

Vacation is essential for mental health, and several times a year this is what Spain has meant for me. Here I have to thank my *bestest* friends in Cáceres and Madrid. **Mónica**, 二力ちゃん、こんにちは。El mes de mi defensa hace trece años que nos conocemos, que se dice pronto, pero hemos conseguido seguir siendo amigos en la distancia sin que cambie nada (salvo que te casas). Me viniste a visitar a Ámsterdam y sé que te quedaste con ganas de venir otra vez. Espero que en el futuro disfrutemos de muchos más viajes juntos. **Chachis**, llevamos siendo amigos más de diez años y todavía ahora, cuando nos vemos, me da la sensación de que sigamos en el Sanagus hablando sin fin después de cenar. Como me apetece haceros la pelota un poco, estas son algunas cosas con las que me habéis ayudado en el doctorado. **Alejandro**, amb tu he pogut aprendre una nova llengua, que no és poc, i les nostres moltes converses per telèfon m'han ajudat a oblidar-me dels meus problemes i recordar les coses que importen de veritat. **Elena**, obviamente tú has sido de ayuda siempre que hemos salido de fiesta, ya sea en limusina o en chándal, cuando hemos visto Eurovisión todos juntos o yendo de viaje a Murcia (perdón, Cartagena). **Flavia**, tu m'as aidé avec nos cours de français très décontractants, ainsi que quelques

voyages en Allemagne, en France et à Malte. Je ne pense pas que j'aurais réussi le DALF sans nos conversations. **Naywa**, *yiuos* hija, pues tú me has ayudado mucho dándome paz mental con tus memes y escuchándome cuando te he necesitado. (He seguido un estricto orden alfabético; es como con los hijos: no hay preferencias).

Saving the best for last: my family. **Mamá y papá**, muchas gracias por todo el esfuerzo que invertisteis en mí para que me formase en Madrid y para que pudiese estudiar el máster en Países Bajos. Sin vosotros y vuestro apoyo no podría haber hecho nada de esto, por lo que esta tesis más vuestra que mía. ¡Muchos besos y abrazos! **Laura**, ¿quién no quiere aspirar a más cuando tienes una hermana mayor a la que admiras, pero que también te hace rabiar? Pues resulta que esa ambición y aspiración que he tenido desde hace muchos años vienen en gran parte de ti. Dices a menudo que somos iguales, pero en muchos sentidos -idiomas, estudiar en Madrid, etc.- soy lo que tú inspiraste, así que ¡muchas gracias! **Pablo**, espero que dentro de unos años leas esto y sepas que tu tío Fer se acuerda mucho de ti todos los días aunque estemos en países distintos. ¡Estoy seguro de que vas a hacer cosas increíbles cuando seas mayor! **El resto de mi familia**, muchas gracias a todos y cada uno por haber estado ahí en lo bueno y en lo malo. Con esta tesis puedo decir por fin que soy doctor (pero no médico) en Bioquímica y eso es gracias a vosotros.

